
Designing Multicaloric Materials with Martensitic Phase Transitions for Future Cooling Applications

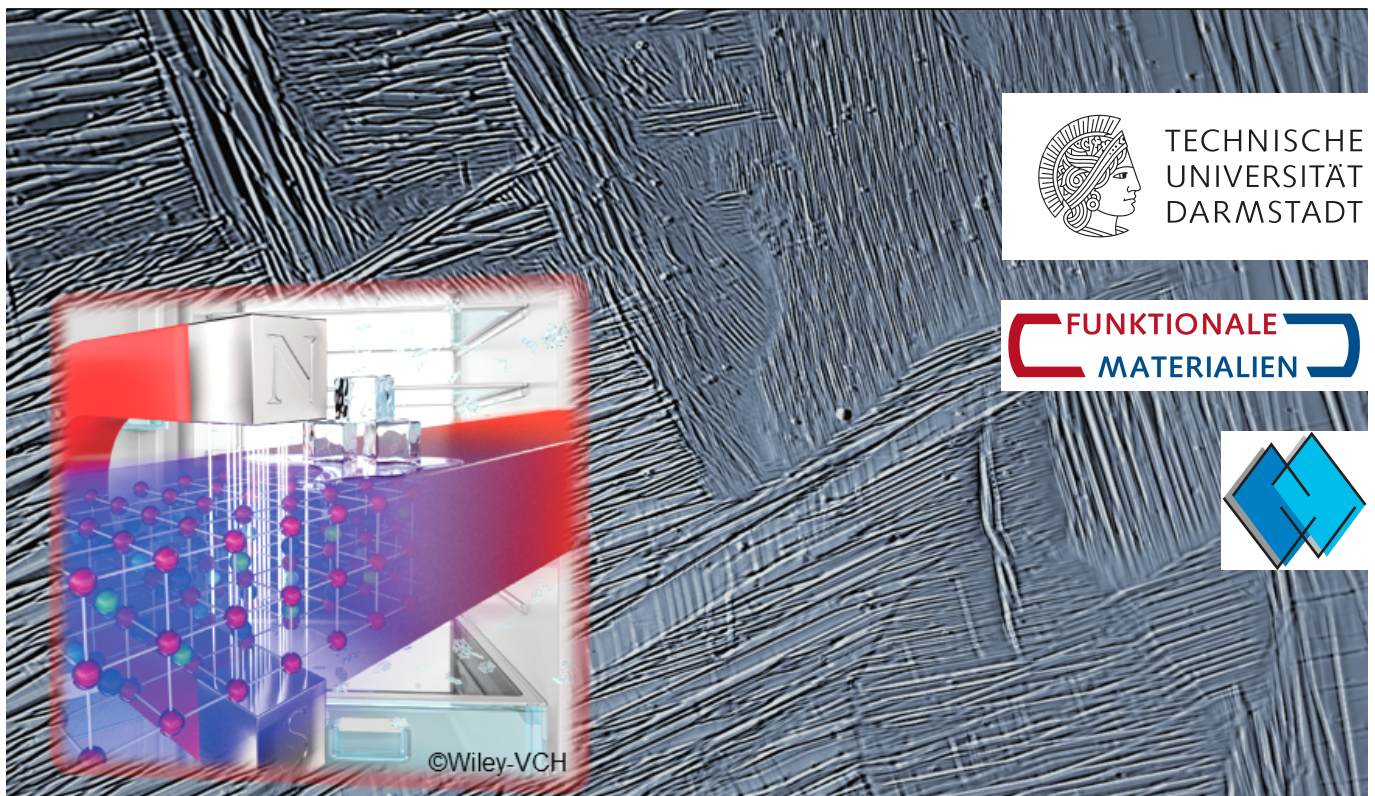
Design-Strategien für multikalorische Materialien mit martensitischem Phasenübergang für zukünftige Kühlanwendungen

Zur Erlangung des akademischen Grades Doktor-Ingenieur (Dr.-Ing.)

Genehmigte Dissertation im Fachbereich Material- und Geowissenschaften von Andreas Taubel aus Gelnhausen

Tag der Einreichung: 13. Oktober 2020, Tag der Prüfung: 9. Dezember 2020

1. Gutachten: Prof. Dr. Oliver Gutfleisch (Technische Universität Darmstadt)
2. Gutachten: Prof. Dr. Heiko Wende (Universität Duisburg-Essen)
Darmstadt



Designing Multicaloric Materials with Martensitic Phase Transitions for Future Cooling Applications
Design-Strategien für multikalorische Materialien mit martensitischem Phasenübergang für zukünftige
Kühlanwendungen

Genehmigte Dissertation im Fachbereich Material- und Geowissenschaften von Andreas Taubel

1. Gutachten: Prof. Dr. Oliver Gutfleisch (Technische Universität Darmstadt)
2. Gutachten: Prof. Dr. Heiko Wende (Universität Duisburg-Essen)

Tag der Einreichung: 13. Oktober 2020

Tag der Prüfung: 9. Dezember 2020

Darmstadt

Bitte zitieren Sie dieses Dokument als:

URN: urn:nbn:de:tuda-tuprints-173651

URL: <http://tuprints.ulb.tu-darmstadt.de/17365>

Dieses Dokument wird bereitgestellt von tuprints,
E-Publishing-Service der TU Darmstadt

<http://tuprints.ulb.tu-darmstadt.de>

tuprints@ulb.tu-darmstadt.de



Die Veröffentlichung steht unter folgender Creative Commons Lizenz:

Namensnennung – Keine kommerzielle Nutzung – Keine Bearbeitung 4.0 International

<http://creativecommons.org/licenses/by-nc-nd/4.0>

Erklärungen laut Promotionsordnung

§8 Abs. 1 lit. c PromO

Ich versichere hiermit, dass die elektronische Version meiner Dissertation mit der schriftlichen Version übereinstimmt.

§8 Abs. 1 lit. d PromO

Ich versichere hiermit, dass zu einem vorherigen Zeitpunkt noch keine Promotion versucht wurde. In diesem Fall sind nähere Angaben über Zeitpunkt, Hochschule, Dissertationsthema und Ergebnis dieses Versuchs mitzuteilen.

§9 Abs. 1 PromO

Ich versichere hiermit, dass die vorliegende Dissertation selbstständig und nur unter Verwendung der angegebenen Quellen verfasst wurde.

§9 Abs. 2 PromO

Die Arbeit hat bisher noch nicht zu Prüfungszwecken gedient.

Darmstadt, 13. Oktober 2020

A. Taubel

Abstract

The demand for cooling devices and the corresponding energy costs are constantly expanding, driven by the growth of global population and the economies of fast-developing countries in warm climates. Novel caloric cooling solutions are an alternative that do not rely on environmentally harmful refrigerants and can provide a better energy-efficiency compared to the conventional vapor-compression technology. Especially magnetocaloric cooling is in focus of research activities including material research and well-performing device development. In order to optimize the material, many requirements need to be taken into account and each material system behaves differently under the application of an external magnetic field. This work focuses on the development of the MM'X material family with a conventional magnetocaloric effect and the various systems of Heusler alloys showing the inverse magnetocaloric effect. Both systems have in common that they experience a martensitic transition between a high-magnetization and a low-magnetization state.

The MM'X base system of MnNiGe can be tuned by the isostructural alloying method, which is investigated in detail in this work. Therefore, Mn is substituted partially by Fe as well as Ge by Si. This enhances the magnetization change of the magnetostructural phase transition, reduces the amount of expensive Ge and allows for tailoring the transition temperature. The resulting alloys show very large isothermal entropy changes for small pieces of material. A difficulty that arises for this system is the mechanical integrity together with the low magnetic-field dependence of the transition temperature. The very good sensitivity of the transition towards hydrostatic pressure reveals barocaloric purposes as a very attractive field of application for these materials.

A direct comparison with the versatile family of Ni-Mn-based Heusler alloys underlines their high potential for magneto- and multicaloric applications. With stoichiometric changes, the phase transition can be adjusted and also the magnetic-field dependence of the transition temperature is found to scale directly with the difference of the transition temperature to the austenite Curie temperature. The most promising system for low magnetic field changes is Ni(-Co)-Mn-In. Even though Ni(-Co)-Mn-Sn shows similar isothermal entropy changes, adiabatic temperature changes cannot compete. The drawback of a significant thermal hysteresis of around 10 K to 15 K, which hinders a good cyclic performance of Heusler alloys, can be turned into an advantage by considering the novel approach of a multi-stimuli cycle, which exploits the thermal hysteresis to lock the material completely in its transformed state after a magnetic-field application. The necessary reverse transformation can be carried out by the application of pressure/stress as a second stimulus requiring a good pressure/stress-sensitivity of the transition temperature. Among the Heusler alloys, the novel all-*d* Heusler alloys of Ni-Co-Mn-Ti represent a promising material system for this approach. Their magnetocaloric performance is compared to the other Heusler alloys in small magnetic field changes of 2 T as well as for higher and faster field changes since the multi-stimuli approach allows for concentrated magnetic fields. Detailed investigations on the microstructure give insights that are crucial in order to understand the transition behavior. Analyzing the temperature-, magnetic field-, and pressure-induced phase transitions allows for assessing the potential of using the different Heusler systems for magnetocaloric and/or multicaloric cooling applications. This thesis puts the general properties of different material systems in a broad context and aims at providing principal design rules for the studied systems in order to develop and tailor well-performing caloric materials.

Zusammenfassung

Wir leben in einer Zeit, in der die Weltbevölkerung stetig anwächst, ebenso wie die Nachfrage an leistungsstarken Kühlgeräten speziell in Länder mit sich rasant entwickelnder Wirtschaft in warmen Regionen der Erde. Neuartige kalorische Kühlanwendungen sind eine Alternative, die nicht auf umweltschädliche Kältemittel angewiesen ist und im Vergleich zu herkömmlichen Gaskompressionsgeräten eine bessere Energieeffizienz bieten kann. Um potentielle Materialien zu optimieren, müssen viele Anforderungen berücksichtigt werden und jedes Materialsystem verhält sich unter Anlegen eines externen Magnetfelds unterschiedlich. Diese Arbeit konzentriert sich auf die Entwicklung der MM'X-Materialfamilie mit einem konventionellen magnetokalorischen Effekt sowie verschiedene Heusler-Legierungen, die einen inversen magnetokalorischen Effekt zeigen. Beiden Systemen ist gemeinsam, dass sie einen martensitischen Übergang zwischen einem Zustand hoher Magnetisierung und einem Zustand niedriger Magnetisierung besitzen.

Das MM'X-System aus MnNiGe kann durch das in dieser Arbeit ausführlich untersuchte isostrukturelle Legierungsverfahren variiert werden. Dabei wird Mn teilweise durch Fe sowie Ge durch Si substituiert. Dies verbessert die Magnetisierungsänderung des magnetostrukturellen Phasenübergangs, verringert die Menge an teurem Ge und ermöglicht die Anpassung der Übergangstemperatur. Die resultierenden Legierungen zeigen sehr große isotherme Entropieänderungen für kleine Fragmente. Eine Schwierigkeit dieses Systems ist die mechanische Beständigkeit zusammen mit der geringen Magnetfeldabhängigkeit der Übergangstemperatur. Die sehr gute Empfindlichkeit des Übergangs gegenüber hydrostatischem Druck zeigt, dass barokalorische Systeme ein geeigneteres Anwendungsgebiet für diese Materialien sein können.

Ein direkter Vergleich mit verschiedenen Heusler-Legierungen auf Ni-Mn-Basis unterstreicht deren hohes Potenzial für magneto- und multikalorische Anwendungen. Durch Anpassen der Stöchiometrie kann sowohl der Phasenübergang als auch die Magnetfeldabhängigkeit der Übergangstemperatur gezielt eingestellt werden. Das vielversprechendste System für geringe Magnetfeldänderungen ist Ni(-Co)-Mn-In. Obwohl Ni(-Co)-Mn-Sn ähnliche isotherme Entropieänderungen zeigt, sind die erzielbaren adiabatischen Temperaturänderungen deutlich geringer. Eine nachteilige thermische Hysterese von etwa 10 K bis 15 K, die eine gute zyklische Leistung von Heusler-Legierungen verhindert, kann durch den neuartigen Ansatz eines Multi-Stimuli-Zyklus zu einem Vorteil umgesetzt werden. Dabei wird die thermische Hysterese genutzt um das Material nach einer Magnetfeldanwendung vollständig in seinem transformierten Zustand zu erhalten. Die notwendige Rückumwandlung kann durch Anlegen von Druck als zweitem Stimulus durchgeführt werden. Unter den Heusler-Legierungen stellen die neuartigen all-*d*-Heusler aus Ni-Co-Mn-Ti ein vielversprechendes Materialsystem für diesen Ansatz dar. Ihre magnetokalorischen Eigenschaften werden mit anderen Heusler-Legierungen vor allem bei höheren und schnelleren Feldänderungen verglichen, da der Multi-Stimuli-Ansatz konzentrierte oder gepulste Magnetfelder ermöglicht um ein möglichst geringes Volumen einer Magnetfeldquelle zu nutzen. Durch die Analyse der temperatur-, magnetfeld- und druckinduzierten Phasenübergänge kann das Potenzial der Verwendung der Heusler-Systeme für magnetokalorische und/oder multikalorische Kühlanwendungen bewertet werden. Diese Arbeit setzt die verschiedenen Eigenschaften der untersuchten Systeme in einen größeren Kontext und zielt darauf ab, grundlegende Regeln herauszuarbeiten, um leistungsfähige kalorische Materialien weiterzuentwickeln und gezielt auf Anwendungsbedürfnisse anzupassen.

Contents

List of Figures	ix
List of Tables	xiii
Nomenclature	xv
1 Introduction and Motivation	1
2 Fundamentals	5
2.1 Fundamentals of phase transitions	5
2.1.1 Martensitic phase transitions	6
2.2 Caloric solid-state cooling effects	8
2.2.1 Magnetocaloric effect and device implementation	8
2.2.2 Multicaloric effects	14
2.3 Magnetocaloric materials	17
2.3.1 Heusler alloys	23
2.3.2 MM'X alloys	25
2.4 Material requirements for the multi-stimuli cycle	26
3 Experimental Methods	31
3.1 Sample preparation	31
3.2 Structural characterization	32
3.3 Microstructure investigations	32
3.4 Magnetic and magnetocaloric characterization	33
3.4.1 Isothermal entropy change	34
3.4.2 Adiabatic temperature change and strain in low fields	36
3.4.3 Fast pulsed magnetic field measurements	38
3.5 Simultaneous measurement setup in quasi-stationary high fields	40
3.6 Calorimetry	42
3.7 Mechanical characterization	43
4 Ni-Mn-based Heusler Compounds	45
4.1 Optimizing the heat treatment	47
4.2 Tuning the properties of the martensitic phase transition	51
4.3 Magnetocaloric performance in low magnetic fields	55
4.4 Magnetocaloric performance in high magnetic fields	59
5 Novel all-<i>d</i>-metal Heusler Alloys	65
5.1 Optimization of the heat treatment	65

5.2	Influence of stoichiometry and magnetic field on the phase transitions	69
5.3	Microstructure evolution of the martensitic phase transition	71
5.4	Magnetocaloric properties in low magnetic fields	83
5.5	Magnetocaloric properties in high magnetic fields	85
5.6	Simultaneous sample characterization	95
5.7	Correlation of microstructure and mechanical properties for a multi-stimuli cooling cycle .	107
6	The MM'X Material Family	115
6.1	Effects of stoichiometry - the method of isostructural alloying	116
6.1.1	Thermomagnetic properties of the tuned phase transition	117
6.1.2	Magnetocaloric properties	121
6.2	Structural results for varying the stoichiometry	124
6.3	Analyzing microstructure and mechanical stability	130
6.4	Effect of magnetic fields on the phase transition	134
6.5	Magnetocaloric effects in high magnetic fields	138
6.6	Effect of hydrostatic pressure	144
6.7	Reducing criticality by Ge-elimination	147
7	Principal Design Rules for Magneto- and Multicaloric Compounds	151
7.1	Designing magnetocaloric compounds by experiment and theory	151
7.2	Assessing the potential of Heusler alloys for a multi-stimuli cycle	156
8	Conclusions and Outlook	159
	Bibliography	165
	Curriculum vitae	189
	List of Publications	191

List of Figures

1.1	Development of global air-condition devices until 2050.	2
2.1	Overview on the different kinds of caloric solid state cooling effects and working principle of caloric cooling cycle.	9
2.2	Schematic temperature-dependent magnetization and entropy evolution for second- and first-order phase transitions with and without external magnetic fields.	12
2.3	Description of necessary steps for a multi-stimuli cooling cycle using magnetic field and pressure.	16
2.4	Necessary properties to be optimized for a magnetocaloric cooling system.	18
2.5	Cyclic magnetocaloric performance and criticality of most prominent magnetocaloric materials under cycling in magnetic-field changes of 1 T and 2 T.	20
2.6	Heusler ($L2_1$) structure and B2 disorder for X_2YZ compounds.	23
2.7	Schematic depiction of a phase diagram for the binary system of MnNiGe and FeNiGe.	26
2.8	Schematic representation of the necessary steps for an optimal multi-stimuli cooling cycle of an inverse magnetocaloric material.	28
3.1	Schematic representation of the phase reset protocol for correct determination of ΔS_T for first-order magnetocaloric materials.	36
3.2	Schematic measurement setup for the simultaneous measurement of ΔT_{ad} and strain.	37
3.3	Measurement curves of ΔT_{ad} for second-order and first-order inverse MCE.	38
3.4	Sample setup for simultaneous measurements of strain and ΔT_{ad} in pulsed magnetic fields.	39
3.5	Time-dependent profiles and field rates of the magnetic-field pulses for the measurement setup of the HLD at HZDR.	40
3.6	Schematic measurement setup for the simultaneous measurement of magnetization, strain, and electrical resistance in the PPMS.	41
4.1	Comparison of $M(T)$ -curves for as-cast and annealed $Ni_{49.8}Mn_{35.0}In_{15.2}$	48
4.2	Influence of annealing temperature on the $M(T)$ -curves for Ni-Mn-In, Ni-Co-Mn-Al, and Ni-Mn-Sn together with DSC measurements.	49
4.3	$M(T)$ -curves at T_t and T_C^A for post-annealing of $Ni_{49.8}Mn_{35.0}In_{15.2}$ at different temperatures.	50
4.4	$M(T)$ -curves for Ni(-Co)-Mn-In, Ni(-Co)-Mn-Sn, and Ni(-Co)-Mn-Al as well as the correlation of A_s with the e/a ratio, the magnetic field dependence of T_t , and the thermal hysteresis.	53
4.5	Directly measured ΔT_{ad} for first field application and upon cycling for Ni(-Co)-Mn-Al, Ni(-Co)-Mn-Sn and Ni(-Co)-Mn-In Heusler systems.	57
4.6	ΔS_T and ΔT_{ad} for $Ni_{50}Mn_{35}In_{15}$ post-annealed at different temperatures.	58
4.7	Measurements of ΔT_{ad} in pulsed magnetic fields between 2 T and 50 T for $Ni_{45}Co_5Mn_{31}Al_{19}$	60
5.1	$M(T)$ -curves and T_C^A for varying annealing temperature and time for $Ni_{37}Co_{13}Mn_{34}Ti_{16}$	66

5.2	Temperature-dependent magnetization measurements showing the martensitic transition and T_C^A for selected samples of the $\text{Ni}_{50-x}\text{Co}_x\text{Mn}_{50-y}\text{Ti}_y$ series.	69
5.3	Phase diagram of all $\text{Ni}_{50-x}\text{Co}_x\text{Mn}_{50-y}\text{Ti}_y$ compounds as a function of e/a and $\frac{dT_t}{\mu_0 dH}$ depending on $T_C^A - T_t$	70
5.4	Microstructure of as-cast and ideally annealed sample obtained by BSE imaging.	72
5.5	Optical microscopy images for the as-cast microstructure of $\text{Ni}_{37}\text{Co}_{13}\text{Mn}_{34}\text{Ti}_{16}$ in comparison to different heat treatments.	73
5.6	Temperature-dependent microstructures for two different heat treatments of $\text{Ni}_{37}\text{Co}_{13}\text{Mn}_{34}\text{Ti}_{16}$	75
5.7	Comparison of optically observed transition temperature and the calculated one from a stoichiometry determination by EDS.	76
5.8	Martensite of $\text{Ni}_{37}\text{Co}_{13}\text{Mn}_{34}\text{Ti}_{16}$ at different magnifications.	77
5.9	Microstructures of austenite and martensite after several thermal cycles with and without an external magnetic field.	80
5.10	Martensite formation upon magnetic-field removal for $\text{Ni}_{37}\text{Co}_{13}\text{Mn}_{34}\text{Ti}_{16}$	82
5.11	Δs_T and ΔT_{ad} of $\text{Ni}_{50-x}\text{Co}_x\text{Mn}_{50-y}\text{Ti}_y$ for magnetic-field changes of 2 T.	84
5.12	Heat capacity and total entropy of $\text{Ni}_{37}\text{Co}_{13}\text{Mn}_{34.5}\text{Ti}_{15.5}$ in different external magnetic fields.	87
5.13	$M(H)$ measurement up to 14 T and magnetic-field-dependent shift of T_t to estimate the maximum MCE for $\text{Ni}_{37}\text{Co}_{13}\text{Mn}_{34.5}\text{Ti}_{15.5}$	89
5.14	Maximum Δs_T and ΔT_{ad} of $\text{Ni}_{37}\text{Co}_{13}\text{Mn}_{34.5}\text{Ti}_{15.5}$ for high magnetic-field changes.	91
5.15	Comparison of temperature- and field-dependent measured Δs_T and ΔT_{ad} with the $S(T)$ -diagram determined from c_p measurements.	94
5.16	Magnetic-field-dependent adiabatic temperature change and strain in pulsed fields of 10 T.	95
5.17	Magnetic-field-dependent adiabatic temperature change and strain in pulsed fields of 20 T.	97
5.18	Comparison of the magnetic-field-dependent ΔT_{ad} and ε_L for different maximum magnetic fields and comparison of the two measured directions of the strain gauges.	98
5.19	Temperature- and time-dependent evolution of the sample strains for two consecutive temperature cycles and for an integrated holding time in the transition region.	99
5.20	Direct comparison of ΔT_{ad} and ε_L for different field application rates and for the temperature-dependent maximum effect.	102
5.21	Comparison of temperature-dependent maximum ΔT_{ad} measured in slow field-change rates of a rotating Halbach setup with the corresponding ΔT_{ad} in pulsed fields.	103
5.22	Temperature- and field-dependent simultaneous measurements of magnetization M , strains ε_L and ε_{II} , and electrical resistivity ρ of $\text{Ni}_{37}\text{Co}_{13}\text{Mn}_{34.5}\text{Ti}_{15.5}$ in magnetic fields up to 14 T.	105
5.23	Stress-strain measurements by compression tests of Ni-Co-Mn-Ti alloys.	108
5.24	Microstructure of the as-cast state and after annealing for two different suction-cast rods of $\text{Ni}_{37}\text{Co}_{13}\text{Mn}_{34}\text{Ti}_{16}$	110
5.25	$M(T)$ -curves and corresponding stress-strain measurements of Ni-Co-Mn-Ti suction cast rods for different annealing conditions.	111
5.26	Temperature-dependent strain measurements of $\text{Ni}_{36}\text{Co}_{14}\text{Mn}_{35}\text{Ti}_{15}$ suction cast rod.	112
6.1	Substitution scheme for isostructural alloying of MM'X compounds.	117
6.2	$M(T)$ -curves and $M(H)$ -curves for the $\text{Mn}_{1-x}\text{Fe}_x\text{NiGe}$ system.	118
6.3	$M(T)$ -curves and $M(H)$ -curves for the $\text{Mn}_{1-x}\text{Fe}_x\text{NiGe}_{1-y}\text{Si}_y$ system together with the evolution of T_t and ΔT_{hyst} as a function of the e/a ratio.	119
6.4	Isothermal entropy change for Fe- and Si-substituted MnNiGe samples.	122
6.5	Measurements of ΔT_{ad} for selected samples of the $\text{Mn}_{1-x}\text{Fe}_x\text{NiGe}_{1-y}\text{Si}_y$ series.	123

6.6	XRD patterns and Rietveld refinements of orthorhombic and hexagonal phase for the $\text{Mn}_{1-x}\text{Fe}_x\text{NiGe}$ system.	125
6.7	XRD patterns and one exemplary Rietveld refinement for the $\text{Mn}_{1-x}\text{Fe}_x\text{NiGe}_{1-y}\text{Si}_y$ system.	126
6.8	Temperature-dependent lattice constants of hexagonal and orthorhombic phase together with volume change, lattice constants, and Mn-Mn distances as a function of e/a for all $\text{Mn}_{1-x}\text{Fe}_x\text{NiGe}_{1-y}\text{Si}_y$ compounds.	128
6.9	Microstructural images of the $\text{Mn}_{1-x}\text{Fe}_x\text{NiGe}_{1-y}\text{Si}_y$ series by optical light microscopy using polarized light.	132
6.10	Magnetization and Δ_{sT} measurements for single piece, loose powder and epoxy bonded powder of $\text{Mn}_{0.84}\text{Fe}_{0.16}\text{NiGe}$	133
6.11	Shift of transition temperatures for externally applied magnetic fields for $\text{Mn}_{0.7}\text{Fe}_{0.3}\text{NiGe}_{0.7}\text{Si}_{0.3}$ and the $\text{Mn}_{1-x}\text{Fe}_x\text{NiGe}_{1-y}\text{Si}_y$ series.	135
6.12	$M(T)$ -, $M(H)$ -curves, and Δ_{sT} in magnetic-field changes of up to 10 T for $\text{Mn}_{0.82}\text{Fe}_{0.18}\text{NiGe}$	138
6.13	DSC measurement and resulting c_p/T for $\text{Mn}_{0.82}\text{Fe}_{0.18}\text{NiGe}$	139
6.14	$M(T)$ - and $M(H)$ -curves of $\text{Mn}_{0.84}\text{Fe}_{0.16}\text{NiGe}$ for a single piece and as bonded powder with silver epoxy in slow magnetic fields up to 14 T.	141
6.15	$M(H)$ -curves of $\text{Mn}_{0.84}\text{Fe}_{0.16}\text{NiGe}$ in form of powder bonded with silver epoxy and as loose powder in pulsed magnetic fields.	143
6.16	$M(T)$ -curves and Δ_{sT} under hydrostatic-pressure application for $\text{Mn}_{0.84}\text{Fe}_{0.16}\text{NiGe}$ and $\text{Mn}_{0.6}\text{Fe}_{0.4}\text{NiGe}_{0.5}\text{Si}_{0.5}$	145
6.17	$M(T)$ -measurements and determination of Δ_{sT} for $\text{Mn}_{0.5}\text{Fe}_{0.5}\text{NiSi}_{1-z}\text{Al}_z$	149
7.1	Magnetic-field sensitivity of T_t for In-, Sn-, and Ti-Heusler systems together with DFT calculations of T_C^A for Ni-Co-Mn-Ti and Ni(-Co)-Mn-Sn.	152
7.2	Calculated DOS around E_F for Ni-CO-Mn-Ti (B2) together with magnetic moments of the atomic species.	154
7.3	Calculated DOS around E_F for Ni-Co-Mn-Sn (L ₂₁) together with the magnetic moments of the atomic species.	155

List of Tables

3.1	Maximum field application rates for different field pulses.	40
4.1	Sample compositions and selected properties of the Ni(-Co)-Mn-Al, Ni(-Co)-Mn-In, and Ni(-Co)-Mn-Sn Heusler alloys.	46
5.1	Nominal sample compositions of the produced $\text{Ni}_{50-x}\text{Co}_x\text{Mn}_{50-y}\text{Ti}_y$ system with selected properties of the phase transitions.	68
6.1	Nominal sample compositions of the produced $\text{Mn}_{1-x}\text{Fe}_x\text{NiGe}_{1-y}\text{Si}_y$ system with the determined structural properties.	116
6.2	Total entropy changes Δs_t for the $\text{Mn}_{1-x}\text{Fe}_x\text{NiGe}_{1-y}\text{Si}_y$ series.	140

Nomenclature

χ	Magnetic susceptibility
χ^2	Quality factor of XRD refinements
$\Delta H/\mu_0\Delta H$	Change of the magnetic field
ΔM	Magnetization change
Δs_T	Specific isothermal entropy change
Δs_t	Total entropy change of full phase transition
ΔT_{ad}	Adiabatic temperature change
ΔT_{ad}^{cyc}	Adiabatic temperature change under cyclic conditions
ΔT_{ad}^{rev}	Reversible adiabatic temperature change for first field-removal step
λ	Thermal conductivity
μ_0	Magnetic permeability of vacuum
ρ	Specific resistance
σ	(uniaxial) Stress
θ	Diffraction angle
Θ_D	Debye temperature
ε	Strain
A	Cross-section area
a, b, c	Lattice constants
A_f	Austenite finish temperature
A_s	Austenite start temperature
C	Curie constant
c_p	Specific heat capacity at constant pressure
C_{total}	Absolute heat capacity of system
d_{hkl}	Interplanar lattice spacing
E	Young's modulus

e/a	Average valence electron count per atom
E_F	Fermi level
G	Gibbs free energy
H/μ_0H	Magnetic field
I	Intensity of XRD signal
J_{ij}	Magnetic exchange interaction between two atoms
K	Thermal conductance
l	Sample length
M	Magnetization
m	Mass
M_f	Martensite finish temperature
M_s	Martensite start temperature
P	Heating power
p	(hydrostatic) Pressure
R	Ideal gas constant
S	Entropy
s_{el}	Electronic entropy
s_{lat}	Lattice entropy
s_{mag}	Magnetic entropy
T	Temperature
T_C	Curie temperature
T_C^A	Curie temperature of austenite
T_C^M	Curie temperature of martensite
T_N	Néel temperature
T_t	Transition temperature
T_t^c	Transition temperature upon cooling
T_t^h	Transition temperature upon heating
U	Inner energy
V	Volume
AC	Air-conditioning

AFM	Antiferromagnetic
AMR	Active magnetic regenerator
bcc	body-centered cubic
BCE	Barocaloric effect
BSE	Backscatter electron
CFC	Chlorofluorocarbon
DFT	Density functional theory
DOS	Density of states
DSC	Differential scanning calorimetry
ECE	Electrocaloric effect
EDS	Energy-dispersive X-Ray spectroscopy
ElCE	Elastocaloric effect
fcc	face-centered cubic
FM	Ferromagnetic
FOMT	First-order magnetostructural phase transition
FWHM	Full width at half-maximum
GWP	Global warming potential
HFC	Hydro(chloro)fluorocarbon
M/A	Martensite-to-austenite fraction
MCE	Magnetocaloric effect
PM	Paramagnetic
PPMS	Physical property measurement system
SE	Secondary electrons
SEM	Scanning electron microscopy
SOMT	Second-order magnetic phase transition
VSM	Vibrating sample magnetometry/magnetometer
XRD	X-ray diffraction

1 Introduction and Motivation

As a result of industrialization, the standards of living across the globe have increased drastically over the last decades and centuries. What has first resulted in an enormous growth in the industrial sector starting with the development of the first steam engine in the 18th century, has led to intense research activities in the fields of medicine, biology, physics, chemistry and engineering sciences. Many discoveries have been made that changed life on earth drastically and paved the way for future technologies. As a result of that accelerating development, world population has been and is still growing exponentially, the average life expectations are increasing as well and the standards of living are rising in many countries [2, 3]. Technological evolutions contributing to make life easier have spread very fast over the last years and decades. The other aspect of that fast technological evolution is the energy demand and the environmental consequences that result from the emerging new technologies. Even though many research activities are devoted to energy efficiency, it happens that the energy consumption even rises after the implementation of a more energy efficient technology. This has been observed first in 1866 by Jevons [4], who reported about a drastic increase in the British coal consumption over decades despite the introduction of the more fuel-efficient version of a steam engine by Watt in 1776 [5, 6]. This phenomenon is known as the Jevons paradox and has been adopted for modern energy consumption society in the 1980's as the Khazzoom–Brookes postulate [7, 8], also denoted as rebound effect [9]. The fast development of technological progress in terms of more energy efficient technologies is therefore strongly connected to more affordable energy for society as well as to an economic growth, both leading to the result that more energy is consumed - but more efficiently. The constantly rising energy consumption, not only in the industrial but also in the residential sector, is directly associated to the rapidly growing amount of CO₂ emissions driving the global climate change [10].

A technology that has not been changed in its fundamental working principle over the past century is refrigeration and the overall contribution of the refrigeration sector to climate change is frequently overlooked. This includes household fridges, commercial refrigeration, refrigerated transport as well as air conditioning systems and heat pumps, which are all mainly based on gas compression cycles. Today a total number of roughly 3 billion devices associated with these applications are in use [11]. As a result, the refrigeration sector accounts for 7.8% of global greenhouse gas emissions, of which one third result from direct emission of fluorocarbons and two thirds are due to indirect emission from the electricity production needed to operate the devices [12]. This also means that 17% of the global energy consumption is required for refrigeration and air-conditioning (AC) [11]. A study of Issac and van Wuren from 2009 [13] predicts

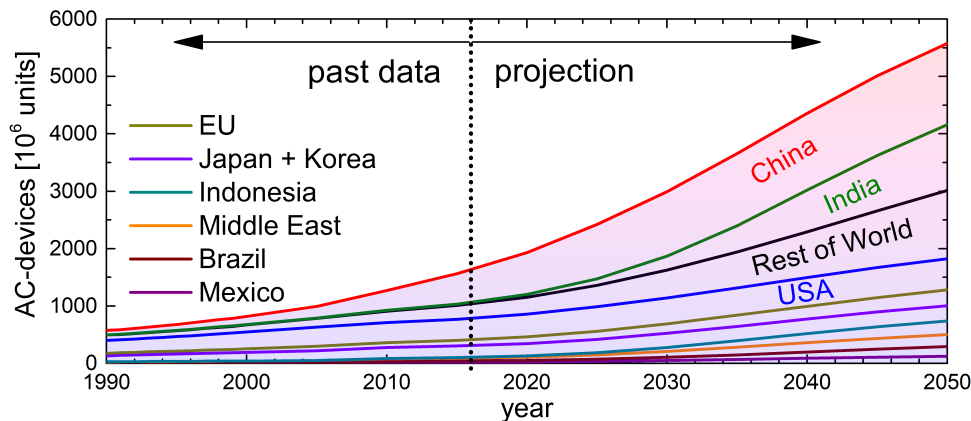


Figure 1.1: Past evolution of global air-condition devices since 1990 and projection of future development until 2050. Data is taken from [19].

that the global energy demand that is required for cooling purposes will outrage the energy that is needed for heating within the second half of this century. This is not only a direct consequence of global warming but also of the rapidly growing economies and standards of living in fast developing countries located in the warm and tropical regions of the earth. It is predicted that in 30 years, two-third of all households worldwide will be equipped with air-conditioning systems, especially the amount in India, Indonesia and China is expected to grow drastically (see Fig. 1.1) [14]. These assumptions lead to a baseline scenario estimating that the energy demand for space cooling will triple by 2050 [14]. On the one hand, the result is an increase in CO₂ production as the worldwide energy mix mainly consists of non-renewable resources. On the other hand, the usage of cooling liquids that often contain environmentally harmful cooling agents with a drastically high Global Warming Potential (GWP) will increase [15]. In the framework of the environmental programme of the United Nations, new regulations have been introduced in order to phase down the use of chlorofluorocarbons (CFC) by the Montreal Protocol in 1987 [16] and of the afterwards emerging hydro-chlorofluorocarbons (HFC) by the F-gas Regulation of the European Union in 2014 [17] and the Kigali-Amendment to the Montreal Protocol in 2016 [18].

In order to provide an alternative solution, magnetocaloric cooling is a topic that has been in focus of intense research since the end of the 1990's. However, the magnetocaloric effect has already been discovered for nickel in the beginning of the 20th century by Weiss and Piccard [20]. It was used initially as a way to decrease the temperature below the boiling point of helium, which was carried out in 1933 by Giauque and MacDougall [21] reaching for the first time an absolute temperature of 0.25 K by using Gd-based paramagnetic salts. The importance of these pioneering works are underlined by the Nobel price in chemistry that has been awarded to William Giauque in 1949 for his low temperature experiments [22].

Magnetic refrigeration is based on the entropy change that results from the orientation of magnetic moments or an induced magnetostructural phase transition in an external magnetic field. This solid-state cooling technique has been proposed to be more energy efficient than the conventional gas compression

cooling and can therefore represent a promising alternative [23–26]. In addition, the main parts that are needed for the operation are a magnetocaloric material, a magnetic field source and a heat exchanger system, which can consist of a simple liquid like water, for example. This would mean a renunciation of environmentally harmful HFCs, thus supporting the claimed goals of the United Nations and the European Union to achieve a phase down of HFCs [17, 18] and control the man-made global warming impact on below 1.5 °C compared to pre-industrial times according to the Paris Agreement [27]. It has to be considered that also the conventional cooling industry develops and adapts to the legislative changes. Refrigerants with a negligible GWP (mainly R-600a/isobutane) are already in use for household refrigerators without a significant loss in energy efficiency compared to CFCs and HFCs [28]. Nevertheless, many alternatives are flammable and very close to the theoretical efficiency limit [29]. Despite saving direct emissions, indirect emissions by energy consumption are still improvable. On the other hand, new low-GWP refrigerants for other power or temperature regimes are not as efficient. For example, energy-efficient alternatives for applications below room temperature (below –20 °C) for centrifugation of blood cells bear a risk of explosiveness, which is a critical issue for contaminated or valuable samples. Such niche applications that are not too price-sensitive need to be determined in order to establish caloric cooling technologies on the market and develop it further to achieve energy savings also on large scale applications.

However, there are still problems that have to be solved for the magnetocaloric cooling technology in order to enter the market. Despite the fact that a certain amount of demonstrators and prototypes has been built and presented by companies and institutes [23, 30–35], the proposed energy efficiency has not been proven yet in an overarching manner for a working device. Thus, the commercialization and market entry of this potentially advantageous technology for the environment has not been realized yet. In addition, many of the promising material systems contain critical/expensive elements like cobalt, indium, gadolinium or germanium [36]. The most crucial goal for magnetocaloric research is becoming economically competitive with the existing refrigerators. One important aspect of this competitiveness is the cyclic performance of the material as well as the long-term stability [37]. Materials with a large magnetocaloric effect are often based on a first-order magnetostructural phase transition that is characterized by a thermal hysteresis. This hysteretic behavior leads to losses during cyclic application of the phase-change material, which decreases the performance of the material in cyclic fields [38]. For this reason, the understanding of the thermal hysteresis and its reduction in known compounds as well as the finding of novel compounds with outstanding properties is an important research topic for efficient magnetocaloric materials.

One additional challenge that arises for magnetocaloric devices is the production of a varying magnetic field that is as large as possible. The easiest solution is to use permanent magnet arrays [39]. However, strongest hard magnets are made out of Nd-Fe-B, which is critical in terms of environmental issues during extraction as well as the high prize of the rare-earth element Nd [40]. For this reason, also other solid state caloric cooling techniques are in focus of research [41, 42]. These alternatives use a phase transition that is induced by electric fields (electrocaloric effect), hydrostatic pressure (barocaloric effect) or uniaxial pressure (elastocaloric effect). All of them also deal with major problems hindering their easy application in refrigeration applications.

In order to tackle the problem of expensive permanent magnets and a large thermal hysteresis simultaneously, a multicaloric cooling cycle has been proposed recently [43]. It combines a completely irreversible magnetocaloric effect with a short time magnetic field application that induces a phase transition and locks the material in the induced state. In order to transform the material back to its initial state, uniaxial or hydrostatic pressure can be used as a second stimulus. This is carried out after heat transfer to a heat exchange liquid. By this, the difficult task of reducing the thermal hysteresis can be eliminated and instead, a large hysteresis can even be beneficial. The new approach reduces the volume of the magnetic field required because the material is locked after the field removal in its transformed state by the thermal hysteresis. As a consequence, the magnetic field does not have to be maintained during the heat exchange. However, a precise design of the material's phase transition is necessary to adjust the thermal hysteresis in order to reduce the magnetic field strength and the pressure that is required to induce a completed transition.

This work investigates two material families with a first-order magnetostructural phase transition that is of martensitic nature and exhibits a magnetocaloric effect. By investigating the tuning of the transition by stoichiometry, external pressure and magnetic field for different material systems, the manifold aspects of optimizing a magnetocaloric material will be discussed. The versatile material family of Heusler alloys will be considered in addition to explore the benefits and challenges of optimizing a multicaloric material for the new multi-stimuli cycle. First of all, the deviating material requirements will be investigated compared to the conventional magnetocaloric cooling cycle. In addition, the systematic development of the novel Ni-Co-Mn-Ti material system is carried out in detail. The comprehensive scope of this work is to summarize principle design rules for tackling the challenges of developing existent and novel material systems towards their application in a working caloric cooling application.

After a detailed explanation on the fundamental principles of the magnetocaloric effect and its application as well as the most promising material systems, the experimental techniques applied for the results of this work will be introduced in Chapter 3. The Ni(-Co)-Mn-X Heusler alloys with X being main group elements ($X=Al, In, Sn$) and the potential of these different materials for magnetocaloric applications are discussed in Chapter 4. The new concept of all-d-metal Heusler alloys will be introduced in Chapter 5. The magnetocaloric and mechanical properties of the Ni-Co-Mn-Ti alloy system will be shown here with respect to the performance in low and high magnetic-field changes as well as the suitability for a multi-stimuli caloric cooling approach. The design of the MM'X material system of MnNiGe and the magnetocaloric properties are presented in Chapter 6. Chapter 7 will give an overview on the different material systems considered in this work and propose principal design rules for the development of known and novel magnetocaloric materials.

2 Fundamentals

In the following chapter, the fundamental background of physical phenomena underlying the work in this thesis will be discussed. This will mainly cover the fundamentals of phase transitions including especially martensitic transitions, which play an important role for promising magnetocaloric materials. In addition, the magnetocaloric and related caloric cooling effects are discussed in combination with the requirements that need to be fulfilled by a well-performing caloric material. Subsequently, an overview on the most prominent materials will be given followed by an introduction of the relevant materials that are investigated in this thesis.

2.1 Fundamentals of phase transitions

According to the theories of Landau [44] and Ehrenfest [45], phase transitions can be separated into different categories. In 1933, Keesom and coworkers found evidence for a phase transition in liquid helium by measuring the dielectric constant and additionally by observing a "jump" in heat capacity, despite the absence of latent heat at the so-called lambda point (named after the shape of the measurement curve) [46, 47]. This motivated Ehrenfest to describe the categorization of phase transitions as changes in the respective derivatives of the Gibbs free energy G by the occurrence of "jumps" [45]. The total G is given as the sum of the inner energy U and the thermodynamic potential products for entropy S multiplied with temperature T as well as volume V multiplied with pressure p :

$$G = U - ST + Vp \quad (2.1)$$

Assuming a system of constant pressure, the first derivative of Gibbs free energy G with respect to temperature gives the entropy S :

$$S = - \left(\frac{\partial G}{\partial T} \right)_p \quad (2.2)$$

The second derivative with respect to temperature describes the corresponding heat capacity c_p of a

system at constant pressure:

$$c_p = \left(\frac{\partial S}{\partial T} \right)_p = - \left(\frac{\partial^2 G}{\partial T^2} \right)_p \quad (2.3)$$

The Ehrenfest classification states that the order of a phase transition is equal to the respective derivative of G with temperature (or pressure) that is discontinuous at the transition. Thus, a phase transition is of first-order when featuring two different slopes of the temperature-dependent G at the phase-transition temperature leading to a discontinuous (jumping) change in entropy that features a divergence in the heat capacity. A phase transition with a continuous change in entropy but a discontinuous change of the heat capacity is termed as second-order. The same argumentation applies for the pressure-dependent G and the volume.

The Landau theory of phase transitions describes the contributing phases by the order parameter as a power series of the thermodynamic potential, which exhibits a symmetry break upon phase transition [44]. The order of a phase transition is here given by the continuous or discontinuous change in this order parameter, which can vary between zero (full disorder) and one (completely ordered). For example magnetic systems are described by the magnetization as the order parameter. Many materials exhibit for example a phase transition from paramagnetic (PM) to ferromagnetic (FM) at a certain temperature, which is denoted as the Curie temperature T_C . By decreasing the temperature in zero magnetic field, the magnetic spins are aligning parallel at the Curie temperature because the system is not provided with enough thermal energy to maintain the spin disorder. Because this phase transition is characterized by a continuous change of the magnetization (see Fig. 2.2 (a)), the Curie temperature is the critical phase-transition temperature belonging to a transition of second order.

As a second example, a system with a magnetostructural phase transition will be considered, which is often the case for prominent magnetocaloric materials. Here, the phase transition is often described by a structural change of the material. Therefore, not only the magnetization needs to be regarded as an order parameter, but also the crystal symmetry. At the structural phase transition temperature, the material changes either the crystal symmetry or the lattice constants in a discontinuous manner. The first case is denoted as a structural phase transition and the latter one is termed dilational phase transition [48]. Both belong to the class of first-order transitions. These phase transitions have in common that they are characterized by a discontinuous change of the volume and a resulting peak of c_p at the transition temperature (in accordance with the Ehrenfest classification). Additionally, they are accompanied by a latent heat that is absorbed or released when going through the phase transition as it is well-known for the phase transition from a solid to a liquid state and vice versa.

2.1.1 Martensitic phase transitions

The martensitic phase transition describes a special case of a first-order phase transition. It is named after the German metallurgist Adolf Martens and classically describes the transformation of steel into

the martensitic phase. This kind of transition is a structural phase change from a high-symmetry (often cubic) high-temperature phase to a low-symmetry low-temperature phase. In accordance to the naming of the involved phases in steel, the high-temperature phase is called austenite and the low-temperature phase is called martensite. The main characteristic of the martensitic transition is its diffusionless nature. The martensite structure is formed from the austenite only by distorting the lattice and the formation of twin boundaries. Referring to the example of steel, the martensite formation is carried out by the so called Bain transformation path [49], where the face-centered cubic (fcc) austenite is converted to a tetragonally distorted body-centered cubic (bcc) structure by a diffusionless transformation path. The martensitic transition in steel is depending on the cooling rate because it is connected to the suppressed diffusion of solute carbon atoms on the bcc austenite interstitial sites that are not soluble any more in the low-temperature fcc phase due to the reduced size of the available interstitial positions. Consequently, the martensite phase of steel is a metastable phase and its formation depends on dynamic effects. In contrast, a diffusionless martensitic transition in general can appear also between two thermodynamically stable phases that are named according to the situation in steel as martensite for the low-temperature phase and austenite for the high-temperature phase.

Due to the first-order nature of martensitic phase transitions, a thermal hysteresis separates the transformation depending on the temperature history of the sample. The martensite formation during cooling takes place at lower temperatures than the austenite formation upon heating. The reason is the interface energy between the two different crystal structures that needs to be overcome by undercooling/overheating below/above the equilibrium transition temperature in order to form stable nuclei of the new phase. For non-ideally sharp transitions, both branches are characterized by a continuous change of the phase fraction. However, the low-temperature and high-temperature end of the transition evolution are usually asymmetric because the formation of austenite is more a growth process of residual austenite phase in voids of the martensite needle structure, which is happening more gradually compared to the sharp growing of martensite nuclei upon cooling [50]. The characteristic temperatures for the martensitic transition are called martensite start and finish (M_s and M_f) for the martensite formation and austenite start and finish (A_s and A_f) for the austenite formation.

Characteristic for the martensitic structure is the occurrence of twin boundaries. For the case of a cubic to tetragonal transition, the cubic unit cell can be distorted so that the new c -axis of the martensite lies along one of the three parent lattice directions a , b , and c of the austenite. This tetragonal martensite is denoted as non-modulated $L1_0$. Consequently, three different martensitic variants are possible for one parent austenite grain [51, 52]. The diffusionless distortion of the lattice leads to large elastic energies at the phase boundary between austenite and martensite. The resulting stresses at the interfaces due to the lattice mismatch are accommodated by the alternating formation of variants with long c -axis and short a -axis along the phase boundary. A highly symmetric, therefore energetically favorable, twin boundary is occurring between these different variants [52].

In addition, different modulated martensitic variants can occur as a result of phonon softening and adaptive nanotwinning [52–55]. They combine a certain sequence of tetragonal variants separated by twin

boundaries in order to match the parent austenite lattice and to form an adaptive martensite with a coherent phase boundary [56]. For example, a sequence of 5 and 2 building blocks of two different tetragonal unit cell variants separated by a twin boundary forms a so called 14M martensite with a monoclinic unit cell. Other often appearing modulated forms are the 5M, 7M and 10M martensite. Each possibility of modulation is connected to the c/a ratio of the non-modulated tetragonal unit cell.

2.2 Caloric solid-state cooling effects

The whole world uses cooling for everyday life purposes. While in former times cutting ice blocks and shipping them around the globe was an attractive business, the development of vapor-compression refrigeration systems started to revolutionize the cooling industry in the end of the 19th century. Due to the large size of the first devices, they were predominantly used for industrial large-scale applications. With further development, the vapor-compression refrigerators began to be distributed also for household uses from the 1930's on. This technology is mainly based on the expansion and compression of gases using the latent heat of the first-order phase transition in a heat exchanger and has been applied in the same manner since its development in the late 19th century. However, the demand for cooling will rise drastically within this century [14]. In order to save energy, a more energy-efficient solution can make a significant contribution to a reduction of worldwide CO₂ emissions. In addition, many refrigerants used for cooling contain environmentally harmful substances like chlorofluorocarbons (CFC) and hydrofluorocarbons (HFC) that contribute drastically to the ozone layer depletion. Nowadays new regulations have been passed, which aim at phasing down the use of many of those environmentally harmful refrigerants possessing a high GWP [17, 18]. The main alternatives are either toxic, flammable or inefficient at moderate pressures.

An alternative option can be provided by cooling techniques using the caloric effects of solid-state materials. Most prominent examples are the magnetocaloric (MCE), electrocaloric (ECE), elastocaloric (ElCE) and barocaloric effect (BCE) (see Fig. 2.1 (a)). These caloric effects use a phase transition between two solid states, which is accompanied by a large change of an order parameter (MCE: magnetization, ECE: polarization, ElCE: uniaxial strain, BCE: volume). This phase transition is therefore characterized by a considerable entropy change, which can be used for cooling effects by inducing the phase transition with an external stimulus that is changing in a cyclic manner.

2.2.1 Magnetocaloric effect and device implementation

In the following section, the magnetocaloric effect induced by an external magnetic-field application will be explained in detail because it is the highest developed method towards applications and the most relevant for this thesis. This schematic cycle shown in Fig. 2.1 (b) can be transferred to the other caloric cooling effects by substituting the order parameter and the respective external stimulus which induces a change for this physical property as depicted in Fig. 2.1 (a). In the starting state of the magnetocaloric cycle, the material is at a certain temperature and in a well-defined magnetic state. For this explanation we

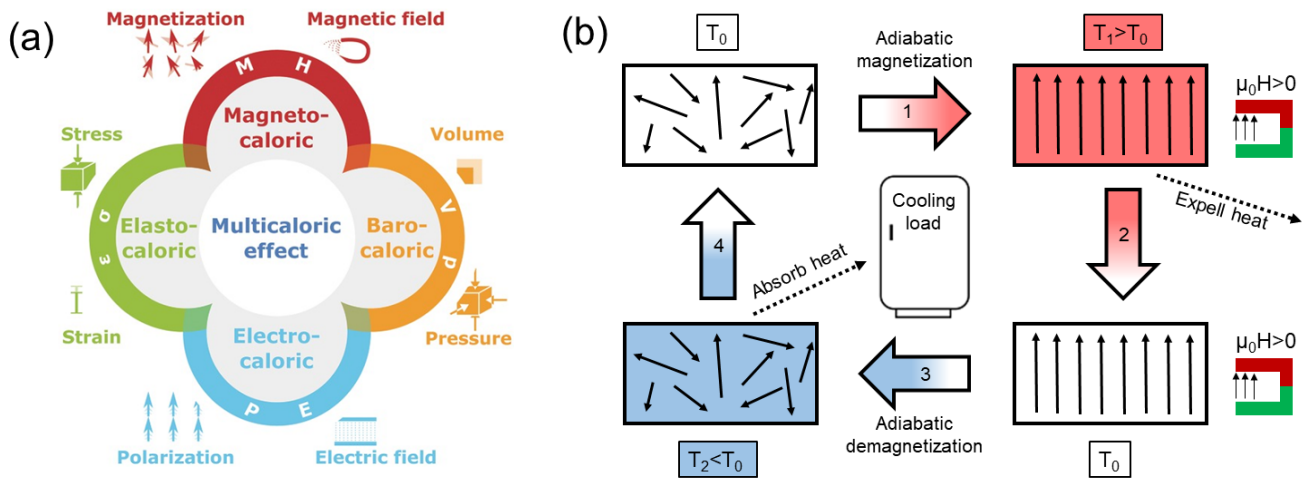


Figure 2.1: Overview on the different kinds of caloric solid state cooling effects with their respective order parameters (magnetization, volume, polarization and strain) and the external stimuli that can be applied to induce the effect (a). This image is taken from [57]. The main steps of a magnetocaloric cooling cycle are shown schematically in (b).

consider the material to be in the paramagnetic state with a random orientation of the magnetic moments. The classical magnetocaloric cooling cycle consists of four main steps [58]:

- (1) In a first step, a magnetic field as the external stimulus is applied to the magnetocaloric material adiabatically. As a result, the randomly oriented magnetic spins of the initial state are aligned along the external field and the macroscopic magnetization changes. Because of the adiabatic conditions, the overall entropy of the system needs to be constant. Consequently, the decreased entropy of the magnetic subsystem due to the orientation of the moments needs to be compensated by an increased lattice entropy. This is realized by stronger lattice vibrations, which means an increase in temperature from T_0 to T_1 .
- (2) Subsequently, the produced heat is released while the magnetic-field strength is maintained. The result is a magnetized material that is again at the starting temperature of the cycle.
- (3) Now the magnetic field is decreased again adiabatically leading to a demagnetization of the material. As an opposite effect of step (1), the increasing entropy of the randomized magnetic spins is compensated by reduced lattice vibrations. Thus, this step leads to a cooling of the magnetocaloric material.
- (4) Finally, the reduced temperature of the magnetocaloric material can be used for a heat exchange with the cooling target (the inside of a fridge for example) by a heat exchanger setup. In the end, the material is in the demagnetized state and at the starting temperature T_0 of step (1), where the cycle can be carried out again.

For carrying out this cycle, the magnetocaloric material being used needs to fulfill certain requirements in order to harvest a maximum possible effect. The two most important figures of merit for the assessment

of magnetocaloric materials are the isothermal entropy change Δs_T and the adiabatic temperature change ΔT_{ad} . While Δs_T gives an estimate for the maximum amount of heat that can be transferred for the regarded phase transition induced by an external stimulus, ΔT_{ad} provides the maximum temperature difference that can be obtained accordingly. Both are equally important for establishing an applicable cooling power by using a magnetocaloric material in a refrigeration device.

The thermodynamic description of these quantities can be derived from the Gibbs free energy. In order to consider the energy contribution of a magnetic phase and an external magnetic field, the Zeeman energy term $-\mu_0 MH$ is added to the description of G from Equation (2.1) leading to Equation (2.4) with the permeability of vacuum μ_0 , magnetization M and magnetic field H . This additional term describes the stabilization of a magnetic phase in an external magnetic field by reducing G .

$$G = U - ST + Vp - \mu_0 MH \quad (2.4)$$

From the magnetization behavior at varying temperatures and magnetic fields, Δs_T can then be derived by considering the partial derivative of the Gibbs free energy G of the system [59, 60]:

$$dG = -SdT + Vdp - \mu_0 M dH \quad (2.5)$$

Forming the second mixed partial derivatives of G at constant pressure with respect to T and H in different order must give the same result and leads to one of the so-called Maxwell relations:

$$\left(\frac{\partial S}{\partial H}\right)_T = \mu_0 \left(\frac{\partial M}{\partial T}\right)_H \quad (2.6)$$

From the Maxwell relation in Equation (2.6), the determination of a finite isothermal entropy change Δs_T for a phase transition can be carried out at a temperature T for a magnetic-field change $\Delta H = H_2 - H_1$ by integration:

$$\Delta s_T(T, \Delta H) = \mu_0 \int_{H_1}^{H_2} \left(\frac{\partial M(T, H)}{\partial T}\right)_H dH \quad (2.7)$$

The corresponding adiabatic temperature change is in addition dependent on the heat capacity at constant pressure c_p according to Equation (2.8). For a detailed derivation of the thermodynamic relations relevant for the magnetocaloric effect, the reader is referred to [61–63].

$$\Delta T_{ad}(T, \Delta H) = -\mu_0 \int_{H_1}^{H_2} \left(\frac{T}{c_p(T, H)}\right)_H \left(\frac{\partial M(T, H)}{\partial T}\right)_H dH \quad (2.8)$$

By approximating that c_p is independent on the magnetic field [58], the relation between ΔT_{ad} and Δs_T

can be simplified given by:

$$\Delta T_{ad}(T, \Delta H) = -\frac{T}{c_p(T)} \Delta s_T(T, \Delta H) \quad (2.9)$$

In reality, c_p can be influenced significantly by a magnetic-field application around a first-order phase transition. That's why Equation (2.9) is applicable only for second-order transitions [58].

All magnetocaloric materials work for moderate magnetic-field changes efficiently around a magnetic phase transition. This can be a simple second-order magnetic transition (SOMT), where a magnetic material changes its properties from paramagnetic above the Curie temperature T_C to ferromagnetic below T_C , which is depicted schematically in Fig. 2.2 (a). According to Equations (2.7) and (2.8), the important property that is sought to be maximized is the change of magnetization with temperature $\frac{dM}{dT}$, which is largest for ferromagnetic materials at their T_C as well as for paramagnets at very low temperatures. The underlying entropy diagram for zero magnetic field and an external magnetic field is shown in Fig. 2.2 (c). By starting in zero field at a certain temperature, a horizontal line to the entropy curve in a non-zero magnetic field represents the adiabatic (=under constant entropy) magnetization process resulting in ΔT_{ad} . The vertical line at constant temperature represents the isothermal process with the respective Δs_T . Since the entropy-temperature curves are unambiguously defined for each thermodynamic state, Δs_T and ΔT_{ad} are fully reproducible under cyclic changes of the external magnetic field ($\Delta T_{ad}(\Delta H) = \Delta T_{ad}^{rev}(\Delta H)$).

Furthermore, even larger magnetization changes in a narrow temperature interval are achieved with first-order magnetostructural transitions (FOMT), where the change in magnetization is realized by being coupled to a structural phase change between a high-temperature and a low-temperature phase. A magnetocaloric material undergoes a magnetostructural phase transition upon cooling or heating the material through the respective transition temperature T_t . Since first-order transitions are driven by a nucleation and growth mechanism, they are accompanied by a thermal hysteresis. This means that an additional thermal energy needs to be provided to overcome the energy barrier that is necessary in order to form stable nuclei of the new phase. Thus, the transition temperature upon heating and cooling deviates from the equilibrium T_t , which is determined by the equilibrium of the Gibbs free energies of the high-temperature and low-temperature phase. The respective transition temperatures are now labeled as T_t^h and T_t^c as it is shown in Fig. 2.2 (b). Consequently, the state of the material is not defined unambiguously within the hysteresis region, it rather depends on the history of the sample. The two branches are shown here in red and blue for heating and cooling procedure, respectively. It must be emphasized that for the depicted ideal first-order transition, the Maxwell relation (2.6) as well as the thermodynamic definitions of Δs_T and ΔT_{ad} (Equations (2.7) and (2.8)) are not valid. The reason is that $(\frac{\partial M}{\partial T})_H$ does not exist due to the fundamental definition of the discontinuous change in G for a first-order transition and c_p is infinite at the transition point by definition. However, for the measurements of real transitions showing a certain transition width, these formulas can be applied correctly [64].

First-order magnetocaloric materials are furthermore divided into conventional and inverse materials. A conventional material shows a transition from a low-temperature high-magnetization state to a high-

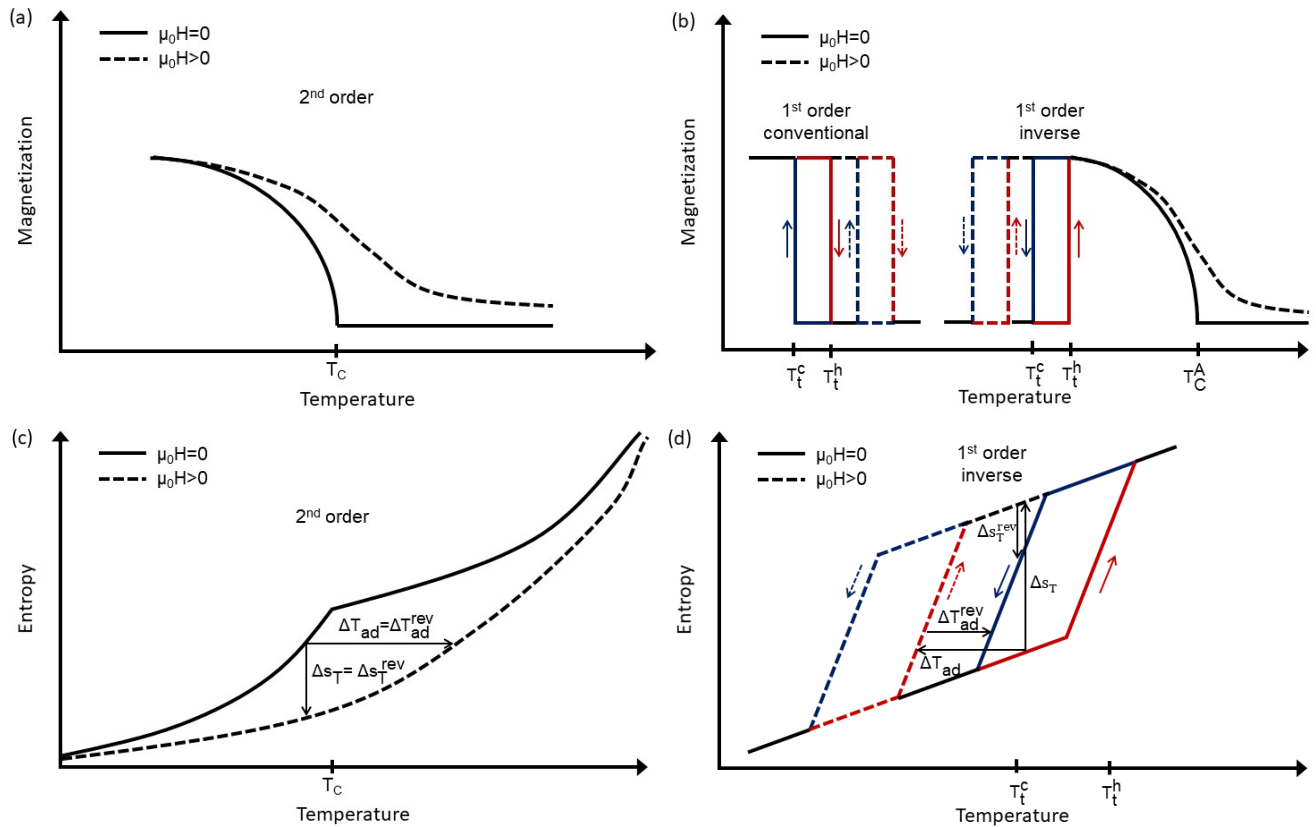


Figure 2.2: Schematic temperature-dependent magnetization without (solid lines) and with external magnetic field (dashed lines) for a second-order transition (a) and for an ideal (infinitely sharp) conventional and inverse first-order transition with thermal hysteresis (b). The schematic temperature-dependent entropy diagram for the second-order transition is shown in (c) with fully reversible Δs_T and ΔT_{ad} . The inverse first-order transition in (d) is depicted in contrast to image (b) with a finite transition width and the cyclic parts Δs_T^{rev} and ΔT_{ad}^{rev} are indicated by the arrows. All images label the Curie temperature T_C and the transition temperatures upon heating (T_t^h) and cooling (T_t^c) in zero field. In addition, the heating and cooling branches of the first-order transition are drawn in red and blue, respectively.

temperature low-magnetization state, whereas inverse materials exhibit a transition from a low-temperature low-magnetization state to a high-temperature high-magnetization state. Because the high-temperature state is in a high-magnetization state, it usually also shows an austenite Curie temperature T_C^A . As a result, the sign of $(\frac{\partial M}{\partial T})_H$ is different for both cases. Consequently, Δs_T is negative and ΔT_{ad} is positive for a conventional first-order transition and vice versa for the inverse case. Since also the MCE at a second-order transition is usually denoted as conventional, this thesis will use the convention to differentiate between the namings second-order transition, conventional first-order transition and inverse first-order transition for the sake of clarity. Since the phase transition is taking place between two phases of different magnetization, it can not only be induced by a change in temperature but also by an externally applied magnetic field. According to Equation (2.4), the application of a magnetic field adds the respective Zeeman term $(-\mu_0 H M)$ to the total Gibbs free energy. As a result, G is reduced proportionally to the material's magnetization and the phase with higher magnetization is thermodynamically stabilized. Consequently, the transition temperature of conventional (inverse) materials is being shifted towards higher (lower) temperatures by a magnetic-field application (see dotted lines in Fig. 2.2 (b) and (d)). Thus, the transition itself can be induced upon a varying external magnetic field.

The corresponding entropy diagram in Fig. 2.2 (d) illustrates the reduced performance that result from the thermal hysteresis in cyclic processes. It must be noted here that - in contrast to the ideal (infinitely sharp) transition in Fig. 2.2 (b) - the transition has a finite width, as it is usually the case in reality. It follows that the transition has a start and a finish temperature and the transition temperatures (T_t^h and T_t^c) are defined in the center of the respective transition branch for zero magnetic field. Upon first field application, a MCE expressed by Δs_T and ΔT_{ad} is induced by a sufficiently large magnetic field. However, the field removal step needs to overcome the additional nucleation barrier for the reverse transition when starting in the two-phase region of thermal hysteresis initially. As a result, Δs_T^{rev} and ΔT_{ad}^{rev} upon field removal are reduced because a lesser amount of phase is transformed back.

The total entropy change for a phase transition Δs_t is divided into several terms that contribute to the total entropy of the involved phases. It consist of contributions from the magnetic subsystem (Δs_{mag}), the lattice subsystem (Δs_{lat}) and the electronic subsystem (Δs_{el}) [60].

$$\Delta s_t = \Delta s_{mag} + \Delta s_{lat} + \Delta s_{el} \quad (2.10)$$

Even though the terms are just summed up in a simple approximation, they may depend on each other and cannot be separated clearly in all cases since for example electron-phonon interactions can play a role for itinerant 3d-electrons [60]. Furthermore the sign and magnitude of the terms can vary and the subsystems may also contribute oppositely to the total entropy change of the phase transition. For example in La-Fe-Si and FeRh alloys, the electronic part plays a significant role due to strong changes in the density of states (DOS) near the Fermi level E_F during the transition [38, 65]. In contrast, for the transition of inverse magnetocaloric Heusler alloys, the electronic part is very small and can be neglected [66]. The two remaining parts show a contrary contribution with a positive entropy change for the lattice part and a

negative one for the magnetic subsystem [67]. As a result, a large magnetization change would deplete the total entropy change of the phase transition and the maximum theoretical entropy change is achieved for a pure structural transition with very low magnetization changes. Nevertheless, a large magnetization change is needed in order to drive the transition by an external magnetic field. This contradictory role of the magnetization change is denoted as the dilemma of inverse magnetocaloric materials [67].

The implementation of magnetocaloric materials into a working refrigeration cycle can be carried out for different thermodynamic cycles. The most common one is the active magnetic regenerator (AMR), which has already been applied for the first prototype designs in the late 1970's [68–70]. By using permanent magnets as a field source, the maximum magnetic fields available are around 1 T to 1.5 T. The largest temperature changes that can be obtained under cyclic application of these field changes by the most promising materials are around 3 K to 5 K (see Fig. 2.5) [71]. Since this is not large enough for a feasible cooling device, the magnetocaloric material must act as a regenerator itself to achieve reasonable temperature spans. Consequently, every infinitesimal part of material performs its own thermodynamic cycle and all of them are coupled by the heat exchange fluid [63, 72]. The most used approach for prototypes and demonstrators is a Brayton-like AMR cycle [73]. A magnetic Brayton thermodynamic cycle is characterized by two adiabatic (de)magnetization processes and two isofield processes. This represents the four steps of a magnetocaloric cooling cycle described above (see Fig. 2.1 (b)). For the additional consideration of a Brayton-like AMR cycle, the amount of heat exchange liquid that is pumped through the active magnetocaloric material is adjusted for optimal thermal span of the device. This leads to a temperature profile that is built up within the magnetocaloric regenerator between the hot and cold end as a periodic steady state [63, 70]. This gradient is the basis for obtaining a thermal span between cold end and hot end, which is larger than the individual ΔT_{ad} of one (de)magnetization cycle. Other possible thermodynamic cycles are the Ericsson cycle, Stirling cycle or Carnot cycle, detailed descriptions with respect to magnetocaloric energy conversion can be found in [63].

2.2.2 Multicaloric effects

In addition to the magnetocaloric effect induced by a magnetic field, other forms of caloric effects induced by an external stimulus can be used for phase transition materials with a changing order parameter [74]. For example, a hydrostatic pressure energetically favors the phase with a lower unit cell volume (per formula unit) whereas a uniaxial pressure (in compression mode) favors the phase with lower strain in the direction of the applied force. Applying and removing a hydrostatic pressure under adiabatic conditions can induce a barocaloric effect and is equivalent to achieving a magnetocaloric effect by applying and removing a magnetic field. Application and removal of a uniaxial load to a phase transition material can lead to the elastocaloric effect. These two effects, which both depend on the application of a mechanical force to the sample, can be merged to be named in general as mechanocaloric effects. In addition, the electrocaloric effect leads to an adiabatic temperature change when a changing polarization is induced by applying an electric field.

All these caloric solid state cooling effects show an isothermal entropy change and an adiabatic temperature change, which can be harvested by using a suitable phase-change material and applying an external stimulus under adiabatic conditions in a cyclic manner [74]. Regarding material performance, system performance and level of development, magnetocaloric cooling is considered the most promising at the moment with prospects to be even superior to vapor-compression systems in a long-term perspective [24, 26, 75]. However, the evaluation criteria to judge the individual cooling technologies of such studies need to be considered carefully because the parameter input plays an important role on the result and variation of aspects like thermal span, temperature range, or target application can lead to different conclusions.

An elevated level of caloric cooling can be reached by combining the above mentioned effects since a caloric material can be sensitive to more than one stimulus. Consequently, a phase change can be induced simultaneously or alternatively by different stimuli leading to multicaloric effects [57, 76–80]. The first-order phase transition of magnetocaloric compounds additionally comes along with a change of lattice parameters usually leading to a volume change (Fe_2P is an exception here, where an anisotropic change of the lattice constants overall maintains the cell volume), which is due to the expansion/contraction of the unit cell (dilatational effect) or the complete change of the crystal structure (structural effect). Consequently, the phase transition can be induced by a magnetic field or an external pressure [57]. This can be used to tackle the problem of thermal hysteresis for magnetocaloric cooling cycles with first-order materials. As an example, Liu *et al.* [76] proposed to induce the phase transition from martensite to austenite of an inverse magnetocaloric Heusler alloy by applying a magnetic field and to use a pressure for supporting the back transformation upon field removal. Since the thermal hysteresis would prevent a complete back transformation to the martensite state upon field removal, an applied pressure shifts the phase transition for the back transformation to higher temperatures and favors the low-volume martensitic state energetically. The magnetic field is then removed under pressure enabling a complete back transformation to the single phase martensite state. Removing the pressure afterwards leads to the starting point of the cycle again. This approach has also been proposed to enhance the cyclic caloric performance of hydrogenated La-Fe-Si [81]. A similar method has been used to reduce the hysteresis effect by an electric-field assisted removal of the magnetic field in FeRh thin films on a BaTiO_3 substrate [78]. On the other hand, Czernuszewicz *et al.* [79] proposed to apply a magnetic field and pressure simultaneously at T_C of a Ni-Mn-In Heusler alloy in order to add up both effects and enhance the caloric response or reduce the required amount of field strength/pressure. Recently, Gottschall *et al.* [43] introduced a new multicaloric cooling cycle by using the large thermal hysteresis of first-order materials instead of trying to reduce it. The cycle consists of alternately applying magnetic field and uniaxial pressure, as it is shown in Fig. 2.3.

The proposed cycle is explained exemplarily for an inverse magnetocaloric and at the same time conventional barocaloric material in Fig. 2.3 (a). The principle also works vice versa for a conventional magnetocaloric and inverse elasto-/barocaloric material. Similar to a MCE setup, the cycle starts with the material being in its low-temperature state at a temperature close to A_s (using the notation for an assumed martensitic transition). In a first step, the magnetic field is applied inducing a transition from

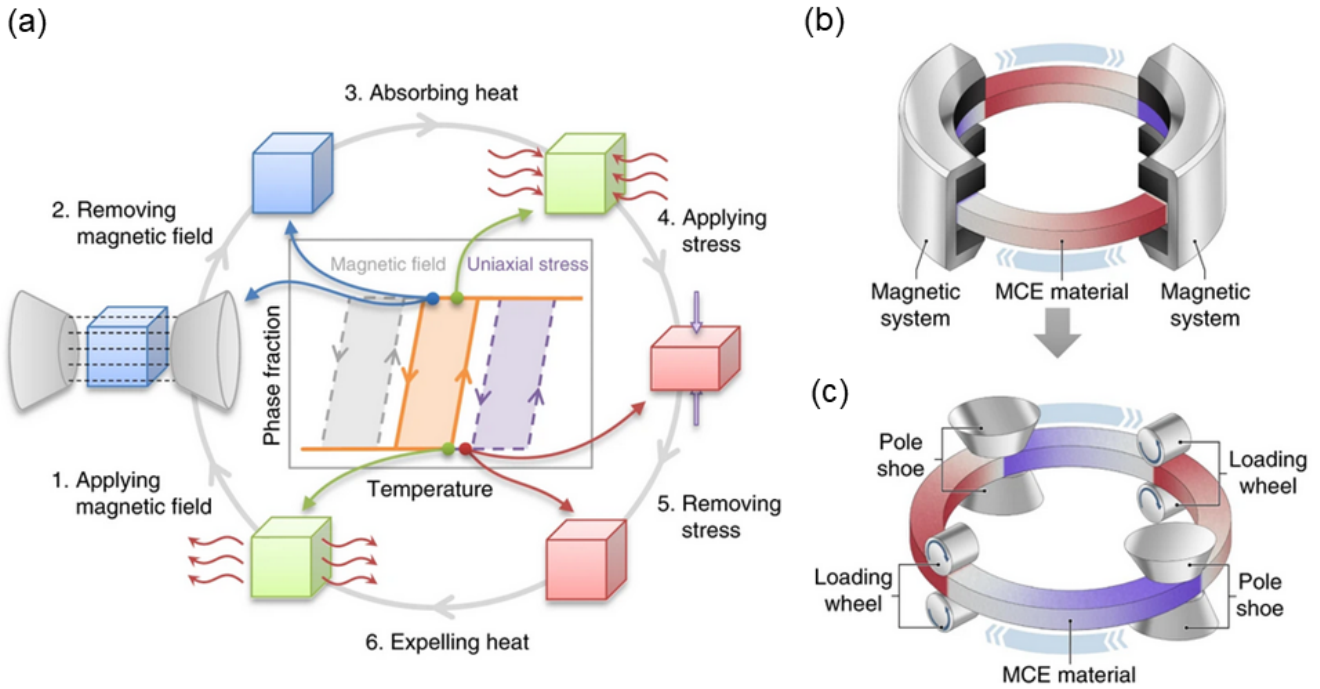


Figure 2.3: The necessary steps of the multicaloric cooling cycle using magnetic field and stress as stimuli are illustrated in (a) for an inverse magnetocaloric material with the help of a phase fraction-temperature diagram in zero external field (orange curve) and for an applied magnetic field and pressure (dashed grey curves). The absolute temperature of the sample is indicated in green for the initial starting temperature, in blue for a cooled state after field application (negative ΔT_{ad}) and in red for a heated state after pressure application (positive ΔT_{ad}). Schematic representation of a conventional magnetocaloric setup (b) together with the newly proposed multi-stimuli cooling system using a magnetic-field source combined with pressure application, depicted here by wheels, to the caloric material (c). The image is taken from [43].

low-magnetization to high-magnetization state (1). This leads to a negative adiabatic temperature change and thus to a cooling of the material. Subsequently, the magnetic field is removed, but the material will stay in its high-magnetization state due to the large thermal hysteresis and the absolute temperature is maintained (2). At this point, heat can be absorbed from the cooling target in order to equilibrate the temperature of the magnetocaloric material (3). In order to transfer the material back to its original state, an external (uniaxial) pressure is applied (4). Under adiabatic conditions, this results in a positive ΔT_{ad} of the barocaloric (elastocaloric) effect and a heating of the material. After (or even before/during) removing the stress (5), the excess heat can be emitted to the surrounding and the material is back in the low-magnetization state at the starting temperature (6).

One main advantage of this novel cooling cycle is the efficient use of a magnetic-field source. For the conventional approach of a magnetocaloric cooling cycle, the temperature change is induced by a magnetic

field and this effect should be as reversible as possible. As a result, the subsequent removal of the magnetic field causes the back transformation to the initial state and induces a ΔT_{ad} opposite in sign. Consequently, the material is required to stay in the magnetic field as long as the heat exchange takes place and the induced ΔT_{ad} can be exploited. A setup that moves the material relative to an immobile field source therefore requires a certain amount of permanent magnet material as it is illustrated in Fig. 2.3 (b). In contrast, the phase transition for the multicaloric cycle is in an ideal case not reversible at all due to a large enough thermal hysteresis and the achieved adiabatic temperature change of the magnetocaloric material can be used even after the magnetic field has been removed. Therefore, a much smaller amount of magnetic-field source is needed and the sample has to be exerted to the maximum field strength only for a short time without limiting the time that is available for heat transfer. By this, the expensive permanent magnet field source can be reduced to a minimum, which is a crucial factor determining the criticality and resource supply for market penetrating magnetocaloric cooling applications [36]. Even the complete abstinence of a permanent magnet may be possible by using pulsed magnetic fields produced by capacitor discharge.

2.3 Magnetocaloric materials

In order to optimize a material for its application in magnetocaloric heat exchanger systems, the properties to be considered are manifold. Figure 2.4 illustrates the most important quantities that are relevant for the material optimization on the one side (left part of image) and the integration into an efficiently working cooling application on the other side (right part). Important to note here is that both sides have to be considered in order to combine the two aspects of an excellent material and an efficient device.

The main figures of merit in order to assess the suitability of a material for magnetocaloric cooling purposes are the already described ΔT_{ad} and Δs_T . These two properties indicate strongly how well a material can perform in a magnetocaloric cooling cycle. The maximization of these two properties is mainly influenced by a phase transition experiencing a large magnetization change that is taking place according to Equations (2.7) and (2.8) in a temperature interval as sharp as possible. It is important to note that the cyclic performance is of interest here and therefore the quantities of Δs_T and ΔT_{ad} have to be discussed in terms of cyclic effects, even though literature often provides values for the first field application only. In fact, the determination of the cyclic Δs_T is not trivial from usual magnetization or calorimetric measurements. The main factor that influences the reversibility of these two properties under cyclic conditions is the thermal hysteresis that appears for first-order transitions. As a result, the maximum magnetocaloric effect is reached at a starting temperature close to the transition temperature for the first field application cycle and decreases for the case that the magnetic field is not strong enough to overcome the thermal hysteresis and also induce the back transformation completely. Consequently, for the cyclic application of a magnetocaloric material in a cooling device, a reduction of the thermal hysteresis is desired. Furthermore, the shift of the transition temperature in external magnetic fields $\frac{dT_i}{\mu_0 dH}$ is an important property that indicates how efficient the magnetocaloric effect can be induced by an external magnetic field. The higher this property,

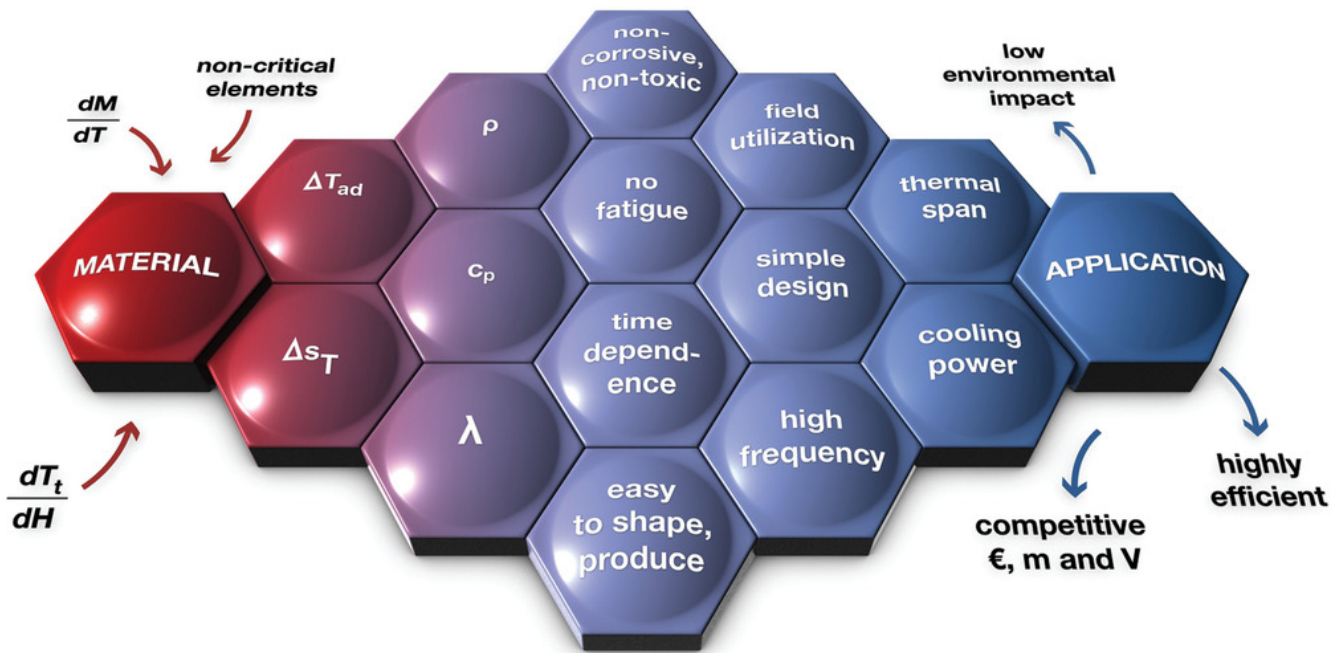


Figure 2.4: Properties that have to be considered for an efficiently working magnetocaloric cooling system, which illustrates the interplay of materials development and device optimization. The image is taken from [71].

the lower magnetic-field strength is needed to complete the induced phase transformation. Furthermore, the transition temperature of a material defines its temperature range of operation. Therefore, it must be easily tunable without losing the strength of the MCE significantly. This allows for a distinct tailoring of a material for the desired field of application. Considering ambient cooling applications, the transition temperature is expected to be around room temperature.

In addition, secondary physical material properties play an important role for assessing the potential of magnetocaloric refrigerants as it is illustrated in Fig. 2.4. Important to mention here are the heat capacity c_p and the thermal conductivity λ since they determine the amount of heat that can be exploited for a heat exchange system. According to Equation (2.8), c_p should be small in order to maximize ΔT_{ad} since it is by definition the amount of heat needed to change the temperature of a substance [82]. The resulting temperature change of a material would need to be transported fast through the sample and also to the heat exchanger (liquid). This means that a high λ of the material itself as well as of the interface to the heat exchange liquid is required. The analysis of time-dependent effects can also give important information on the effectiveness to use a certain material in a refrigerator. For reaching large efficiencies, estimated frequencies lie in the range of 1 Hz to 10 Hz, which means that the material must be able to follow the changing magnetic-field strength of one cycle within 100 ms [63]. Assuming a maximum field strength of 2 T and one field application plus removal per cycle, this would be equal to rates of 40 T s^{-1} for

a first and simple approximation of a constant field change rate. Innovative solutions of alternative designs for magnetocaloric application devices may also be feasible for much higher frequencies of up to 50 Hz to 200 Hz [83]. For these fast frequencies, the materials must be further evaluated practically in terms of MCE, hysteresis effects and heat transfer under such extreme conditions.

In order to fulfill the conditions of a competitive cooling technology, a magnetocaloric material also needs to obey certain functional, economic and ecologic requirements. It is essential to maintain chemical and mechanical stability in its working environment reliably. This means that the contact to a heat exchange liquid should not lead to corrosion or fatigue. This also includes functional fatigue over millions to billions of cycles [84], meaning that the MCE must not decrease significantly over the lifetime of a cooling device. Furthermore, the material must be easy to process into certain geometries that enable the largest possible heat transfer in combination with an optimal fluid flow [63, 84]. Recently, the method of additive manufacturing via 3D-printing has emerged as a possible alternative for producing near-net-shape magnetocaloric materials in complex geometries [85–87]. Other possibilities are the pressing of polymer- or metal-bonded plates, microchannel arrangements, packed beds of powder or spheres as well as sintered bodies [84, 88–92].

In order to be economically competitive, not only the production but also the material itself must consist of non-critical and abundant elements. As the ecologic advantage over conventional vapor compression systems must be maintained, a magnetocaloric cooling system must contain non-toxic elements and possess an overall low environmental impact [36]. This is described in general by the criticality index of a material. In order to assess a resource criticality, many aspects need to be considered and different approaches exist. Most commonly, the assessment is based on the factors of supply risk, environmental implications and vulnerability to supply restrictions [93]. Therefore, each material used for a potentially new technology must be evaluated with respect to its resources needed for large-scale applications. This does not imply only geological availability of the raw elements, also geopolitical factors, recyclability, substitutability or the global demand for competing technologies are important to consider [36]. Consequently, a critical element is not necessarily rare regarding its geological abundance. Preferred element extraction in a region with unstable political situation can also lead to a certain criticality of a material because of a supply risk that can be significant if export or mining is stopped for political or economical reasons. A prominent example are the export restrictions of China, which plays the central role for the rare earth element criticality by producing, consuming and exporting 90 % of the global supply [94]. This political decision led to the rare earth crisis in 2011 with the price increases for the raw elements of up to 2000 %.

In terms of applications, the most crucial properties to be maximized are the thermal span that can be reached by a device and the corresponding cooling power of the system providing a certain thermal span between the hot and the cold end of the heat exchanger.

Since the discovery of the giant magnetocaloric effect of $\text{Gd}_5(\text{Si}_2\text{Ge}_2)$ in 1997 by Pecharsky and Gschneidner [95], the research and development on new material systems for magnetocaloric cooling applications has evolved into a strong field of research. However, this pioneering compound of the late 1990's is not considered as a promising candidate for cooling applications today for cost reasons because it contains the

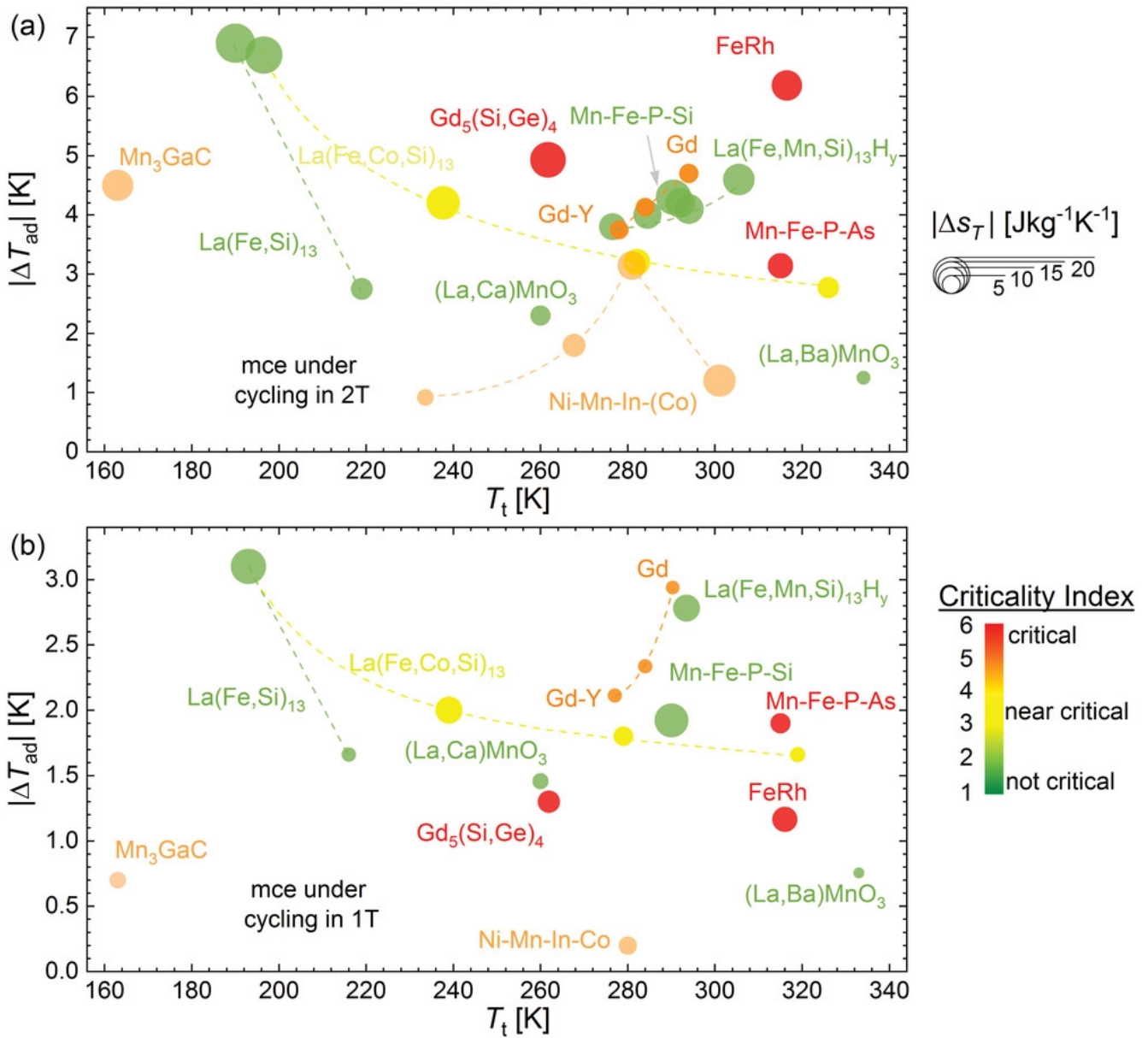


Figure 2.5: Cyclic magnetocaloric performance of most prominent magnetocaloric materials under cycling in magnetic-field changes of 2 T (a) and 1 T (b). Besides the values for ΔT_{ad} on the y-axis, Δs_T is represented by the size of the respective circle. The criticality index of the necessary elements is indicated by the color code. The image is taken from [71].

rare earth element Gd as well as critical Ge [36, 40]. A comprehensive overview on the present library of most prominent magnetocaloric materials and their properties can be found in [71]. Most relevant compounds are shown by the magnetocaloric figures of merit ΔT_{ad} and Δs_T as well as the criticality of the contained elements for the cyclic behavior in 1 T and 2 T in Fig. 2.5.

Already in 1990, a very large inverse magnetocaloric effect has been reported for the binary FeRh, which shows a transition from a ferromagnetic high-temperature to an antiferromagnetic low-temperature phase (inverse FOMT) [96, 97]. Its stoichiometric transition temperature is slightly above room temperature and can be adjusted by the chemical composition, doping elements or the heat treatment procedure [98–101]. Due to an extraordinary sharp transition and a large shift of the transition temperature in magnetic fields, FeRh shows the largest magnetocaloric effect in low fields with ΔT_{ad} up to -13 K for first magnetic-field applications of 2 T [96] and 6.2 K upon cycling [102]. However, the development of this material system for applications is limited by the high costs of Rh. It often serves as a model system due to the simplicity of the binary compound and the large MCE. Also the large thermal hysteresis decreases the cyclic performance especially in fields of 1 T below the values of other candidate materials (see Fig. 2.5) [71].

Despite its high costs, the standard reference material for the MCE is still elemental Gd with a second-order Curie temperature at 293 K. It shows a ΔS_T of around $5 \text{ J kg}^{-1} \text{ K}^{-1}$ and a ΔT_{ad} of 5 K to 6 K for a magnetic-field change of 2 T [71, 95, 103]. Due to its second-order nature, these values are also obtained under cyclic conditions. For this reason, it was elemental Gd that was first and most often used to prove working refrigeration systems based on the magnetocaloric effect. The study of Brown in 1976 [68] represents a pioneering work for near room temperature magnetic refrigeration. It has been shown that a temperature span of 47 K can be reached between the hot and cold end of a regenerator after only 50 cycles using elemental Gd as active magnetocaloric material, a water-ethyl alcohol mixture as heat exchange liquid and a 7 T superconducting magnet for the production of an alternating magnetic field. Another main advantage of using the second-order transition is the large temperature range, in which a single material can be operated. This is essential for building up these large temperature spans without using stacks of different alloys in an AMR.

Most prominent magnetocaloric materials that are considered for being used in demonstrator devices and application-near systems are $\text{La}(\text{Fe},\text{Si})_{13}$ and its hydrides [104–107] as well as Fe_2P -type alloys [108–110]. The phase transition of interest in both of these material families is a first-order transition showing a conventional magnetocaloric effect. Both systems exhibit a dilational phase transition with a significant change of volume or lattice constants at the transition temperature while maintaining the crystal symmetry of the phase.

The phase transition of $\text{La}(\text{Fe},\text{Si})_{13}$ takes place between two cubic structures with a discontinuous volume expansion from high-temperature to low-temperature phase of around 1 % to 1.5 % [111–113] making it an inverse barocaloric system. The transition temperature is situated around 200 K and therefore too low for room temperature applications. By changing the Fe/Si ratio [105] or doping the system with Co [114], the transition temperature can be shifted towards higher temperatures. As a side effect, the nature of the transition changes from first-order to second-order, which reduces the magnetocaloric effect of the transition [115]. As a further doping element, Mn is used in order to reduce the transition temperature. A widely used method to adjust the transition temperature is the hydrogenation of the La-Fe-Si alloy [106, 116, 117]. Introducing hydrogen atoms on interstitial lattice sites creates a chemical pressure that stabilizes the low-temperature phase and increases the transition temperature [116, 118].

Since a full hydrogenation leads to a T_t above room temperature, additional doping of Mn is used to adjust T_t precisely. The control of the amount of hydrogen is not easily applicable and partial hydrogenation can lead to instabilities [115]. Despite containing the rare-earth element La, these alloys are not expensive from the element side because the La prize is one of the lowest of the rare-earths. The reason is that the rare-earth elements are always co-occurring and mined together in different amounts. Therefore, some elements with high demand drive the extraction, while others are produced in excess [36]. The rare-earth element of Nd, for instance, is of large importance for the production of permanent magnets needed in electronic devices, electric motors and wind turbines. During the extraction of Nd, the products always come together with other light rare-earths (La, Ce) that are not industrially used in large amounts and thus are available for low prices (around 4 \$/kg for La and Ce, 30 \$/kg for Gd, and 67 \$/kg for Nd in September 2020 (most recent prize for pure Gd metal available of March 2020) [119]). The production of heat exchanger geometries of La-Fe-Si(-H) alloys can be carried out by hot-pressing [120], cold-pressed plates of polymer-bonded [89] or metal-bonded powder [90] subsequent to powder processing. Due to the narrow thermal hysteresis, the reversible ΔT_{ad} at room temperature in magnetic-field changes of 1 T to 2 T can be as large as the MCE in Gd (see Fig. 2.5).

Magnetocaloric Fe_2P -type alloys have the stoichiometric composition of $(\text{Mn}, \text{Fe})_2(\text{P}, \text{X})$, where X can be As, Ge or Si. The use of Si forming a Mn-Fe-P-Si compound is highly favored for a well-performing magnetocaloric alloy without resource critical elements [36]. The compounds exhibit a transition between two hexagonal crystal structures with an anisotropic change of the lattice constants. Whereas the c -axis shrinks, the a - b plane expands and the volume of the whole unit cell is not changing drastically [109, 121]. These alloys are usually produced by powder metallurgical routes via sintering [110, 122]. The transition temperature can be adjusted by the stoichiometry, usually by changing the Mn-to-Si ratio [109]. A special characteristic of Fe_2P -type alloys is the so called virgin effect [123, 124]. Since not all grains of the material transform uniformly at the same time and in the same direction, the anisotropic length change of transforming fractions of the material is mechanically hindered by surrounding volume. The transition is partly suppressed and T_t^c of the first cycle is delayed until the material cannot withstand the built-up pressure and relaxes by mechanical damage. This first transformation is accompanied with the formation of cracks throughout the material [110, 122]. Upon further cycling, the material can transform at the respective local equilibrium transition temperature and expand into the newly formed voids. As a result, the first transition cycle is characterized by a very large thermal hysteresis whereas the further cycles reach the equilibrium shape of the phase transition curve with a narrow thermal hysteresis. It has been suggested (similar to the La-Fe-Si system) that a critical point can be reached, where the first-order transition can be tuned towards a second-order transition with nearly no thermal hysteresis but still significantly sharp MCE [110].

In addition, Ni(-Co)-Mn-X Heusler alloys (X=Al, Ga, In, Sb, Sn) are often considered as a promising material class for magnetocaloric refrigeration. Except for X being Ga, these alloys exhibit an inverse magnetocaloric effect because they possess a martensitic phase transition from high-magnetization austenite to low-magnetization martensite. This transition can be induced by a magnetic field because of the significant

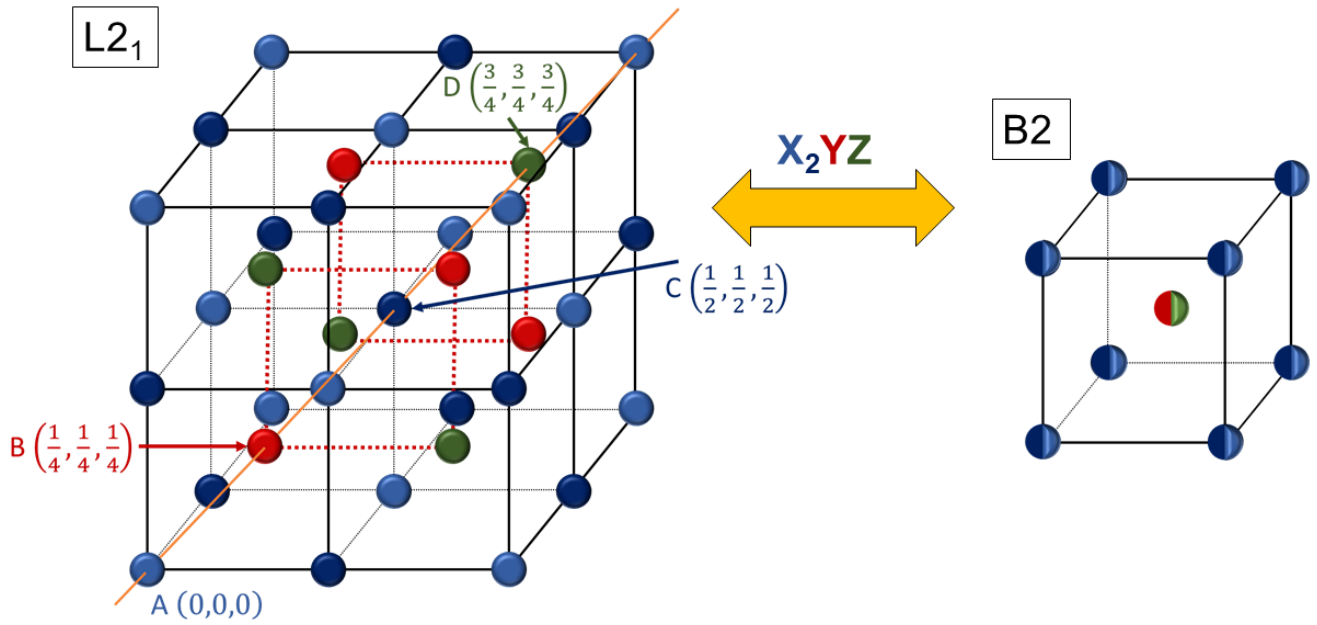


Figure 2.6: Heusler ($L2_1$) structure and B2 disorder for X_2YZ compounds. The shown representation of $L2_1$ is shifted by $(\frac{1}{4}, \frac{1}{4}, \frac{1}{4})$ compared to the classic representation of the $Fm\bar{3}m$ unit cell.

ΔM of the two phases. Highest MCE is reported for Ni-Co-Mn-In alloys with a maximum ΔT_{ad} of 8 K for the first field application of 2 T and 3 K under cyclic conditions [125]. This kind of material system will be presented in more detail in the following section.

2.3.1 Heusler alloys

Heusler alloys in general have the chemical formula X_2YZ , where X and Y are transition metals and Z is usually a main group element from the columns III-V of the periodic table. The first Heusler alloy was discovered by and named after Friedrich Heusler [126]. It attracted attention because the Cu_2MnAl alloy showed ferromagnetic properties even though none of the alloyed elements is ferromagnetic. The explanation for this phenomenon is based on the magnetic properties of Mn, which plays a crucial role in many Heusler alloys. Since the interatomic distance between the Mn atoms is increased in the crystal structure of the Heusler alloy compared to elemental Mn, which is antiferromagnetic, the magnetic interactions change to ferromagnetic coupling. This behavior of magnetic exchange interaction being dependent on the ratio of interatomic distance and the radius of the unfilled electron shell is explained by the Bethe-Slater curve [127, 128].

Heusler alloys crystallize in the accordingly named Heusler structure or $L2_1$ structure [129] with crystal symmetry $Fm\bar{3}m$ (space group number 225). It consists of four interpenetrating face-centered cubic (fcc) lattices that are shifted each for a vector of $(\frac{1}{4}, \frac{1}{4}, \frac{1}{4})$ along the body diagonal of the cubic unit cell. The

resulting structure is shown in Fig. 2.6. Each of these four fcc sublattices consists of one of the four stoichiometric elements of the X_2YZ compound. The sublattices are usually named by considering their position with respect to the (0, 0, 0) position of the $L2_1$ unit cell. It must be noted that the shown representation is shifted by $(\frac{1}{4}, \frac{1}{4}, \frac{1}{4})$ compared to the classic representation of the $Fm\bar{3}m$ unit cell for better visualization. The lattice with the base atom at (0, 0, 0) is called A-site, whereas the base atoms of the shifted fcc sublattices are named B-site at $(\frac{1}{4}, \frac{1}{4}, \frac{1}{4})$, C-site at $(\frac{1}{2}, \frac{1}{2}, \frac{1}{2})$ and D-site at $(\frac{3}{4}, \frac{3}{4}, \frac{3}{4})$, respectively [130]. The convention for the stoichiometry and the distribution of the atoms on the lattice sites is usually related to each other. For an X_2YZ compound, the X atoms with the highest amount of valence electrons occupy the A- and C-sites, the Y atoms with the second highest valence occupy the B-sites and the Z atoms with the lowest valence are situated at the D-sites [130]. However, the Heusler structure is very prone to metastable configurations and disorder. Therefore, many Heusler compounds show a certain amount of disorder between respective lattice sites [130, 131]. The most common one is the disorder between Y and Z atoms, which leads for the case of equal atomic occupation on the A- and C-sites as well as for complete disorder to eight equally probable base-centered cubic (bcc) subcells. This structure can be reduced to a bcc structure with one atomic species on the corners (X) and another one in the center (representing a mixture of Y and Z with a probability of 0.5 each), which is equal to the B2 structure [131, 132]. Furthermore, it is possible to produce Heusler compounds that deviate from the stoichiometric composition. For example, Z atoms can be partially substituted by Y atoms, which then occupy the remaining D-sites or vice versa. The corresponding notation of the substitutional space would be $X_2Y_{1+x}Z_{1-x}$ or unified to 100 at. % $X_{50}Y_{25+x}Z_{25-x}$. This then results for the $L2_1$ structure in a regular site distribution for the elements of $(X_{25})_A(Y_{25})_B(X_{25})_C(Y_x/Z_{25-x})_D$. A special configuration of Heusler alloys is represented by the so-called half-Heusler compounds with the stoichiometry XYZ, where one fcc sublattice of the $L2_1$ structure is completely unoccupied leading to the $C1_b$ structure with crystal symmetry $F\bar{4}3M$ (space group number 216) [131, 132].

Due to the large variety of element combinations that can be used to form a Heusler compound, a large range of different properties can be covered [133]. Therefore, Heusler and half-Heusler compounds are considered for many different kind of functionalities and applications. A special peculiarity of Heusler compounds in general is the strong influence of the average valence electron count per atom on the electronic, magnetic and structural properties. Half-Heusler compounds are mainly used for thermoelectric materials [134]. Full-Heusler compounds are often considered for magnetic materials, especially Co_2 -based alloys possess large magnetic moments. The Curie temperature as well as the magnetic moment of the compound is hereby depending on the valence electron count per atom/formula unit (e/a ratio). In addition, many compounds (half-Heusler and Co_2 -based full-Heusler alloys) have been reported as half-metallic ferromagnets with large spin polarizations, thus being attractive for spintronic applications like giant magnetoresistance and tunneling magnetoresistance junctions for data storage [135–137].

A coupled magnetic and martensitic transition in Ni(-Co)-Mn-X ($Ni_{50-x}Co_xMn_{50-y}X_y$) Heusler alloys leads to a magnetocaloric effect and to a magnetic shape-memory effect. Especially Ni-Mn-Ga alloys show large strains and are considered as shape-memory alloys and as elastocaloric materials [51, 138]. These

Ni(-Co)-Mn-X Heusler alloys (X=Al, Ga, In, Sb, Sn) are in focus of research for their good magnetocaloric properties [76, 139–142]. Especially Ni(-Co)-Mn-In alloys show the most promising magnetocaloric properties with highest ΔT_{ad} for a Heusler alloy of -8 K in fields of around 2 T [125]. The corresponding ΔT_{ad} upon magnetic-field cycling is reduced to -3 K. This highly reduced MCE of further field cycles is due to the large thermal hysteresis that is inherent in the structural change of crystal symmetry in combination with the incommensurability of the two lattice structures. In addition, the martensitic transition in Heusler alloys is accompanied by a volume change of 0.75 % to 1 % [143, 144].

2.3.2 MM'X alloys

An additional class of compounds that show attractive properties for magnetocaloric considerations are MM'X materials. These alloys consist of two 3d metals, often Mn, Fe, Co or Ni (M and M') and a main group element, often Sn, Ge or Si (X). They possess a hexagonal high-temperature phase with Ni₂In-structure ($P6_3/mmc$, space group number 194) and an orthorhombic low-temperature phase with TiNiSi-structure ($Pnma$, space group number 62) [145].

Besides this structural transition, a magnetic phase transition occurs for MnNiGe, from paramagnetic to antiferromagnetic at the Néel temperature of 346 K [146], with the structural transition taking place at 493 K [145, 147]. Therefore, both transitions exist independently and the structural transition is not accompanied by a significant magnetization change. However, the structural phase transition can be coupled to a magnetic transition by tailoring both transition temperatures to establish a FOMT. This is achieved for example by substituting Fe for Mn like it is shown schematically in Fig. 2.7. The introduced Fe atoms reduce the structural transition temperature below the magnetic one, which leads to a direct transformation of the paramagnetic hexagonal phase to the (anti)ferromagnetic orthorhombic phase. Additionally, the substitution of Fe induces ferromagnetism in the low-temperature orthorhombic phase by breaking the antiferromagnetic coupling of the Mn atoms [148]. This effect results in high changes in magnetization during the phase transition. Similarly, the system of MnCoGe undergoes a structural transition at 420 K upon cooling [147]. Here the orthorhombic martensite becomes ferromagnetic at the Curie temperature of 355 K [145] and both transitions can be coupled to result in a FOMT. Those transitions are tunable in a certain temperature range around room temperature for several similar MM'X material systems and by different means.

Zhang *et al.* [150] reported in this context a tunable magnetostructural transition for off-stoichiometric Mn_{1.9-x}Ni_xGe being suitable for magnetocaloric applications. Later, a tunable giant magnetocaloric effect (GMCE) with entropy changes up to -47 J kg⁻¹ K⁻¹ in 5 T was reported in 2010 for MnCoGe with additional interstitial boron [151]. Recent works showed other possibilities to control this system further by substitutions [152–154] or the introduction of vacancies [155–157]. For the material family of MnCo_{0.95}Ge_{0.97}, a direct measurement of ΔT_{ad} up to 1.5 K in a field change of 1.9 T has been reported [156]. Beyond that, direct measurements of the adiabatic temperature change of this particular material system are only rarely reported. The similar Mn-Ni-Ge system undergoes a martensitic phase transition with high changes in

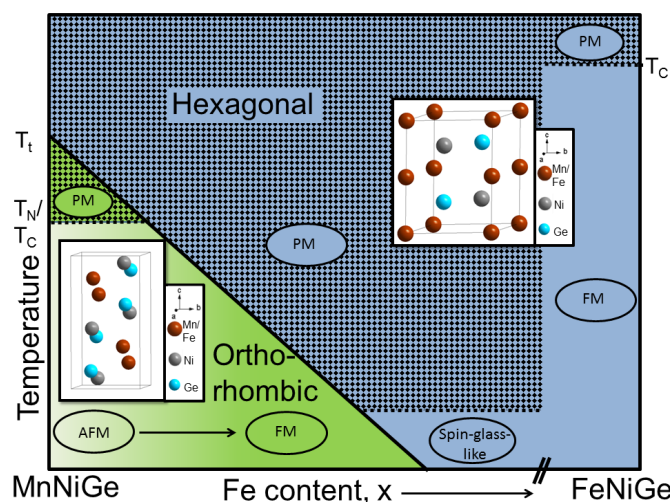


Figure 2.7: Schematic depiction of a phase diagram for the isostructural binary system of MnNiGe and FeNiGe representing the varying Fe content as substitution for Mn. The magnetic transition can be coupled to the structural transition by increasing Fe content, which induces ferromagnetism in the otherwise antiferromagnetic martensite. The image is published in [149].

magnetization. Recently, sharp transitions with a very small thermal hysteresis and a tunable transition temperature could be obtained in the $\text{Mn}_{1-x}\text{Fe}_x\text{NiGe}$ material system [148]. A problem for this material family is the enormous volume change between hexagonal austenite and orthorhombic martensite. During the phase transformation, the material increases its volume by approximately 2.7% [148] upon cooling, which leads to large strains between the expanding grains. The bulk material therefore loses its mechanical integrity and decriptates into powder.

The central challenge for this material family is to substitute the expensive and critical element of germanium [40, 158]. As shown in many works [148, 151, 159], the material possesses promising properties towards magnetocaloric cooling purposes. Although the reduction of the used Ge content was demonstrated for transitions around room temperature [160], a significant amount of Ge is still required.

2.4 Material requirements for the multi-stimuli cycle

For the usage of a compound in multicaloric applications, the phase transition responsible for the caloric effect needs to be influenced by more than one external stimulus. Most prominent is the consideration of magnetic shape-memory alloys such as Ni-Mn-Ga or Ni-Mn-In Heusler alloys that show both magnetocaloric and mechanocaloric effect as a result of the martensitic phase transition experiencing both a magnetization change and a volume change [76, 161]. Also the well-known magnetocaloric material system of hydrogenated La-Fe-Si has been proposed for multicaloric cooling [81] by using both magnetic field and external pressure. In addition, a combination of electrocaloric and baro-/elastocaloric effect can be used for example in ferroelectric BaTiO_3 [162] or $\text{Pb}(\text{Mn}_{1/3}\text{Nb}_{2/3})\text{O}_3$ -32 PbTiO_3 (PMN-PT) single crystals [163].

The combination of magnetocaloric and electrocaloric effect is rather rare but an electric-field control of the phase transition has been realized by placing Ni-Co-Mn-In ribbons on a PMN-PT substrate, which creates a straining of the ribbons when the substrate changes dimensions due to a piezoelectric effect [164].

When considering the described multi-stimuli cooling cycle that exploits the thermal hysteresis of a multicaloric first-order phase-change material, a combination of magnetocaloric and elastocaloric effect is necessary and the requirements for the materials selection deviates slightly from the ones for classic magnetocaloric materials. The base for a good material, however, stays the same: a sharp first-order phase transition with a large magnetization difference between the two phases is desired and this transition should be induced effectively by a magnetic field ($\frac{dT_t}{\mu_0 dH}$ should be sufficiently large). Also the focus of secondary properties like thermal conductivity, element criticality, or processability is maintained as summarized in Fig. 2.4. The first main difference is represented by the width of the thermal hysteresis. In order to prevent a back transformation of the material when the magnetic field is removed, the thermal hysteresis must be large. Furthermore, a reaction on a second stimulus is necessary. Therefore, the phase transition temperature needs to be shifted by an applied (uniaxial) pressure ($\frac{dT_t}{d\sigma}$ should be sufficiently large). The application of pressure during the cycle also requires the material in particular to be mechanically stable. On the one hand, the material must withstand the necessary pressure to induce the phase transition. On the other hand, the long term properties require the material to be stable among millions of transition cycles that include mechanical and functional fatigue resistance due to the applied pressures as well as the volume changes of the transition itself.

For the selection of a proper material, it must be considered that the application of pressure cannot be done contactless like it is the case for a magnetic field. Consequently, the adiabatic conditions of this step will be difficult to achieve and a significant part of the positive/negative heat change of the material will be dissipated to the pressurizing setup immediately, depending on the thermal conductivity of the interface and the used technique/material for applying the pressure. Inverse magnetocaloric materials cool down when inducing the phase transition by a magnetic field and heat up when using pressure (conventionally barocaloric). By considering them as preferred candidates for the multi-stimuli cooling cycle, the negative temperature change upon magnetic-field application can be used for cooling the load and the produced heat upon pressure application is transported away immediately. For designing an optimal material, the real values of transition width, transition hysteresis and sensitivity to the external stimuli must match for the whole cycle to work out. Therefore, several conditions can be formulated. The schematic representation of the transition cycle is shown in Fig. 2.8. It must be noted here that the temperature scale on the x -axis is only to represent the phase transition at a constant magnetic field and pressure. However, the change of the material's temperature due to stimuli-induced caloric effects is indicated by a change of the color for the respective points of the cycle for easier visualization. In fact, the whole curve is shifted to higher (pressure) or lower (magnetic field) temperatures by the application of an external stimulus. The position of the drawn curve with respect to $T_s = A_s$ is valid for zero external magnetic field and no additional pressure application.

First of all, the transition width must be balanced with the sensitivity towards a magnetic field because

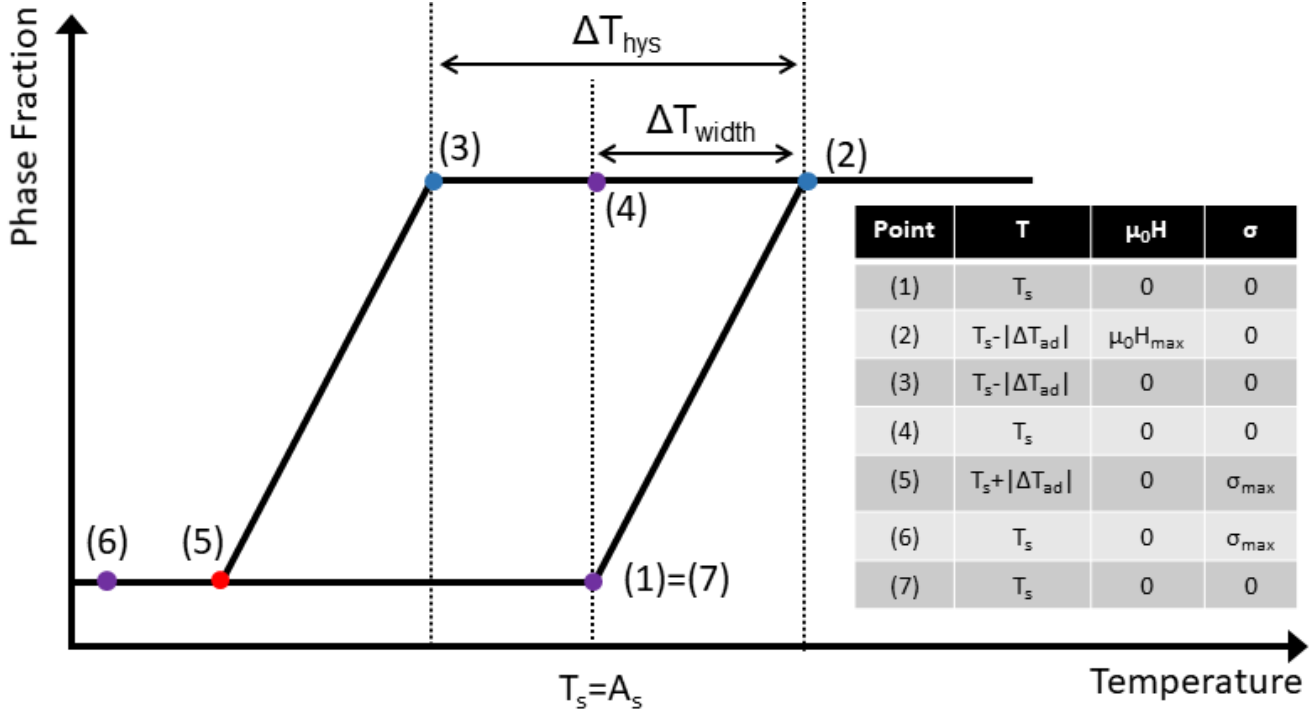


Figure 2.8: Schematic representation of the necessary steps for an optimal multi-stimuli cooling cycle, represented by the thermal hysteresis curve for an inverse magnetocaloric material. The position of the sample phase fraction is shown for the currently applied stimulus at each point (see table) universally for one curve (relative temperature scaling on the x -axis varies for each point) instead of shifting the whole curve along the temperature axis. The absolute temperature of the sample is indicated by the color of the point, where red means heating and blue cooling with respect to the starting temperature in purple.

the applied field must be able to induce a complete phase transition. Since an inverse material is cooling down during this step, the real temperature of the material changes, which must be taken into account for this consideration. Therefore, the shift of T_t with a magnetic field must be large enough to overcome the transition width ΔT_{width} and the resulting temperature change for this field strength in order to reach the full austenite state at point (2). For the easiest approach, the starting point (1) of the cycle at T_s is assumed to be directly at the austenite start temperature of an inverse magnetocaloric material that is in complete martensite state.

$$\left| \frac{dT_t}{\mu_0 dH} \right| \mu_0 \Delta H \geq \Delta T_{width} + |\Delta T_{ad}(\Delta H)| \quad (2.11)$$

In order to prevent the back transformation, the thermal hysteresis must be larger than the transition width plus the adiabatic temperature change because the temperature of the material after field removal is reduced compared to T_s . The field removal step is shown in Fig. 2.8 from point (2) to point (3). In

addition, the thermal hysteresis must not be too large in order to keep the needed pressure for inducing the back transformation as low as possible. Ideally, the temperature of the material after magnetic-field removal should be exactly at the martensite start temperature M_s . This is giving an exact ideal value for the width of the thermal hysteresis:

$$\Delta T_{hys} = \Delta T_{width} + |\Delta T_{ad}(\Delta H)| \quad (2.12)$$

After the heat exchange step, the material is assumed to reach point (4) with its initial temperature T_s again, now being in a complete austenite state. For a completed back transformation, the shift of the transition temperature with pressure has to overcome now the exchanged value of $|\Delta T_{ad}(\Delta H)|$ again, the transition width of the martensite formation (which is assumed to be equal/symmetric to the austenite formation - in reality they can differ and it must be distinguished between ΔT_{width}^h and ΔT_{width}^c for heating and cooling branch) as well as the positive temperature change that results from the induced barocaloric phase transition, reaching point (5):

$$\left| \frac{dT_t}{d\sigma} \right| \sigma \geq \Delta T_{width} + |\Delta T_{ad}(\Delta H)| (+ |\Delta T_{ad}(\Delta \sigma)|) \quad (2.13)$$

In order to reach the starting point of the cycle again, it is necessary now to remove the heat before removing the pressure reaching point (6). Otherwise, the temperature of the material would be still higher than T_s and a partial transformation to austenite would take place. Due to the necessary direct contact of the material to the pressurizing medium/material, this technique is preferred anyway. In reality, the heat dissipation takes place during the whole process of applying and removing the pressure. Nevertheless, for the case of a slow heat transport, the additional heating of the material must be considered for the worst case scenario in Equation (2.13) in order to assure a completely induced phase transition. In experimental conditions, heat dissipation will already occur during pressure application and the contribution of $|\Delta T_{ad}(\Delta \sigma)|$ in Equation (2.13) might be canceled out reducing the necessary pressure for a completed back transformation. By equating both sides of Equations (2.11) and (2.13), the saturation field and pressure that are needed to obtain a completed optimal multi-stimuli cooling cycle can be defined:

$$\mu_0 H_{sat} = \frac{\Delta T_{width} + |\Delta T_{ad}(\Delta H)|}{\left| \frac{dT_t}{\mu_0 dH} \right|} \quad (2.14)$$

$$\sigma_{sat} = \frac{\Delta T_{width} + |\Delta T_{ad}(\Delta H)| (+ |\Delta T_{ad}(\Delta \sigma)|)}{\left| \frac{dT_t}{d\sigma} \right|} \quad (2.15)$$

It needs to be emphasized that both ΔT_{ad} and the shift of T_t with respect to the external stimulus are no constants, they rather depend on the magnitude of the applied field.

From these stated requirements, it becomes clear that a material of choice needs to be selected now mainly on the sensitivity towards magnetic field and pressure in order to keep the strength of these external stimuli as low as possible. However, the desired irreversible back transformation upon field removal now

offers the new possibility to use larger fields because they do not need to provide the space and time to allow for a heat transfer before the field removal step. As a consequence, concentrated fields for example by superconducting or pulsed magnets can be used. They can provide stronger fields compared to the ones produced by permanent magnets for regular magnetocaloric refrigeration setups, which are limited to around 1 T to 2 T. The selection of a suitable material mainly deviates from the classical systems of La-Fe-Si and Fe₂P-type alloys because an inverse transition with a large thermal hysteresis is most favorable. Here, the Ni(-Co)-Mn-X Heusler alloys come into focus as promising candidates, which has already been considered for pressure assisted cycles [76] and simultaneous application of two stimuli [79]. These alloys show good properties for the first field application but possess a usually large thermal hysteresis of around 10 K to 15 K, which is due to the significant lattice mismatch between austenite and martensite crystal structure. In low magnetic fields, this thermal hysteresis hinders an efficient long-term operation in solely magnetocaloric cycles. A first test using a Ni-Mn-In sample that shows nearly no reversibility upon magnetic-field removal of 2 T could prove a fully reversible temperature change by using a magnetic field of 1.8 T and a uniaxial pressure of 80 MPa alternately [43].

One drawback that arises from the first suggested Ni-Mn-In Heusler alloys is the mechanical stability. Arc molten and homogenized Ni(-Co)-Mn-X alloys usually have grain sizes of several 100 μm up to the mm-range. The mechanical stability under uniaxial compressive load amounts to absolute strength values of only around 150 MPa to 400 MPa [165, 166]. This can be enhanced by using suction-cast or directionally solidified material with a preferential grain growth starting at the cooled copper mold and resulting microstructures with much finer grain sizes [166]. The newly proposed all-*d* Heusler alloys can also be an alternative worth investigating for the purpose of the multi-stimuli cycle. The Ni-Co-Mn-Ti Heusler alloys are reported to not only show good magnetocaloric properties but also to show an increased mechanical stability compared to the regular Heusler compounds with a main group element on the D-sites. Wei *et al.* explain this enhanced mechanical strength with the hybridization of the *d-d* orbital bondings changing their covalent character [167].

3 Experimental Methods

In the following chapter, the experimental techniques that are used for achieving the results of this work will be explained in detail. The sample preparation will differentiate between the MM'X material system and the Heusler alloy samples. The basics of the characterization techniques used in this thesis will be described in the following subchapters.

3.1 Sample preparation

Nominal $\text{Mn}_{1-x}\text{Fe}_x\text{Ni}_1\text{Ge}_{1-y}\text{Si}_y$, $\text{Ni}_{50-x}\text{Co}_x\text{Mn}_{50-y}\text{Al}_y$, and $\text{Ni}_{50-x}\text{Co}_x\text{Mn}_{50-y}\text{Ti}_y$ samples were prepared by arc melting in Ar atmosphere. Due to evaporation losses of Mn during melting, an excess of Mn was added. However, the amount of excessive Mn needed is dependent on the material system and has been found out empirically. Scaling the sample after the melting process and comparing the mass loss with the original weight of used Mn gives the needed excess by assuming that only Mn evaporates during the melting and the evaporation is constant for each sample production process. For the MnNiGe system, 2 % of excess Mn was added, the Ni(-Co)-Mn-Al Heusler alloys required 4 % of excessive Mn and Ni-Co-Mn-Ti Heusler alloys 3 %, respectively. The samples were melted five times and turned around after each melting step to establish a homogeneous alloying. In order to fully homogenize the samples, a proper heat treatment had to be carried out. The conditions for this heat treatment are different for each material system and also depend on the production route. Therefore, an optimization of the heat treatment was carried out for each material system. The homogenization process was performed with various pieces from the exact same parent sample at different annealing temperatures for a fixed duration. In order to check for the right annealing time, sample pieces have been annealed for a fixed temperature but different durations. For each heat treatment, the samples were sealed in quartz tubes in Ar atmosphere with a slight overpressure of Ar at the target annealing temperature. The samples of the MnNiGe system were furnace cooled at a rate of 2 K min^{-1} , the samples of the Heusler systems were always quenched subsequently in cold water. The quenching of Ni(-Co)-Mn-Al samples was done upon keeping the surrounding tube intact, transferring the cooling rate indirectly, whereas the Ni-Co-Mn-Ti samples have been quenched by breaking the tube to ensure direct contact of the samples with the cooling water in order to achieve higher quenching rates. All samples were placed in the hot furnace at the target temperature without a controlled heating rate.

Suction casting technique has been carried out for some samples of the Ni-Co-Mn-Ti Heusler system. Therefore, samples were re-molten in Ar atmosphere above a pit in the copper plate of the arc melter. By

opening a valve that connects this pit with an evacuated chamber, the resulting underpressure takes the molten material into a vertical copper mold beneath. This technique leads to larger cooling rates compared to arc melting as well as to directional solidification from the circumference of the rod, which is in contact with the mold, towards the center. For producing the rods, a mold with a diameter of 3 mm has been used.

Polymer bonding has been carried out for the MM'X alloys by mixing the two-component system of epoxy resin and hardener *Epoxydharz L* from *R & G Faserverbundwerkstoffe GmbH* with sample powder. The powder processing was done by thermally cycling bulk samples through the transition temperature using liquid nitrogen and a heat gun. The resulting powder was sieved in fractions of $>250\ \mu\text{m}$, $40 - 250\ \mu\text{m}$ and $<40\ \mu\text{m}$. For the preparation of the polymer-bonded samples, 500 mg of the fraction $40 - 250\ \mu\text{m}$ was mixed with 5 wt. % of epoxy glue. The mixture was filled in a 10 mm x 5 mm press form and consolidated with a hydraulic uniaxial press with a force of 5 kN resulting in a pressure of 100 MPa.

3.2 Structural characterization

Phase purity of the samples was ensured by X-ray diffraction (XRD) investigation with a *STOE STADI P* diffractometer from *STOE & Cie GmbH* using $\text{Mo K}_{\alpha 1}$ radiation in transmission geometry. For the accurate determination of the lattice parameters, a Si standard (*NIST 640d*) was added. The analysis of the lattice parameters was carried out by Rietveld refinement method [168] using the *FullProf* software [169]. Distances between the Mn atoms were determined by using the 3D visualization program *VESTA* [170]. For the MM'X compounds, the powders have been produced by thermal cycling of bulk pieces for several times as well as gentle hand grinding by using an agate mortar in order to avoid inducing stresses in the material. The measurements have been carried out with powder consisting of particle sizes below $40\ \mu\text{m}$.

3.3 Microstructure investigations

A *Zeiss Axio Imager.D2m* optical microscope equipped with polarized light function has been used for the determination of the microstructural features of the investigated samples. This microscope was equipped with a temperature stage feeded by a liquid nitrogen dewar, which enables a flow control by a needle valve. The heating, cooling and temperature stabilization was realized by an additional resistive heater. Furthermore, a stage carrying a Halbach permanent magnet array producing a maximum magnetic-field strength of 1.1 T was utilized, which allowed for positioning the bore of the magnet around the sample stage. The magnet stage was moved up and down by a linear step motor, which has been calibrated by a Hall probe for the magnetic field present at the sample position as a function of the magnet stage position. The full application from zero field to 1.1 T was carried out within 10 s.

Scanning electron microscopy (SEM) using secondary electron (SE) and backscatter electron (BSE) imaging was carried out on a *Tescan Vega3* electron microscope equipped with an *EDAX Octane Plus* system for electron dispersive X-ray spectroscopy (EDS). Surface contrast imaging by using SE mode has been

performed at a working distance of 8 mm, phase contrast imaging in BSE mode as well as chemical analysis by EDS measurements have been conducted at 15 mm working distance. The images were acquired by using an acceleration voltage of around 10 keV to 20 keV. For the stoichiometric analysis by EDX, area scans as well as point scans have been used. For utilizing point scans to determine the chemical composition, at least five points were considered to achieve a statistically valid average.

Especially Heusler alloys are often described by their e/a ratio, which is the averaged valence electron count per atom. It has been calculated by weighing the number of valence electron for each element with the fraction c of the element present in the compound (in at. %). The calculation is shown exemplarily for a Ni-Co-Mn-Ti compound by Equation (3.1).

$$e/a = \frac{10 \cdot c_{Ni} + 9 \cdot c_{Co} + 7 \cdot c_{Mn} + 4 \cdot c_{Ti}}{c_{Ni} + c_{Co} + c_{Mn} + c_{Ti}} \quad (3.1)$$

For a correct utilization of the e/a ratio, the actually measured composition of a compound was considered since it can deviate significantly from the nominal one.

3.4 Magnetic and magnetocaloric characterization

Magnetization measurements were performed by vibrating sample magnetometry (VSM) on a *LakeShore VSM 7410* and a Physical Properties Measurement System (PPMS) from *Quantum Design*. The magnetization in these systems is measured over induction. The sample vibration leads to a change of the magnetic flux caused by the sample's magnetic moment over time, which induces a voltage in pick-up coils due to Faraday's law. This induced voltage depends on the constant vibration frequency and is proportional to the moment of the sample. The moment calculation of the VSM system is based on a calibration with a certified standard Ni sample with well-known moment.

The VSM was equipped with a temperature option sweeping from 77 K to 450 K by using a liquid nitrogen feed in combination with a resistive heater. Since the sample was not in direct contact with the thermal sensor measuring the temperature, the heating/cooling rate of 2 K min^{-1} was interrupted by a temperature stabilization time of 0.5 min for each data point of the temperature-dependent magnetization ($M(T)$) measurements.

The PPMS was used for VSM measurements in higher magnetic fields since the superconducting magnet system was able to provide fields of up to 14 T. In addition, the available temperature range was reaching down to 1.9 K due to the use of liquid He as cooling source. The samples were connected to the quartz holder by a grease or a silver paste to ensure good thermal contact. In order to reach to thermal equilibrium without stabilization time at each data point, the heating/cooling rate was set to 1 K min^{-1} .

For isothermal field-dependent magnetization ($M(H)$) measurements at both systems, a waiting time of 5 min has been established to equilibrate and stabilize the actual sample temperature. Subsequently, the magnetic field was swept with a rate of 5 mT s^{-1} and the data points were taken instantaneously during

the linear sweep.

Transition temperatures and fields were determined by two different methods. On the one hand, the first derivative of magnetization with respect to temperature was calculated. The maximum of this $\frac{dM}{dT}$ or $\frac{dM}{dH}$ is considered as the central value for the transition temperature T_t or field H_t . The transition temperatures must be differentiated between heating (T_t^h) and cooling (T_t^c) protocol, respectively. The same holds true for the magnetic field upon increasing and decreasing field. This method will be called ‘ derivative-method ‘. On the other hand, the start and finish temperatures of the martensitic phase transition were determined by fitting linear functions to the magnetization curves before, after and in the center of the transition region for both heating and cooling protocol. The intersections of these lines were considered as the transition temperatures for martensite (austenite) start M_s (A_s) and finish M_f (A_f), respectively. This method will be called ‘ tangent-method ‘.

Furthermore, the minimum magnetization of the austenite and maximum magnetization of the martensite (and vice versa for inverse materials) close to the transition was taken as the reference to convert the magnetization into percentages of the transition’s ΔM for austenite and martensite fractions. The starting point of the austenite formation and finish point of martensite formation was set to the temperature where the austenite fraction accounted for 5 %. Finishing point of austenite formation and starting point of martensite formation was set to an austenite fraction of 95 %.

For compounds with no significant magnetization change associated with the martensitic phase transition (decoupled magnetic and structural transition), the structural transition temperature was determined by a differential thermal analysis (DTA) of powder under Ar atmosphere with a heating rate of 10 K min⁻¹.

For magnetization measurements under hydrostatic pressure, a Cu-Be pressure cell has been used as an option of the VSM sample holder of the PPMS. A small piece of the material (approximately 1 mg) was dispersed in daphne oil as pressure transmitting medium and encapsulated in a teflon tube. The sample container was put inside a channel of the pressure cell. Hydrostatic pressure was adjusted via a screw system by mechanical movement that was transmitted onto the sample container by pistons. The obtained pressure value was determined by measuring the well-known superconducting transition of a high-purity Sn sample, which was additionally placed in the sample container. Temperature-dependent magnetization measurements were performed under a decreased heating/cooling rate of 0.5 K min⁻¹ to account for the large thermal mass of the pressure cell that was required to follow the temperature change of the system.

3.4.1 Isothermal entropy change

The determination of the isothermal entropy change Δ_{sT} was carried out by temperature-dependent (isofield protocol, $M(T)$) and field-dependent (isothermal protocol, $M(H)$) magnetization measurements. First derivatives of the resulting $M(T)$ -curves were determined for numerical integration according to Equation (2.7) [61].

The isothermal entropy change calculations from $M(T)$ curves of bulk samples were done by measuring the magnetization at varying fields from 0.1 to 2 T with a step size of 0.1 T or 0.2 T. For the calculations,

first derivatives of isofield magnetization curves with respect to the temperature were carried out at each temperature data point. The integration was done by the trapezoidal approximation with equidistant field steps:

$$\Delta_{sT} = \int_0^{H_{max}} \left(\frac{\partial M(T, H)}{\partial T} \right)_H dH \approx \sum_{n=1}^{H_{max}} \frac{(\frac{\partial M}{\partial T}(T, H_n)) + (\frac{\partial M}{\partial T}(T, H_{n-1}))}{2} \Delta H \quad (3.2)$$

The temperature range of the measurement was set according to Fig. 3.1 between the respective temperatures T_{under} and T_{over} to cover the full transition for heating and cooling protocol and to avoid the detection of minor loops of magnetization. The temperature step size has been adjusted according to the sharpness of the transition between 1 K and 2 K in order to account for a trade-off between detecting the peak of the transitional entropy change and reducing the overall measurement time. Magnetic-field steps have been chosen as 0.1 T or 0.2 T. A reference test using elemental Gd and La-Fe-Si sphere did not reveal a significant difference for the calculated Δ_{sT} when choosing 0.1 T- or 0.2 T-steps.

Alternatively, Δ_{sT} was calculated from isothermal $M(H)$ measurements at different temperatures. The curves were measured from zero up to the maximum field strength with a field sweeping rate of 5 mT s^{-1} . The temperature has been swept between the measurements with a rate of 2 K min^{-1} followed by a holding time of 5 min to assure a temperature equilibrium between sample and temperature sensor of the device. The measured temperature of the chamber was constant during the measurement with an accuracy better than $\pm 0.05 \text{ K}$. In order to ensure a defined starting state that is not depending on the history of first-order magnetocaloric samples, the loop process has been applied to avoid an overestimation of the Δ_{sT} value [171, 172]. Therefore, the sample has been brought back to the full martensite/austenite state after each $M(H)$ measurement followed by sweeping to the next measurement temperature. For a conventional magnetocaloric material, the sample needs to be heated up to T_{over} above the hysteresis region. Afterwards, it can be cooled down to the next measurement temperature (see Fig. 3.1(a)). Accordingly, an inverse material needs to be cooled down to T_{under} before heating to the next temperature of interest (Fig. 3.1(b)).

The calculation of Δ_{sT} from the measured $M(H)$ curves has been carried out by subtracting the curve of the next lower temperature followed by direct integration up to the desired maximum field value. This value was then divided by the temperature step between the two curves in order to account for the derivative with respect to the temperature.

$$\Delta_{sT}(T_m, H_{max}) = \frac{\sum_{n=1}^{H_{max}} \frac{(M(T_m, H_n)) + (M(T_m, H_{n-1}))}{2} \Delta H - \sum_{n=1}^{H_{max}} \frac{(M(T_{m-1}, H_n)) + (M(T_{m-1}, H_{n-1}))}{2} \Delta H}{T_m - T_{m-1}} \quad (3.3)$$

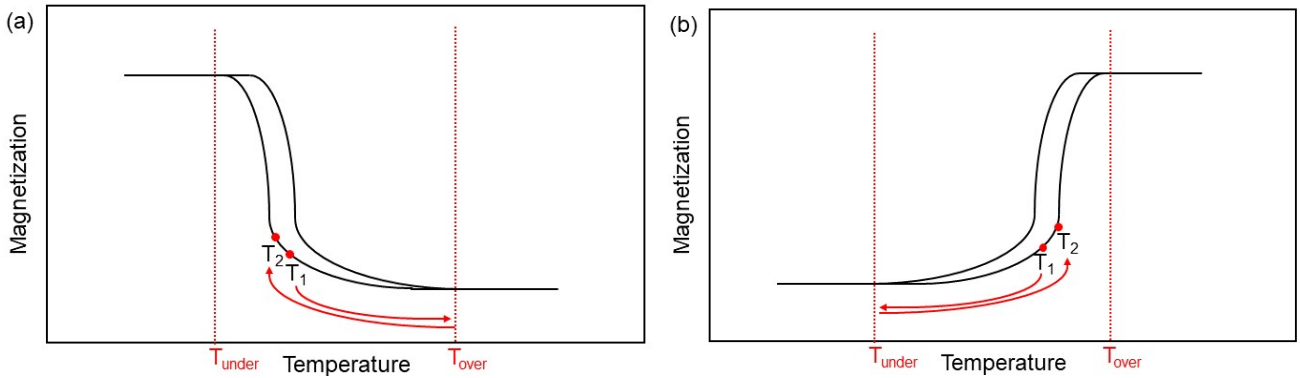


Figure 3.1: Schematic representation of the loop process for a phase reset protocol between isothermal $M(H)$ measurements for conventional (a) and inverse (b) magnetocaloric materials with a first-order phase transition for the correct determination of the isothermal entropy change. The same borders were used for the measurement of full transition loops by $M(T)$ measurements.

3.4.2 Adiabatic temperature change and strain in low fields

Adiabatic temperature changes were measured directly in a purpose-built device shown schematically in Fig. 3.2 and described in detail in [76]. The temperature change was measured by an attached thermocouple under sinusoidal field change by two Halbach cylinders that rotate in opposite directions creating a maximum field strength of 1.93 T. For each measurement, the Halbach magnets are driven by a full rotation being equal to two cycles of magnetic-field application and removal. During the first cycle, a maximum positive field of 1.93 T is reached and for the second cycle, the field is equally strong but with negative sign. Both cycles are equivalent in terms of the MCE since only the absolute value of the magnetic field plays a role here and not its direction. The maximum field-sweeping rate for the cycle can be adjusted from 0.1 T s^{-1} to 1.2 T s^{-1} . When not stated differently, 0.7 T s^{-1} has been chosen as a standard rate. The sinusoidal method of field application leads to largest rates for each cycle when passing through zero field. The magnetic field was measured by a Hall probe connected to a *LakeShore* gaussmeter. Heating and cooling rates were set to 2 K min^{-1} to ramp between the measurement temperatures and 0.1 K min^{-1} for approaching the measurement point in order to minimize background heating or cooling of the sample during the measurement.

In addition to ΔT_{ad} , the setup has also been able to process data from maximum two strain gauges in parallel. The gauges were glued to the sample surface and read out over a Wheatstone bridge [173] measuring the electrical resistance caused by a length change of the gauge (detailed description of the used strain gauges can be found in Section 3.4.3).

The samples were packed in *Pyrogel* isolation wool and the sample chamber was evacuated in order to establish near-adiabatic conditions and to avoid a direct contact of the sample with the sample holder. The thermocouple was placed between two halves of a sample ('sandwich-setup') or on top ('top-setup') and glued to it by small amounts of thermally conductive silver-based epoxy. An ice-water mixture with 0°C

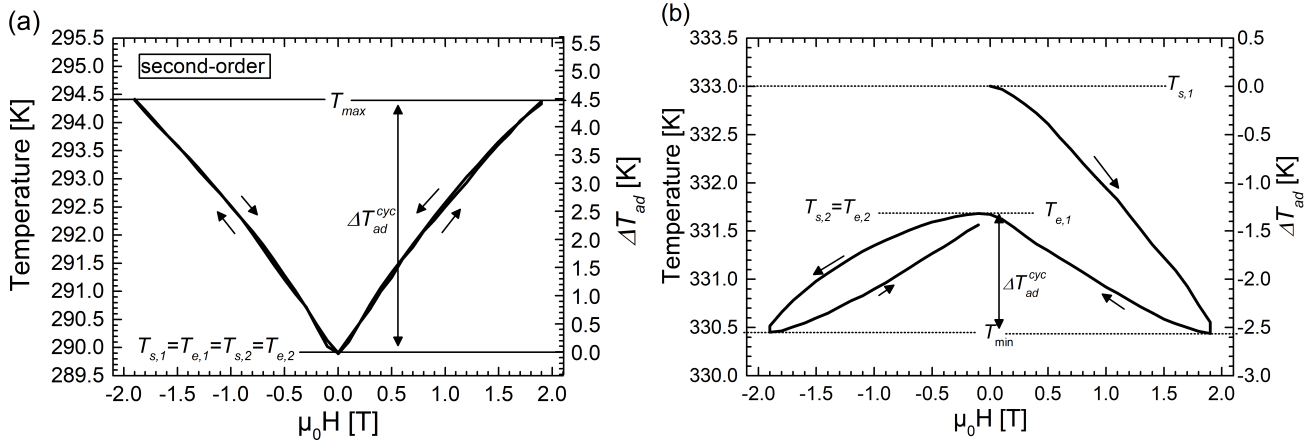


Figure 3.3: Measurement curve of ΔT_{ad} (right axis) shown together with the absolute temperature (left axis) for a second-order MCE that is completely reversible (a) and for a first-order inverse MCE with a reduced cyclic response (b). The right part corresponds to the first field application and removal for positive magnetic-field values, whereas the left part illustrates the ΔT_{ad} for the second field cycle with negative field values. Start (T_s) and end (T_e) temperatures of each cycle are labeled with the respective indexes 1 and 2 for first and second cycle.

Exemplary measurement curves for the adiabatic temperature change are shown in Fig. 3.3 for a second-order transition (a) as well as for an inverse first-order magnetocaloric material (b). For the case of a second-order transition, ΔT_{ad} is positive and fully reversible under cyclic conditions. All starting temperatures in zero field (T_s) coincide with the end temperatures T_e of each cycle after field removal. Thus, the absolute value for the adiabatic temperature change is equal for each half-cycle of field application and removal. For the inverse first-order material, ΔT_{ad} of the first field application is determined by taking the difference between $T_{min}(H_{max})$ and $T_{s,1}(H_0)$. After field removal the thermal hysteresis leads to a reduced temperature change of the back transition, which is determined by the difference between $T_{min}(H_{max})$ and the end temperature of the first cycle $T_{e,1}(H_0)$. This cyclic value will then also be measured upon further field cycles, which can be seen by the difference between $T_{min}(H_{max})$ and $T_{s,1}(H_0)$ (second field application) and between $T_{min}(H_{max})$ and $T_{e,2}(H_0)$ (second field removal). The respective measurement of a conventional first-order material is the same but mirrored at the field axis since the values of ΔT_{ad} are positive.

3.4.3 Fast pulsed magnetic field measurements

In order to study magnetization behavior and magnetocaloric effects in large fields, measurements have been conducted at the Dresden High Field Laboratory (HLD) of the Helmholtz-Zentrum Dresden-Rossendorf (HZDR). In addition, the pulsed fields can be used to study kinetic effects since the magnetic-field change rate is depending on the absolute field strength that is applied during the pulse.

Magnetization has been measured for the MM'X alloys in a bonded state with 5 wt. % of a two-component silver epoxy binder as well as on loose powder.

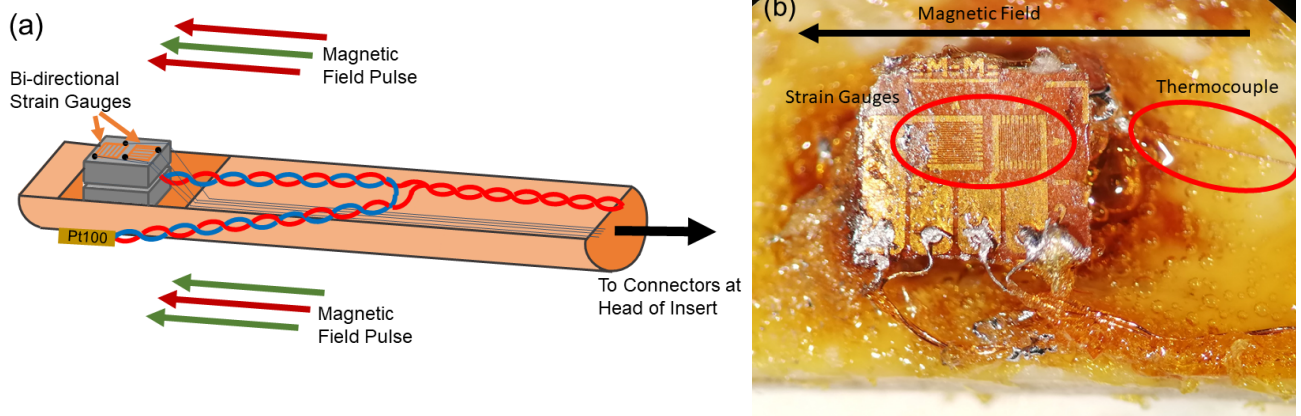


Figure 3.4: Schematic sample setup for the simultaneous measurements of bi-directional strain and adiabatic temperature change in pulsed magnetic fields (a) and an actual image of the prepared sample on the holder before inserting into the evacuated tube.

Furthermore, the setup of the HLD allows for a direct measurement of ΔT_{ad} in large magnetic-field changes and rates. Therefore, two parts of a sample are glued together with small amount of silver epoxy glue and are equipped with a type-T thermocouple in between ('sandwich setup'). The thermocouple consists of a drilled pair of wires of copper and constantan with a thickness of $25 \mu\text{m}$ each. This method assures a direct contact of the thermocouple to the sample on both sides and via the thermally conductive silver epoxy. The reference of the differential thermocouple is in contact with the back side of the sample holder, where the absolute temperature is measured by a PT100 thermometer. The holder is inserted into a vacuum tube, which is evacuated to ensure thermal isolation to the surrounding.

In addition, the strain of the sample can be measured simultaneously. This is performed by linear pattern strain gauges of $0.79 \text{ mm} \times 0.79 \text{ mm}$ length and grid width. In order to measure the strain in two directions, two strain gauges are glued on the sample surface in field direction and perpendicular to the external magnetic field. The arrangement of the measurement setup with thermocouple and strain gauges is shown schematically as well as by an actual image of the $\text{Ni}_{37}\text{Co}_{13}\text{Mn}_{34.5}\text{Ti}_{15.5}$ sample attached to the sample holder prior to the measurement in Fig. 3.4. A straining of the sample is measured by a length change of the strain gauge, which changes its resistance. The strain gauge contacts are connected to a 4-point measurement setup with digital lock-in. Therefore, a function generator created a periodic current and the corresponding voltage was measured by an oscilloscope. After passing through a lock-in filter, the resistance is determined from current and voltage data. For temperature-sweep measurements without an external field, the resistance of the strain gauges is directly measured by a multimeter.

The pulsed magnetic field was produced by a solenoid magnet, which applied the maximum field always at 13 ms after starting the pulse. A pick-up coil measured the strength of the magnetic field during the experiment. The corresponding time-dependent field profiles are shown for maximum fields of 2 T, 5 T, 10 T, 20 T, and 40 T in Fig. 3.5 (a). As a result, the magnetic-field application rate as the first derivative of

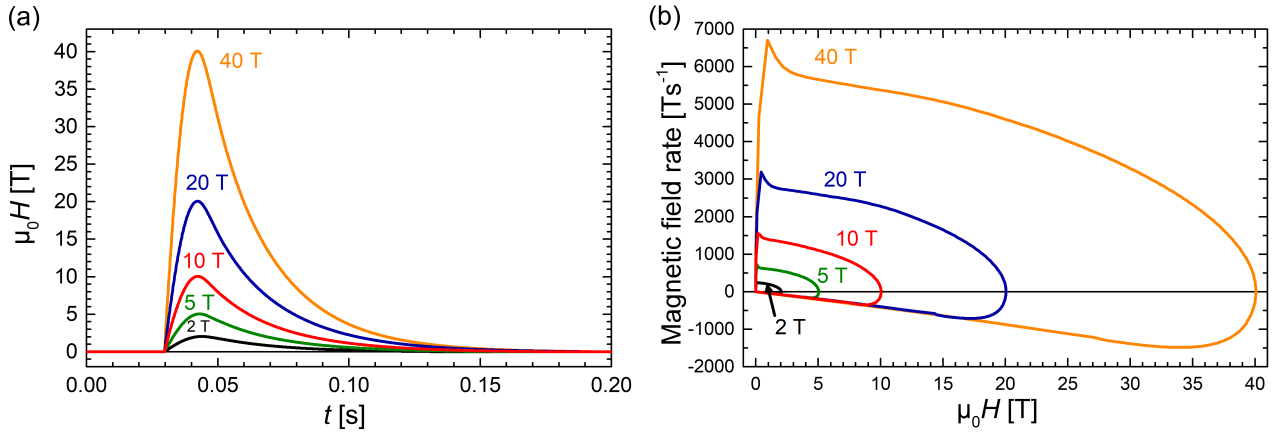


Figure 3.5: Time-dependent profiles of the magnetic-field pulses of 2 T to 40 T for the measurement setup of the HLD at HZDR (a) and the corresponding magnetic-field rates as a function of the magnetic field present during field application and removal (b).

Table 3.1: Maximum field application rates at the beginning of each pulses as a function of the maximum magnetic field reached by the corresponding pulse. The values have been determined from the first derivative of the magnetic-field evolution over time.

$\mu_0 H_{max}$ [T]	max. $\frac{\mu_0 dH}{dt}$ [$T s^{-1}$]
2	270
5	710
10	1550
20	3190
40	6710
50	7940

magnetic field over time is increasing with larger maximum fields as shown in Fig. 3.5 (b). The maximum rates that are applied at the start of the pulse are listed in Table 3.1. However, the rates decrease slightly compared to this maximum until the maximum field of the respective pulse is reached. Upon field removal, the field rate is mainly a function of the present field and coincides independent on the maximum applied field of the respective pulses.

3.5 Simultaneous measurement setup in quasi-stationary high fields

The simultaneous measurement of magnetization, strain, and electrical resistivity was carried out in an in-house developed measurement insert in the *Quantum Design* PPMS, schematically shown in Fig. 3.6. The magnetization was measured in analogy to regular magnetic measurements (see Section 3.4) by pick-up coils. The strain was measured by the strain gauge alignment in two directions as described for

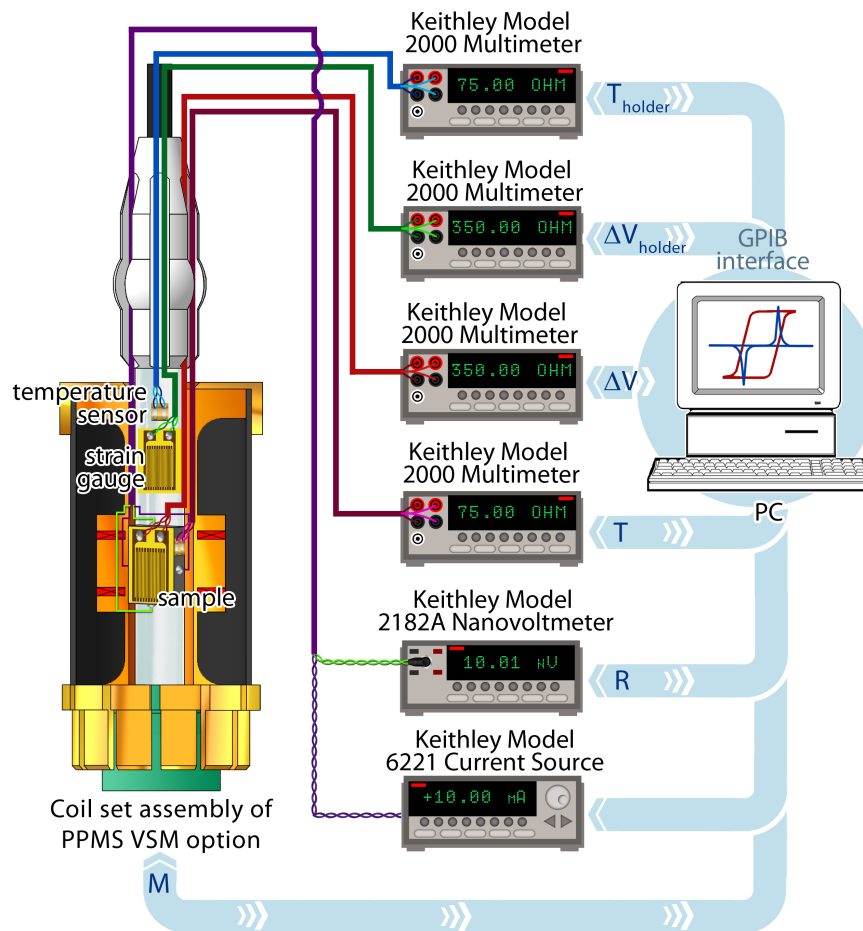


Figure 3.6: Schematic measurement setup for the simultaneous measurement of magnetization, strain, and electrical resistance as an insert for the PPMS. The magnetic field of up to 14 T is produced by a superconducting magnet. Courtesy of Alexey Karpenkov (TU Darmstadt).

the simultaneous measurements in pulsed fields in Section 3.4.3. In addition, an identical strain gauge setup has been attached to the quartz sample holder with known thermal expansion coefficient in order to subtract temperature effects of the holder and of the gauge itself. The resistance R was directly measured using a current source in combination with a voltmeter and converted to the specific resistance ρ by Equation (3.4) with the initial sample length l and cross-section A measured at room temperature. The temperature of the sample has been measured directly by a Cernox[®] thermometer in ‘top-setup’.

$$\rho = R \cdot \frac{A}{l} \quad (3.4)$$

3.6 Calorimetry

Heat capacity measurements were performed on the PPMS by *Quantum Design*. The measurement was carried out using the two-tau-model™ (trademark of *Quantum Design*), where a short heat pulse is applied to the sample. As a consequence, the sample heats up and the time that the sample needs to relax to its initial temperature is proportional to the heat capacity. The simple model assumes that the sample is in perfect thermal contact to the sample platform and the time-dependent temperature evolution can be described by Equation (3.5) [174]

$$C_{total} \frac{dT}{dt} = -K_w(T - T_b) + P(t) \quad (3.5)$$

with the total heat capacity of sample and stage C_{total} , thermal conductance of the wire system K_w , the temperature of the thermal bath T_b and $P(t)$ being the heater power, which is P_0 during heating and zero during cooling section. This results in an exponential solution for the expression of $T(t)$, which is characterized by the time constant τ being equal to $\frac{C_{total}}{K_w}$. However, for a non-ideal contact, the heat capacity of sample (index "s") and platform (index "p") need to be separated and the value for the sample is determined from the time-dependent behavior described by Equation (3.6)

$$C_{sample} \frac{dT_s}{dt} = -K_g(T_s(t) - T_p(t)) \quad (3.6)$$

with K_g being the thermal conductance between sample and platform by a connecting grease. By this method, c_p can be measured as a function of temperature and in external magnetic fields of up to 14 T.

The determination of an entropy-temperature diagram has been carried out from c_p data of the PPMS measurement. By this method, c_p has been determined from room temperature down to 10 K in different applied magnetic fields. For each field, the entropy curve was calculated according to Equation (2.3) by dividing c_p by T and integrating over the temperature:

$$S(T) - S_0 = \int_{T_0}^T \left(\frac{c_p}{T} \right)_H dT \quad (3.7)$$

The value for T_0 has been chosen as the lowest measured data point in zero magnetic field at 4 K. Further measurements that were not carried out down to this temperature were corrected by the absolute entropy offset at the respective T_0 of each measurement compared to the reference data in zero field. It must be considered here that the calculation of the total entropy can lead to slight deviations to the actual real value because the integration does not start at 0 K. However, T_0 is chosen low enough, so that no effects of the phase transition were contributing significantly to c_p any more. Moreover, the diagram was used in order to determine relative entropy changes and the absolute entropy value will not be part of the discussion.

Differential scanning calorimetry (DSC) measurements on In-, Al-, and Sn-Heusler alloys were carried out at *Fraunhofer IWKS Alzenau* on a *NETZSCH STA 449F3* calorimeter with a heating/cooling rate of 10 K min^{-1}

under protective Ar atmosphere. The sample signal is measured by the difference of heat flow from the sample and the respective heat flow of an empty reference Al₂O₃ crucible. Further DSC measurements on MM'X compounds and Ti-Heusler samples were executed on a *NETZSCH DSC 404 Pegasus F1* with a heating/cooling rate of 5 K min⁻¹ under protective Ar atmosphere.

From the measurement of the heat flow $\frac{dQ}{dt}$, the specific heat capacity can be first calculated with the inverse heating rate $\frac{dt}{dT}$ and the sample mass m by Equation (3.8).

$$c_p = \frac{dQ}{dt} \cdot \frac{dt}{dT} \cdot \frac{1}{m} \quad (3.8)$$

In analogy to Equation (3.7), the integration of c_p/T with boundaries at the start and finish of the transition and using a baseline correction gives the total entropy of the phase transition Δs_t according to Equation (3.9).

$$\Delta s_t = \int_{T_1}^{T_2} \left(\frac{c_p}{T} \right) - \left(\frac{c_p}{T} \right)_{baseline} dT \quad (3.9)$$

The integration boundaries T_1 and T_2 are chosen at the points where the signal of heat flow or c_p/T starts to deviate from the baseline as a consequence of the phase transition.

3.7 Mechanical characterization

Mechanical tests have been carried out on a *Universal Testing Machine 5967* by *Instron* in compression mode. Suction-cast rods of 3 mm diameter were cut to a length of 5 mm to 6 mm by a wire saw and processed by grinding in order to obtain two plane-parallel surfaces for the piston contact. Arc molten samples were cut to cuboids of 2.5 mm x 2.5 mm x 5 mm and processed accordingly. In order to account for slight misalignments of the contact surfaces, a pre-force of 50 N was applied prior to recording the data set. During the measurement, the force F applied to the sample was recorded by a load cell as well as the length change Δl of the sample by the traveling distance of the traverse. These two quantities were converted into the technical stress σ and the technical strain ε by using equations (3.10) and (3.11)

$$\sigma = \frac{F}{A} \quad (3.10)$$

$$\varepsilon = \frac{\Delta l}{l_0}, \quad (3.11)$$

where A is the rectangular or circular cross-section of the sample and l_0 the initial sample length. Since the measurement of Δl by the movement of the piston is just a rough estimation and does not consider elongations in the device itself (material as well as bearings), the evaluation of the absolute strain and Young's modulus E from these measurements must be regarded with care and does not necessarily reflect

the true elongation of the sample.

In order to measure stress-dependent strains at varying temperatures, the system was equipped with a temperature chamber, which enabled to set the temperature of the mechanical testing setup between 100 K to 500 K using liquid nitrogen in combination with a heater setup and a ventilation system to control the air temperature inside the closed chamber. The actual sample temperature was directly measured by an attached thermocouple. In order to achieve more accurate strain values that neglect the contribution of the setup, an extensometer was attached between the contact surfaces of the pistons with the sample. Temperature-dependent strain measurements were carried out by setting a constant force and sweeping the temperature of the system. The elongation/contraction of the sample has been followed by a piston movement in order to keep the force constant. The resulting length change of the extensometer was used as signal for the sample strain. Since the sensors of the extensometer were not positioned directly at the top and bottom of the sample, the actual sample strain has to be calculated by dividing the length change Δl with the relation of extensometer length (12.5 mm) and sample length l_0 :

$$\varepsilon = \frac{\Delta l}{l_0} \cdot \frac{12.5 \text{ mm}}{l_0} \quad (3.12)$$

4 Ni-Mn-based Heusler Compounds

One of the most promising material systems considered for magnetocaloric cooling are alloys of the Ni-Mn-X Heusler family. The largest effects can be reached for Ni-Mn-In with a certain amount of Co doping on the Ni lattice site. Since the thermal hysteresis is pretty large for the majority of these compounds, the reduced cyclic effects prevent a stronger consideration for using these alloys in MCE demonstrators for close-to-application conditions [175]. Besides the most-commonly used second-order transition of Gd, conventional first-order compounds of the La-Fe-Si system are usually favored for tests of the cyclic performance of magnetocaloric materials in integrated AMR systems establishing a thermal span/cooling power [63]. In addition, the critical element In that is necessary for the best performing Heusler alloys is hindering the consideration for extensive price-sensitive cooling applications.

This chapter will compare different systems of the Ni-Mn-X Heusler family and work out the differences why some perform better than the others in magnetic fields below 2 T. The basic properties of the phase transition, namely magnetization change, influence of e/a on T_t , transition width, thermal hysteresis, and magnetic-field sensitivity are discussed comprehensively. This analysis allows to cross-correlate the determined properties for the different related Heusler systems to work out similarities and differences. The samples that are used for producing this large data set are shown in Table 4.1.

In addition, the adiabatic temperature change of different Heusler compounds will be investigated in higher magnetic fields in order to compare their maximum possible MCE. The technique of using pulsed magnetic fields also allows for an assessment of kinetic aspects that play a role for the nucleation and growth processes of the martensitic first-order phase transition.

Parts of this chapter are published in

- **A. Taubel**, T. Gottschall, M. Fries, S. Riegg, C. Soon, K. P. Skokov, and O. Gutfleisch, *A Comparative Study on the Magnetocaloric Properties of Ni-Mn-X(-Co) Heusler Alloys*, *physica status solidi (b)* **255** (2), 1700331 (2018).

Table 4.1: Nominal sample compositions of the produced $\text{Ni}_{50-x}\text{Co}_x\text{Mn}_{50-y}(\text{In/Sn/Al})_y$ systems with actual stoichiometries determined from EDS (Ni(-Co)-Mn-Al) and ICP-OES (Ni(-Co)-Mn-In and Ni(-Co)-Mn-Sn) and the resulting e/a ratio. Samples of the Ni(-Co)-Mn-In system have been produced and measured by Tino Gottschall (TG) within the framework of his dissertation at TU Darmstadt [144], Ni(-Co)-Mn-Sn samples have been produced, partly measured and provided for further characterization by Tino Gottschall as well as by Christopher Soon (CS) as part of his Bachelor thesis at TU Darmstadt [176]. The remaining measurements have been carried out by myself (AT) within this thesis, while samples of Ni-Mn-Al for the heat treatment optimization have already been produced previously for my Master Thesis at TU Darmstadt [177]. The individual contributions are clarified for each sample and measurement addressed in this chapter.

nominal	stoichiometry	e/a	produced by	measured by		
				$M(T)$	ΔT_{ad}	Δs_T
x=0, y=14.5 (In)	$\text{Ni}_{50.2}\text{Mn}_{35.0}\text{In}_{14.5}$	7.91	TG	TG	TG	TG
x=0, y=15 (In)	$\text{Ni}_{49.6}\text{Mn}_{35.6}\text{In}_{14.8}$	7.91	TG	TG	TG	TG
x=0, y=15.5 (In)	$\text{Ni}_{49.8}\text{Mn}_{35.0}\text{In}_{15.2}$	7.89	TG	TG	TG	TG
x=5, y=12.5 (In)	$\text{Ni}_{45.0}\text{Co}_{5.0}\text{Mn}_{37.5}\text{In}_{12.5}$	7.95	TG	TG	TG	TG
x=5, y=13 (In)	$\text{Ni}_{45.2}\text{Co}_{5.1}\text{Mn}_{35.6}\text{In}_{13.1}$	7.86	TG	TG	TG	TG
x=5, y=13.5 (In)	$\text{Ni}_{45.7}\text{Co}_{4.2}\text{Mn}_{36.6}\text{In}_{13.5}$	7.92	TG	TG	TG	TG
x=0, y=14 (Sn)	$\text{Ni}_{51.5}\text{Mn}_{35.1}\text{Sn}_{13.7}$	8.16	TG	TG	AT	AT
x=0, y=15 (Sn)	$\text{Ni}_{50.7}\text{Mn}_{34.3}\text{Sn}_{15.0}$	8.07	TG	TG	AT	AT
x=0, y=15.5 (Sn)	$\text{Ni}_{49.8}\text{Mn}_{34.8}\text{Sn}_{15.4}$	8.03	CS	CS	CS	CS
x=0, y=16 (Sn)	$\text{Ni}_{50.5}\text{Mn}_{34.0}\text{Sn}_{15.5}$	8.05	TG	TG	AT	AT
x=5, y=11.5 (Sn)	$\text{Ni}_{45.7}\text{Co}_{4.9}\text{Mn}_{37.9}\text{Sn}_{11.5}$	8.12	TG	TG	AT	AT
x=5, y=12 (Sn)	$\text{Ni}_{47.2}\text{Co}_{5.1}\text{Mn}_{35.5}\text{Sn}_{12.2}$	8.15	TG	TG	AT	AT
x=5, y=12.5 (Sn)	$\text{Ni}_{46.2}\text{Co}_{5.0}\text{Mn}_{36.6}\text{Sn}_{12.2}$	8.12	TG	TG	AT	AT
x=0, y=19 (Al)	$\text{Ni}_{49.6}\text{Mn}_{31.2}\text{Al}_{19.2}$	7.72	AT	AT	AT	AT
x=0, y=19.5 (Al)	$\text{Ni}_{49.4}\text{Mn}_{31.3}\text{Al}_{19.4}$	7.71	AT	AT	AT	AT
x=0, y=20 (Al)	$\text{Ni}_{50.0}\text{Mn}_{30.0}\text{Al}_{20.0}$	7.70	AT	AT	AT	AT
x=5, y=18.5 (Al)	$\text{Ni}_{45.0}\text{Co}_{5.0}\text{Mn}_{31.5}\text{Al}_{18.5}$	7.71	AT	AT	AT	AT
x=5, y=19 (Al)	$\text{Ni}_{44.5}\text{Co}_{5.1}\text{Mn}_{31.5}\text{Al}_{18.9}$	7.68	AT	AT	AT	AT
x=5, y=19.5 (Al)	$\text{Ni}_{44.5}\text{Co}_{5.2}\text{Mn}_{31.0}\text{Al}_{19.3}$	7.67	AT	AT	AT	AT

4.1 Optimizing the heat treatment

The selection of proper annealing conditions is an important step of the sample production for the resulting quality of a magnetocaloric compound. Especially for Heusler alloys, the (local) transition temperature is highly sensitive towards the actual stoichiometry. Thus, a fully homogeneous sample composition is the key to reach highest possible magnetocaloric effects. The most prominent Heusler alloy systems for magnetocaloric considerations are investigated in this section with respect to their ideal annealing conditions. For different samples without Co and with 5 at. % of Co of the systems $\text{Ni}_{50-x}\text{Co}_x\text{Mn}_{50-y}\text{In}_y$, $\text{Ni}_{50-x}\text{Co}_x\text{Mn}_{50-y}\text{Sn}_y$ and $\text{Ni}_{50-x}\text{Co}_x\text{Mn}_{50-y}\text{Al}_y$, a heat treatment study was carried out at different temperatures but for the same annealing time of 24 h. The optimal conditions for the Ni(-Co)-Mn-In system are at 1173 K for 24 h. The comparison of the magnetization curve for this annealing condition (green) with the as-cast state (purple) in Fig. 4.1 (a) demonstrates the urgent need for a proper heat treatment. The temperature-dependent magnetization curve of the as-cast state depicts the magnetization increase of the austenite state as a result of the austenite Curie temperature T_C^A around 315 K. This second-order transition is broadened due to the external magnetic field of 1 T, which also aligns moments in the paramagnetic state. The drop of magnetization upon further temperature decrease indicates the martensitic transition. This phase transition is broad for the as-cast state and spans over a temperature interval of more than 50 K. The magnetization of the low temperature state still amounts to $50 \text{ A m}^2 \text{ kg}^{-1}$ illustrating an incomplete phase transition since the magnetization of the full martensite state is expected to be much lower (paramagnetic). In contrast, the magnetization curve for the annealed sample (green) shows a sharp magnetostructural phase transition below 240 K from high-magnetization austenite to low-magnetization martensite. The width of the transition amounts to 12 K. The magnetization change ΔM of this phase transition is not fully exploited because the magnetization of the formed martensite is still not close to zero as expected for a paramagnetic state. The reason is the Curie temperature of the martensite T_C^M being near the transition temperature. As a consequence, the formed martensite state already possesses aligned moments at T_t . The Curie temperatures can be identified much clearer by the measurement in a very low external magnetic field of 0.01 T shown in (b). A steep magnetization change is visible for T_C^A at 315 K. This transition temperature can be determined precisely from the sharp transition because the Curie temperature is only unambiguously defined in zero external magnetic field. In addition, T_C^M is visible here as a step in the magnetization curve at 210 K even though it is not as sharp as for T_C^A .

For the two systems of Ni(-Co)-Mn-Al and Ni(-Co)-Mn-Sn, a systematic study has been carried out to find the optimal annealing conditions. It can be seen for the Al system with Co in Fig. 4.2 (b) that the homogeneity of the transition is increased with higher annealing temperature. At the ideal conditions of Ni(-Co)-Mn-In (1173 K), no martensitic transition is obtained. The ideal heat treatment temperature is found to be at 1323 K, which leads to the most narrow transition width with the highest magnetization change. An even higher annealing temperature leads to a slightly worse ΔM . In addition, the evolution of the austenite Curie temperature results in an increase of T_C^A for higher annealing temperature with the maximum value at 1323 K followed by a drop. This indicates the highest atomic disorder for the

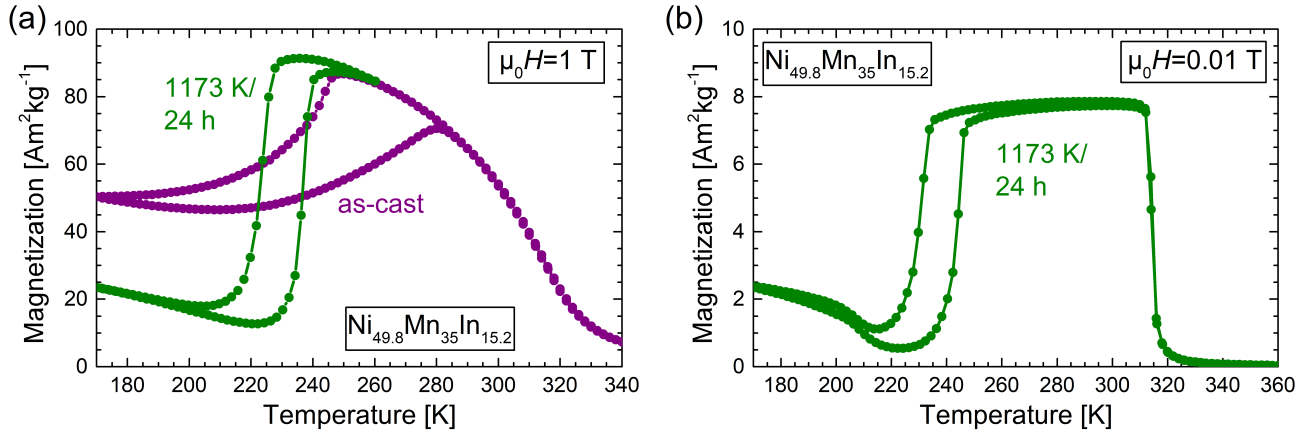


Figure 4.1: Temperature-dependent magnetization curves in a magnetic field of 1 T for $\text{Ni}_{49.8}\text{Mn}_{35.0}\text{In}_{15.2}$ in as-cast state (purple) and for a heat treatment (green) at 1173 K for 24 h (a). The corresponding $M(T)$ curve for an external field of 0.01 T is shown in (b). The sample has been produced by Tino Gottschall within the scope of his dissertation (TU Darmstadt).

found annealing temperature of 1323 K. All investigated heat treatments were performed far above the $L_{21}/B2$ disordering temperature, which is around 773 K for Ni-Mn-Al [178, 179]. The system is therefore expected to be in B2 state after quenching from the annealing temperature. The best phase transition for Ni-Mn-Sn shown in Fig. 4.2 (c) is resulting from a heat treatment at 1223 K for 24 h. In agreement with the observations for Ni-Co-Mn-Al, T_C^A increases for increasing annealing temperature. In contrast, the drop of T_C^A at a temperature higher than the optimal one is not observed here.

Different ideal annealing temperatures are figured out for the three investigated Heusler systems. Since the atomic order/disorder plays an important role for the martensitic transition [180], a correlation with the annealing temperature is expected. Since all found temperatures for the heat treatment are to different extents above the $L_{21}/B2$ ordering temperature (Al needs a higher annealing temperature than In whereas the ordering temperature is lower [179, 181]), an additional parameter must contribute. Figures 4.1 and 4.2 provide evidence that the ideal annealing temperature for achieving a sharp phase transition is mainly a consequence of the proper homogenization of the stoichiometry. Therefore, the activation of diffusion processes for the atoms during the heat treatment is the major parameter of interest. Since the melting point of a compound gives an estimate for the required activation energy of self-diffusion [182], the solid/liquid transition is investigated by a DSC measurement. The exothermic peaks for the heat flow measured upon cooling in Fig. 4.2 (d) represent the solidification temperatures of the respective Heusler system for one Co-free sample and one sample with Co. The peak signal for the Ni(-Co)-Mn-Al samples is lower and broader than for the other two systems but clearly at higher temperatures. Lowest solidification points of around 1240 K are found for the In-system. The Sn-system exhibits a split signal due to a two-step solidification process, which is consistent with previous reports for this system [183]. Also the melting/solidification temperature of around 1300 K is conform with literature values [183, 184]. The

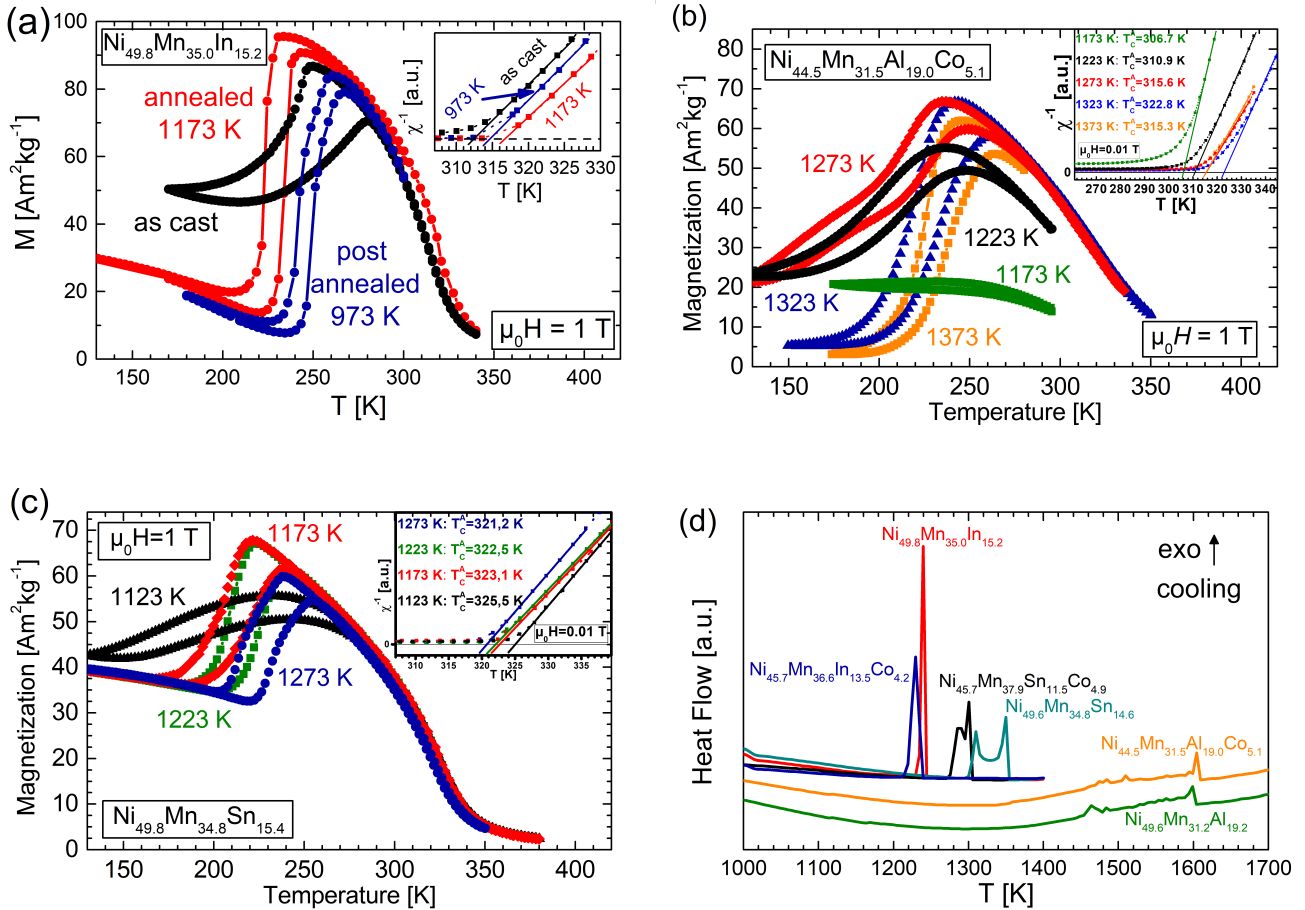


Figure 4.2: Influence of annealing temperature on the $M(T)$ -curves for $\text{Ni}_{49.8}\text{Mn}_{35.0}\text{In}_{15.2}$ (a), $\text{Ni}_{44.5}\text{Mn}_{31.5}\text{Al}_{19.0}\text{Co}_{5.1}$ (b), and $\text{Ni}_{50.7}\text{Mn}_{34.3}\text{Sn}_{14.5}$ (c) in a magnetic field of 1 T. Inverse susceptibility as a function of temperature for the three samples is depicted in the respective insets. DSC measurements upon cooling for the three Ni-(Co)-Mn-X systems show the solidification temperatures (d). The Ni-Mn-In sample of (a) has been produced and measured by Tino Gottschall (TU Darmstadt) within the scope of his dissertation [144], the Ni-Mn-Sn sample of (c) has been produced and measured by Christopher Soon (TU Darmstadt) within the framework of his Bachelor Thesis [176].

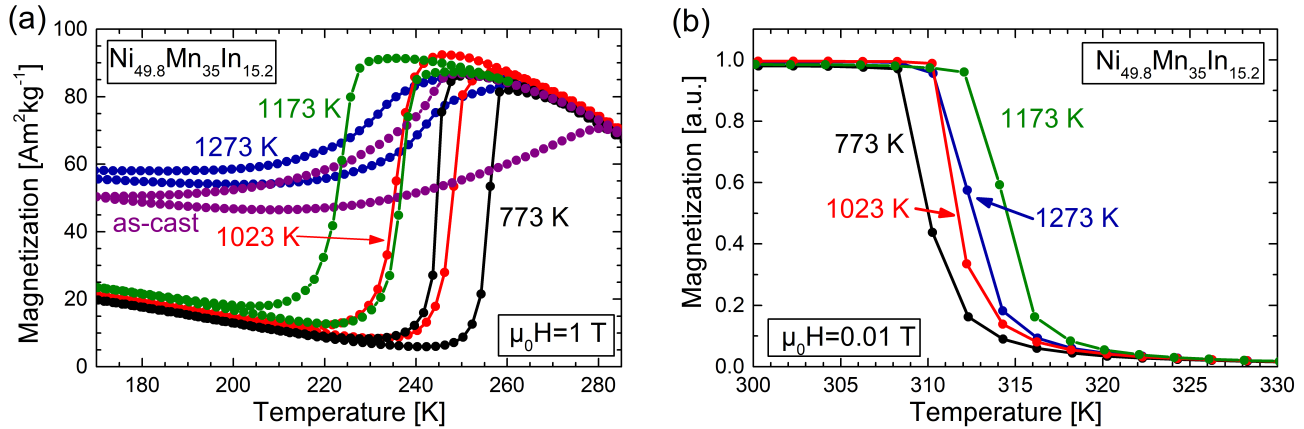


Figure 4.3: Temperature-dependent magnetization curves for different annealing conditions of a post-treatment at 773 K (black), 1023 K (red) and 1273 K (blue) compared to the initial annealing at 1173 K (green) and the as-cast state (purple) for $\text{Ni}_{49.8}\text{Mn}_{35.0}\text{In}_{15.2}$ (a). The respective magnetization around the Curie temperature is shown in (b).

solidification temperature for the samples with Co is slightly lower than the corresponding Co-free sample for all three systems, except for the Al-alloys where both temperatures are nearly equal. In summary, the trend for the optimum annealing temperature correlates with the trend for the solidification/melting temperatures. For Ni-Mn-In and Ni-Mn-Sn, the ideal annealing temperature is found to be around 50 K to 70 K below the melting point.

In an additional step, the influence of a post-annealing step on the martensitic transition is examined for the Ni-Mn-In system. Therefore, one sample piece of $\text{Ni}_{49.8}\text{Mn}_{35}\text{In}_{15.2}$ that has been annealed optimally at 1173 K for 24 h has been cut into four pieces (the sample has been produced initially by Tino Gottschall within the framework of his dissertation, TU Darmstadt). One piece was taken as reference and the others were taken for an additional annealing step at 773 K, 1023 K and 1273 K, respectively. The resulting temperature-dependent magnetization curves for the post-annealing steps compared to the as-cast sample and the initial heat treatment in Fig. 4.3 (a) show significant differences. Compared to the broad phase transition of the inhomogeneous as-cast sample (purple), the annealing at 1173 K (green) as well as the post-annealings at 773 K (black) and 1023 K (red) show a sharp magnetostructural phase transition. The annealing at the highest temperature of 1273 K leads to a broad phase transition because it is already too close to the melting point, which is in agreement with the results from the DSC analysis in Fig. 4.2 (d). The post-annealing steps at 1023 K and 773 K lead to an increase of T_i in combination with a reduced transition width. This effect is most pronounced at the lowest tested heat treatment temperature of 773 K. A possible explanation can be that the sharper phase transition is a result of the higher transition temperature.

The influence of the different post-annealing procedures is also reflected in the Curie temperatures determined from magnetization measurements in 0.01 T in Fig. 4.3 (b). Highest T_C^A is observed for the initial annealing at 1173 K. The additional post-treatments that enhance the sharpness of the transition also

lead to a decrease of T_C^A . This is in agreement with the trend for the heat treatment study of Ni-Co-Mn-Al and Ni-Mn-In in Fig. 4.2 (a) and (b). Since the post-treatment should not influence the homogenization of the sample, it can be assumed that the decrease of T_C^A and consequently the order state of the sample also favors a sharper phase transition. It must be noted that also the highest annealing temperature of 1273 K decreases T_C^A . The influence on the magnetostructural transition is however overlaid by the worsening of the homogenization due to the proximity to the melting point.

4.2 Tuning the properties of the martensitic phase transition

In order to compare the three Heusler systems of Ni(-Co)-Mn-In, Ni(-Co)-Mn-Sn and Ni(-Co)-Mn-Al, the respective magnetization curves are shown for different stoichiometries in a magnetic field of 1 T in Fig. 4.4 (a)-(c). All systems show the collective behavior of the tunable transition temperature by changing the stoichiometry. By variations in the Mn-X ratio in $\text{Ni}_{50}\text{Mn}_{50-x}\text{X}_x$ (circles), the transition can be adjusted precisely over a wide temperature range. An increased In-, Sn- and Al-content decreases the transition temperature, which is related to a reduction of the valence electron concentration per atom e/a [185]. These sensitive changes also explain why small chemical inhomogeneities of a non-ideal heat treatment have a significant impact on the transformation properties. The evolution of the magnetization of the austenite and martensite state for each sample suggests that the magnetization change during the martensitic transition is guided by the magnetization curves of pure martensite and austenite [67].

A substitution of 5 at. % of Ni by Co leads to a similar behavior for varying Mn-X ratios (squares). As an example, an increase of 1 at. % of In in the $\text{Ni}_{45}\text{Co}_5\text{Mn}_{50-x}\text{In}_x$ series shifts the transition by about -120 K. The addition of Co decreases T_t , which leads to a reduced In content to achieve a transition near room temperature. Furthermore, the Co substitution also decreases T_C^M reducing the magnetization of the martensite for low temperatures. The latter feature is especially apparent for the magnetization curves of the Ni(-Co)-Mn-Sn Heusler system in Fig. 4.4 (b). The Co-free system is characterized by a higher Curie temperature of the martensite phase T_C^M . As a result, the martensitic state possesses a significant magnetization in the regarded temperature range. Therefore, the magnetization change between martensite and austenite is only modest over the whole temperature range for the Co-free system. The transformation in Ni-Mn-Sn is much sharper than for the Ni-Mn-In system but also the thermal hysteresis is slightly broader. The partial substitution of Ni by Co again increases the Curie temperature of the austenite T_C^A , but decreases T_C^M as well as T_t [186]. As a side effect, the thermal hysteresis can be decreased below 10 K. These effects of the Co-substitution are illustrated by the direct comparison of $\text{Ni}_{50}\text{Mn}_{35}\text{Sn}_{15}$ (blue) and $\text{Ni}_{45}\text{Co}_5\text{Mn}_{37.5}\text{Sn}_{12.5}$ (yellow), where the Co containing sample has a larger M of the austenite, a smaller M of the martensite, a more narrow hysteresis, and less Sn-content at the same transition temperature. The amount of Co can in principle be increased up to 10 % but the possibility of Co precipitations has to be considered carefully for this substitution range. By further decreasing the Sn content, the magnetostructural transition can be shifted towards temperatures above 400 K and still a significant magnetization change is obtainable [187]. This could make Ni-Co-Mn-Sn an interesting material

for the application of thermomagnetic power generation from waste heat [188–191].

Significant differences compared to the previously introduced systems are obvious for Ni(-Co)-Mn-Al in Fig. 4.4 (c). The $M(T)$ -curves in a magnetic field of 1 T reveal sharp transitions with rather low hysteresis in the order of 10 K around room temperature for the Co-free samples. However, the transition exhibits a very low magnetization change of around $2 \text{ A m}^2 \text{ kg}^{-1}$. This is attributed to the phase transition close to the Curie temperature of the austenite, which is close to room temperature [179]. Therefore, the austenite phase can be in the paramagnetic state around room temperature until the transition takes place [141]. The magnetization of the martensite state increases below T_t reaching similar values compared to the austenite magnetization just above T_t . By adding Co, the magnetization of the ferromagnetic state is enhanced significantly. The magnetization of the paramagnetic state is constantly low even at temperatures around 150 K. This is attributed to a change of the magnetic properties of the martensite from antiferromagnetic to paramagnetic by the addition of Co [141]. This transition of the low-temperature phase with changing composition is also under discussion in literature for Ni-Mn-Sn and Ni-Mn-In Heusler alloys, shown for example by means of ferromagnetic resonance studies [192]. Recently, an antiferromagnetic order on the Ni and Mn site has been reported for the martensitic state of a Ni-Co-Mn-Ga alloy by neutron diffraction experiments [193]. Therefore, a distinct proposition of the present state cannot be made here unambiguously and both paramagnetic or antiferromagnetic contributions are possible. Anyway, the result of the Co substitution is a strongly enhanced ΔM for the phase transition, similar to the ones of the Ni-Co-Mn-Sn system. On the other hand, the transition width and hysteresis increases compared to the Co-free system [194]. Due to the proximity of the transition in Ni-Mn-Al to T_C^A and the low ΔM , the T_{width} is naturally decreased proportionally when the slope of $\frac{dM}{dT}$ stays constant. The $\text{Ni}_{45}\text{Co}_5\text{Mn}_{31}\text{Al}_{19}$ sample shows a T_{width} of 45 K and a hysteresis of 15 K. For all the three investigated systems, the width and hysteresis decrease when the transition temperature gets closer towards T_C^A . Such trends are evaluated in more detail by plotting data points for all investigated samples over the respective transition temperature.

The transition temperatures represented by A_s are summarized for a set of samples as a function of the e/a ratio for all three Heusler systems (Fig. 4.4 (d)). The transition is shifted linearly towards lower temperatures by decreasing e/a , which is equivalent to a larger In/Sn/Al-to-Mn ratio as well as to a larger amount of Co substitution for Ni. However, the slope is varying for each system and matching the proposed evolution by the dotted lines, which run towards the common point for the Co-free systems of $\text{Ni}_{50}\text{Mn}_{50}$. The slope of the Ni-Co-Mn-Al system is much larger, which is an indication for a higher sensitivity of T_t (A_s in this particular case) towards variations of the alloy composition. This effect can be the reason for the broader transition of this system in Fig. 4.4 (c). The larger slope for the Sn system seems to contradict this as sharp transitions are observed in Fig. 4.4 (b). However, Sn contributes to e/a with one more valence electron than Al and In and shows a varied correlation between e/a and stoichiometry. Moreover, the general guidance by e/a can only be applied within one Heusler system. The exchange of Al and In shifts the martensitic transition drastically in spite of an equal valence electron count [185]. On the one hand, the changed electronic properties influencing the density of states is assumed to play a role here. On the other hand, the exchange of elements at the D-sites (Al and In) are located in different rows of the periodic

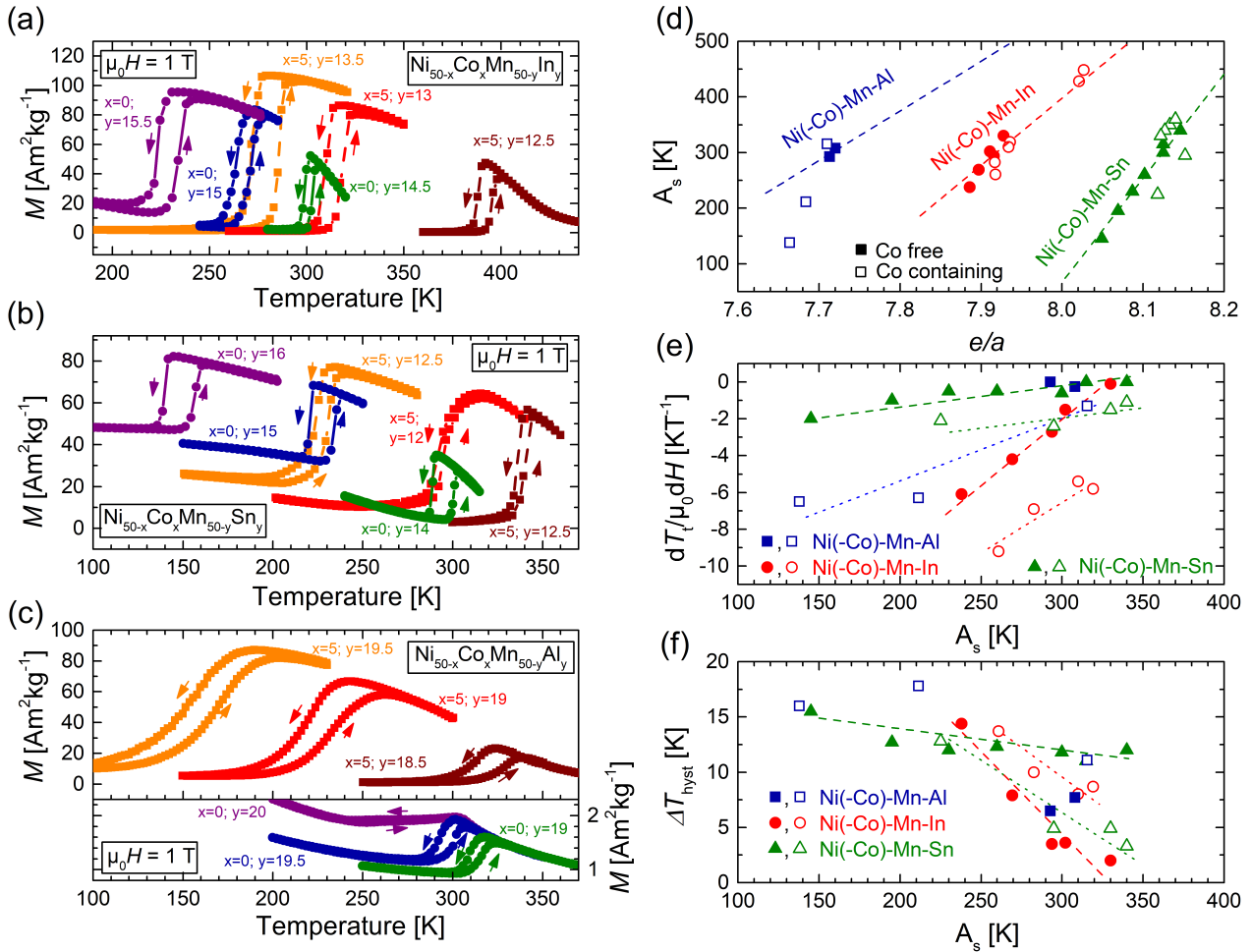


Figure 4.4: Temperature-dependent magnetization curves for Ni(-Co)-Mn-In (a), Ni(-Co)-Mn-Sn (b) and Ni(-Co)-Mn-Al (c) for samples without Co (circles) and with 5 at. % of Co substituted for Ni (squares), measured in an external magnetic field of 1 T. Additionally shown are the correlations between the phase transition temperature in terms of A_s and the valence electron count e/a (d), between the magnetic field dependence of the phase transition and the corresponding transition temperature of the compound (e) as well as between width of the thermal hysteresis and the transition temperature (f) for the three Heusler systems Ni(-Co)-Mn-Al (blue squares), Ni(-Co)-Mn-Sn (green triangles), and Ni(-Co)-Mn-In (red circles). Data points of the Co-free samples are shown as solid symbols, open symbols represent the systems with 5 at. % of Co substitution for Ni. Dotted lines in (d) are linear fits for the Co-free data points including the transition temperature for the common Ni₅₀Mn₅₀ compound, whereas the ones in (e) and (f) are drawn as a guide to the eye. Ni(-Co)-Mn-In and Ni(-Co)-Mn-Sn samples have been produced and measured ($M(T)$) by Tino Gottschall within the scope of his dissertation (TU Darmstadt) [144].

table and have different atomic radii, which changes the lattice constants and contributes to the stability of the involved phases.

The most important quantity from a practical point of view is the dependence of the transition temperature on an external magnetic field. The quantity of $\frac{dT_t}{\mu_0 dH}$ describes to what extent a phase transition can be induced by an external magnetic-field change. This correlates directly with the possible field-induced MCE. In general, $\frac{dT_t}{\mu_0 dH}$ increases with decreasing absolute temperature of the transition, which is observed for all investigated Heusler alloys in Fig. 4.4 (e). However, the slope as well as the maximum possible values around room temperature vary significantly. The highest values at room temperature (-6 K T^{-1}) can be achieved for Ni-Co-Mn-In samples, which can still be enhanced for lower transition temperatures reaching values of -9 K T^{-1} at 260 K. Since the magnetization change is negligibly small for Ni-Mn-Al (blue symbols), also the phase stabilization by an external field is not significant and $\frac{dT_t}{\mu_0 dH}$ is nearly zero. Enhancing ΔM by the addition of Co also enables larger values of $\frac{dT_t}{\mu_0 dH}$ up to -7 K T^{-1} at 140 K, which is not as efficient as for Ni-Co-Mn-In. Lowest absolute values of $\frac{dT_t}{\mu_0 dH}$ as well as lowest dependencies on T_t are obtained for Ni(-Co)-Mn-Sn. The comparison with Fig. 4.4 (b) yields the direct correlation between $\frac{dT_t}{\mu_0 dH}$ and the magnetization change of the transition. Since T_C^A and T_C^M are close together, the absolute ΔM of the transition is not changing drastically with temperature and the same holds true for the magnetic-field sensitivity. This finding is based on the shift of T_t with changing magnetic field being a result of the stabilization of a magnetic phase by the Zeeman term in the free energy, which is proportional to the magnetization.

The general trend of the thermal hysteresis in Fig. 4.4 (f) yields an increasing hysteresis for decreasing transition temperature. From two different points of view, this result is in agreement with the observations from Fig. 4.4 (e): Since the shift of the transition is stronger at lower temperatures, the absolute temperature difference between martensite and austenite formation branch leads to a variation of the shift with changing temperature. The increasing hysteresis with decreasing temperature can therefore be correlated to the evolution of $\frac{dT_t}{\mu_0 dH}$ by assuming that it is not relevant whether the transition temperature is shifted by a magnetic field or compositional changes [195]. Second, the increasing hysteresis is consequently also connected to the magnetization change of the transition. The strong trend for ΔT_{hyst} with T_t is pronounced much weaker for Ni-Mn-Sn, where also ΔM as well as $\frac{dT_t}{\mu_0 dH}$ do not show large changes as a function of A_s . Thus, the thermal hysteresis is not only depending on the temperature of the phase transition itself, also the magnetic properties of the phase transition seem to play a role for tuning the thermal hysteresis.

Interestingly, the introduction of Co for Ni reduces the quite large thermal hysteresis for Ni(-Co)-Mn-Sn, but increases it for Ni(-Co)-Mn-Al and Ni(-Co)-Mn-In. A reason can be a diverse effect of the introduction of the Co atoms on the lattice constants of austenite and martensite influencing the conformity of both phases, which can result in an increased or decreased nucleation barrier.

4.3 Magnetocaloric performance in low magnetic fields

The most important figures of merit to categorize the performance of a magnetocaloric material are Δs_T and ΔT_{ad} . A determination of Δs_T for the samples of the commonly considered most promising Ni(-Co)-Mn-In system are around $20 \text{ J kg}^{-1} \text{ K}^{-1}$ for transitions at room temperature ($\text{Ni}_{45}\text{Co}_5\text{Mn}_{37}\text{In}_{13}$). As a consequence of the large magnetic-field sensitivity, the magnetic-field-induced entropy change is already saturated for field changes of 2 T. Lowering T_t results in a decrease of the maximum achievable Δs_T because of the increasing contribution of the magnetic entropy change, which is counteracting the constant entropy change of the structural transformation [66]. It is important to emphasize that this effect of increasing ΔM with decreasing temperature is on the other hand necessary in order to drive the magnetic-field-induced transition. This controversy is denoted in literature as the dilemma of inverse magnetocaloric materials [67]. As a result, the achievable Δs_T for magnetic-field changes of 2 T is reduced by half for a transition temperature of 230 K compared to room temperature.

The entropy changes for Ni(-Co)-Mn-Sn are also in the range of 10 to $20 \text{ J kg}^{-1} \text{ K}^{-1}$, the highest value for the present sample series is determined as $24 \text{ J kg}^{-1} \text{ K}^{-1}$ for a transition temperature of 330 K ($\text{Ni}_{45}\text{Co}_5\text{Mn}_{38.5}\text{Sn}_{11.5}$), which is therefore comparable to best values of Ni(-Co)-Mn-In. These values for the Sn-system are not saturated for field changes of 2 T because $\frac{dT_t}{\mu_0 dH}$ is low compared to the In-system. Therefore, even higher values can be expected for larger magnetic-field changes that are able to saturate the field-induced MCE. As a consequence of the broad transition observed for the Ni-Co-Mn-Al samples combined with a medium $\frac{dT_t}{\mu_0 dH}$, the entropy changes for this Heusler system are only moderate in the range of $3 \text{ J kg}^{-1} \text{ K}^{-1}$.

The next step is to compare the systems by means of the adiabatic temperature change for the first field application as well as the cyclic ΔT_{ad} upon further field changes, which are both shown in Fig. 4.5 (a) and (b) for a magnetic-field change of 1.93 T. For the cyclic effect ΔT_{ad}^{cyc} , the difference of ΔT_{ad} for the maximum field of the second field-application cycle and for the corresponding completed field removal is considered. The absolute temperature is corrected for the new starting temperature of the second field cycle by subtracting the irreversible part of ΔT_{ad} after the first field cycle: $T_{new} = T_s + \Delta T_{ad,1}$.

For Ni(-Co)-Mn-Al, ΔT_{ad} has only been measured for the Co containing samples because the low values of Δs_T and the $\frac{dT_t}{\mu_0 dH}$ close to zero suggest vanishing and noisy ΔT_{ad} signals for the Co-free system. The $\text{Ni}_{45}\text{Co}_5\text{Mn}_{31}\text{Al}_{19}$ sample experiences an adiabatic temperature change of -1.0 K for the first field cycle of discontinuous protocol, which is a notable value for a FOMT compared to the low Δs_T of $3 \text{ J kg}^{-1} \text{ K}^{-1}$. However, such a small magnetocaloric effect is not promising for actual magnetocaloric cooling applications.

Ni-Mn-Sn samples reach maximum ΔT_{ad} values of around -1.5 K . This represents no substantial enhancement compared to the Ni-Co-Mn-Al sample considering that Δs_T is approximately five times larger. Furthermore, the MCE is not reversible at all for the applied field changes of 1.93 T. Both observations indicate that the low field dependence together with the considerable thermal hysteresis inhibit a cyclic magnetocaloric effect in magnetic fields below 2 T. The typical ΔT_{ad} behavior for a Co-free sample in Fig. 4.5 (c) explains why a negative ΔT_{ad} is measured for the first field application cycle but a positive

value for the second one for Ni₅₀Mn₃₆Sn₁₄ (blue curves). At a starting temperature of 310 K, a purely second-order effect is observed due to the proximity to T_C^A . The MCE is 100 % reproducible upon field removal as well as for the second field cycle. At 299 K, a negative ΔT_{ad} is obtained for the first field application due to the induced FOMT. However, the thermal hysteresis cannot be overcome by the field removal and a conventional MCE of the irreversibly induced austenite is seen for further field cycles. The very small hysteresis for the second cycle indicates a partial first-order contribution, which is overlaid by the dominating effect of the SOMT upon field cycling.

Largest value of -2.6 K for this system is obtained for the Ni₄₅Co₅Mn_{38.5}Sn_{11.5} sample, of which -1.2 K is obtained under cyclic conditions. The cyclic contribution of the FOMT is illustrated by the field-dependent ΔT_{ad} in comparison to the non-cyclic behavior of the Co-free sample in Fig. 4.5 (c). This directly measured temperature change outperforms previously measured values [196, 197]. The matching curves for continuous and discontinuous measurements (filled and open symbols) shows that the full effect is being exploited by the measurement protocol for this field change. Consequently, the large values of Δs_T that are comparable to the ones for Ni-Co-Mn-In system cannot be reflected in a usable ΔT_{ad} . The influence of the heat capacity, which links Δs_T to ΔT_{ad} , is similar for the investigated Heusler compounds and should not cause this large difference [198, 199]. The crucial point is the reduced field dependence of the transition temperature for Ni-Co-Mn-Sn, which hinders a completely induced phase transition in magnetic-field changes of below 2 T, despite the sharp increase of $\frac{dM}{dT}$. According to studies of the thermal hysteresis behavior, Ni(-Co)-Mn-Sn samples need an estimated magnetic field of 9 to 12 T to overcome the hysteresis and to experience a reversible phase transition [197, 200, 201].

The best performance in terms of ΔT_{ad} in magnetic-field changes of 1.93 T is achieved for the Ni-Co-Mn-In system. Maximum temperature changes are obtained between -2.7 K and -7.9 K, the latter one representing one of the highest values measured for this field change, as already reported for this exact sample in [125]. Furthermore, the In-system also exhibits the highest temperature changes upon cycling (-3 K), which is again a result of the strong $\frac{dT_i}{\mu_0 dH}$. For samples with low transition temperatures, the MCE is already saturated in magnetic-field changes of 1.93 T, which is indicated by the plateau of ΔT_{ad} for Ni₄₅Mn₃₅In₁₅ in Fig. 4.5 (a). However, the large value of Ni₄₅Co₅Mn_{36.5}In_{13.5} is not saturated yet and even larger values for ΔT_{ad} are expected for larger field changes. Despite the good reversibility compared to the other Heusler systems, the largest achievable absolute value of -3 K as well as the relative cyclability of the MCE of 37 % are not competing with material systems of La-Fe-Si and Fe₂P-type alloys exhibiting a conventional effect with narrow thermal hysteresis and very little reduction of ΔT_{ad} upon cycling [38]. The cyclic ΔT_{ad} compared to the first field application amounts to approximately 80 % for La-Fe-Si [202] and 75 % for Mn-Fe-P-Si [110].

In addition, the magnetocaloric properties Δs_T and ΔT_{ad} are determined for the different post-annealing treatments carried out for the Ni₅₀Mn₃₅In₁₅ sample in Section 4.1. The results for Δs_T shown in Fig. 4.6 (a) confirm the already discussed sharpening of the phase transition with decreasing post-annealing temperature. By an enhanced $\frac{dM}{dT}$ with maintained absolute magnetization change, the entropy change of the transition induced by a magnetic-field change of 2 T is increased by 45 % from 9.9 J kg⁻¹ K⁻¹ to

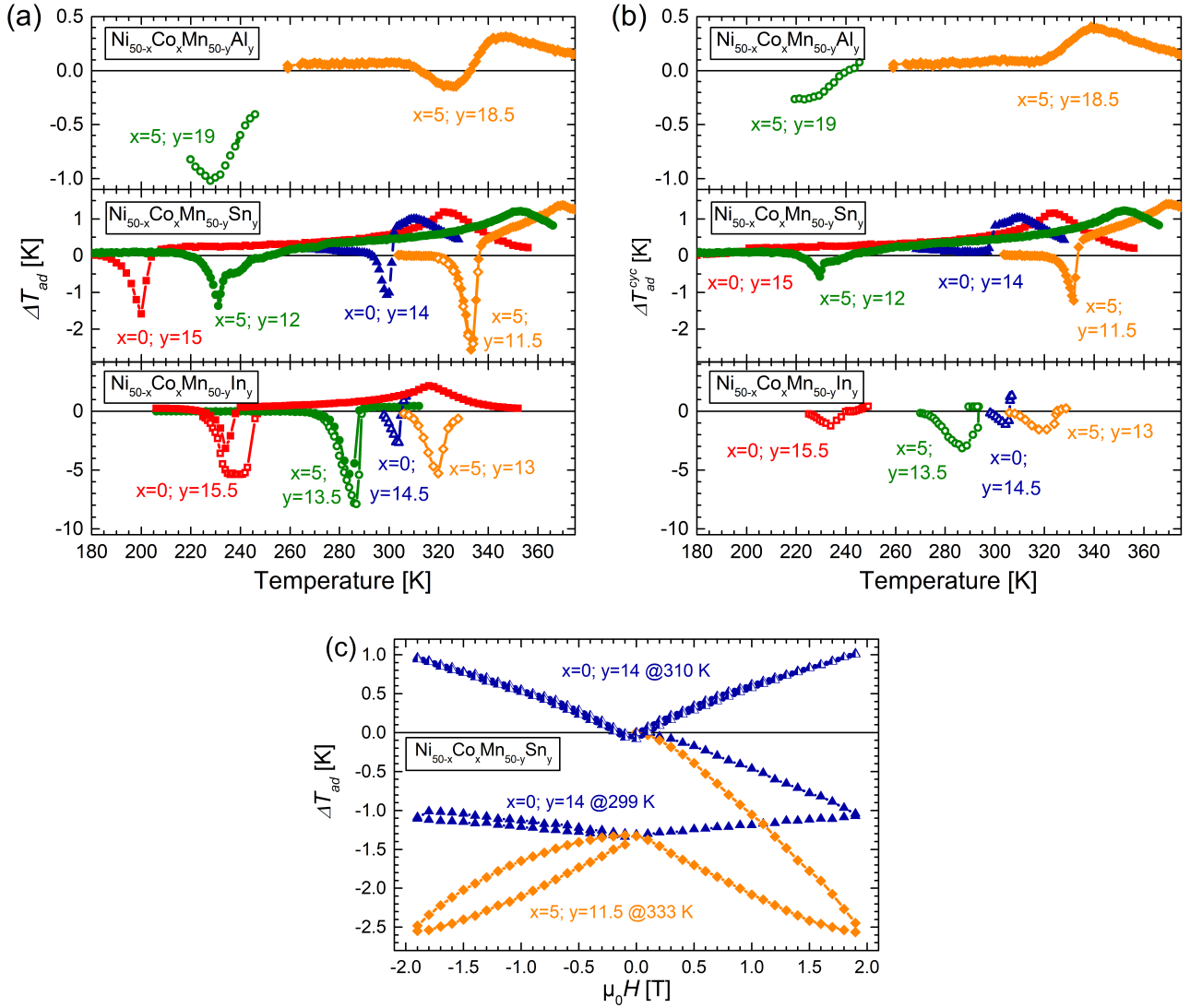


Figure 4.5: Directly measured ΔT_{ad} in "sandwich-mode" upon the first field application (a) and under cyclic conditions (b) in discontinuous (filled symbols) and continuous (open symbols) protocol for selected samples of the Ni-(Co)-Mn-Al, Ni-(Co)-Mn-Sn and Ni-(Co)-Mn-In Heusler systems in a maximum magnetic-field change of 1.93 T under heating. The magnetic-field-dependent evolution of ΔT_{ad} for $\text{Ni}_{50}\text{Mn}_{36}\text{Sn}_{14}$ (blue triangles) and $\text{Ni}_{45}\text{Co}_5\text{Mn}_{38.5}\text{Sn}_{11.5}$ (yellow diamonds) at different temperatures is shown in (c). The measurements of the Ni-(Co)-Mn-In samples have been performed by Tino Gottschall within the scope of his dissertation (TU Darmstadt) [144].

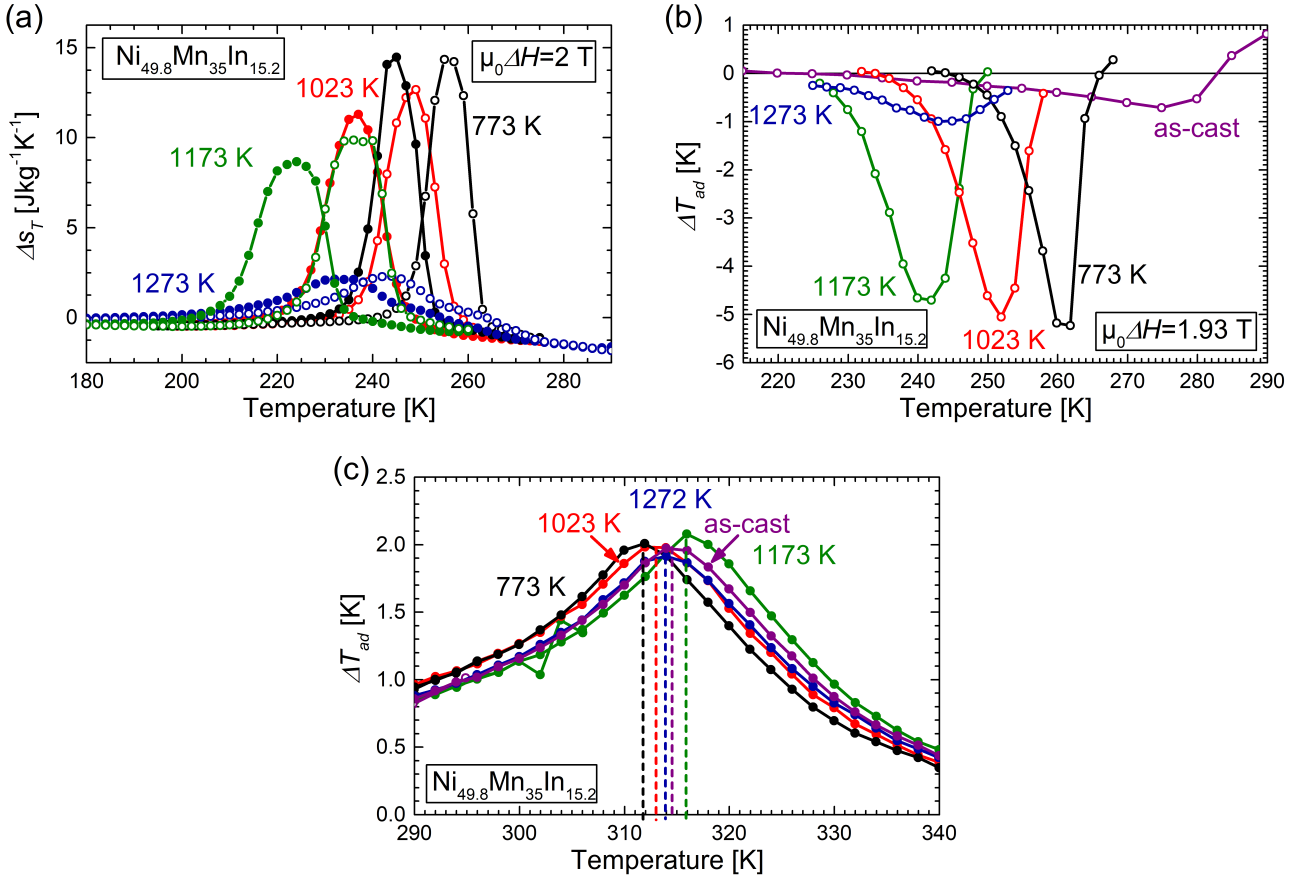


Figure 4.6: Isothermal entropy change determined from $M(T)$ measurements upon heating (open symbols) and cooling (filled symbols) for different annealing conditions of a post treatment at 773 K (black), 1023 K (red) and 1273 K (blue) compared to the initial annealing at 1173 K (green) and the as-cast state (purple) for $\text{Ni}_{50}\text{Mn}_{35}\text{In}_{15}$ (a) in a magnetic-field change of 2 T. Respective adiabatic temperature change of the martensitic transition (b) and the Curie temperature (c) are shown for direct measurements upon a magnetic-field change of 1.93 T under heating with continuous (filled symbols) and discontinuous (open symbols) protocol in "top-mode".

$14.4 \text{ J kg}^{-1} \text{ K}^{-1}$ by the additional heat treatment step at 773 K. In contrast, the entropy change of the transition is drastically decreased down to $2.3 \text{ J kg}^{-1} \text{ K}^{-1}$ for the too high post-annealing at 1273 K.

In accordance, the directly measured ΔT_{ad} is increased from a maximum value of -4.7 K for the initial sample to -5.3 K for the post-annealing at 773 K. In contrast to the strongly pronounced increase in Δs_T , this enhancement of ΔT_{ad} only amounts to roughly 10%. In addition, the ΔT_{ad} measurements confirm the shift of the austenite Curie temperature shown in Fig. 4.6 (c). The trend of the decreasing T_C^A for all carried out post-annealing steps at higher and lower temperatures than the initial homogenization is confirmed by the shift of the position for the peak value of ΔT_{ad} . The accuracy is hereby represented by the temperature step size of the measurement, which is 2 K. The largest shift is observed for the post-annealing at 773 K,

shifting T_C^A from 316 K down to 312 K. Even though, this is representing the largest enhancement for the MCE of the FOMT, the absolute ΔT_{ad} around the Curie temperature is even decreased slightly from 2.1 K to 2.0 K.

4.4 Magnetocaloric performance in high magnetic fields

Since most of the samples investigated in this chapter do not exhibit a saturated ΔT_{ad} for the applied magnetic-field changes, the possibility of applying larger fields can provide information about the maximum possible effect of the different Heusler systems and what fields are necessary for achieving this. The application of magnetic fields with different rates can also give insights into the kinetic characteristics of the martensitic transition. Therefore, a sample of Ni-Co-Mn-Al was measured in pulsed magnetic fields from 2 T to 50 T at the HLD of the Helmholtz Zentrum Dresden-Rossendorf. In order to evaluate the quality of the thermocouple and its field-rate dependence, pulses of 5 T and 50 T being equivalent to maximum field application rates of 710 T s^{-1} and 7940 T s^{-1} , respectively, are applied at the Curie temperature of the sample. The corresponding signals of ΔT_{ad} are shown in Fig. 4.7 (a). The maximum MCE of the SOMT amounts to 2 K for a field change of 5 T and to a maximum of 12 K for a field change of 50 T. These values are fully reversible due to the nature of the second-order transition. However, they are much lower compared to the best-performing second-order material Gd, which exhibits adiabatic temperature changes of around 4.5 K in moderate field changes of 2 T and over 50 K for 50 T [203]. By comparing the signals for the field-application path and the field removal, it is obvious that a magnetic-field application of 50 T causes a delay in the ΔT_{ad} signal. The inset confirms that for a field change of 5 T, no delay is present, which is indicated by the perfect agreement of field-application and field-removal signal. Therefore, the thermocouple provides good signals for low field rates, but possesses an artificial delay for extreme field change rates. Nevertheless, the ΔT_{ad} value determined at 5 T for both pulses is in good agreement (see inset).

The evolution of ΔT_{ad} around the magnetostructural phase transition is shown in Fig. 4.7 (b) for field pulses of 20 T at different starting temperatures. At T_C^A (320 K, red curve), the field-rate-induced delay of the thermocouple is not observed for the 20 T pulses (maximum field application rate of 3190 T s^{-1}) and a maximum temperature change of 6 K is measured. For a starting temperature of 220 K, a negative ΔT_{ad} of the inverse MCE can be observed upon field application. The resulting ΔT_{ad} value at the highest field is nevertheless positive. The reason is the little contribution of the FOMT due to the mixed starting state with majority of austenite present in the material. After the completion of the martensite transformation (at 7 T), the conventional MCE of the austenite is dominating, leading to a temperature increase with rising external magnetic field. Upon field removal, the positive conventional ΔT_{ad} is inverted. The back transformation to martensite is not taking place at 7 T like for the forward transformation because the thermal hysteresis must be overcome additionally. Therefore, the continuing negative ΔT_{ad} of the austenite phase upon field removal is decreasing the absolute temperature even below the lowest value of the forward transition upon field application. This characteristic shape of the measurement curve is also obtained for the other starting

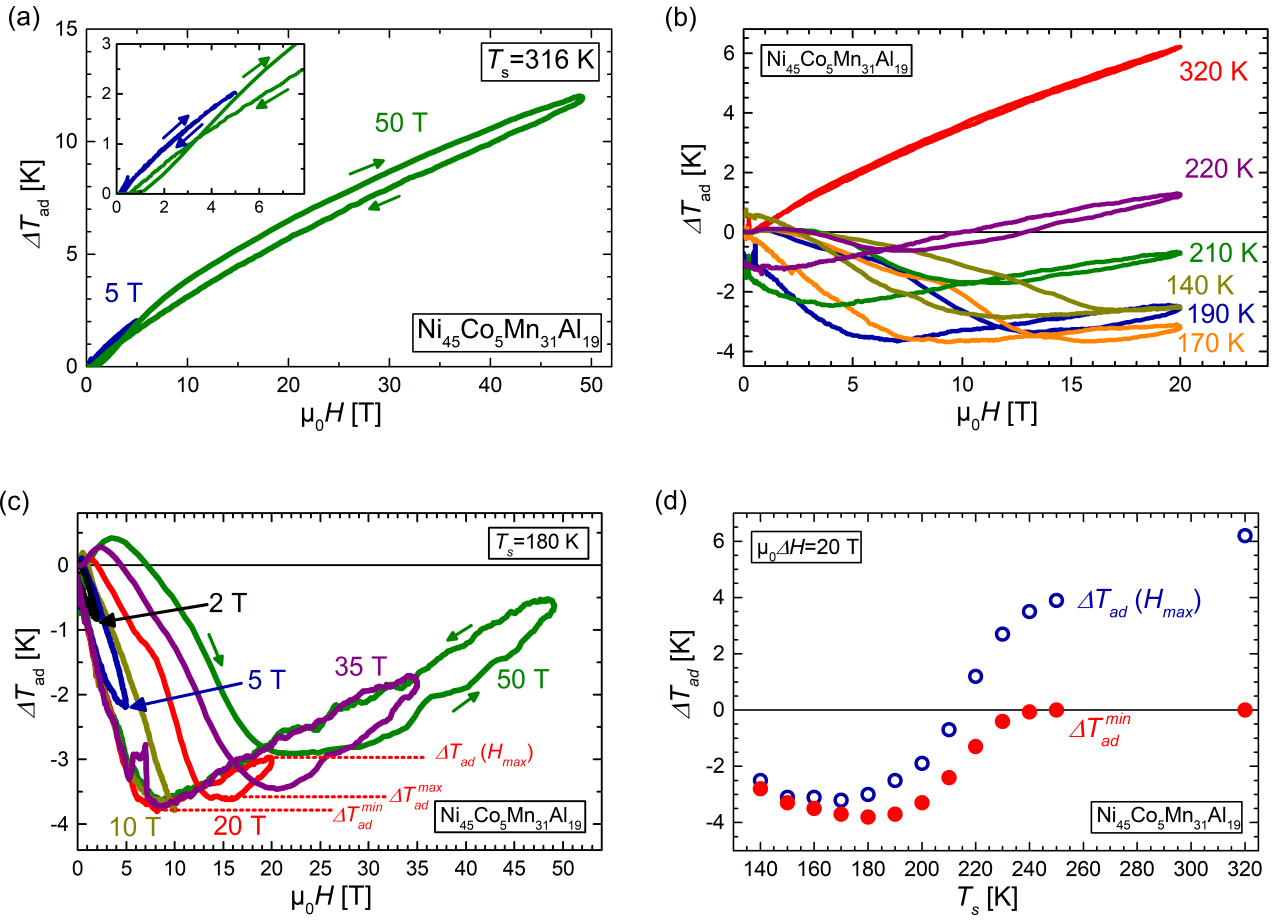


Figure 4.7: Measurements of ΔT_{ad} in pulsed magnetic fields carried out at the Helmholtz Zentrum Dresden-Rossendorf for $\text{Ni}_{45}\text{Co}_5\text{Mn}_{31}\text{Al}_{19}$ at the austenite Curie temperature (316 K) for different field strengths (a), for 20 T pulses at different starting temperatures (b) and for the maximum effect at the A_s temperature (180 K) for different field strengths (c). The representation of the maximum ΔT_{ad} determined from different methods for field pulses of 20 T is shown as a function of T_s in (d).

temperatures. Decreasing T_s results in a larger amount of martensite being present before the pulse, which increases the negative ΔT_{ad} observed for the inverse magnetic-field-induced FOMT. Also the magnetic field in which the transition is completed is increasing. With larger temperature differences to T_t , a stronger field change is necessary to shift the transition temperature (A_f as the relevant temperature in this case) accordingly and induce a complete austenite formation. In addition, the contribution of the conventional MCE of the austenite is reduced with decreasing T_s because of the rising temperature difference to T_C^A . This is indicated by the decreasing slope of the rising absolute temperature after completing the FOMT. A further reduction of T_s down to 140 K results in a decrease of the maximum negative ΔT_{ad} observed for the FOMT since the applied external field of 20 T is not sufficient any more to shift A_f down to the sample temperature.

In order to study the influence of the magnetic-field rate on the MCE, the induced ΔT_{ad} is regarded at a constant starting temperature of 180 K for different field pulses of 2 T to 50 T in Fig. 4.7 (c). A magnetic-field change of 10 T is necessary to induce a completed phase transition and to reach the saturation of ΔT_{ad} . As a result, the maximum negative temperature change is determined to reach -3.7 K in 10 T. For lower magnetic fields, the maximum ΔT_{ad} of the field application is reduced and the field removal is not showing a delay with a temperature decrease due to the conventional MCE for the back transformation. It is induced here without any hysteresis delay due to minor-loop behavior. Since the forward transition is not complete, residual martensite is still present in the material and acting as nucleation sites for new martensite formation. This reduces the energy barrier and therefore favors the initialization of the back transformation upon field removal. A comparison of the largest field rates for applications of 20 T, 35 T and 50 T with the lower field changes indicates that ΔT_{ad} of the forward transition (austenite formation upon field application) is following the same path for the fields of 2 T, 5 T and 10 T. For the larger fields, not only a field-rate-dependent delay of ΔT_{ad} is observed, also a hysteresis is present for the conventional MCE of the completely induced austenite. This measurement hysteresis is confirmed by the reference pulse at T_C^A in Fig. 4.7 (a). For this reason, a field-rate-dependent effect on the kinetics of the phase transition cannot be stated unambiguously. Furthermore, the temperature signal experiences an artificial increase at the beginning of the large field pulses, which increases for higher field application rates. Thus, it is assumed to be a measurement artifact. The question whether the strong field delay of ΔT_{ad} for fields above 10 T is due to hindered transition kinetics or a delay of the thermocouple signal or a mixture of both cannot be answered clearly at this point.

For the description of the maximum ΔT_{ad} achievable, the overlay of the conventional MCE is influencing the determination, for which three methods are possible. The easiest way is to consider the ΔT_{ad} value for the maximum applied field, denoted as $\Delta T_{ad}(H_{max})$. This value represents an application related point of view since the absolute temperature difference that is reached after the full field application is relevant for the amount of heat that can be generated by the magnetocaloric material. However, this is obviously highly influenced by the field strength of the pulse. A higher maximum field automatically increases this value by the positive ΔT_{ad} of the austenite after completing the martensitic transition. In Fig. 4.7 (c), ΔT_{ad} is approaching zero again for the highest field pulse of 50 T, even though a completed FOMT has been induced before. Another option is to determine the lowest temperature after the completion of the forward transition (ΔT_{ad}^{max}), which described the maximum temperature change that can be reached by a magnetic-field-induced phase transition for the first field application. However, this value is influenced by the field-application rate because larger rates lead to the described field delay of the forward transition. In combination with the overlaid field-dependent positive ΔT_{ad} , also ΔT_{ad}^{max} varies for different applied field pulses for a completely induced transition at the same starting temperature. Furthermore, ΔT_{ad}^{min} represents the lowest value of ΔT_{ad} that is observed for the full cycle of field application and removal. It is located at the point where the conventional MCE cools down the sample upon field removal before the critical field for the onset of the back transformation of the first-order effect is reached. This value is in Fig. 4.7 (c) below ΔT_{ad}^{max} (therefore larger in absolute values of temperature change) due to the hysteresis

of the martensitic phase transition and is equal for all applied field rates. The absence of the field delay is originated here in the equal magnetic-field-change rate of the field-removal process of the pulse (see Fig. 3.5). Consequently, the onset field for the back transformation to martensite and the corresponding curves of ΔT_{ad} are in perfect agreement for all applied field pulses. Since the absolute field rates are also lowest at this point, the determination of ΔT_{ad}^{min} is considered as the most reliable measure for ΔT_{ad} . Because of the absent hysteresis effect as a result of the minor-loop behavior, ΔT_{ad}^{min} and ΔT_{ad}^{max} are equal for not completely induced transitions.

The representation of the temperature-dependent maximum values of ΔT_{ad}^{min} (red) and $\Delta T_{ad}(H_{max})$ (blue) in Fig. 4.7 (d) highlights the difference between these two quantities. While the ΔT_{ad} determined at the maximum field strength also reflects the conventional MCE when T_s approaches T_C^A , the positive contribution to ΔT_{ad}^{min} is not playing a role. Thus, ΔT_{ad}^{min} approaches zero for increasing starting temperatures of the measurement. The determined ΔT_{ad}^{min} is always lower than $\Delta T_{ad}(H_{max})$, but the difference gets smaller for lowering T_s because the impact of the second-order MCE is decreasing with the temperature as well.

Highest values for the maximum possible magnetic field induced MCE of the FOMT are determined as -3.7 K. It is found that a magnetic field of 10 T is necessary in order to induce a completed phase transition from martensite to austenite. This ΔT_{ad} value is even lower than the ones for Ni(-Co)-Mn-In samples for moderate magnetic-field changes of 2 T. An analog study for the high-field behavior of Ni-Co-Mn-In shows a maximum effect of -13 K for a magnetic-field change of 10 T [204]. Due to the large shift of T_t in external magnetic fields combined with the sharp phase transition, large MCE can be obtained for moderate field changes. Compared to the maximum effect of Ni-Co-Mn-In in 2 T (up to -8 K), the performance in low fields is not extremely far away from saturation.

On the other hand, a study of Ni-Co-Mn-Sn in high fields results in a maximum ΔT_{ad} of -17 K for field changes of 20 T (private communication, unpublished results of Franziska Scheibel, TU Darmstadt). This system is highly favored for usage in larger field changes because the enhancement compared to the maximum ΔT_{ad} in moderate fields of 2 T is huge. This supports the findings of the previous section that the potential MCE represented by Δ_{sT} of Ni-Co-Mn-Sn is similar to Ni-Co-Mn-In, but much larger field changes are necessary to exploit this effect due to the reduced $\frac{dT_t}{\mu_0 dH}$ of the Sn-system.

The comprehensive analysis of different Heusler alloy systems demonstrates that sharp phase transitions with a large magnetic field dependence and low thermal hysteresis lead to large isothermal entropy changes and useful cyclic values of ΔT_{ad} for the Ni-Co-Mn-In system. These basic properties to denote a magnetocaloric material as promising need to be optimized all together in order to achieve a very good (cyclic) ΔT_{ad} . If only one of them cannot be tuned properly, the reversible magnetocaloric effect is reduced drastically. The large magnetocaloric effect cannot be transferred equally to the related Heusler systems of Ni-Co-Mn-Sn and Ni-Co-Mn-Al. Even though the Sn-system shows sharp transitions leading to large values of Δ_{sT} , the low $\frac{dT_t}{\mu_0 dH}$ prevents an induced MCE in low magnetic fields. However, for the possibility of applying larger magnetic-field changes of 10 T to 20 T, very large temperature changes can be achieved that outperform the saturated MCE of Ni-Co-Mn-In. On the other hand, Ni-Co-Mn-Al shows a reasonable,

tunable $\frac{dT_t}{\mu_0 dH}$ and a similar ΔM like the other two systems. Here, the large transition width reduces the maximum achievable ΔT_{ad} , even for a completely induced effect by high magnetic fields. Consequently, a sharp phase transition is the prerequisite for a promising MCE of the investigated Heusler alloys. The magnetic-field-dependence of the transition temperature then determines whether a good effect can be induced by low fields (just "good" because a large $\frac{dT_t}{\mu_0 dH}$ reduces the maximum possible MCE according to the Clausius-Clapeyron equation) or a very large effect can be expected. For the latter case, also large fields are necessary to exploit the full potential of the respective phase transition. It must be emphasized that these thoughts hold true for the first field application. For a good cyclic response, also the thermal hysteresis needs to be considered. This can lead to even higher cyclic fields necessary for the latter case of a low magnetic-field sensitivity of T_t .

5 Novel all-*d*-metal Heusler Alloys

Recent studies on all-*d*-metal Heusler alloys with a transition metal occupying the D-sites of the Heusler lattice showed a magnetostructural phase transition of first-order type for Ni-rich and Mn-rich Ni-Co-Mn-Ti systems with large isothermal entropy changes [167, 205, 206]. An increasing amount of Ti stabilizes the austenitic phase, whereas Co substitution additionally increases the austenite Curie temperature T_C^A . For a certain amount of Co atoms on the Ni sites, the desired martensitic transformation from ferromagnetic austenite to weak-magnetic martensite is enabled. One drawback of many magnetocaloric compounds is the brittleness leading to mechanical degradation after a certain amount of magnetocaloric cycles [37, 122, 149, 207]. The all-*d*-metal Heusler alloys are suggested to solve this problem since the strength of hybridized *d-d* bonding leads to a higher mechanical stability [167, 208] making them interesting for magnetocaloric [167, 205, 209], barocaloric [210] and elastocaloric [211, 212] purposes. In this chapter, an optimization of the production procedure will be carried out for this new type of Heusler alloys. Main findings of a comprehensive characterization will be compared to the well-known Heusler alloys discussed in Chapter 4. Finally, the potential for magnetocaloric and multi-stimuli applications will be evaluated in detail by observing the magnetization, strain, and microstructural changes during the phase transition upon varying magnetic field, uniaxial pressure and temperature.

Parts of this chapter are published in

- **A. Taubel**, B. Beckmann, L. Pfeuffer, N. Fortunato, F. Scheibel, S. Ener, T. Gottschall, K. P. Skokov, H. Zhang, and O. Gutfleisch, *Tailoring magnetocaloric effect in all-*d*-metal Ni-Co-Mn-Ti Heusler alloys: a combined experimental and theoretical study*, Acta Materialia 201, 425-434 (2020).

5.1 Optimization of the heat treatment

In order to produce Heusler samples with sharp phase transitions leading to large magnetocaloric effects, the homogenizing heat treatment has been optimized. Figure 5.1 (a) shows that the phase transition for a heat treatment for 96 h at 1173 K and below is very broad for the exemplarily shown $\text{Ni}_{37}\text{Co}_{13}\text{Mn}_{34}\text{Ti}_{16}$ sample. This broad transition behavior leads to reduced magnetocaloric effects due to the diminished $\frac{dM}{dT}$. For higher annealing temperatures, the phase transition of the samples becomes sharper indicating a better homogenization. This effect saturates at a temperature of 1323 K and the transition becomes worse for an annealing at 1373 K. The factors considered for the quality of the phase

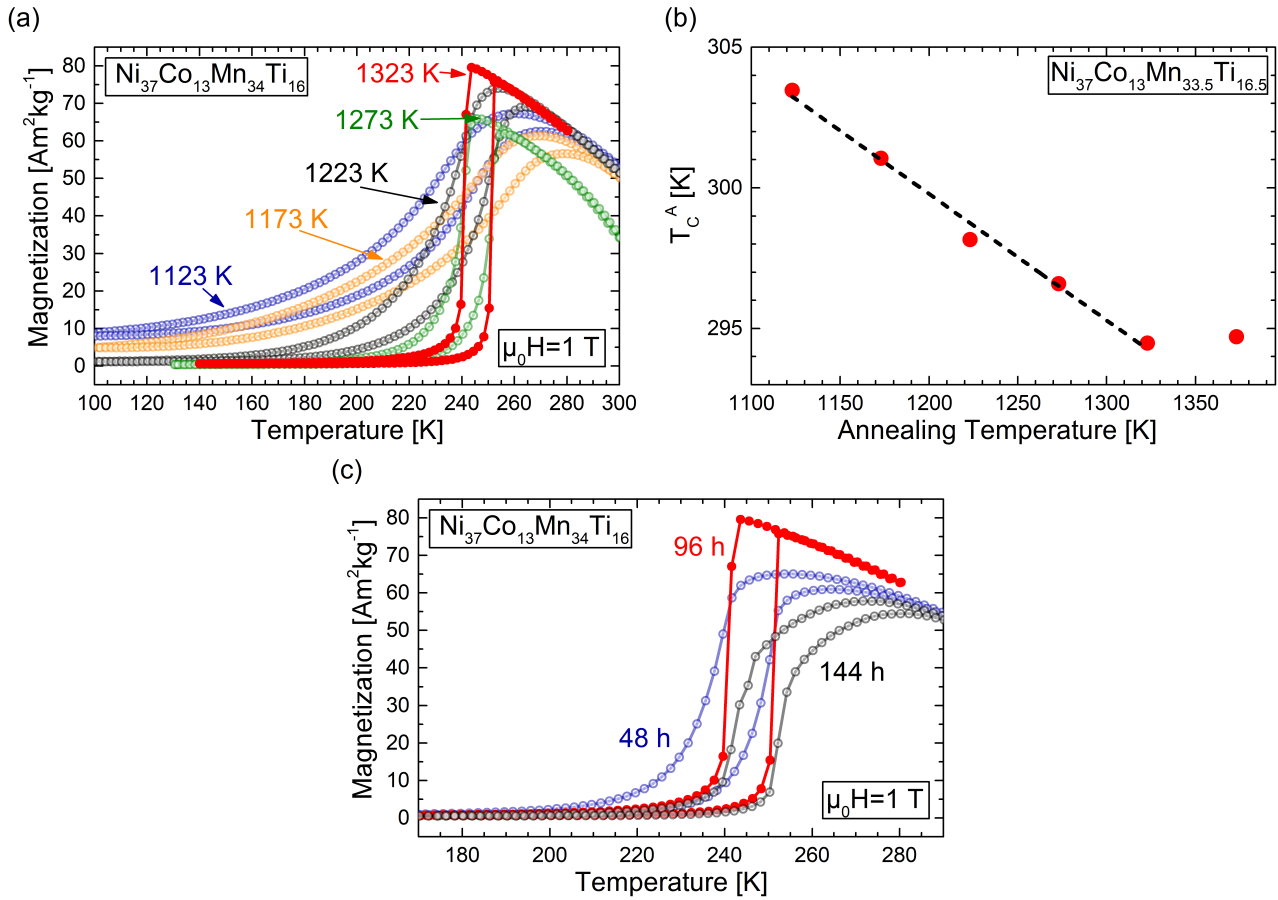


Figure 5.1: Magnetization as a function of temperature for samples produced under different annealing conditions by varying (a) temperature and (c) duration shown for Ni₃₇Co₁₃Mn₃₄Ti₁₆. The evolution of the austenitic Curie temperature for different annealing temperatures for Ni₃₇Co₁₃Mn_{33.5}Ti_{16.5} sample is shown in (b). The magnetization curves have been measured in a magnetic field of 1 T, whereas T_C^A has been determined in a magnetic field of 0.01 T. Consequently, the most suitable properties can be obtained by a heat treatment at 1323 K for 96 h followed by water quenching. This heat treatment optimization has been carried out by Benedikt Beckmann (TU Darmstadt) within the framework of his Master Thesis [213].

transition are the transition width, the magnetization change of the transition, and the thermal hysteresis. In addition, the austenite Curie temperature T_C^A plotted for different annealing temperatures in Fig. 5.1 (b) reveals that a better homogenization with larger annealing temperature is accompanied by a reduction of T_C^A . This trend is followed by a slight increase of T_C^A for the annealing temperature of 1373 K, which is identified from magnetization data as too high. Besides atomic ordering, the homogenization of the stoichiometric variations present in as-cast state are responsible for this effect, which will be underlined by the microscopical investigations in Section 5.3. This analysis allows us to select an optimal temperature for the homogenization step. Like for other magnetocaloric Heusler alloys, this temperature must be high enough with respect to the melting point in order to enable optimized diffusion processes that result in best chemical homogeneity [142]. The melting point of Ni-Co-Mn-Ti has been determined by a differential

scanning calorimetry (DSC) measurement to be at 1380 K. This is around 50 K to 100 K larger than for the Ni(-Co)-Mn-Sn system [142, 183, 184] being conform with the optimal annealing temperature, which is 100 K larger for Ni-Co-Mn-Ti compared to Ni(-Co)-Mn-Sn. An ideal annealing is thus obtained in agreement with the observations from Chapter 4 for Ni(-Co)-Mn-Sn and Ni(-Co)-Mn-In at temperatures that are approximately 50 K to 70 K below the melting point. The heat treatment temperature must not be closer than 50 K to the melting point to prevent local melting of the sample and immoderate evaporation of Mn.

In a second step, the optimal annealing temperature is kept constant whereas the annealing time is varied. The results of this experiment in Fig. 5.1 (c) show that the initial time of 96 h leads to the optimal result. A shorter time of 48 h results in a broader transition due to insufficient homogenization and a longer annealing time also broadens the phase transition. This can be due to an enhanced evaporation of Mn for long annealing times (in analogy to high annealing temperatures) leading to stoichiometric variances in the compound and thus to a broader distribution of local transition temperatures. If the time is chosen too short, the necessary diffusion processes are not effective to homogenize the stoichiometry to achieve a phase transition as sharp as possible. It must be noted here that the optimal annealing conditions are an interplay between temperature and duration, which means that defining an ideal set of annealing parameters by considering all relevant properties is a complex issue. The optimal annealing for the Ni-Co-Mn-Ti sample series is here found to be at 1323 K for 96 h.

Table 5.1: Nominal sample compositions of the produced $\text{Ni}_{50-x}\text{Co}_x\text{Mn}_{50-y}\text{Ti}_y$ system with actual compositions determined from EDS together with the corresponding e/a ratio, austenite start temperature (A_s) determined in 1 T, width of the transition (ΔT_{width}), thermal hysteresis (ΔT_{hyst}), shift of the transition temperature with applied magnetic fields ($dT_t/\mu_0 dH$) and austenite Curie temperature (T_C^A) determined in 0.01 T. Fields without values ("-") correspond to samples which did not show a magnetostructural phase transition.

Nominal	Ni [at. %]	Co [at. %]	Mn [at. %]	Ti [at. %]	e/a	A_s [K]	ΔT_{width} [K]	ΔT_{hyst} [K]	$dT_t/\mu_0 dH$ [K T ⁻¹]	T_C^A [K]
$\text{Ni}_{37}\text{Co}_{13}\text{Mn}_{35}\text{Ti}_{15}$	36.6	12.0	36.3	15.1	7.885	310.1	16.0	8.4	-1.2	340.2
$\text{Ni}_{37}\text{Co}_{13}\text{Mn}_{34.5}\text{Ti}_{15.5}$	35.4	12.8	36.8	15.0	7.866	293.3	11.7	5.5	-1.6	333.8
$\text{Ni}_{37}\text{Co}_{13}\text{Mn}_{34}\text{Ti}_{16}$	36.0	12.7	35.2	16.1	7.848	249.7	7.2	9.9	-1.7	311.6
$\text{Ni}_{37}\text{Co}_{13}\text{Mn}_{33.5}\text{Ti}_{16.5}$	35.9	12.7	34.7	16.7	7.831	225.5	14.4	11.4	-2.1	294.5
$\text{Ni}_{37}\text{Co}_{13}\text{Mn}_{33}\text{Ti}_{17}$	34.1	13.1	36.2	16.6	7.785	121.5	33.3	20.0	-7.4	303.5
$\text{Ni}_{35}\text{Co}_{15}\text{Mn}_{39}\text{Ti}_{11}$	33.6	14.6	40.8	11.0	7.967	485.1	23.0	19.1	-0.1	480.5
$\text{Ni}_{35}\text{Co}_{15}\text{Mn}_{38}\text{Ti}_{12}$	33.6	14.7	39.6	12.1	7.939	432.7	28.5	28.4	-1.7	462.1
$\text{Ni}_{35}\text{Co}_{15}\text{Mn}_{37}\text{Ti}_{13}$	33.6	14.6	38.8	13.0	7.910	346.4	42.3	17.6	-2.8	442.1
$\text{Ni}_{35}\text{Co}_{15}\text{Mn}_{36}\text{Ti}_{14}$	33.3	14.8	37.7	14.2	7.871	278.2	22.1	14.2	-3.4	414.7
$\text{Ni}_{35}\text{Co}_{15}\text{Mn}_{35}\text{Ti}_{15}$	33.8	14.8	36.4	15.0	7.859	211.0	32.8	17.0	-5.0	387.0
$\text{Ni}_{35}\text{Co}_{15}\text{Mn}_{34}\text{Ti}_{16}$	33.7	14.8	35.4	16.1	7.823	136.3	31.7	20.6	-9.3	358.7
$\text{Ni}_{33}\text{Co}_{17}\text{Mn}_{40}\text{Ti}_{10}$	31.6	16.5	41.8	10.1	7.975	509.8	22.0	30.3	-1.0	535.3
$\text{Ni}_{33}\text{Co}_{17}\text{Mn}_{39}\text{Ti}_{11}$	31.6	16.6	40.8	11.0	7.949	454.5	29.8	35.0	-3.1	517.7
$\text{Ni}_{33}\text{Co}_{17}\text{Mn}_{38}\text{Ti}_{12}$	31.6	16.6	39.7	12.1	7.916	378.0	43.1	41.3	-5.1	498.5
$\text{Ni}_{33}\text{Co}_{17}\text{Mn}_{37}\text{Ti}_{13}$	31.8	16.7	38.4	13.1	7.894	-	-	-	-	478.9
$\text{Ni}_{33}\text{Co}_{17}\text{Mn}_{36}\text{Ti}_{14}$	31.9	16.6	37.4	14.1	7.866	-	-	-	-	458.2
$\text{Ni}_{33}\text{Co}_{17}\text{Mn}_{35}\text{Ti}_{15}$	31.8	16.6	36.4	15.2	7.832	-	-	-	-	435.0

5.2 Influence of stoichiometry and magnetic field on the phase transitions

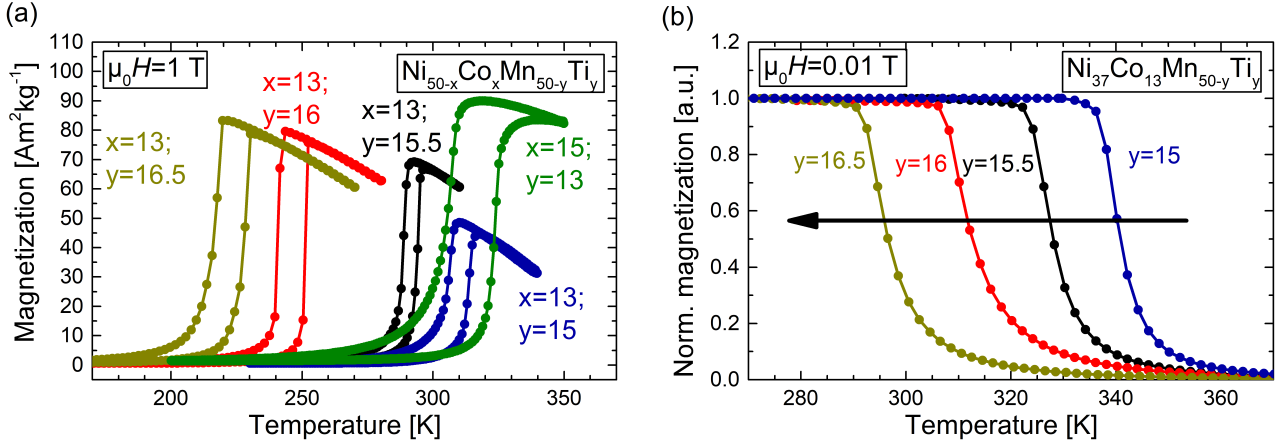


Figure 5.2: Temperature-dependent magnetization curves for $\text{Ni}_{50-x}\text{Co}_x\text{Mn}_{50-y}\text{Ti}_y$ with a constant Co content of 13 at. % as well as for one sample with $x = 15$ and $y = 13$ showing the martensitic phase transition in 1 T for heating and cooling (a) as well as T_C^A in 0.01 T for heating protocol (b).

The resulting phase transitions for the $\text{Ni}_{50-x}\text{Co}_x\text{Mn}_{50-y}\text{Ti}_y$ system are depicted by temperature-dependent magnetization measurements in Fig. 5.2 for four samples with a Co content of $x = 13$ and with varying Ti content of $y = 15, 15.5, 16$ and 16.5 . In addition, one sample of higher Co content ($x = 15; y = 13$) with a transition temperature at room temperature is included. The phase-transition temperatures are decreasing with increasing Ti content within a series of constant Co amount, which is in agreement with literature [167, 205, 206]. This effect is a result of the decreasing e/a ratio, which is well-known for other Ni-Mn-X Heusler systems [185]. The shift of the martensitic transition temperature amounts to an estimate of 50 K per at. % of Ti. Furthermore, it is found that T_C^A is decreasing for increasing Ti content (decreasing e/a ratio). Such a variation of T_C^A is not present for the Ni(-Co)-Mn-X systems of $X = \text{In}, \text{Al}$ with stoichiometries experiencing a martensitic transition around room temperature, where the Curie temperature is influenced mainly by the Co content but not by the variation in the Mn-X ratio of the compound [67]. In contrast, a changing T_C^A with stoichiometry has also been observed for the systems with $X = \text{Sn}, \text{Ga}$. The new finding for the all- d -metal Heusler system with $X = \text{Ti}$ is that the austenite Curie temperature is increasing for larger e/a ratio, which is in contrast to the well-studied Heusler systems so far [139, 214]. However, the absolute shift of T_C^A is lower than the shift of the transition temperature. The phase diagram including the martensitic transition temperatures as well as the austenite Curie temperatures for all produced alloys of the $\text{Ni}_{50-x}\text{Co}_x\text{Mn}_{50-y}\text{Ti}_y$ system is shown in Fig. 5.3 (a). It combines the overall behavior of the transition temperature shift for different stoichiometries with varying Ti and Co content by considering the e/a ratio. The behavior of T_C^A is depicted by dashed lines since it is not only depending on e/a but also on the Co content of the alloy. Therefore, trend lines exist for constant Co concentrations within the different sample series.

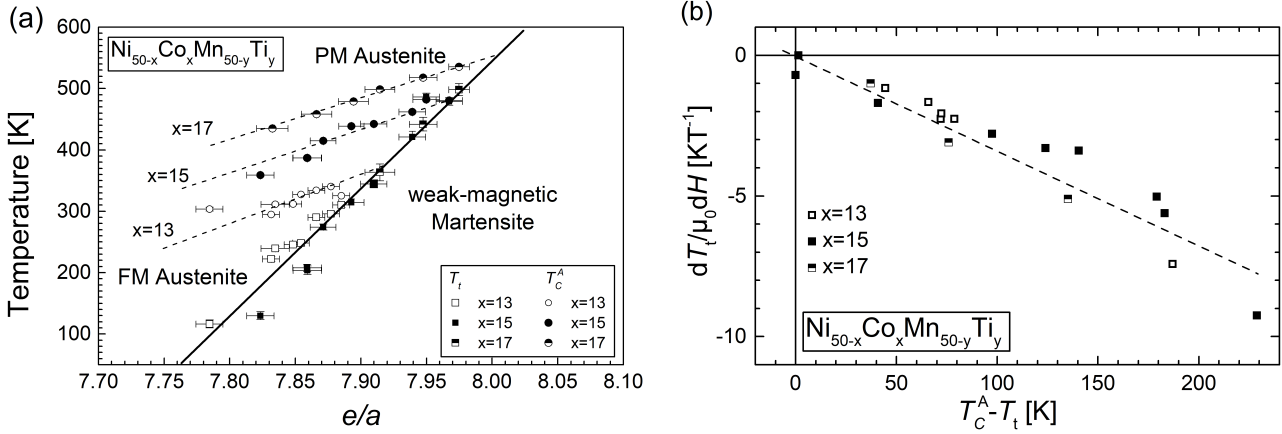


Figure 5.3: Phase diagram showing the martensitic transition temperatures of all $\text{Ni}_{50-x}\text{Co}_x\text{Mn}_{50-y}\text{Ti}_y$ compounds (squares) as well as the austenite Curie temperatures T_C^A (circles) depending on the e/a ratio (a). The shift of the transition temperature with respect to an external magnetic field is shown in (b) depending on its difference to the corresponding T_C^A of the same sample. The lines are drawn by hand as a guide to the eye.

The magnetization behavior in Fig. 5.2 (a) depicts the narrow width of the phase transition for optimally annealed compounds. The difference between martensite/austenite start and finish temperatures are in the range of 5 K to 10 K (see Tab. 5.1), which is similar to the best Ni(-Co)-Mn-In and Ni(-Co)-Mn-Sn Heusler alloys [76, 125, 142]. Especially the transition of the $\text{Ni}_{37}\text{Co}_{13}\text{Mn}_{34}\text{Ti}_{16}$ sample is exceptionally sharp, it transforms from martensite to austenite state (and vice versa) within 5 K. The thermal hysteresis of the samples with $x = 13$ amounts to 8 K to 12 K. This is better than for Ni-Mn-Sn and similar to Ni-Co-Mn-Sn and Ni(-Co)-Mn-In by comparing samples with similar transition temperatures, which is a significant factor for the thermal hysteresis width [142].

Besides a sharp phase transition and a narrow thermal hysteresis, it is important to induce the transition by an external stimulus. Therefore, the shift of the phase transition with an externally applied magnetic field $\frac{dT_t}{\mu_0 dH}$ is a crucial property to build up a significant magnetocaloric effect for the first field application as well as to overcome the thermal hysteresis for cyclic conditions [37]. By comparing the magnetization curves for the series with 13 at. % of Co in different external magnetic fields, the sensitivity of the magnetostructural phase transition to applied magnetic fields is estimated to be -1.2 K T^{-1} for a transition around room temperature. For transitions at lower temperatures, the field sensitivity is increased to -2.1 K T^{-1} . The addition of Co enhances the magnetic-field sensitivity. For samples with the same transition temperature at room temperature, $\frac{dT_t}{\mu_0 dH}$ can be increased from -1.2 K T^{-1} (for $x = 13$) to -2.8 K T^{-1} (for $x = 15$).

As already known from other Ni(-Co)-Mn-X systems, $\frac{dT_t}{\mu_0 dH}$ is dependent on the martensitic transition temperature and gets larger at lower temperatures [142]. This trend is also observed here: Within all series of constant Co content (Co_{13} , Co_{15} and Co_{17}), the absolute value of $\frac{dT_t}{\mu_0 dH}$ increases for increasing Ti content. This behavior results from the larger magnetization change of the phase transition due to the reduced transition temperature. By plotting all data points for $\frac{dT_t}{\mu_0 dH}$ depending on the difference of

the martensitic transition temperature T_t from T_C^A in Fig. 5.3 (b), it can be seen that this difference is mainly influencing the field sensitivity. The difference between the transition and the austenitic Curie temperature provides an estimate of how efficient the phase transition can be induced by an external magnetic field regardless of the stoichiometry. By assuming a linear dependence, the estimated slope for the Ti-Heusler system amounts to 0.033 T^{-1} . This value is giving a sensitivity for the design of a strong $\frac{dT_t}{\mu_0 dH}$ by changing the transition temperature - being equivalent to changing the composition (e/a ratio). However, for Ni(-Co)-Mn-In alloys, a divergent behavior has been observed [67]. The plot in Fig. 5.3 (b) resembles a linear dependence, which is an approximation for small values of $T_C^A - T_t$. Comparing the plotted temperatures with the behavior for Ni(-Co)-Mn-In, the supposed linear region covers a larger temperature range indicating a lower compensation point [67].

As a drawback, increasing $\frac{dT_t}{\mu_0 dH}$ by raising the Co content leads to a broadening of the transition width and an increased thermal hysteresis (see Fig. 5.2 (a) and Tab. 5.1) in agreement with the observations of previous studies [167, 206]. The increased thermal hysteresis is a crucial issue for the reversibility of a magnetocaloric cooling cycle for Heusler alloys [38, 175, 201]. It is desired to turn this into an advantage by reversing the phase transition with applying pressure and using the compound in a multi-stimuli cooling cycle, where a large thermal hysteresis is needed [43].

5.3 Microstructure evolution of the martensitic phase transition

In this section, the microstructure of the martensitic transition will be investigated in detail by temperature- and magnetic-field-dependent *in-situ* optical microscopy. Especially the influence of different heat treatments will be regarded in detail in order to examine the differences and correlate it to the observed magnetization behavior. First of all, the resulting microstructure from the alloying process is investigated as the original state prior to any heat treatment. The as-cast state of the sample in Fig. 5.4 (a) shows two phases, one Ti-rich (dark) and one Mn-rich (bright) compared to the nominal composition ($\text{Ni}_{37}\text{Co}_{13}\text{Mn}_{33.5}\text{Ti}_{16.5}$). The averaged composition of the Ti-richest phase region from EDS is $\text{Ni}_{35.2}\text{Co}_{14.4}\text{Mn}_{30.6}\text{Ti}_{19.8}$, whereas the Mn-richest phase region consists of $\text{Ni}_{36.3}\text{Co}_{11.0}\text{Mn}_{39.8}\text{Ti}_{12.9}$. Therefore, it can be assumed that different (off-stoichiometric) Heusler phases with different Mn-Ti ratio are formed during solidification from the melt. The larger magnification reveals that martensitic structures are visible in the Mn-rich phase even though the overall transition temperature of the nominal composition is around 250 K. This deviation is due to the locally varied transition temperature by the large Mn content. It is worth noting that the overall as-cast microstructure does not look columnar but globular even though the direction of solidification lies in the regarded image plane. This is evidence for slow solidification kinetics.

The typical grain size of the annealed Ni-Co-Mn-Ti samples is in the range of $50 \mu\text{m}$ to $300 \mu\text{m}$, as shown representatively in Fig. 5.4 (b). In accordance to the observations from the as-cast state, the grains have a globular shape. This finding deviates from the microstructure observed in Ni-Co-Mn-In Heusler alloys indicating a different solidification behavior [215]. Also the observed grain size is significantly lower than for conventional Ni(-Co)-Mn-X Heusler alloys, where the grains are in the range of several hundreds

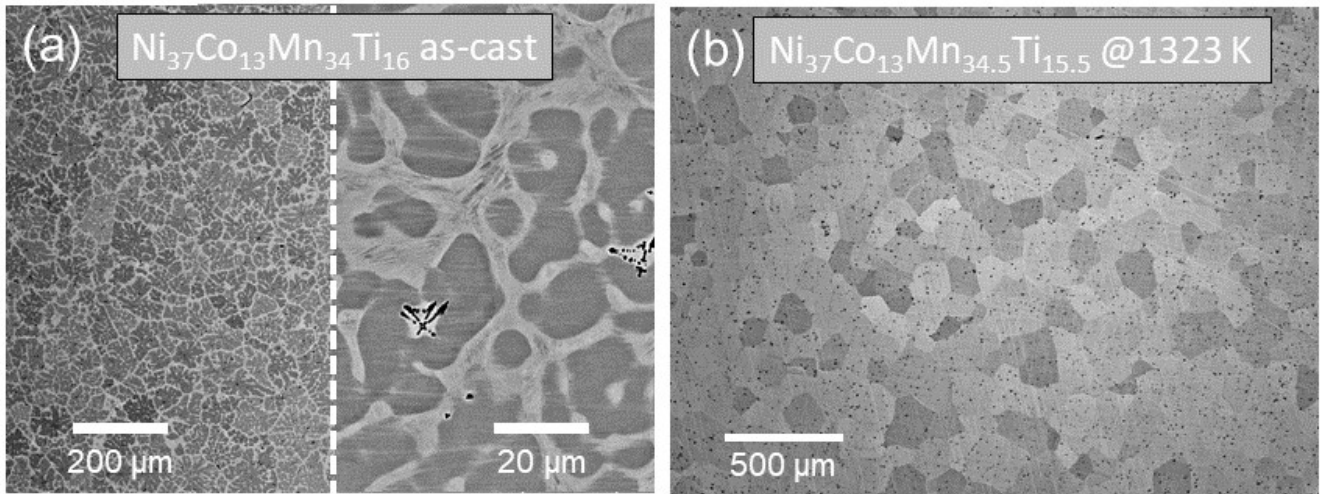


Figure 5.4: SEM image of as-cast structure of $\text{Ni}_{37}\text{Co}_{13}\text{Mn}_{34}\text{Ti}_{16}$ obtained by BSE imaging (a) and of $\text{Ni}_{37}\text{Co}_{13}\text{Mn}_{34.5}\text{Ti}_{15.5}$ after ideal annealing at 1323 K for 96 h showing the resulting grain structure (b).

of micrometer and up to the millimeter-range. This occurrence of significantly finer grains can be an important aspect for the enhanced mechanical strength that has been reported [167]. It is well known that the yield strength of a metal is inversely proportional to the average grain size diameter after the relation of Hall-Petch [216, 217].

A distinct variation of the grain size as a function of the heat treatment is observed for the highest annealing temperatures that lead to a homogeneous sample (1323 K). The microstructures for the as-cast sample and the different annealing temperatures and times are shown in Fig. 5.5 imaged by polarized light microscopy. Despite the multiphase microstructure, the grain arrangement can already be seen in the as-cast state in (a). The increasing annealing temperature does not change the grain size or shape significantly up to a heat treatment at 1273 K. Apparently, a radical change in microstructure happens for the next higher annealing temperature of 1323 K, where the grain structure vanishes completely and only two small isolated grains can be seen within a matrix of an abnormally large grain (Fig. 5.5 (f)). In order to prove this as a systematic effect, the microstructures of the samples annealed at the same temperature but for different times are shown in Fig. 5.5 (g) and (h). For both time variations of 48 h and 144 h, the observation of drastically enlarged grain sizes can be confirmed. For the annealing time of 48 h, some smaller grains with the size of the characteristic ones for lower heat-treatment temperatures are still present. This indicates that the abnormal grain growth is mainly activated by the annealing temperature of 1323 K but not completed on a time scale of 48 h. In contrast, the longer annealing time of 144 h only features one grain boundary in the regarded area separating two large grains in the millimeter-regime. As a matter of fact, the annealing temperature of 1323 K leading to the abnormal grain growth coincides with the optimal temperature identified to obtain ideally homogenized stoichiometries and sharp phase

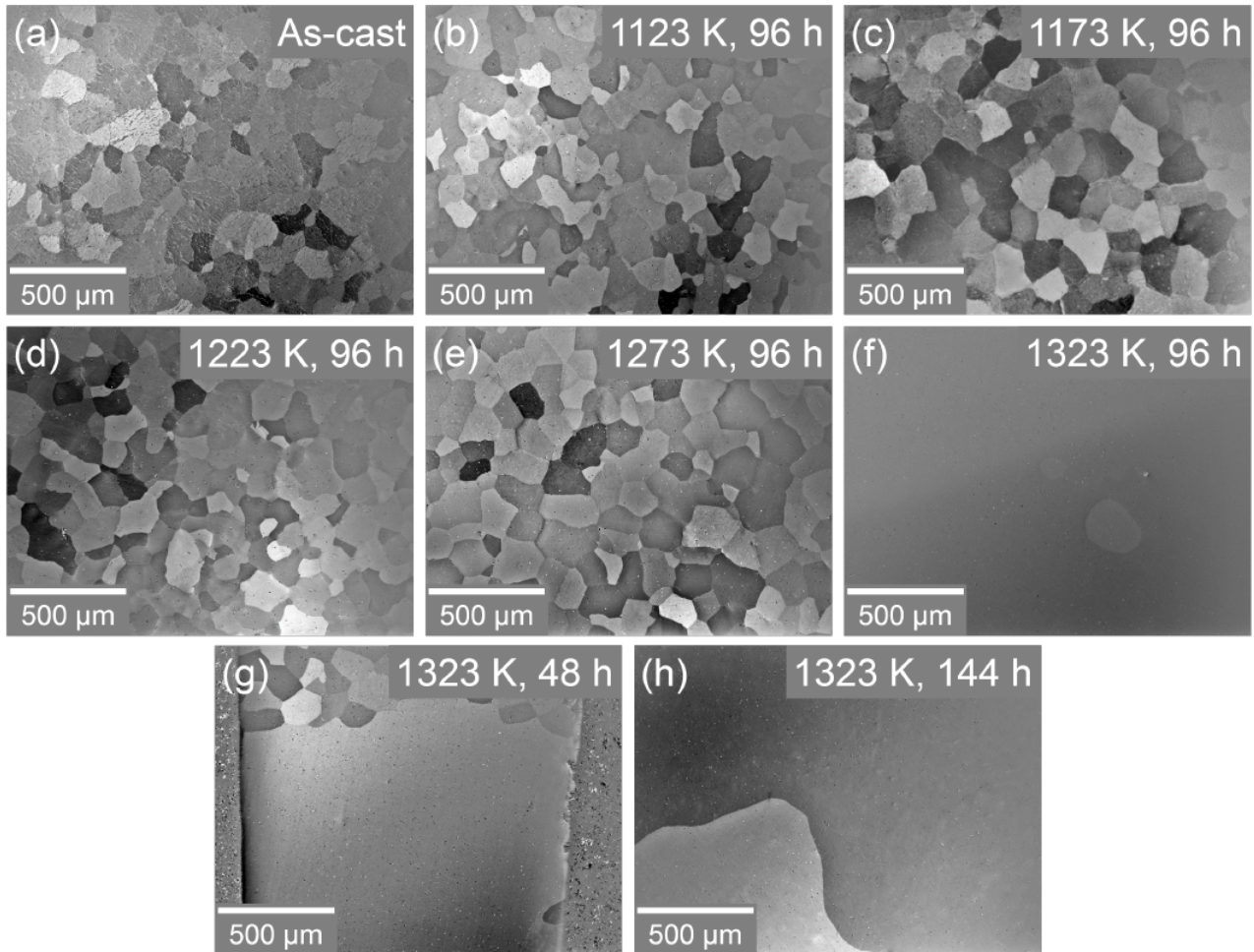


Figure 5.5: Optical microscopy images using polarized light for the as-cast state of $\text{Ni}_{37}\text{Co}_{13}\text{Mn}_{34}\text{Ti}_{16}$ in comparison to different annealing temperatures and times for the very same parent sample. The sample preparation and heat treatment study has been carried out by Benedikt Beckmann (TU Darmstadt) within the framework of his Master Thesis [213].

transitions.

In order to investigate the difference between the phase transitions resulting from different annealing conditions on a microstructural basis in more detail, temperature-dependent microscopy is used and shown in Fig. 5.6 to compare the martensitic phase transition for a non-ideal (1173 K) and an optimized (1323 K) annealing temperature of the same parent as-cast sample ($\text{Ni}_{37}\text{Co}_{13}\text{Mn}_{34}\text{Ti}_{16}$, see Fig. 5.4 (a)). Both heat treatments lead to fully austenitic samples at room temperature. Upon cooling of the sample that has been homogenized at 1173 K (Fig. 5.6 (a)-(d)), the first martensitic structures appear at a temperature of 285 K. This is in agreement with the magnetization curve showing a first drop of the sample magnetization at the martensitic start temperature of 280 K (see Fig. 5.1 (a)). These structures appear at grain boundaries of the austenitic grains and the variants grow along the direction of these grain boundaries. Upon further cooling, new martensite needles nucleate in parallel to the already present martensite structures as well as on new, previously untransformed, positions on other grain boundaries. At a temperature of 250 K, most of the material in the vicinity of grain boundaries is already transformed to martensite, whereas the center of the grains is still in completely austenitic state (see Fig. 5.6 (b)). At 180 K, a larger amount of completely martensitic grains is visible and the overall phase fraction of martensite is growing. At the lowest temperature of 140 K, most of the sample is in martensite state, only one grain still has residual austenite present in the center. The final structure of the martensite variants resembles the way how the phase is growing upon cooling: small martensite needles represent the former grain boundaries of the austenite phase. From these needles along the grain boundaries, martensite formation happens step-wise in parallel to the present structures towards the inside of the grain. An analysis by EDS indicates that the reason for this broad phase transition is a broad distribution of the stoichiometry within the sample.

The composition along two different EDX linescans starting at grain boundaries towards a grain center is converted into a transition temperature by using the universal phase diagram of Fig. 5.3 (a) and compared to the local transition temperature found from temperature-dependent microscopy at the respective points of the very same grain (see Fig. 5.7 (a) and (b)). The grain boundary is here set as the starting point of the linescan at zero distance. Even though the internal uncertainty of the EDS measurement combined with the high sensitivity of T_t towards stoichiometric changes prevents a perfect consistency, the trend is matching very well with the optically observed transition temperatures for a rather flat stoichiometric change shown in (a) as well as for a steeper change towards the center of the grain in (b). Consequently, the microstructure is still separated in Ti-rich regions and Mn-rich regions after an insufficient heat treatment. There is no sharp phase boundary identified, but a compositional gradient between the maximum and minimum of each stoichiometric variation from the grain boundaries towards the grain center. This compositional difference is less pronounced compared to the as-cast state in Fig. 5.4 (a) indicating a progress in the homogenization process which is not completed for this non-ideal heat treatment. In addition, the grain boundary region represent areas of highest mechanical stresses and defect density, which act as preferred nucleation sites and favor the formation of first martensite structures at grain boundaries. These observations lead to the conclusion that the annealing at 1173 K is not sufficient to homogenize the sample properly. As a result, the phase transition from austenite to martensite and vice versa happens over a broad temperature region

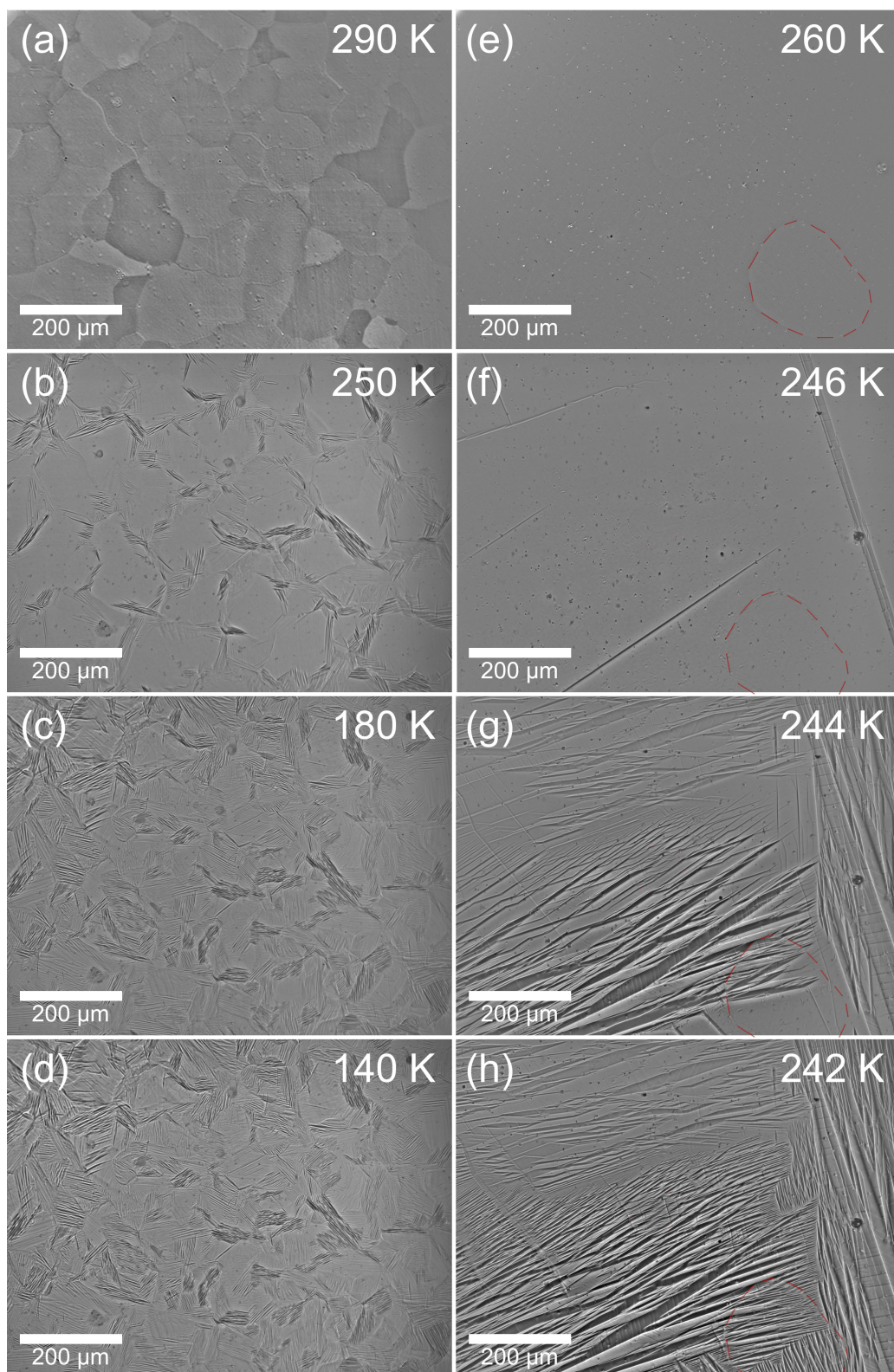


Figure 5.6: Temperature-dependent microstructures of $\text{Ni}_{37}\text{Co}_{13}\text{Mn}_{34}\text{Ti}_{16}$ imaged by optical microscopy using polarized light for different heat treatments: the non-ideal sample annealed at 1173 K is shown in (a)-(d) and the optimized sample annealed at 1323 K in (e)-(h).

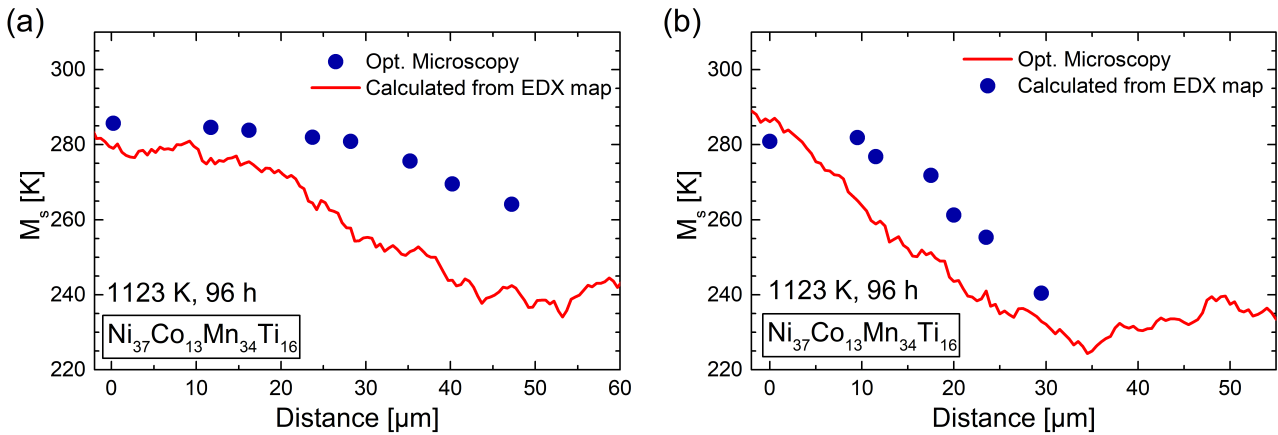


Figure 5.7: Calculated evolution of M_s (red) by converting the e/a ratio of local stoichiometries from EDS into a transition temperature with the help of the phase diagram in Fig. 5.3 along a linescan from a grain boundary (zero distance) towards the center of the grain. The observed transition temperatures (blue points) have been determined optically by noting the temperature where martensite needles appear upon cooling by polarized light microscopy for the same grain. This analysis has been performed by Benedikt Beckmann within the framework of his Master Thesis [213].

because the transition temperature is strongly depending on the exact stoichiometry and therefore varies locally.

In a second step, the martensite formation upon cooling is investigated for the ideal heat treatment at 1323 K for another piece of the same parent as-cast sample (Fig. 5.6 (e)-(h)). At room temperature, the sample is also completely in the austenite state, but the grain structure is different as already discussed for Fig. 5.5. It shows only a small grain in the regarded area, the remaining surface consists of one large grain. The austenite is stable down to a temperature of 246 K, where the first martensite variants appear (Fig. 5.6 (f)). These martensite variants are slightly growing upon further cooling and additional martensite nucleations appear at 245 K. Subsequently the phase fraction of martensite is growing rapidly and within a temperature range of 4 K (Fig. 5.6 (g) and (h)), the whole area is transformed to the martensite phase at 242 K. This investigation is in perfect agreement with the magnetization curve, where the sharp start temperature of the martensite formation is determined at 243 K (in a magnetic field of 1 T). At 238 K (represented by Fig. 5.6 (h)), the martensite phase fraction determined from the magnetization of the sample is around 90%. In the final martensite state, large regions of straightly parallel grown variants exist in the left part of the image, where no grain boundaries are present. In contrast, the growth of the variants is slightly hindered at the grain boundary of the small grain visible in the bottom right part of the image. As a result of the tilted grain orientation, also the growing direction of the martensite is affected. A direct comparison of the martensite at low temperatures for the two different heat treatments in Fig. 5.6 (d) and (h) reveals obvious differences. The martensite nucleations for the non-ideal heat treatment start at grain boundaries and form very narrow structures upon further nucleation and growing. Contrary, the ideal annealing leads to a very sharp phase transition resulting in larger martensitic structures because the

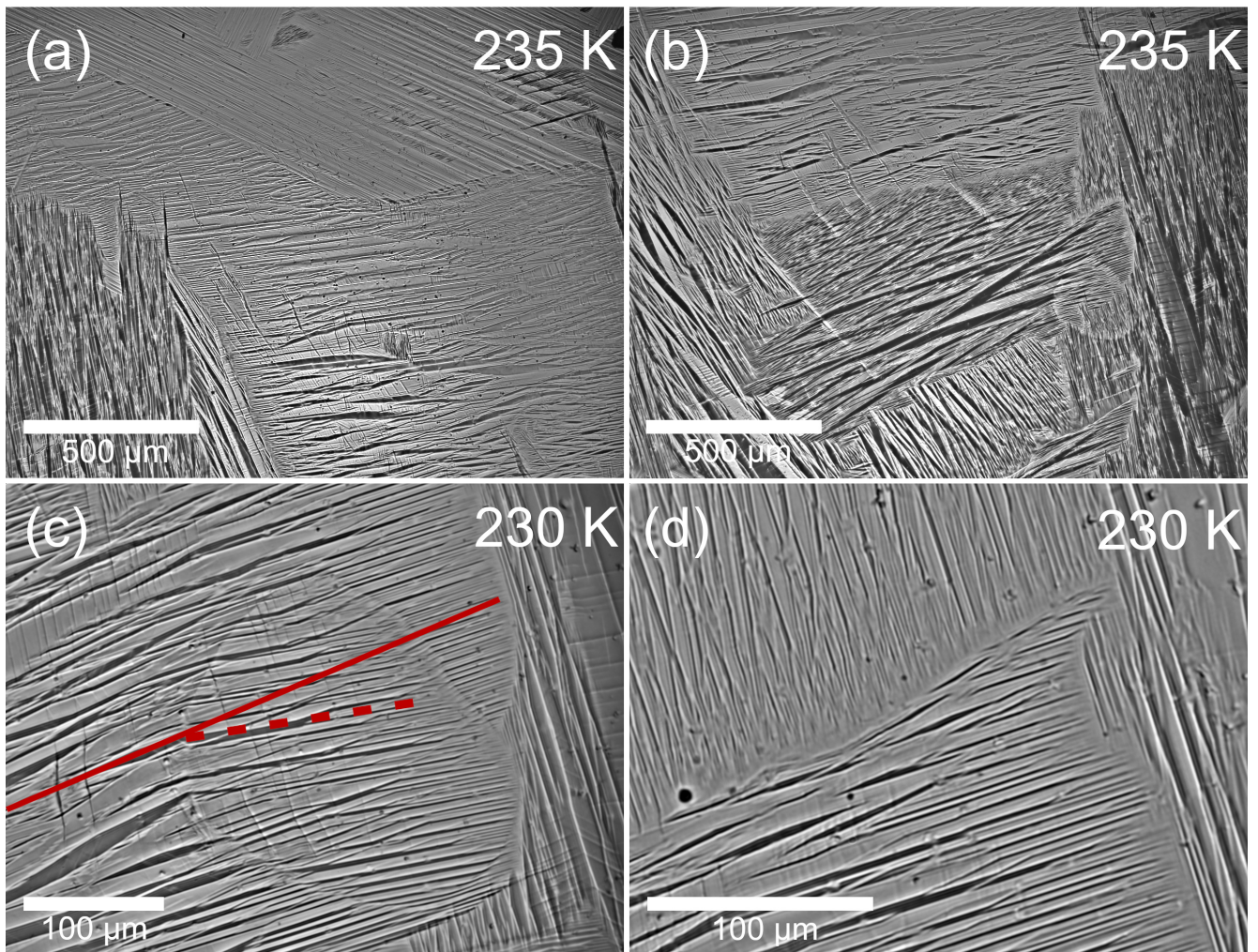


Figure 5.8: Martensitic structures of $\text{Ni}_{37}\text{Co}_{13}\text{Mn}_{34}\text{Ti}_{16}$ at 235 K with 5x magnification (a)+(b) and at 230 K with 20x (c) and 32x (d) magnification imaged by optical microscopy using polarized light.

growth is rarely stopped or hindered due to the huge grain size.

This unique evolution of the microstructure forming abnormally large grains that result in much larger martensitic structures for the ideally annealed sample is investigated in more detail. Figure 5.8 (a) and (b) depict two different surface positions for a lower magnification, where (b) shows the spot of the temperature-dependent observations of Fig. 5.6 (e)-(h). The images demonstrate that the areas with one martensite variant orientation are large, reaching dimensions of $500\ \mu\text{m}$ up to more than 1 mm. This is comparable to the behavior of large grain structures in Ni-Co-Mn-In [125]. The angle between the growing directions of the needles is mostly around 90° . This is attributed to the cubic austenite phase, which gives three equivalent, orthogonally arranged, possibilities for a tetragonal [206] or orthorhombic [210, 218] distortion upon the martensite formation [52]. However, these angles change for modulated structures that can be

coexisting with tetragonal martensite depending on the stoichiometry [167, 205], but the deviations are rather small. The small grain highlighted in Fig. 5.6 (e)-(h) is also visible here in Fig. 5.8 (b) showing much finer martensitic structures than the surrounding large grain area. To have a closer look on this special area of the sample surface, a higher magnification image in Fig. 5.8 (c) shows that the growth of the martensite phase is happening from left to right in this image detail (as observed upon cooling down to the imaged state) and is not stopped at the grain boundary but deflected slightly (indicated by red lines). After propagation through the grain, the direction is changed again and the orientation of the martensite needles is adapted again to the large surrounding grain. This is an indication for a certain deviation of both lattice orientations forming a low-angle grain boundary. The angle between the solid and dashed red line is determined to be 14° . Moreover, the large martensitic structures nucleating from the large grain (left part of image) become finer when propagating through the smaller grain from left to right. Whereas largest structures outside the grain have a needle width of $10\ \mu\text{m}$ to $15\ \mu\text{m}$, the fine structures within the grain are in the order of $1\ \mu\text{m}$ to $5\ \mu\text{m}$. This gives evidence that the finer martensite structures of the non-ideally annealed sample (Fig. 5.6 (a)-(d)) are not only due to the broad phase transition stopping the growth locally but also result from the smaller grain sizes. This means that the martensite formation is confined within a small area, which leads to a reduction of the needle width [53]. This is conform with the very small martensitic structures found in Heusler alloy thin film that confine the martensite nucleation and growth within the very small film thickness [219]. This behavior has been investigated by modelling the martensite formation in low-carbon steel, where a reduced austenite grain size results in more narrow needle width and less variants per parent austenite grain [220]. Also transition kinetics are expected to be favored because of the higher grain boundary density and the increased number of nucleation sites [221]. This effect cannot be observed for the present Ni-Co-Mn-Ti Heusler alloy study, since the effect of grain size on the martensitic growth is overlaid by the significant difference in transition width due to the different chemical homogeneity.

The even higher magnification in Fig. 5.8 (d) depicts a similar effect of martensite structures becoming finer when growing towards the intermartensitic quasi-boundary between two growing directions of different variants. The two structures separated by an angle of roughly 90° possess very fine structures in the order of $1\ \mu\text{m}$ and even going below the resolution limit of the image, which is $0.2\ \mu\text{m}$ per pixel. Due to the lattice incoherency of martensite and austenite crystal structures it is believed that very small areas at these inter-martensitic interfaces, where two growing variants meet, cannot be filled with martensite structures (due to geometrical reasons) and remain austenitic [50]. The needles that grow further away from the intersection of variants have dimensions around $5\ \mu\text{m}$ to $10\ \mu\text{m}$. This observation again confirms the tendency of smaller martensitic structures for reduced grain sizes since growing martensite variants tend to form finer structures when being confined in the vicinity of grain- or variant-boundaries [53].

A cycling of the sample in minor loops of hysteresis shows that remaining martensitic features can act as nucleation sites for further growth of the low-temperature phase. Therefore, the martensite formation after starting from a non-complete austenite formation is leading to larger amounts of martensite at the same temperature compared to cooling from a full austenite state. The thermal hysteresis of the phase-transition

cycle is a consequence of the energy barrier for nucleation processes, which is lowered in minor loops due to already present nucleation sites. The forming martensite variants in minor loops also show the same appearance like the initial low-temperature state after nucleating at residual martensite structures, which guide the growth of the variants. This behavior is in agreement with observations from microscopy studies of minor loops for the Ni-Co-Mn-In system [125].

For the In-system, it is reported in addition that the martensite structures look very different for each cooling from a completed hysteresis loop starting in the 100 % austenite state [125]. This observation will be checked for the Ni-Co-Mn-Ti sample of this work by comparing the full martensitic state after several thermal cycles at 235 K well below the phase-transition temperature in Fig. 5.9. Differences occur between the martensite state resulting from the first and fourth cooling procedure (Fig. 5.9 (a) and (c)). Especially the region in the top left corner changes from rather vertically oriented needles towards higher amounts of horizontally grown structures. Nonetheless, the majority of the two images show very similar martensitic structures. Particularly the wide vertically growing variant as well as the first horizontal needle above the small grain, which have also been identified in Fig. 5.6 (f) as the first growing structures, are dominating the appearance of the overall variant formation.

In Fig. 5.9 (b), the sample surface is shown in the pure austenite state at 300 K with an applied subtraction of opposing light polarizations as well as a drastically enlarged contrast. Despite the complete austenite state with a regular homogeneous surface structure, the adjusted image setting shows that still a slight residual contrast of the martensite structures is observable. Most explicit are the horizontal needles in the bottom left part of the image, which are attributed to the first growing martensite structures for all cooling experiments. They appear in this orientation at this position for all microscopy experiments with this sample. The observed contrast of Fig. 5.9 (b) can be transferred to the martensite state of the subsequent cooling shown in Fig. 5.9 (c) with good agreement. This effect can be related to residual tensions in the surface generated by the surface deformation of the formed twin boundaries that are responsible for the surface contrast of the martensite images. These small stresses can then act as preferred nucleation sites and growing directions that guide the formation of the temperature-induced martensite structure upon cooling. Consequently, the overall appearance of martensitic structures is maintained over several heating and cooling cycles, even for completed transitions, which is a considerable difference to the behavior of Ni-Co-Mn-In [125].

In an additional step, a magnetic field of 1.1 T is applied in order to investigate whether it has an influence on preferred variant growth like it has been reported for example for Ni-Mn-Ga [138, 222, 223]. The resulting microstructure after cooling the sample down in a magnetic field of 1.1 T aligned vertically in the surface plane is depicted in Fig. 5.9 (d). The direct comparison with the microstructure from the previous zero-field cooling in (c) shows that the martensite orientation changed to an exclusive horizontal growing direction of the long axis in the top left part. In contrast, the bottom right image detail features an increasing amount of vertically aligned needle structures that propagate halfway into the small grain. Due to these two contrary observations and the fact that changes in the martensitic microstructure are found for each cooling cycle, no profound conclusion can be drawn here. The subsequent cooling cycle without

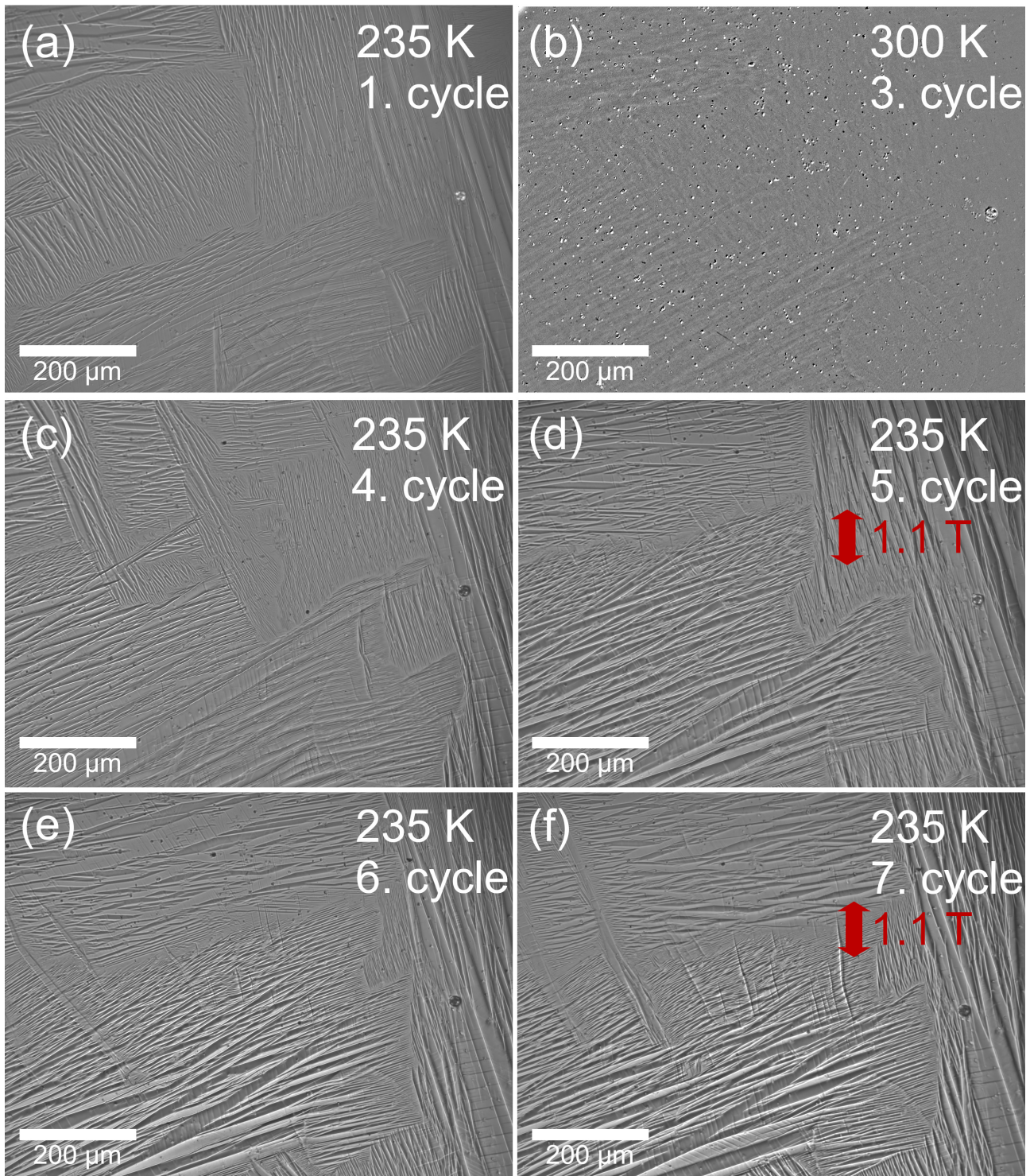


Figure 5.9: Resulting microstructure of $\text{Ni}_{37}\text{Co}_{13}\text{Mn}_{34}\text{Ti}_{16}$ after first (a), fourth (c), and sixth (e) cooling without external magnetic field by optical microscopy using polarized light. The austenite state after third heating is shown in (b) with an applied subtraction of opposing light polarizations as well as a drastically enlarged contrast. The martensite state after fifth and seventh cooling in an external field of 1.1 T is shown in (d) and (e). The direction of the magnetic field lies in the surface plan and is indicated by the red arrow.

an external field in Fig. 5.9 (e) again shows many similarities to the state created by the field-cooling. However, two larger vertical variants are emerging in the middle left region. A repeated comparison with the subsequent cooling in an external magnetic field of 1.1 T in Fig. 5.9 (f) shows an increased appearance of the vertically aligned martensite structures that are appearing to be isolated from each other and overlay the before observed microstructure in this area. This observation can be caused by a growing variant into the depth of the sample, which is then overlaid with the adjacent microstructure that is observed on the image plane of the surface.

As a conclusion, there are tendencies of newly formed martensite variants with the long axis along the field direction, but this effect is too sporadic to be considered as a proof for a field-induced reorientation of the martensitic variants. Since the martensite is in a weak magnetic state, the influence of an external magnetic field on the orientation is thus expected to be very small. This is different than for the ferromagnetic martensite of Ni-Mn-Ga, where significant martensite reorientation can be induced by magnetic-field changes [138, 222, 223]. An isothermal experiment inducing the martensitic microstructure by a magnetic-field removal from 1.1 T to 0.1 T does not contribute new evidence. Nonetheless, this experiment can show that a considerable amount of martensite can be induced by the field change of 1 T, when starting in a mixed state close to the M_s temperature.

An examination of the detailed kinetics of the martensite formation is carried out by removing the magnetic field stepwise with the implementation of a waiting time between the field steps. The freeze frames for the step of reducing the external magnetic field from 0.5 T to 0.3 T as well as for different times after the field removal step are shown in Fig. 5.10. The direct comparison between images (a) and (b) shows that directly at the moment of reaching a field of 0.3 T, only individual variants grow in horizontal direction from left to right in the center of the image as well as in the bottom left area. Already after the first two seconds of the stable magnetic field state, a large portion of martensitic phase is induced and growing predominantly in the central left part of the images in Fig. 5.10 (c) and (d). The comparison with the state after 5 s and 10 s in (e) and (f) demonstrates that even on this time scale martensitic phase is still formed even though the driving force has not been changed for the past 10 s. This can be an indication for a certain time-dependency of the martensitic growth reaction as a response to an external stimulus inducing the phase change. Especially in the regard of magnetocaloric cycles, the field application rate plays an important role for an efficient device operation. It must be emphasized that the behavior observed here does not necessarily be caused by a time delay of the field-induced martensitic transition. Even though the contact to the sample stage justifies the assumption of isothermal conditions, it must be considered that the temperature is changed locally due to the temperature change of the phase transition. In addition, local stresses are induced that also result in a local variation of the transition temperature. It is possible that material transforms into martensite creating locally increased temperatures and stress fields, which both hinder a further transformation of all the sample that would transform from the field removal step. Due to thermal exchange and stress release processes, these conditions are changed and it takes a certain time until all material reaches its equilibrium state for the steady magnetic field condition.

This investigation shows that a proper homogenization of the sample stoichiometry by an optimized

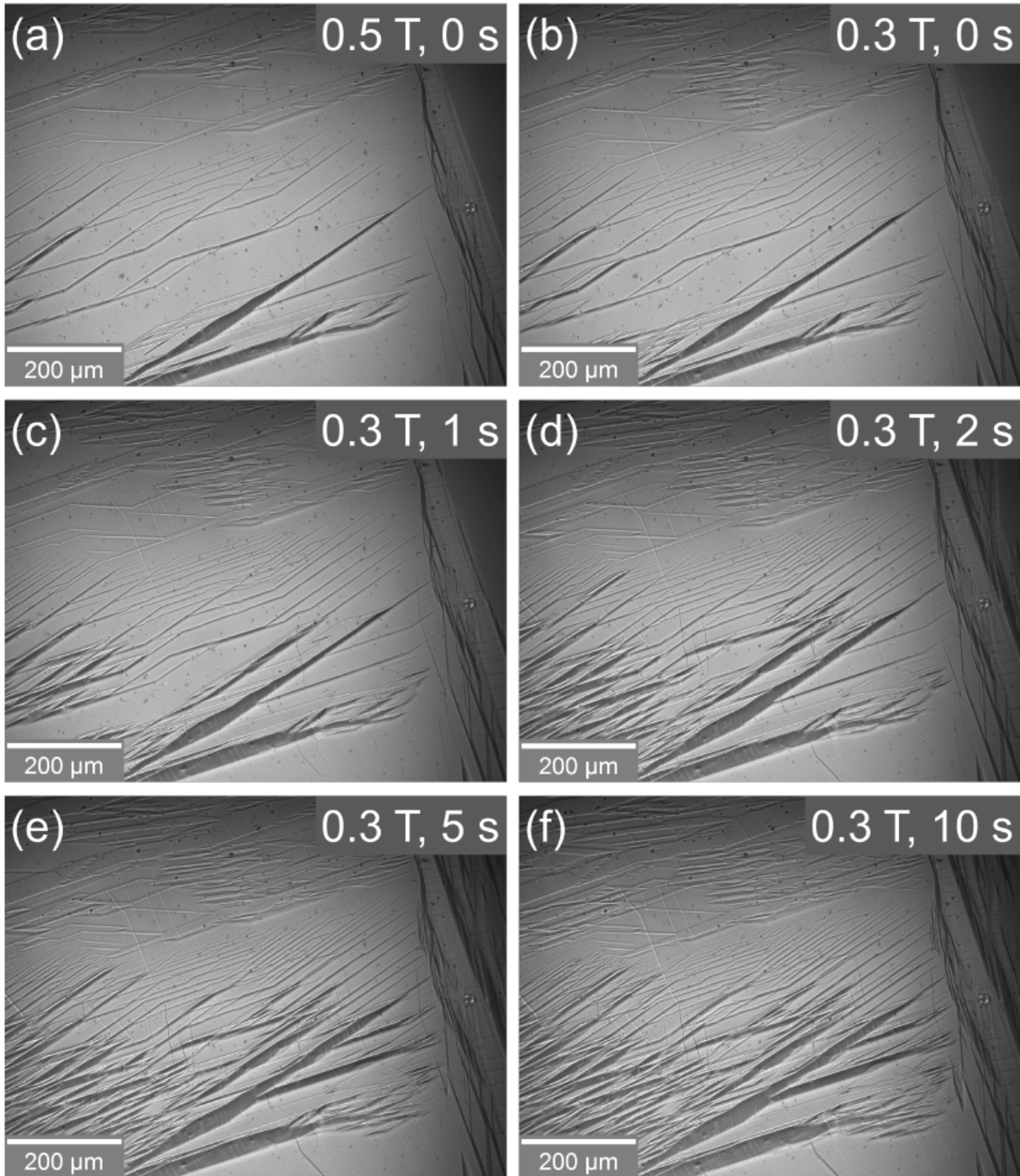


Figure 5.10: Martensite formation of $\text{Ni}_{37}\text{Co}_{13}\text{Mn}_{34}\text{Ti}_{16}$ by optical microscopy image using polarized light for an external magnetic-field removal from 0.5 T (a) to 0.3 T (b) and for a subsequent steady field of 0.3 T after waiting times of 1 s to 10 s (c)-(d).

heat treatment is essential for a sharp magnetostructural phase transition in Ni-Co-Mn-Ti Heusler alloys. As a result of an increased annealing temperature, the grain structure can tend to form very large grains because of the provided thermal energy. Such a grain growth can then lead to grains that are in the range of those in other Ni-Mn-X Heusler alloys, but in contrast to the smaller grain size that has been found typically for the samples of the Ni-Co-Mn-Ti Heusler system in the present study (see Fig. 5.4 (b)). As a matter of fact, this sample with the untypical grain structure shows an exceptionally sharp phase transition (see red curve in Fig. 5.2(a)), which can be a result of the reduced amount of grain boundaries that can act as a barrier for the growth of the martensitic phase.

5.4 Magnetocaloric properties in low magnetic fields

In order to assess the potential of the magnetocaloric Ni-Co-Mn-Ti compounds for cooling applications, the isothermal entropy change Δs_T as well as the adiabatic temperature change ΔT_{ad} are evaluated. The isothermal entropy change as a measure for the heat that can be transferred from a magnetocaloric material is determined for magnetic-field changes of 2 T and shown in Fig. 5.11 (a) (compare respective $M(T)$ -curves in Fig. 5.2 (a)). Due to the exceptionally sharp phase transition, $\text{Ni}_{37}\text{Co}_{13}\text{Mn}_{34}\text{Ti}_{16}$ provides the largest Δs_T for this series. It has been determined from isofield $M(T)$ measurements to avoid overestimation [171] and amounts to $38 \text{ J kg}^{-1} \text{ K}^{-1}$ in a magnetic-field change of 2 T at a transition temperature of around 250 K. This is a giant value for a bulk Heusler alloy at this field change, which is significantly larger compared to the magnetocaloric Δs_T determined from magnetization measurements for the all-*d*-metal Heusler alloys in literature [167, 205, 206]. The $\text{Ni}_{37}\text{Co}_{13}\text{Mn}_{34.5}\text{Ti}_{15.5}$ compound with a transition around room temperature shows a Δs_T of around $30 \text{ J kg}^{-1} \text{ K}^{-1}$. Despite the broader phase transition, the $\text{Ni}_{35}\text{Co}_{15}\text{Mn}_{37}\text{Ti}_{13}$ sample still shows a large Δs_T of around $20 \text{ J kg}^{-1} \text{ K}^{-1}$, which is comparable to the one of $\text{Ni}_{37}\text{Co}_{13}\text{Mn}_{35}\text{Ti}_{15}$ with a similar transition temperature.

The shape of the curves with the sharp peak indicates that the maximum possible Δs_T is not reached in 2 T and larger fields would be necessary to obtain the plateau of the saturated Δs_T . Other works show that this saturation is not even observed for field changes of 5 T [167]. Considering the magnetization change ΔM of $75 \text{ A m}^2 \text{ kg}^{-1}$ and a shift of the transition $\frac{\Delta T_t}{\mu_0 \Delta H}$ of -1.6 K T^{-1} , a rough estimation of the maximum possible isothermal entropy change by the Clausius-Clapeyron approximation by Equation (5.1) would give a Δs_T of $47 \text{ J kg}^{-1} \text{ K}^{-1}$.

$$\Delta s_T = -\frac{\Delta M}{\frac{dT_t}{\mu_0 dH}} = -\frac{75 \text{ A m}^2 \text{ kg}^{-1}}{-1.6 \text{ K T}^{-1}} = 46.9 \text{ J kg}^{-1} \text{ K}^{-1} \quad (5.1)$$

In Ni-Mn-In alloys, depending on the transition temperature, a complete transition can be reached in 2 T for some compounds because of the large sensitivity of the transition temperature towards applied magnetic fields [67, 142]. For the Ni-Co-Mn-Ti alloys, $\frac{dT_t}{\mu_0 dH}$ is significantly smaller leading in combination with a very sharp transition to the observed large entropy changes but to much higher saturation fields.

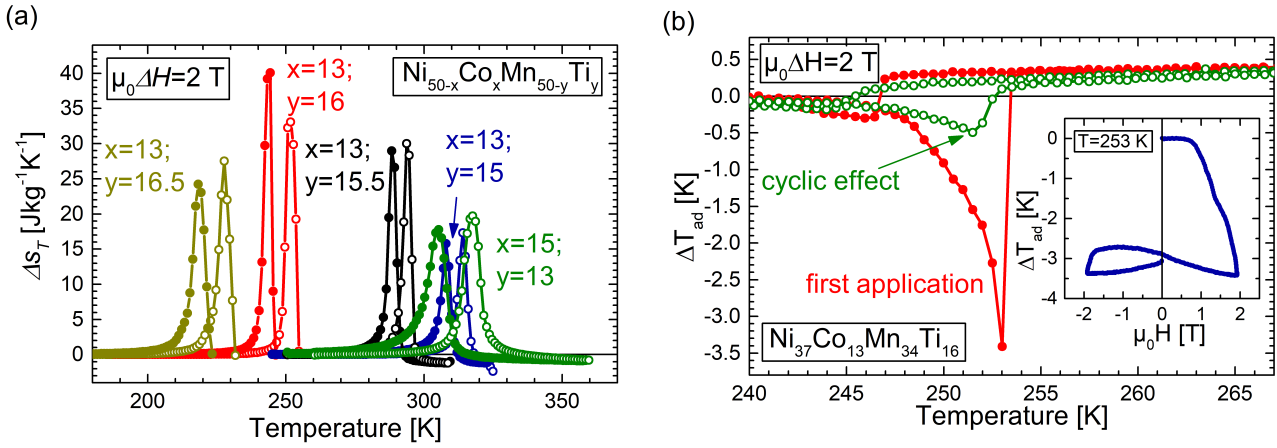


Figure 5.11: Δs_T curves of $\text{Ni}_{50-x}\text{Co}_x\text{Mn}_{50-y}\text{Ti}_y$ for the series with $x = 13$ and one sample with $x = 15$ determined from temperature-dependent magnetization measurements (isofield protocol) upon heating (open symbols) and cooling (full symbols) for magnetic-field changes of 2 T (a). Directly measured adiabatic temperature change for $\text{Ni}_{37}\text{Co}_{13}\text{Mn}_{34}\text{Ti}_{16}$ in continuous mode for the first field application (red full symbols) and for the reversible effect upon the second magnetic-field cycle (green open symbols) for field changes of 1.93 T is shown in (b). The magnetic-field-dependent ΔT_{ad} at the starting temperature T_s of 253 K for the first two magnetic-field cycles is depicted in the inset.

From this estimation of the maximum Δs_T , the saturation value of ΔT_{ad} can be calculated by using Equation (2.9). The transition temperature is taken at room temperature 293 K and the heat capacity is approximated to be $500 \text{ J kg}^{-1} \text{ K}^{-1}$, which is a typical value for Ni-Mn-based Heusler alloys [144, 199]. In Section 5.5 the assumption of c_p is validated to be close to real values for a Ni-Co-Mn-Ti alloy.

$$\Delta T_{ad} = -46.9 \text{ J kg}^{-1} \text{ K}^{-1} \frac{293 \text{ K}}{500 \text{ J kg}^{-1} \text{ K}^{-1}} = -27.5 \text{ K} \quad (5.2)$$

The adiabatic temperature change for the $\text{Ni}_{37}\text{Co}_{13}\text{Mn}_{34}\text{Ti}_{16}$ sample with the largest Δs_T is shown in Fig. 5.11 (b). The maximum ΔT_{ad} of -3.5 K for the first field application can be obtained at a temperature of 253 K. In agreement with the observations for Δs_T , the evolution of ΔT_{ad} over the applied magnetic-field strength shown in the inset indicates that the transition cannot be induced completely in external magnetic fields below 2 T. At the largest field value, the temperature is still decreasing with considerable slope, which stops immediately when the field is being removed again. Due to the reduced $\frac{dT_t}{\mu_0 dH}$ compared to other Ni-(Co)-Mn-X systems [125, 142], a field change of 2 T cannot shift the transition temperature properly to fully induce the austenite state, even though the phase transition is exceptionally sharp. Moreover, the decreasing sample temperature due to the negative adiabatic temperature change of the inverse magnetocaloric effect works against the austenite formation of the field-induced phase transition. Therefore, the temperature shift per field unit multiplied by the applied magnetic field ($\frac{dT_t}{\mu_0 dH} \cdot \Delta H$) must be equal or larger than the sum of the transition width and the adiabatic temperature change for the corresponding field change at a certain starting temperature. If this is fulfilled, the phase transition can

be completely induce by a magnetic field and the maximum magnetocaloric effect can be exploited. The relation between ΔT_{ad} and Δs_T by Equation (2.9) can give an estimate of the expected maximum ΔT_{ad} from the approximated Δs_T^{max} .

The response of the material to the field removal as well as to the second field-application step depicts the low cyclic MCE of this compound. As a magnetic field of 2 T shifts the transition temperature around 3 K to lower temperatures, the thermal hysteresis of around 10 K cannot be overcome. Nevertheless, a certain temperature change of around 0.5 K is present for the second field cycle (green open symbols in Fig. 5.11 (b) and negative fields in the inset), which is due to the lowered energetic barrier that results from the not completed first transition cycle leading to minor loops of thermal hysteresis [125].

5.5 Magnetocaloric properties in high magnetic fields

For the construction of the temperature- and field-dependent total entropy curve, the heat capacity of $\text{Ni}_{37}\text{Co}_{13}\text{Mn}_{34.5}\text{Ti}_{15.5}$ was measured for different external magnetic fields. The resulting c_p in zero field measured upon heating from 2 K is shown in Fig. 5.12 (a). For low temperatures, the heat capacity approaches zero because the thermal lattice vibrations are decreasing drastically and the ability of the compound to absorb heat increases largely. The evolution of c_p for low temperatures follows the Debye model for solids with an exponential increase proportional to T^3 [224], as shown in Fig. 5.12 (b). This is followed by a flattening at higher temperatures towards a saturation value, which is according to the model happening well above the Debye temperature Θ_D [225]. This saturation behavior of c_p is described by the Dulong-Petit law to be universal for solids at a value of three times the gas constant R , which amounts to $c_p = 3R = 24.9 \text{ J mol}^{-1} \text{ K}^{-1}$ [226]. A conversion of the determined c_p for $\text{Ni}_{37}\text{Co}_{13}\text{Mn}_{34.5}\text{Ti}_{15.5}$ with an average molar mass of 54.4 g mol^{-1} gives an experimental value of $27.2 \text{ J mol}^{-1} \text{ K}^{-1}$, which fits well to the Dulong-Petit law. The evolution of c_p as a function of temperature is according to the Debye model for low temperatures ($T \ll \Theta_D$) described by Equation (5.3).

$$c_p \approx \gamma \cdot T + \frac{12\pi^4 \cdot R}{5\Theta_D^3} \cdot T^3 \quad (5.3)$$

The first term corresponds to the electronic part of the heat capacity, which is proportional to T in the low-temperature region, whereas the second term describes the phonon contributions. Plotting c_p/T versus T^2 in Fig. 5.12 (b) thus yields a linear approximation with the graphically determined intercept for the electronic coefficient $\gamma = 2.4 \times 10^{-3} \text{ J mol}^{-1} \text{ K}^{-2}$ and a slope of $m = 4.74 \times 10^{-5} \text{ J mol}^{-1} \text{ K}^{-4}$, which is used to estimate Θ_D as 350.4 K (Equation (5.4)). For a Ni-Mn-Sn Heusler alloy, Θ_D has been determined as 310 K [227], which is in good agreement (even though it is slightly lower) with the present measurement of c_p for $\text{Ni}_{37}\text{Co}_{13}\text{Mn}_{34.5}\text{Ti}_{15.5}$.

$$\Theta_D \approx \sqrt[3]{\frac{12\pi^4 \cdot R}{5 \cdot 4.51 \cdot 10^{-5} \text{ J mol}^{-1} \text{ K}^{-4}}} = 350.4 \text{ K} \quad (5.4)$$

At 293 K, the first-order phase transition is documented by the sharp increase of c_p . The infinite discontinuity of the signal is reduced to a finite maximum value of $5700 \text{ J kg}^{-1} \text{ K}^{-1}$ (see inset of (a)) due to the finite resolution of the measurement and, most importantly, the finite width of the non-ideal phase transition. The heat capacity is around $500 \text{ J kg}^{-1} \text{ K}^{-1}$ for the martensitic phase before approaching the phase transition and $550 \text{ J kg}^{-1} \text{ K}^{-1}$ for the austenite at temperatures above T_t . The value for the ferromagnetic austenite is higher compared to the martensite because it includes the magnetic contribution to the total heat capacity. The shift of the phase transition with the application of external magnetic fields is shown by plotting the temperature-dependent $\frac{c_p}{T}$ in the inset for 2 T (blue), 5 T (green) and 10 T (orange). The decreasing maximum of the peak and of the area under the curve is a result of the decreasing entropy change and the increasing contribution of the magnetic subsystem to the phase transition with lowering the transition temperature [67]. This is confirmed by integrating the respective curves over temperature (for all data between 250 and 300 K) for the peak areas by subtracting the baseline as linear connection between the integration boundaries, which results in entropy changes of $43.5 \text{ J kg}^{-1} \text{ K}^{-1}$ (0 T), $41.4 \text{ J kg}^{-1} \text{ K}^{-1}$ (2 T), $40.9 \text{ J kg}^{-1} \text{ K}^{-1}$ (5 T) and $38.7 \text{ J kg}^{-1} \text{ K}^{-1}$ (10 T). A closer look on c_p of the austenite in external magnetic fields (not depicted here), reveals a decrease of c_p for larger external magnetic fields. This effect is a consequence of the increased magnetic ordering of the austenite, which counteracts the thermally induced disorder.

The total entropy in zero magnetic field has been determined by integration of $\frac{c_p}{T}$ according to Equation (3.7) and is shown in Fig. 5.12 (c). The base temperature of 2 K for the integration is being considered as close enough to zero in order to assume the determined entropy to be close to the actual total entropy of the compound on an absolute scale. Therefore, the entropy at this temperature is assumed to be the zero reference S_0 , even though the actual entropy at this temperature is in reality not exactly zero. The total entropy starts to increase at around 30 K and rises continuously until reaching the martensitic transition temperature. The increase is fairly linear from around 200 K to the transition temperature. At T_t , the entropy experiences a finite jump while the sample transforms from the martensitic to the austenitic crystal structure, thus changing the lattice entropy (increase) as well as the magnetic entropy (decrease). In agreement with the c_p and $M(T)$ measurements, T_t is decreasing with larger external magnetic fields applied. The measurements in zero field and in 2 T show no deviation in the entropy at temperatures well below the martensitic transition, thus a temperature of 200 K was chosen as starting point for the measurements in 5 T and 10 T and the total entropy curve has been shifted according to the reference value of the measurement in zero field at this temperature. The total entropy above T_t follows again a continuous increase with temperature for the austenite. Since the austenite is ferromagnetic at these temperatures, the increase is not linear because the reduced ferromagnetism with increasing temperature increases the total entropy compared to an increase resulting purely from the lattice and electronic contributions, like it is the case for the PM martensite. In addition, the entropy is reduced with increasing applied magnetic fields because of the FM ordering of the austenite. At 317 K, the entropy change of the austenite for an external field change from 0 T to 10 T is $6 \text{ J kg}^{-1} \text{ K}^{-1}$. By applying linear approximations to the evolution of the entropy for the purely austenitic and martensitic regions of the $S(T)$ -diagram in Fig. 5.12 (d),

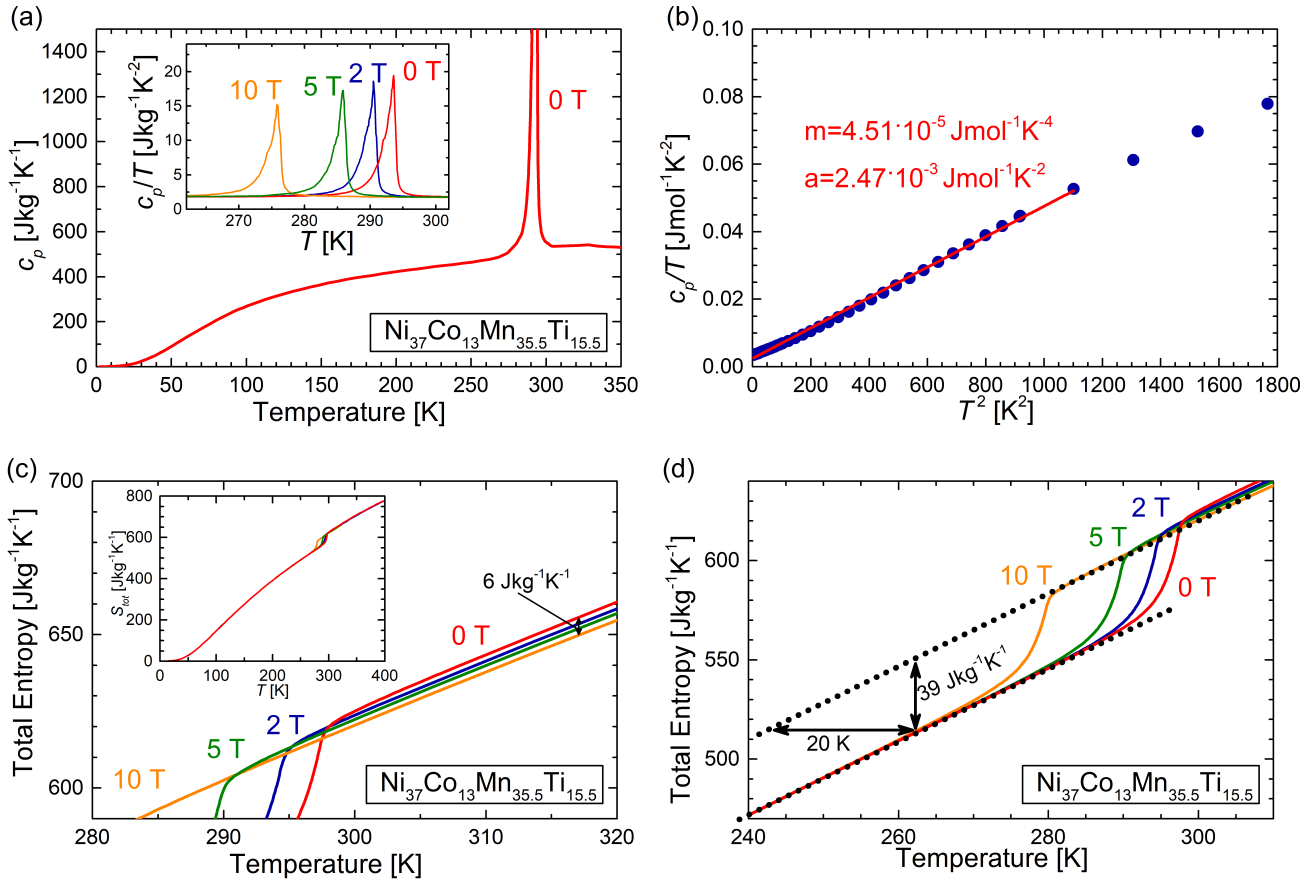


Figure 5.12: Heat capacity of $\text{Ni}_{37}\text{Co}_{13}\text{Mn}_{34.5}\text{Ti}_{15.5}$ upon heating in zero external magnetic field (a) as well as c_p/T in fields of 0 T (red), 2 T (blue), 5 T (green) and 10 T (orange) shown around the transition temperature in the inset. The plot of c_p/T over T^2 in (b) shows the agreement with the Debye model at low temperatures. The resulting total entropy curves are shown in the inset of (c) from 2 K to 400 K and in detail in the temperature range above (c) and around the martensitic phase transition (d). The measurements shown in (a) were carried out by Konstantin Skokov (TU Darmstadt).

the maximum values for Δs_T and ΔT_{ad} to be expected for a completely induced phase transition can be estimated as $39 \text{ J kg}^{-1} \text{ K}^{-1}$ and -20 K . These linear lines are fitted manually to the slope of the entropy in the martensite region (below T_t , equal for all fields) and the austenite region (above T_t , for highest field of 10 T). The linear regression is oriented at the entropy curve for the highest applied field in this study because the alignment of FM domains of the austenite decreases its entropy in large magnetic fields. However, these large fields are necessary in order to induce a complete phase transition. Therefore, it is reasonable to estimate the entropy change and temperature change between the two phases for the case of an austenite in large magnetic fields. For the case of a linear approximation of the zero field curve only, higher values would be determined for a completed transition.

For further experimental validation of the maximum magnetocaloric effect, Δs_T is determined from

isothermal magnetization measurements. The $M(H)$ -curves recorded at different temperatures are shown in Fig. 5.13 (a). The field-induced phase transition from the low-magnetization martensite to the high-magnetization austenite is shifted to smaller onset fields with increasing temperature. By using the derivative-method, the magnetic fields corresponding to the inflection points of the magnetization curves have been determined as the central transition field H_t . These values are plotted for each measurement temperature - being equivalent to T_t for the respective magnetic field value - in Fig. 5.13 (b) in order to determine the shift of T_t in externally applied magnetic fields. An overlay of a straight line (dashed red) shows that $\frac{dT_t}{\mu_0 dH}$ can only be approximated with a constant slope for low fields of up to 5 T. For higher fields, the data points deviate from this behavior indicating an increased sensitivity for larger external magnetic fields. It is possible to assume a linear region for low fields of 1 T to 5 T with a slope of -1.6 K T^{-1} . In order to estimate the increase of this value in higher fields a linear average between 6 T to 14 T gives a slope of -2.2 K T^{-1} , even though a linear behavior in this field region has no physical meaning. A more suitable description for the evolution of $\frac{dT_t}{\mu_0 dH}$ can be approximated with an exponential function (blue curve) that fits the data points very well for the range of 1 T to 14 T. The increasing field sensitivity in larger magnetic fields is a result of the increasing ΔM for lowered transition temperatures. This can be expected assuming that it is not relevant whether the transition temperature is lowered because of stoichiometric changes or an applied magnetic field [195]. Consequently, an application of the Clausius-Clapeyron equation has to consider the range of the external magnetic field that is used to induce the full phase transition.

The next step is to estimate the magnetic field that is necessary to induce a complete phase transition. This is possible by using the width of the transition and the evolution of the field sensitivity according to Equation (5.5). Assuming a linear region of $\frac{dT_t}{\mu_0 dH}$ for low magnetic fields leads to a saturation field of 6.4 T for a starting temperature of 296 K.

$$H_{sat}^{isothermal} = \frac{T_{width}}{\left| \frac{dT_t}{\mu_0 dH} \right|} = \frac{10.2 \text{ K}}{1.6 \text{ K T}^{-1}} = 6.4 \text{ T} \quad (5.5)$$

For a more accurate determination, the field-dependent evolution of $\frac{dT_t}{\mu_0 dH}$ has to be considered here, which is visualized on an absolute temperature scale in Fig. 5.13 (c). Based on the actual austenite start temperature in zero field, the criterion for a complete phase transition is that the shifted transition temperature is equal to the difference of $A_s - T_{width}$ (red line). In reality, T_{width} is usually not constant for varying external magnetic fields, which is not considered here for simplicity. The shift of A_s is represented by the exponential approximation (black line) from Fig. 5.13 (b) and the intersection of both curves visualizes H_{sat} as the minimum field required to induce a complete phase transition under isothermal conditions. It is determined to be 5.9 T, which is only slightly lower compared to the assumption of a constant $\frac{dT_t}{\mu_0 dH}$ as determined from low magnetic fields.

By assuming adiabatic conditions, the adiabatic temperature change of the sample during the magnetically induced transition has to be considered in addition. Consequently, the negative adiabatic temperature change lowers the temperature of the sample. This effect leads to higher necessary fields because the absolute temperature difference to A_f is increased, which is visualized by the dotted blue line in Fig. 5.13 (c).

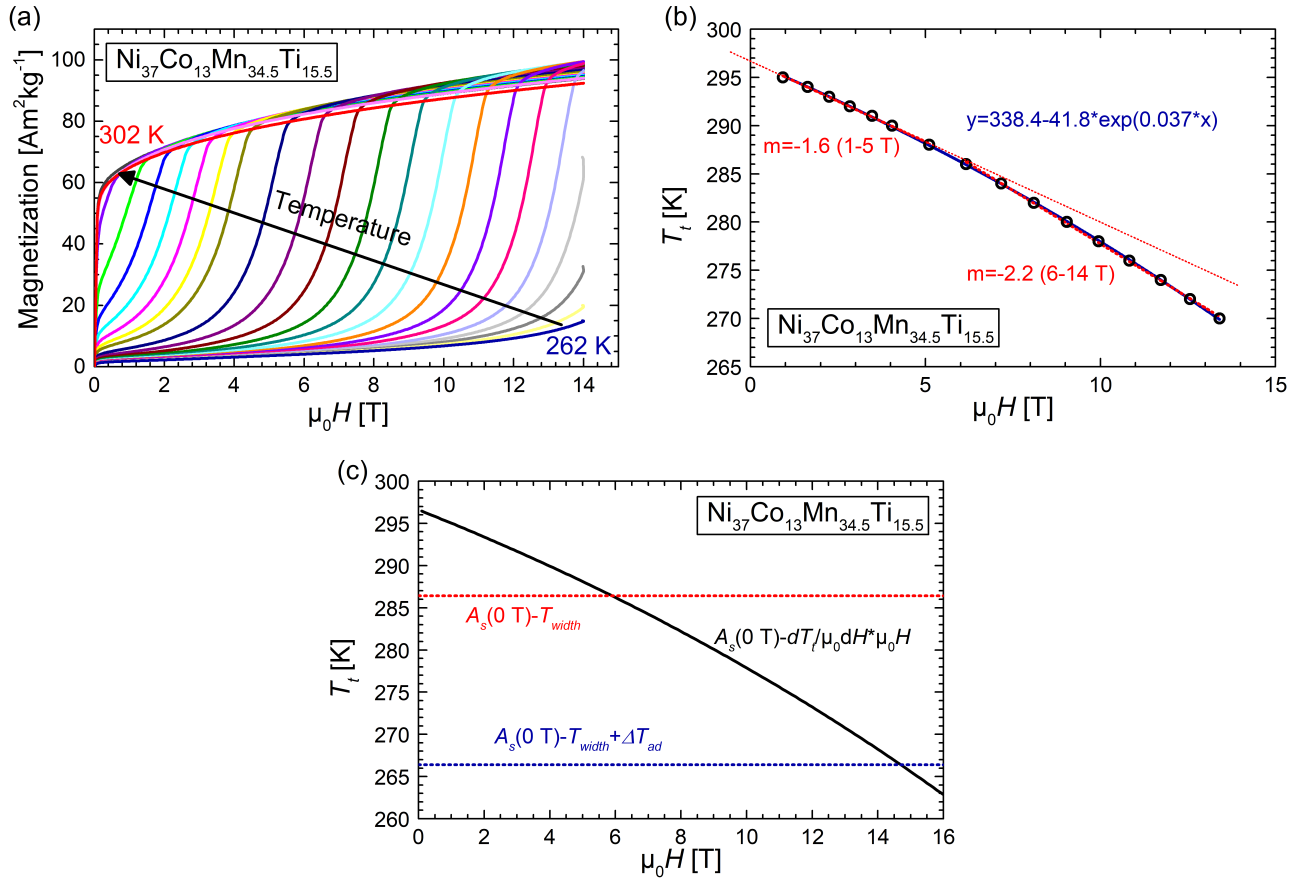


Figure 5.13: Isothermal magnetization measurement at different temperatures in sweeping magnetic fields of up to 14 T for $\text{Ni}_{37}\text{Co}_{13}\text{Mn}_{34.5}\text{Ti}_{15.5}$ (a). The magnetic-field-dependent values of $\frac{dT_t}{\mu_0 dH}$ are plotted in (b) with two separated linear fits (red) for the low field and high field region as well as an exponential fit to the whole field range. The determination of the saturation field under isothermal (red) and adiabatic conditions (blue) is depicted in (c) by considering a maximum ΔT_{ad} of -20 K.

This approach considers the maximum measured ΔT_{ad} in high fields of -20 K (a detailed discussion on these measurements will follow in this chapter as well as in Chapter 5.6), which is added to the difference of $A_s(0\text{ T})$ and T_{width} . This temperature sum has to be overcome in total by the shift of T_t in external magnetic fields. This assumption does not represent the actual evolution of the required shift as a function of H_{ext} and ΔT_{ad} fully accurately. In reality, the application of a magnetic field is a dynamic process and the induced ΔT_{ad} depends on the magnetic field and the absolute temperature of the sample at every incremental field step. By using the maximum ΔT_{ad} for the sake of simplicity, an upper value for H_{sat} can be estimated as the intersection with the field-dependent evolution of $\frac{dT_t}{\mu_0 dH}$ (black curve) because the magnetic field necessary for saturation of ΔT_{ad} must also imply that the saturation value for ΔT_{ad} is actually reached at this point. As a result, the saturation field of the magnetocaloric effect under adiabatic

conditions amounts to 14.7 T.

$$H_{sat}^{adiabatic} = \frac{|T_{width} + \Delta T_{ad}^{max}|}{\left| \frac{dT_t}{\mu_0 dH} \right|} = \frac{10.2 \text{ K} + |20 \text{ K}|}{\left| \frac{dT_t}{\mu_0 dH} (H) \right|} = 14.7 \text{ T} \quad (5.6)$$

This information can now be used to recalculate the estimated maximum Δ_{sT} and ΔT_{ad} from Equations (5.1) and (5.2). For the case of H_{sat} under isothermal conditions, forming the derivative of the fit-function and averaging from 0 T to 5.9 T gives $\frac{dT_t}{\mu_0 dH} = 1.73 \text{ K T}^{-1}$ resulting in $\Delta_{sT} = 43.4 \text{ J kg}^{-1} \text{ K}^{-1}$ and $\Delta T_{ad} = -24.5 \text{ K}$. The same approach for H_{sat} under adiabatic conditions results in an averaged $\frac{dT_t}{\mu_0 dH}$ of 2.1 K T^{-1} and $\Delta_{sT} = 35.7 \text{ J kg}^{-1} \text{ K}^{-1}$ as well as $\Delta T_{ad} = -20.2 \text{ K}$.

These determinations of Δ_{sT} and ΔT_{ad} will now be further explored by comparing them with direct measurements of both properties for the very same sample of $\text{Ni}_{37}\text{Co}_{13}\text{Mn}_{34.5}\text{Ti}_{15.5}$. The direct determination of Δ_{sT} is done by evaluating isothermal $M(H)$ -measurements at various temperatures (already shown in Fig. 5.13 (a)) by using the loop-protocol [171] and by numerical integration according to Equation (3.3). The evolution of Δ_{sT} for the inverse first-order phase transition is shown for magnetic-field changes of 1 T to 10 T in Fig. 5.14 (a). It shows clearly that the large entropy changes of this sample in 2 T as shown in Fig. 5.11 (a) do not represent the maximum entropy changes achievable. The maximum value of $40 \text{ J kg}^{-1} \text{ K}^{-1}$ is first reached for a magnetic-field change of 6 T. This value is slightly lower than the estimated Δ_{s_t} from the Clausius-Clapeyron equation ($43.4 \text{ J kg}^{-1} \text{ K}^{-1}$ for considering an average value of $\frac{dT_t}{\mu_0 dH}$ in the range of 0 T to 5.9 T) with a relative deviation of 8%. The approximation of the saturation field under isothermal conditions of 5.9 T fits very well to the measurement. In higher fields, a plateau of Δ_{sT} is evolving. This plateau is growing towards lower temperatures because the transition can be fully induced also for lower starting temperatures with the total shift of T_t being proportional to the external magnetic-field change. For the largest fields 8 T and 10 T, the Δ_{sT} value for the plateau is slightly lowered for decreasing temperatures. This is due to the increasing magnetization change which raises the negative magnetic contribution to the total entropy change, thus lowering the absolute value of Δ_{sT} for the whole transition according to the so-called dilemma of inverse magnetocaloric materials [67]. In addition, the shift of T_t in external magnetic fields increases for higher fields, which reduces the expected maximum Δ_{sT} according to the Clausius-Clapeyron approximation (Equation (5.1)). Before declining drastically below 280 K, the temperature interval for the maximum Δ_{sT} spans about 13 K. For the high-temperature region of the phase transition, the curves overlap for all regarded magnetic fields, which underlines the good accuracy of the measurement and the determination method. The transition cannot be completed upon magnetic-field application for T_s close to A_f and higher fields only lead to small improvements in Δ_{sT} . For temperatures above the magnetostructural transition (above A_f in zero field), the entropy change of the conventional second-order MCE can be identified by the negative sign of Δ_{sT} and the increasing absolute value for increasing magnetic-field changes. This effect becomes more significant for increasing temperature because it has the maximum at T_C^A . The dotted lines represent the calculated evolution of Δ_{sT} from the c_p measurements of Fig. 5.12 for field changes of 2 T, 5 T and 10 T. They have been obtained by subtracting the corresponding isofield $S(T)$ -curves from the $S(T)$ -curve in zero field. The

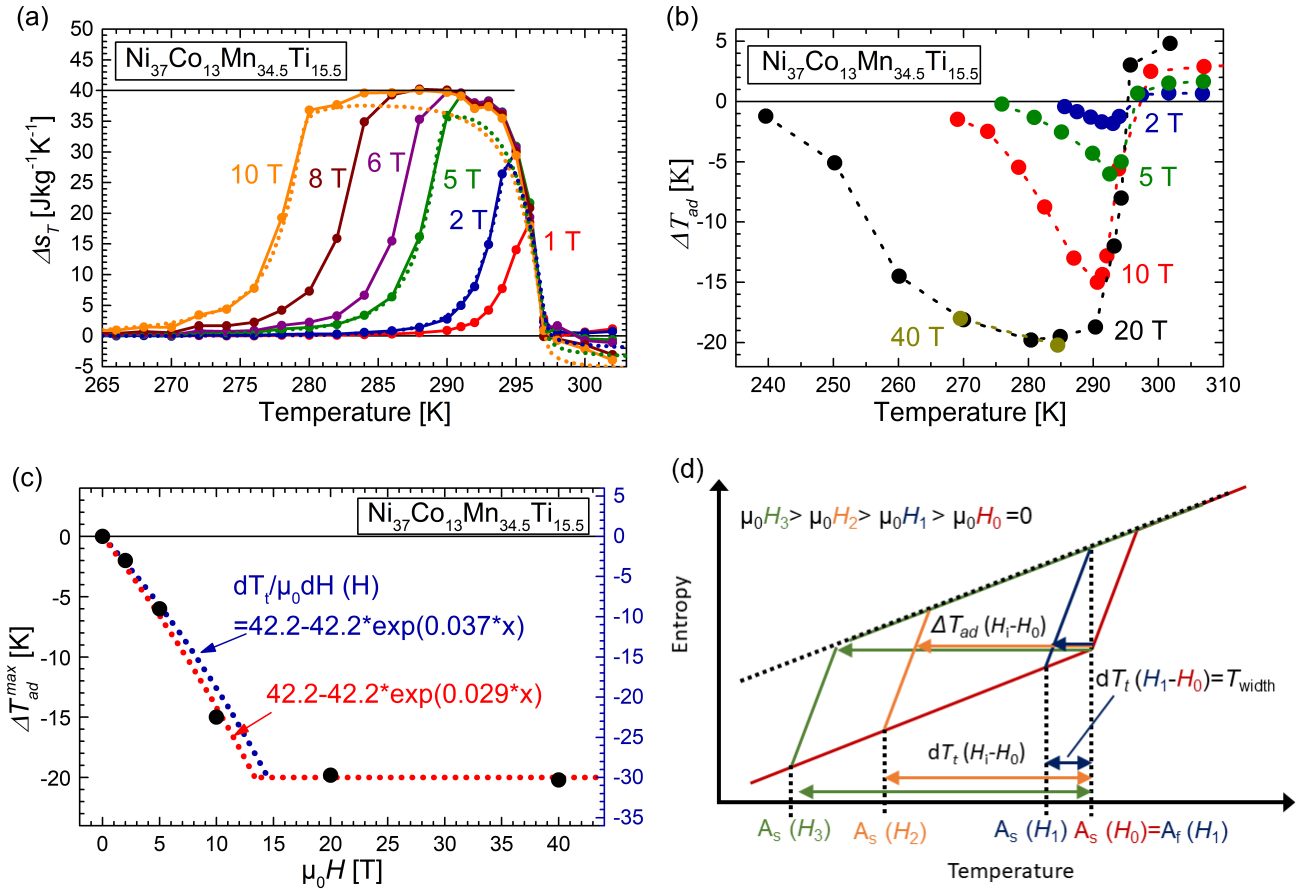


Figure 5.14: Maximum isothermal entropy change Δs_T (a) determined from isothermal $M(H)$ curves in magnetic fields up to 10 T together with the Δs_T behavior calculated from c_p measurements (dotted lines) and maximum adiabatic temperature change ΔT_{ad} determined from direct measurement in pulsed magnetic fields of up to 40 T (b) for the very same sample of $\text{Ni}_{37}\text{Co}_{13}\text{Mn}_{34.5}\text{Ti}_{15.5}$. The evolution of the highest achievable ΔT_{ad}^{max} as a function of the applied magnetic field is shown in (c) together with a fitted curve for the data points (red) as well as with the exponential function determined from the magnetic field evolution of $\frac{dT_t}{\mu_0 dH}$ from Fig. 5.13 (b), which has been scaled to coincide with the saturation of ΔT_{ad} here. The relation between $\frac{dT_t}{\mu_0 dH}$ and ΔT_{ad} is illustrated in (d) by a schematic $S(T)$ diagram for the phase transition in different external magnetic fields.

results show a good accuracy for the increasing entropy change in the transition region for zero field close to A_f . Also the regions of decreasing Δs_T for temperatures below the plateau are matching very good with the determinations from $M(H)$ -curves. Only the maximum value for the plateau of Δs_T is showing higher values for the magnetization measurements compared to the heat capacity data, which is assumed to be the more precise method. The deviation of the maximum value between the two methods amounts to around 5 %.

Figure 5.14 (b) depicts the maximum ΔT_{ad} that has been measured for pulsed magnetic-field applications

of 2 T up to 40 T, where every data point resembles the maximum ΔT_{ad} for one field pulse. The shape of the curves matches with the graph for Δs_T being mirrored vertically at $y = 0$. The evolution of the plateau is however shifted to larger external magnetic fields as a consequence of the adiabatic conditions. Highest temperature changes amount to -20 K measured for magnetic field pulses of 20 T. The two additional measurements at 284.5 K and 269.5 K with the doubled maximum magnetic field of 40 T confirm that this is the saturation value for this quantity since no further increase is obtained. This value fits very well to the calculations done before, which lead to a maximum value for ΔT_{ad} of -20.2 K for a magnetic-field change of 14.7 T (using the average field shift up to this field value). In comparison to Δs_T , the saturation field for the MCE is much higher between 10 T and 20 T. This roughly matches the calculated H_{sat} of 14.7 T, but no detailed comparison can be done since no additional data points are available between 10 T and 20 T (also note that the maximum ΔT_{ad} of the measurement was assumed to be known in order to approximate H_{sat} a priori). Due to the time-consuming measurement setup, no finer step of data points has been done between these two field values. As already discussed, the discrepancy between the two values of H_{sat} for Δs_T and ΔT_{ad} originates from the measurement conditions. The entropy change is determined in an isothermal setup whereas ΔT_{ad} was measured under adiabatic conditions. Therefore, the negative adiabatic temperature change decreases the absolute temperature of the sample and with a larger ΔT_{ad} , the sample temperature drifts further away from $A_f(H)$ requiring larger fields to induce a completed phase transition. The decreasing value for the plateau of the maximum ΔT_{ad} with decreasing temperature as a result of the increasing magnetic contribution to Δs_T is evident for the data points of the 20 T and 40 T-measurement series.

The evolution of the highest value of ΔT_{ad} depending on the maximum magnetic field for each series of maximum-field pulses is shown in Fig. 5.14 (c). The dotted blue line corresponds to the right y -axis and represents the fitting function that has been determined for the evolution of T_t as a function of the applied magnetic field in Fig. 5.13 (b). It has been adapted in order to start at (0,0) and to match the necessary -30.2 K that have to be overcome for saturating the MCE by an adiabatic field application ($T_{width} + |\Delta T_{ad}|$) with the measured saturation value for ΔT_{ad} of -20 K. This curve consequently matches the H_{sat} of 14.7 K determined before in Fig. 5.13 (b). After reaching this applied field, ΔT_{ad} is described here by the horizontal line for the constant saturation value of -20 K. This function also describes the data points of ΔT_{ad}^{max} for small maximum magnetic fields very well. The correlation between the shift of T_t and the expected ΔT_{ad} for external magnetic-field changes is connected by the $S(T)$ -diagram shown schematically in Fig. 5.14 (d). A_s is chosen here as the assumed starting temperature of the magnetic-field application. A shift of the transition temperature being equal to the width of the transition by an adiabatic external magnetic-field change from H_0 (red) to H_1 (blue) does not lead to the maximum ΔT_{ad} but only induces a fraction of the phase transition. Since the absolute temperature shift of A_s is equal to the resulting absolute value of ΔT_{ad} minus the fraction of T_{width} that is not transformed, a correlation between $\frac{dT_t}{\mu_0 dH}$ and ΔT_{ad}^{max} is logical. This schematic also underlines that the completely induced MCE (H_3 , green) under adiabatic conditions in terms of the highest ΔT_{ad} is reached for dT_t being equal to the absolute value of ΔT_{ad}^{max} plus the full transition width.

However, the maximum ΔT_{ad} of the 10 T-series is slightly higher than expected from this approach. The situation to describe ΔT_{ad}^{max} as a function of the maximum applied magnetic field is more complex than shown in the schematics of Fig. 5.14 (d). The scaling of the fitting function for $\frac{dT_t}{\mu_0 dH}$ to match both saturation values of ΔT_{ad} and H_{sat} adds the width of the transition linearly to the slope of the function by assuming a linear transition progress as also shown in the schematic $S(T)$ -diagram. This is not fully accurate as can be seen from the $M(T)$ behavior and the measured $S(T)$ -diagram. In addition, the slope of $M(T)$ not only determines the amount of induced austenite, it also scales directly with the resulting ΔT_{ad} that reduces the absolute temperature of the sample and acts detrimental for the promotion of the phase transition. The largest slope of the $M(T)$ curve for the austenite formation occurs at the inflection point in the middle of the transition, meaning that the strongest contribution to the total MCE happens in a simple approximation considering $H_{sat} = 15$ T around 7.5 T. This could explain the deviation of the data point for 10 T overestimating ΔT_{ad} in this region.

In an additional step, the determined values for Δs_T and ΔT_{ad} were implemented in the $S(T)$ -diagram from Fig. 5.12 (b). The total entropy values were determined for the starting temperature of each measurement from the $S(T)$ -curve in zero external magnetic field. Subsequently, the isothermal entropy changes were added to this entropy value for constant temperature (vertical lines) and the adiabatic temperature changes were added to the temperature value under constant entropy (horizontal lines). The resulting diagram with the total entropy evolution for external magnetic fields of 0 T (red), 2 T (blue), 5 T (green) and 10 T (orange) as dotted lines is shown in Fig. 5.15 (a) for the inverse MCE at the magnetostructural phase transition and in (b) for the conventional effect above T_t in the ferromagnetic austenite regime. All lines start at the red line for zero external magnetic field, the use of arrows is avoided for the sake of clarity. It must be noted that the absolute temperatures of the measurements have been corrected for a small offset originating from the different measurement setups. The absolute temperature of the Δs_T measurement has been taken as reference since this isothermal measurement is supposed to have the highest accuracy. The starting temperatures of the ΔT_{ad} measurements have been shifted to higher temperatures by 2.7 K.

This representation confirms the good agreement of the different measurement techniques used in order to determine the isothermal entropy change and the adiabatic temperature change. The isothermal entropy changes are in general very consistent with the expected values from the $S(T)$ diagram. Especially for 5 T, both Δs_T and ΔT_{ad} lines resemble the shape of the total entropy diagram very accurately. In contrast, it is apparent that the directly measured values of ΔT_{ad} for ΔH_{ext} of 2 T are too low for the measurements around 295 K whereas the ones for 10 T are higher than expected for the maximum MCE around T_s of 285 K to 295 K. A reason for this observed discrepancy can be based on dynamics of the measurement. It has been shown that for Ni-Mn-In, the measured values for ΔT_{ad} can depend on the approaching rate of the measurement temperature and can deviate from the quasistatic measurements of c_p [228].

Furthermore, a very good agreement between direct measurements and the indirect method of measuring c_p is found for the region above the martensitic transition, where a purely conventional MCE occurs due to the magnetization of the ferromagnetic austenite. Even though the temperature range depicted in

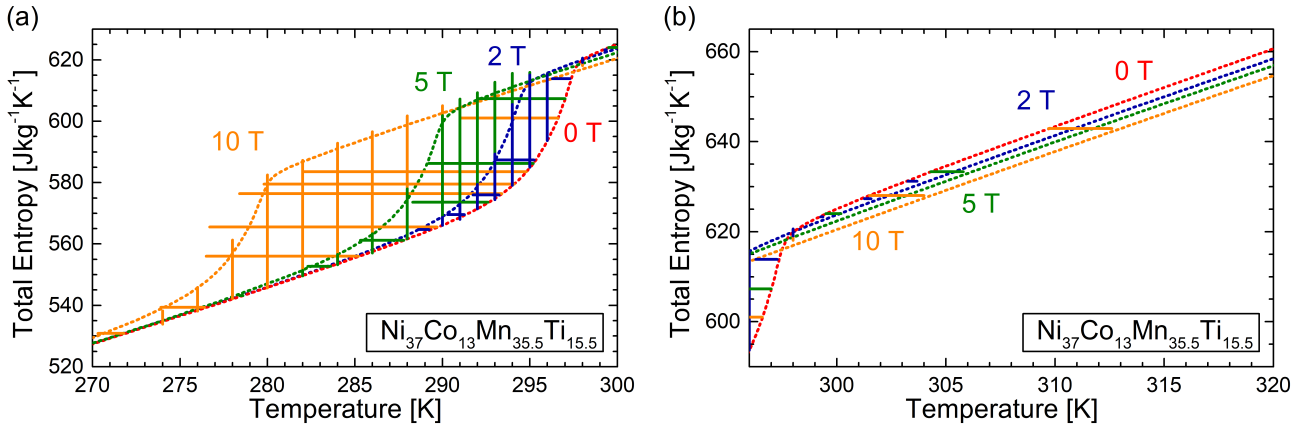


Figure 5.15: Comparison of the temperature- and field-dependent measured isothermal entropy changes (vertical lines) and adiabatic temperature changes (horizontal lines) from Fig. 5.14 with the $S(T)$ -diagram determined from c_p measurements as shown in Fig. 5.12 for magnetic-field changes of 0 T (red), 2 T (blue), 5 T (green) and 10 T (orange) for the inverse MCE around T_t (a) as well as for the conventional effect in the ferromagnetic austenite regime above the magnetostructural transition (b).

Fig. 5.15 (b) is significantly below T_C^A , positive adiabatic temperature changes of 0.6 K (2 T) to 2.9 K (10 T) occur for a T_s of 310 K, which fit very well to the total entropy curves of the respective external magnetic field values.

The comparison of the different methods for determining and estimating the two key properties Δs_T and ΔT_{ad} in order to describe the MCE of a certain material shows that the maximum expected effects, the corresponding saturation fields as well as the detailed evolution of the actual Δs_T and ΔT_{ad} values from the $S(T)$ diagram show a very good agreement. Especially the determination of the saturation fields under isothermal and adiabatic conditions fit very well to the experimentally observed values. Even the absolute value of ΔT_{ad} has been estimated accurately, the first approximation of the maximum Δs_T by the Clausius-Clapeyron equation, however, overestimated the actual value by 8%. It must be emphasized here that the estimation of H_{sat} under adiabatic conditions requires already the saturation value from a measurement in high magnetic fields, otherwise the propagation of the overestimation of Δs_T accounts for errors here. In addition, the accurate determination of the highest expected ΔT_{ad} required many information as input, such as the saturation field (only accurate from the known saturation value of ΔT_{ad} from measurement) in order to determine the correct average value of $\frac{dT_t}{\mu_0 dH}$, for which the evolution up to H_{sat} has to be known additionally, as well as the heat capacity. For this reason the declaration of an accurately determined saturation value of ΔT_{ad} by an a-priori-method is misleading. Nevertheless, this study shows that the used equations can describe the crucial quantities of Δs_T , ΔT_{ad} , H_{sat} (adiabatic) and H_{sat} (isothermal) very accurately for the complex situation of a magnetic-field-induced magnetostructural phase transition for an inverse MCE.

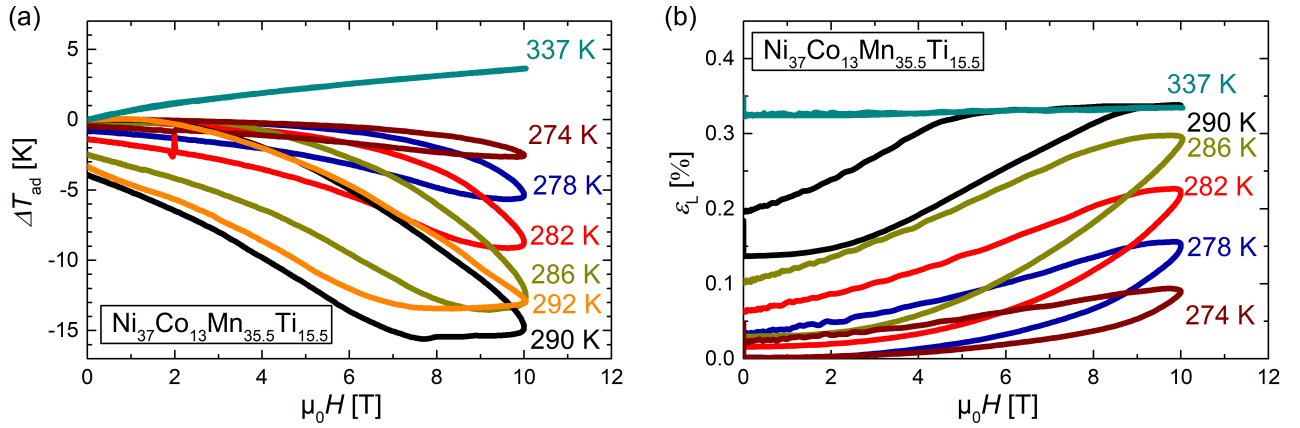


Figure 5.16: Magnetic-field-dependent adiabatic temperature change (a) and strain measured perpendicular to the magnetic-field axis (b) for pulses of 10 T at varying starting temperatures for $\text{Ni}_{37}\text{Co}_{13}\text{Mn}_{34.5}\text{Ti}_{15.5}$.

5.6 Simultaneous sample characterization

In the literature, the newly proposed all-*d* Heusler system of Ni-Co-Mn-Ti has already been reported to have a large volume change of around 2.7% upon the martensitic transition [167], which favors its usage for baro- and elastocaloric applications. In order to study the detailed effects of the martensitic transition, the simultaneous magnetocaloric effect together with the length change along two directions has been investigated in pulsed magnetic fields at the HZDR. Therefore, a thermocouple has been glued with silver epoxy between two cuboids (3.5 mm x 3.5 mm x 1 mm each) from the sample of $\text{Ni}_{37}\text{Co}_{13}\text{Mn}_{34.5}\text{Ti}_{15.5}$, which has been already intensively investigated in the previous Chapter 5.5. In addition, a bidirectional strain gauge has been attached to the surface of one sample block.

The magnetic-field-dependent evolution of ΔT_{ad} is depicted in Fig. 5.16 (a). Here, the curves do all start at the same point since the values for ΔT_{ad} are all given relative to the absolute T_s of each pulse measurement. By considering ΔT_{ad} as the manifestation of the MCE, the amount of induced austenite is increasing the closer T_s approaches T_t . This is in agreement with the decreasing onset field of the temperature change because the shift of T_t with the applied field needs to overcome a smaller temperature difference between T_s and A_s . The maximum effect of a 10 T pulse is achieved for the starting temperature of 290 K (black curve). The slightly higher T_s of 292 K (orange) shows nearly the same ΔT_{ad} behavior in small fields. The phase transition is induced immediately because the starting point is in both cases in a mixed state. For the higher temperature, there is less martensite present that can be transformed into austenite at the beginning of the measurement. Therefore, the effect already begins to saturate when starting at 292 K and the maximum obtainable MCE is reduced. For all the described indicators for the amount of phase conversion (ε_L , ε_{II} and ΔT_{ad}), the thermal hysteresis of the compound is represented in the shown measurements by a field hysteresis. Upon field removal, the back transformation into martensite with a negative strain and a positive ΔT_{ad} is not induced immediately but delayed for several tesla. The

correctness of the measurement is proven by the measurement at the second-order transition between paramagnetic and ferromagnetic state of the austenite (at 337 K). A maximum ΔT_{ad} of 3.6 K is induced by the magnetic-field change of 10 T and the evolution of ΔT_{ad} is identical for the field application and the field removal process. Thus, there is no artificially induced hysteresis by a delayed response time of the thermocouple. In addition, a dependence of the thermocouple signal on the magnetic-field-change rate can be excluded by comparing the two branches for the measurement at T_C^A .

The corresponding magnetic-field-dependent strain that is measured by the directly attached strain gauge is shown for applied field pulses of 10 T in Fig. 5.16 (b) for ε_L perpendicular to the magnetic-field direction. The absolute signal of the strain gauge is converted into strain by setting the resistance value of the respective strain gauge for the martensite starting state of the lowest regarded temperature (here 274 K) as the reference, i.e. zero strain. It is necessary here to define a certain temperature as the zero-strain-value because the strain of the martensite varies with temperature due to regular thermal expansion and there is no uniform martensitic strain value as a reference. The relative straining compared to the starting state is increasing with positive values for each T_s with increasing magnetic field for all starting temperatures below A_s . This indicates a length expansion of the sample in this direction due to the field-induced phase transition from martensite to austenite. This observation is in agreement with the expected volume change from low-volume martensite to high-volume austenite. In addition, the relative sample length before each field pulse is increasing for higher T_s due to the thermal expansion of the martensite as well as to already present austenite for starting temperatures with a mixed phase state in the transition region. The upper limit for the strain is represented by the measurement at 337 K (cyan curve) at the austenite Curie temperature. Since the induced MCE is related to the pure magnetic transition, no length change is evolving and ε_L is constant at 0.33 %. This value therefore also represents the maximum straining between the martensite slightly below the phase transition and the austenite well above the first-order phase transition. The fact that a magnetic field of 10 T is not enough to fully induce the phase transition is visualized here by the measurement at 290 K (black curve), which is the only one with a saturated maximum strain at 9 T to 10 T but with a length change of 0.15 % at the beginning of the measurement due to a mixed phase state as starting condition.

Since the representation of the maximum ΔT_{ad} for different applied magnetic fields (Fig. 5.14 (b)) shows a saturation from 20 T on, the evolution of the field-induced MCE is discussed by means of ΔT_{ad} and ε for magnetic-field pulses of 20 T in Fig. 5.17. The shown measurements at selected temperatures show the increase in the maximum obtained ΔT_{ad} for increasing the starting temperature until the saturation is reached at a starting point of 285 K (red curve). The magnetic-field-dependent ΔT_{ad} for the saturated cases at starting temperatures of 285 K and 290 K show a loop at high fields. After reaching the highest value of ΔT_{ad} , the absolute temperature increases again shortly before approaching the maximum field value of 20 T and keeps increasing upon the beginning of the field-removal process. This is followed by a slight decrease in temperature reaching the maximum ΔT_{ad} again (dashed lines) until the back transformation to martensite is induced. The described emergence of the ΔT_{ad} loop is stronger for higher starting temperatures. It can only be observed for magnetic field pulses of 20 T and higher and only for

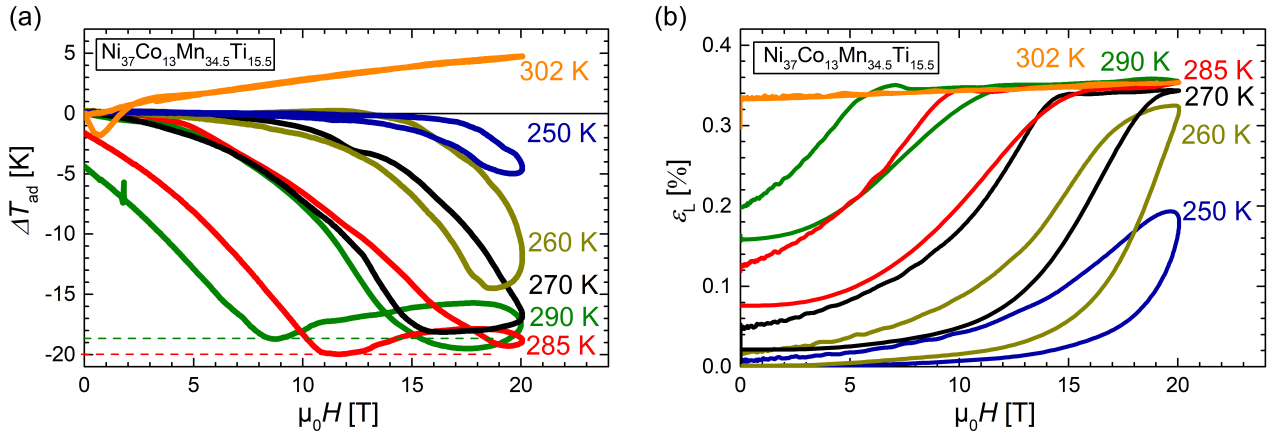


Figure 5.17: Magnetic-field-dependent adiabatic temperature change (a) and strain measured perpendicular to the magnetic field axis (b) for pulses of 20 T at varying starting temperatures for $\text{Ni}_{37}\text{Co}_{13}\text{Mn}_{34.5}\text{Ti}_{15.5}$.

starting temperatures where the saturation of ΔT_{ad} is reached. A comparison with the respective values of ε_L in Fig. 5.17 (b) reveals that this effect is a characteristic for ΔT_{ad} only. The measured strains show a flat saturation plateau after reaching the respective H_{sat} . On the one hand, this indicates that a conventional MCE of the ferromagnetic austenite could play a role here after the transformation is completed. On the other hand, it can be a feature of the thermocouple for high magnetic fields. The fact that it only occurs for fully saturated effects and that it increases for lowered H_{sat} (higher T_s) indicates a correlation with the conventional MCE of the formed austenite. Due to this feature, the determination of the maximum ΔT_{ad} is not trivial for the obtained curves. Therefore, the point at which the back transition starts is taken as ΔT_{ad}^{max} as indicated by the dashed lines in Fig. 5.17 (a).

The maximum field-induced length change that can be obtained amounts to 0.32 % for the measurement starting at 270 K (Fig. 5.17 (b), black curve). Even though slightly larger strain values are present at saturated austenite formation for the highest fields of $T_s = 285$ K and 290 K, the sample length of the initial state is also increased because the value for zero field at 250 K serves as the reference for the strain here. The maximum strains ε_L obtained for a saturated field-induced MCE are in agreement with the observations from the 10 T pulses in Fig. 5.16 (b), indicating that the transition can be close to saturation when considering ε_L as representative for the MCE of the induced phase transition.

The dependence of the adiabatic temperature change on the maximum applied field of a pulse and, therefore, also on the field-application rate is depicted in Fig. 5.18 (a) for T_s at 285 K, which is close to A_s where the largest effects are expected. This series shows that only a very small fraction of the potential MCE can be induced by a magnetic field of 2 T. The measured ΔT_{ad} only accounts for 2 K in 2 T, which is only 10 % of the saturated MCE in 20 T. By comparing the field-application branch for the pulses of 10 T and 20 T, it is apparent that the kinetics of the martensitic transition are changed by the field application rate because the slope of the field-dependent ΔT_{ad} is varying for the two curves. In contrast, the reverse transition having the same magnetic field rate for both pulses is equal in slope. However, this effect can

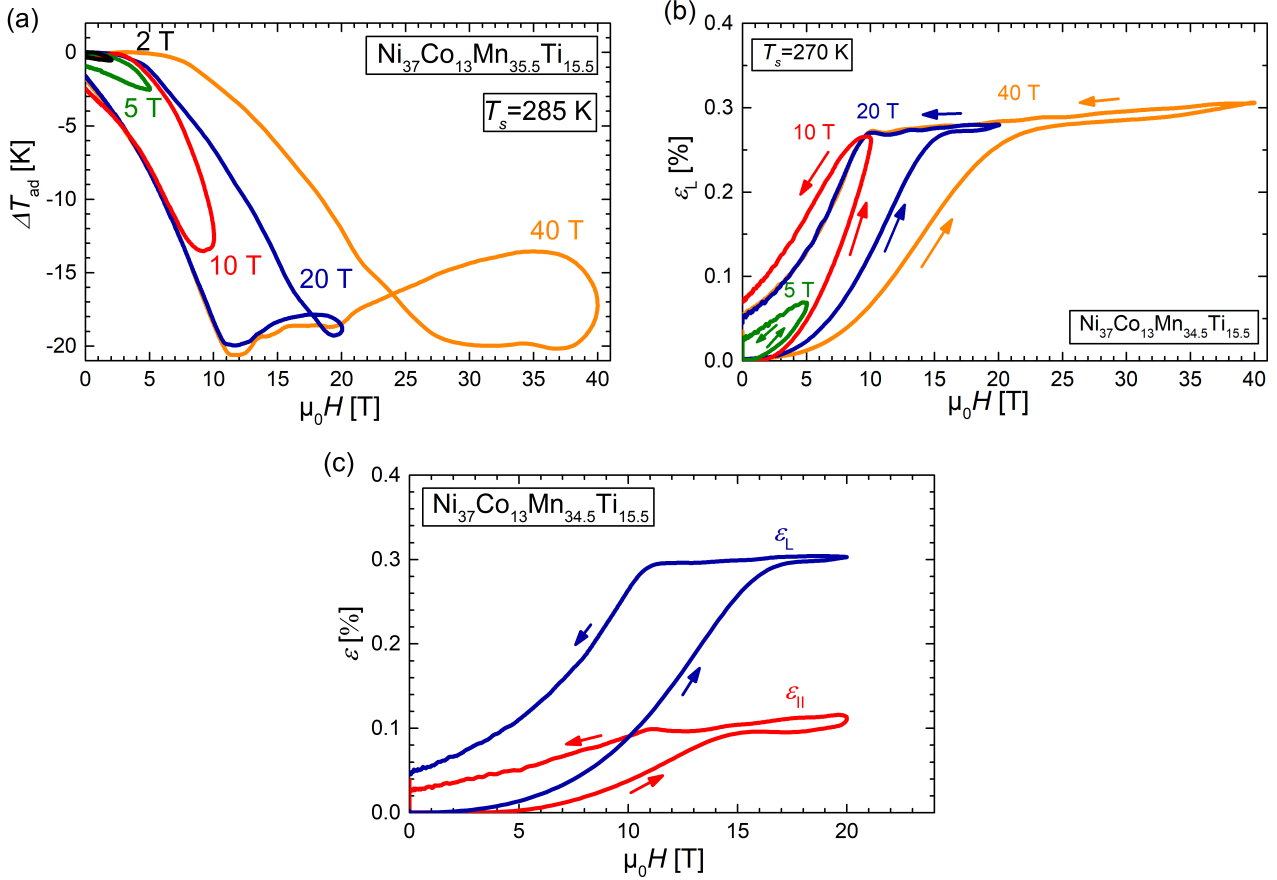


Figure 5.18: Comparison of the magnetic-field-dependent ΔT_{ad} (a) and ε_L (b) for different maximum fields being equivalent to different maximum field-application rates of the pulse. The comparison of the two measured directions of the strain gauges ε_L (blue) and $\varepsilon_{||}$ (red) is depicted in (c).

also be due to the response of the thermocouple to the high magnetic-field rates, which are significantly smaller during field removal.

To eliminate the effect of the potential delay of the thermocouple, the strain is compared for different field rates in large magnetic fields of 5 T (green), 10 T (red), 20 T (blue) and 40 T (orange) in Fig. 5.18 (b). In accordance with the results of comparing ΔT_{ad} in different fields, the increase of the strain during the field-induced transition is delayed for the large applied field rates of the 40 T pulse compared to a faster reaction in 20 T. By this effect, H_{sat} is increased from 18 T to 25 T. The reverse transition upon field removal with the same field rates coincides accurately for both pulses and the onset field for the back transition is equal. The complete removal of the magnetic field for these two pulses confirms the observations from the temperature-dependent strain experiments starting from the field-induced martensite. By considering the corresponding ΔT_{ad} , it can be assumed that the back transition can be completed at T_s of 270 K (Fig. 5.17 (a), black curve). However, there is still a residual strain of 0.025 % present after removing the magnetic field completely back to zero.

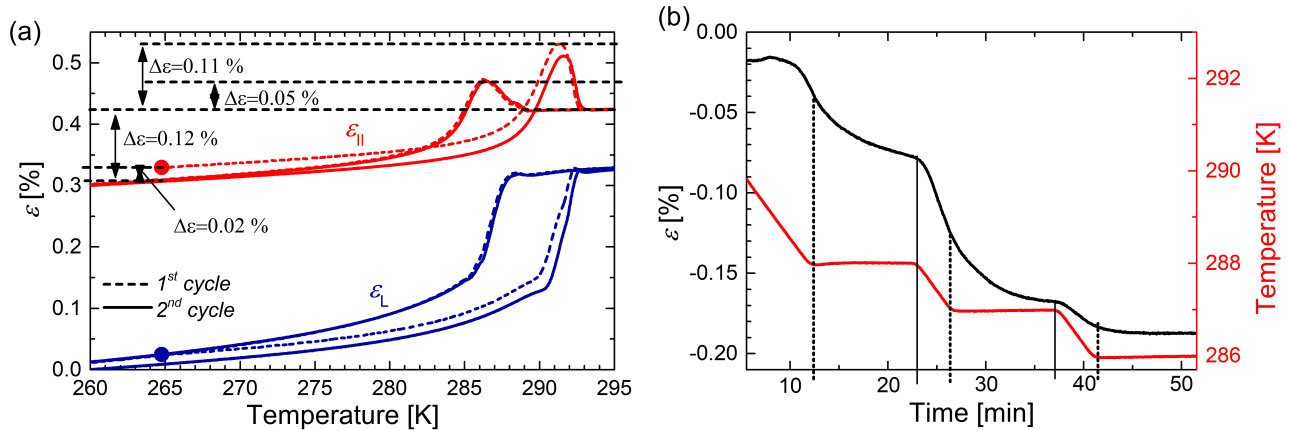


Figure 5.19: Temperature-dependent evolution of the strains perpendicular (ϵ_L) and parallel (ϵ_{II}) to the magnetic field direction for two consecutive temperature cycles (a). The starting point is highlighted, which stands for the martensitic state after the application of a 40 T pulse representing a completely induced martensite state upon field removal subsequent to a fully field-induced austenite. The simultaneous signal of time-dependent sample temperature (red) and strain (black) for temperature ramping steps of 1 K followed by a holding time of 10 min is shown in (b).

The comparison of the two strain directions parallel (blue) and perpendicular (red) to the applied magnetic field in Fig. 5.18 (c) indicates a difference between the macroscopic length changes in these two directions. Whereas a saturation strain of 0.3% is detected for ϵ_L , the maximum values for ϵ_{II} only reach 0.1% in saturation. The saturation field for both quantities is identical, which shows the correlation between the expansion in both directions as a result of the martensitic transformation.

In order to investigate the strain behavior of the martensitic transition itself in more detail, the signal of the strain gauge has been recorded during temperature sweeps. The corresponding curves for ϵ_L (blue) and ϵ_{II} (red) are shown in Fig. 5.19 (a). The strain values are calculated towards the reference value at 260 K and the curve for ϵ_{II} is shifted by +0.3% for the sake of a clear presentation. The respective first temperature cycle is shown as a dashed line and the subsequent second cycle as a solid line. The starting point is highlighted for both strain values and has been reached by applying a 40 T pulse at 265 K in order to completely induce the austenite state and fully induce the martensitic back transformation upon field removal, thus establishing a purely field-induced martensite state. In agreement with the field induced strain comparison before, the length expansion during the phase transition is lower for ϵ_{II} (0.12%) than for ϵ_L (0.32%), resulting in a factor of 3 between the two measured strain directions. This leads to the conclusion that the lattice expansion from martensite to austenite is positive along the magnetic field as well as perpendicular to it, but with different maximum straining. Consequently, the martensite is preferentially aligned with its long axis perpendicular to the magnetic field since this is the direction with the largest length change for the present measurement setting. Since each strain gauge has a dimension of 1 mm x 1 mm, it is assumed to cover a significant amount of grains on the surface and can be regarded as representative. The main peculiarity here is the deviation from the first heating to the second cycle.

Whereas the two curves for the cooling branch overlap, the heating from the field-induced martensite shows higher strain values than the second cycle from an initially temperature-induced martensite state. The absolute deviation between the field-induced and the temperature-induced martensite amounts to a strain difference of 0.02 %.

The second interesting feature to notice is the positive straining of the sample at the high-temperature end of both the martensitic and austenitic phase transition above the sample elongation in austenite state. This is weakly observable for ε_{I} but strongly pronounced for ε_{II} . Thus, the microstructure of the sample first expands at the beginning of the phase transformation upon cooling before building up the negative transformation strain towards the low volume martensite. For ε_{II} , this overstraining effect amounts to absolute values of 0.05 % for cooling and 0.11 % for heating relative to the stable austenite length above the finished (before the started) transition. This is a very significant effect compared to the 0.12 % strain for the complete martensitic transition.

These findings of the difference in strain for a field-induced and a temperature-induced martensite as well as the different strain evolutions for the two investigated directions with respect to the magnetic field suggest a directional dependence of the martensite formation. Since the induced martensite is supposed to be in the paramagnetic state, this is not connected to magnetocrystalline anisotropy and should not be the reason for the different elongation directions. Even though a magnetic ordering is reported for the usually considered paramagnetic martensitic state of Ni-Co-Mn-Ga [193], the magnetization behavior with gradually increasing macroscopic moment for increasing external field suggests the occurrence of paramagnetism for the martensitic state of the present Ni-Co-Mn-Ti alloy. One alternative explanation is the local microstructure of the sample on the surface, where the strain gauge is attached. It is possible that a local texture on the sample surface as a result of the solidification process during arc-melting leads to a preferred orientation of the martensitic growth during the field-induced phase transition. Since the sample has been cut out of a slice from the arc-molten drop, one strain-gauge direction is along the solidification direction (from bottom to top of sample on the cooled Cu plate) and one is perpendicular to it. A deeper study of this behavior, for example a texture analysis by electron backscatter diffraction (EBSD) and microscopical investigation of temperature- and field-induced martensite states, can give more information on the underlying mechanisms. A subsequent measurement with a rotation of the sample by 90° can answer the question whether the difference in strain is due to the direction of the magnetic field or a consequence of the local microstructure of the sample.

The evolution of the sample temperature and the respective strain as a function of time for holding times of 10 min after decreasing the temperature by 1 K in the transition region in Fig. 5.19 (b) provides further insights into the kinetics of the transition. The simultaneous decrease of the temperature and the strain indicated by the solid vertical lines demonstrate that the signal processing is happening simultaneously between the two measured quantities. After establishing a stable temperature of the sample as marked by the dashed lines, the evolving negative straining of the sample upon martensite formation is by far not completed. An asymptotic evolution is observed for the strain over the complete holding time of 10 min towards the start of the next temperature ramp. This effect becomes less pronounced for lower temperatures

meaning a decreasing amount of martensite being formed for the same temperature increment. During the last step from 287 K down to 286 K, the equilibrium strain is reached already after a few minutes and the residual holding time is characterized by a simultaneous constant line for both temperature and strain signal. This experiment indicates that the martensitic phase transition is indeed influenced by kinetic aspects. The transition can drive itself to a certain extent when the necessary amount of nucleation energy is provided by an external stimulus, e.g. a temperature change. A surface effect due to local constraints by the glued strain gauge can also be a reason for the observed gradual strain increase, even though this is not expected to last over a time period of several minutes. This experiment hence underlines the findings from the microscopical observations of a stepwise field removal in Fig. 5.10. The found self-driven growth can, therefore, be regarded as a real effect, even though the discussion associated with the microstructure investigations with local temperature changes and stress fields is also assumed to hold true and contribute to the described effect.

In order to investigate the question of the field-rate dependence further, the simultaneously recorded field-dependent strain (blue) and temperature change (red) are shown for field pulses of 5 T, 10 T and 20 T, each at T_s of 285 K, in Fig. 5.20 (a)-(c). For the sake of a proper comparison, the strain axis has been inverted to match the sign of both values during the phase transition. In addition, both quantities have been scaled so that they start at zero and that the maximum values before the start of the backward transformation upon magnetic-field removal are leveled. The 5 T pulse shows a nearly identical progression of ε_L and ΔT_{ad} for the magnetic-field-induced MCE. A stronger deviation is observed for the larger field-application rates of the 10 T pulse. The signal of ΔT_{ad} is delayed here compared to ε_L . Since ΔT_{ad} is not saturated in the maximum magnetic field of this pulse, a slight heating takes place due to the observed delay resulting in an overlap of ΔT_{ad} and strain upon field removal. The phase transition for the 20 T pulse indicated by ε_L starts at magnetic fields around 5 T, which is similar for ΔT_{ad} . However, the slope of ε_L is much steeper for the strain meaning that the field-induced strain is reacting to the external magnetic field in a faster way than the temperature change. In addition, it seems that for the reverse transition the length change of the sample starts at lower fields than ΔT_{ad} . The slight increase in strain before decreasing again, which has been observed from the temperature-dependent strain measurements (Fig. 5.18 (d)), is the reason for this ostensible signal delay. In fact, the start of the martensite formation by ΔT_{ad} and strain starts at the same magnetic field of 11 T. This effect is not relevant for the shown pulses of 5 T and 10 T because these fields do not complete the phase transition. Thus, this inverted strain behavior for the transition only appears between full austenite and first/last martensite structures being present and is not observed for these two field pulses that lead to minor loops.

The reason for the observed delay of ΔT_{ad} for large field-application rates is not clearly understood. A significant delay of the signal detection and processing seems unlikely from the well overlapping signals for the fast conventional MCE of the ferromagnetic austenite and the slower back transition upon field removal in Fig. 5.16 (a) and 5.17 (a). However, the effect at T_C is much smaller than around the FOMT, and a delay of the signal would be not so strongly pronounced. However, the data has been corrected for the induced noise signal of the thermocouple manually, which can lead to artificial effects of the signal. In

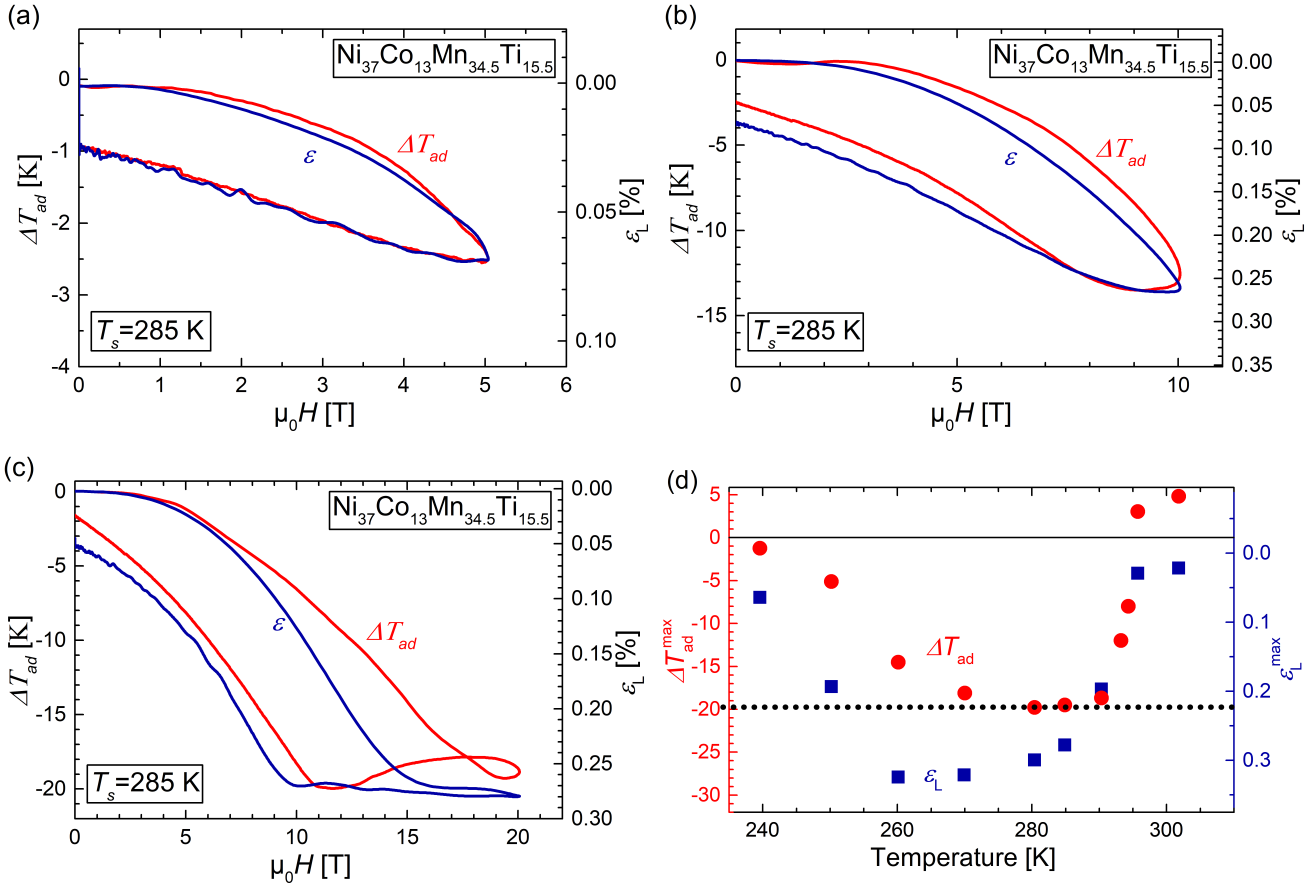


Figure 5.20: Direct comparison of ΔT_{ad} (red) and ε_L (blue) for different field application rates during pulses of 5 T (a), 10 T (b) and 20 T (c), each at T_s of 285 K. Both axis have been scaled so that both curves start at zero and overlay at the largest value before the start of the back transition upon field removal. The positive axis of ε_L has been inverted to match with the negative signal for ΔT_{ad} . The corresponding comparison of the temperature-dependent maximum values for ΔT_{ad} and ε_L are shown in (d), where the dotted line indicates the saturation maximum of ΔT_{ad} .

addition, the strain gauge is attached at the free surface, whereas the thermocouple is in the center of the sample, fixed with silver glue to the two sample pieces. An explanation to the observed discrepancy can be that the phase transition starts at the surface, where the martensite can transform into austenite and expand freely compared to the constraint material inside the bulk. In any case does this effect lead to an earlier saturation of ε_L compared to ΔT_{ad} . This is also apparent from the measurement at 270 K (black curves) in Fig. 5.17 (a) and (b), where ε_L reaches the saturation value but ΔT_{ad} does not.

A direct comparison of the maximum obtained values for ΔT_{ad} (red) and ε_L (blue) in 20 T is depicted in Fig. 5.20 (d). The saturated value of ΔT_{ad} is scaled to the maximum transition strain of the pure phase transition determined from Fig. 5.19 (a). It can be seen that the strain value still increases for lowered starting temperatures, which is due to the negative straining effect of lower starting temperature

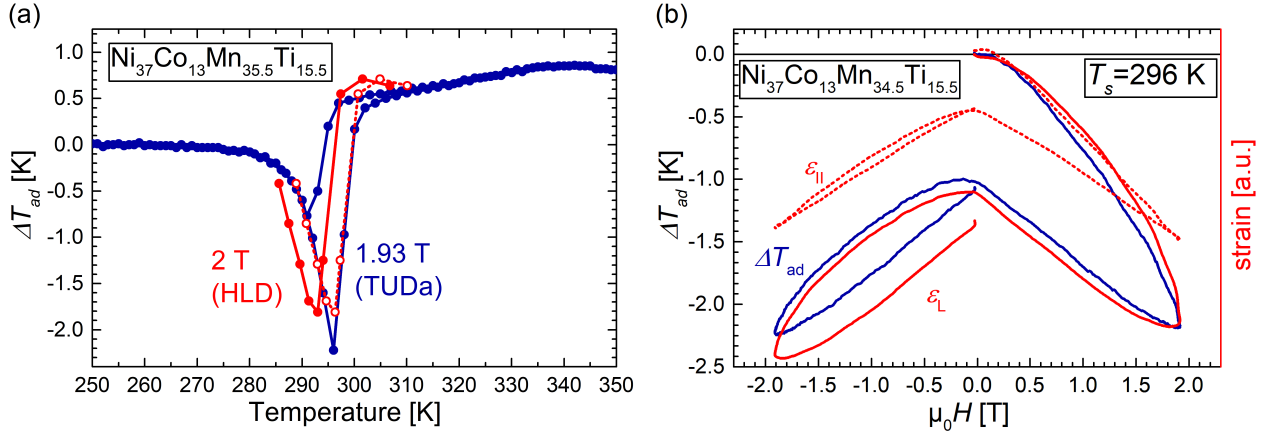


Figure 5.21: Temperature-dependent maximum ΔT_{ad} measured in slow field change rates of a rotating Halbach setup (maximum of 1.2 T s^{-1}) at TU Darmstadt (blue) for a maximum field change of 1.93 T measured in continuous protocol as well as the corresponding ΔT_{ad} for field changes of 2 T in pulsed fields (270 T s^{-1}) at HLD (solid red symbols). The HLD measurement has been corrected additionally by 3.3 K to account for deviations in the absolute temperature detection (open symbols). The corresponding evolution of ΔT_{ad} (blue), ε_L (solid red) and ε_{II} (dotted red) is shown for two consecutive field cycles in the Halbach setup. In order to compare ΔT_{ad} with ε_L directly, both quantities have been scaled according to their maximum value for the first field application.

of the martensite phase. For the same reason, the data points for ε_L are not matching well with ΔT_{ad} for starting temperatures below 250 K . Both values also do not coincide for the starting temperatures above the transition temperature, where ΔT_{ad} becomes positive whereas the maximum ε_L does not change its sign. The reason is the dominating influence of the conventional MCE of the FM austenite which is a purely magnetic effect with no structural change involved. Even though magnetostriction effects can occur and the temperature change of the MCE can lead to thermal expansion, these effects are much smaller than the length changes caused by a martensitic transition. The still measured sample expansion here is due to minor fractions of the phase transformation taking place, which are however overruled by the conventional MCE for the ΔT_{ad} signal at starting temperatures close to the transition (296 K). The non-vanishing strain for even larger temperatures is then due to the thermal expansion of the austenite caused by the heating of the positive ΔT_{ad} from the conventional second-order MCE.

For the validation of the measurements in pulsed fields, the sample with the attached thermocouple and strain gauge has been used for a reference measurement with an adiabatic field change application of 1.93 T by a rotating Halbach setup at TU Darmstadt with field-application rates of up to 1.2 T s^{-1} . The respective measurement of ΔT_{ad} is shown in comparison with the original data obtained from pulsed fields at HLD (solid red symbols) as well as with an absolute temperature correction (open symbols) in Fig. 5.21 (a). The comparison yields that a temperature offset exists for the starting temperatures of both measurement setups. In addition, a deviation for the maximum ΔT_{ad} is observed between -2.2 K for the slow field rates at TU Darmstadt and -1.8 K for the pulsed fields at the HLD. A temperature correction

of 3.3 K for the pulsed-field data, however, leads to a perfect agreement between the two measurements around the FOMT. The deviation of the maximum measured ΔT_{ad} is thereby explained clearly by the choice of starting temperatures around the peak value. Whereas the measurement at TU Darmstadt reproduces the sharp peak value of the non-saturated MCE in 2 T, the measurement at HLD does not reflect this peak point due to the temperature step of 1.5 K between the two closest points around the peak.

The corresponding magnetic-field-dependent evolution of ΔT_{ad} (blue) as well as ε_L (solid red) and ε_{II} (dotted red) is shown for two subsequent field cycles in Fig. 5.21 (b). By scaling the signal of ΔT_{ad} to the maximum of ε_L for the maximum field of the first cycle, the comparison yields a good agreement of both quantities with a slight deviation for the first removal branch. This deviation leads to a residual strain that is larger in relation to the remaining temperature change after the irreversible field removal due to the thermal hysteresis. This is in good agreement with the residually strained martensite state observed after the field-induced transition in pulsed magnetic fields (Fig. 5.19 (a)). Furthermore, the ΔT_{ad} of the second field cycle can be determined as -1.2 K, which is completely reproducible/cyclic also for the second field removal. In contrast, also the second field cycle indicates a residual strain that does not coincide with the starting value in zero field for the second cycle. In addition, the observed strain parallel to the magnetic-field direction is significantly smaller, which also confirms the results in pulsed magnetic fields. This validation by a second measurement technique confirms that the ΔT_{ad} measurement in field changes of 2 T are not dependent on the applied field change rates of up to 270 T s^{-1} and the determined MCE of minor loops is in good agreement.

In order to compare the evolution of ΔT_{ad} and ε during the phase transition in more detail, simultaneous measurements of magnetization, ε_L , ε_{II} and additionally (specific) electrical resistivity ρ in static and slow magnetic fields are shown in Fig. 5.22 for the very same sample from the pulsed-field investigations before. The shift of the martensitic transition temperature from the lowest field of 0.05 T to the highest field of 14 T experiences an exponential increase towards lower temperatures, being consistent with the observations from the corresponding $M(H)$ -measurements in Fig. 5.13. The bidirectional strain features a slight increase for the first martensite nucleations followed by a negative increase of the strain to the low-volume martensite state. This behavior is more pronounced for ε_{II} than for ε_L and is in agreement with the observations from Fig. 5.18 (d) in zero field.

The electrical resistivity shows a higher value for the martensite state, which is expected from the higher defect density in terms of twin and grain boundaries, which act as scattering centers for the conduction electrons. In addition, ρ increases with temperature for martensite and austenite, which is a sign for the metallic character of the electronic band structure for both phases. It is also found that the resistivity of both austenite and martensite state is lowered for larger applied magnetic fields. However, the sequence of the measurement was set from high fields to low fields, which hence means an increasing resistivity with further amount of phase transitions experienced. To investigate this observation further, the measurement has been repeated and it was found that the resistivity value of the austenite for the first transition cycle in 14 T matches exactly with the previous value for the last cycle in 0.05 T and it again increases for all subsequent cycles. Consequently, the increased resistivity is most likely a result of defect formation

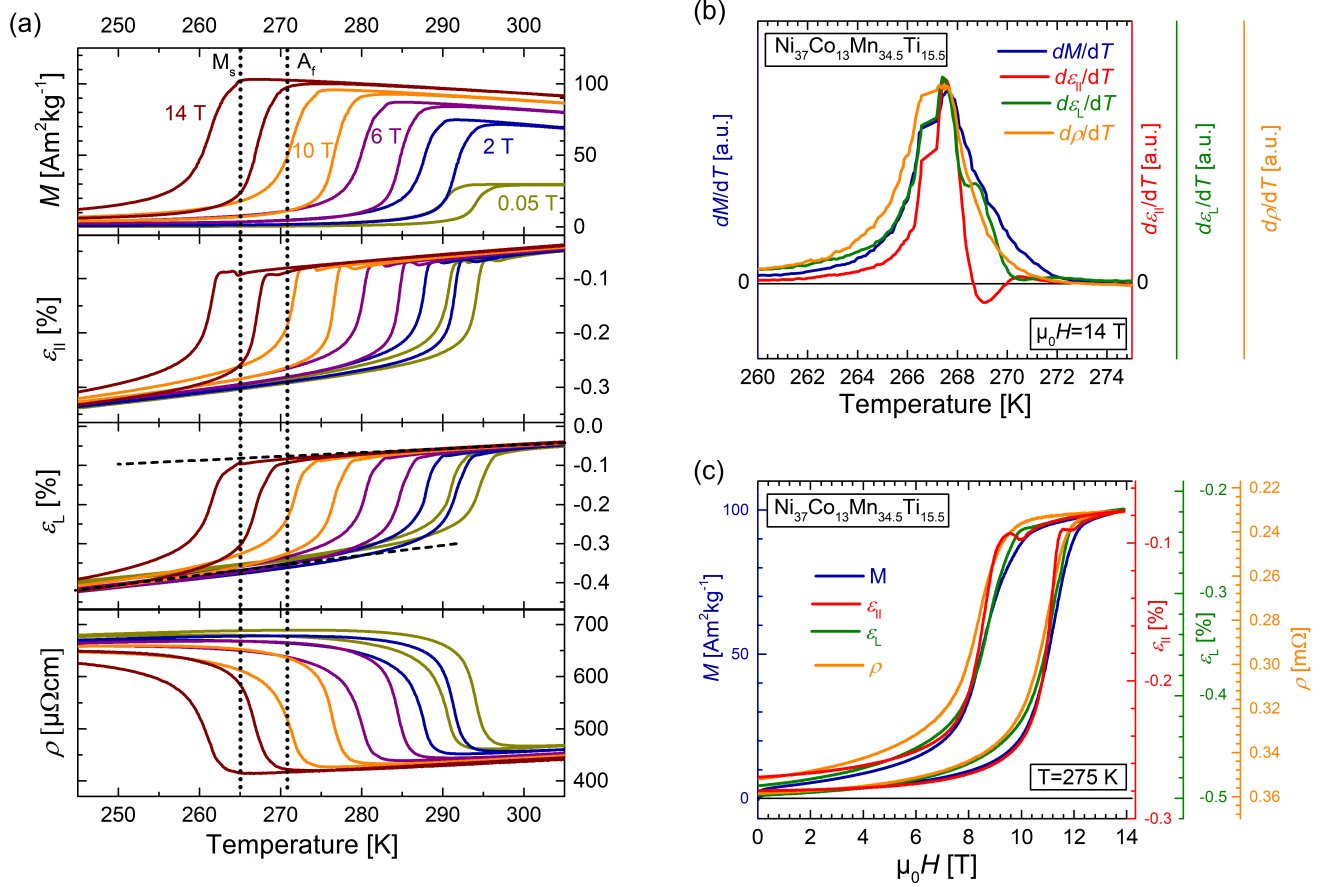


Figure 5.22: Temperature-dependent simultaneous measurements of magnetization M , strains ε_L and $\varepsilon_{||}$, and electrical resistivity ρ of $\text{Ni}_{37}\text{Co}_{13}\text{Mn}_{34.5}\text{Ti}_{15.5}$ in constant magnetic fields of 0.05 T (dark yellow), 2 T (blue), 6 T (purple), 10 T (orange) and 14 T (brown) (a). Vertical dotted lines indicate the martensite start and the austenite finish temperature determined from the magnetization measurement in 14 T. First derivatives with respect to temperature are shown in (b) for the isofield measurement at 14 T upon heating. The magnetic-field-dependent evolution of these quantities for a maximum field of 14 T under isothermal conditions at 275 K is shown in (c). The measurements have been conducted by Konstantin Skokov (TU Darmstadt).

during each phase transition, which act as scattering centers for the conduction electrons. Even though the same sample has experienced hundreds of transition cycles already because it has been used before this experiment for Δ_{ST} measurements and the pulsed-field experiments, training effects are still present depending on the number of phase transition cycles carried out.

The lines that indicate the slope of ε_L reveal that the thermal expansion of the martensite is larger than the one of the austenite phase. As a result, the evolving strain for a field-induced phase transition increases for lower transition temperature. This is in good agreement with the rising transition strain for decreasing T_s in the saturation regime of applied field pulses of 20 T (Fig.5.20 (d)).

For the sake of comparison, two vertical dotted lines are added for the martensite start and austenite finish temperature of the measurement in 14 T. They are defined here as the first deviation of magnetization from the linear behavior of the austenite region. The direct comparison with ε_{II} and ε_L shows that the length contraction for the martensite formation happens significantly after the first magnetization drop. To be more precise, the significant strain evolution towards the low volume martensite is delayed by a prior expansion upon first martensite formations. In addition, it seems that also the resistivity change is shifted but with a flat delay instead of an opposite sign for the first changes like it is the case for ε_{II} . In order to resolve this behavior in more detail, the first derivatives with respect to temperature are depicted in Fig. 5.22 (b) for M , ε_{II} , ε_L and ρ in 14 T upon heating. The sign of $\frac{d\rho}{dT}$ has been inverted to match with the other depicted quantities. The y -axes have been rescaled, so that the curves are leveled at zero as well as at the respective maximum value. Looking at the high temperature end of the transition, there is a first significant increase of the slope for the magnetization at 272 K. Both strain derivatives first start to deviate from zero around 271.5 K but weaker in magnitude compared to M . At 270.2 K, both ε_{II} and ε_L start to change slope significantly: while the slope of ε_{II} gets negative here (contraction upon austenite formation), ε_L increase strongly. At the temperature where ε_{II} becomes positive again (being equivalent to the contraction towards low-volume martensite), ε_L exhibits a shoulder before overlapping with ε_{II} towards the peak value representing the middle of the transition with the largest slope in all measured quantities simultaneously. A distinct feature is observed for ρ , which shows a uniform shift of the transition evolution towards lower temperatures compared to M . The first significant deviation from zero is here observed in good agreement with ε_{II} and ε_L . This indicates an initial change of the magnetization upon first martensite nucleations/last martensite annihilations, while these do not lead to a significant macroscopic straining of the sample. While the length changes negatively and positively for ε_{II} and ε_L respectively, also the resistivity increases simultaneously due to the fact that it is directly coupled to the microstructure.

An analysis of the collective behavior for the simultaneously measured quantities is shown for a slow field application and removal cycle with a maximum field strength of 14 T at 275 K in Fig. 5.22 (c). The martensite formation will be discussed in the following by means of the field removal process. It is apparent that M , ε_{II} and ε_L follow the same path for the field removal from 14 T and deviate first at a magnetic field of 10.8 T. At this point, M decreases further, while the slope of ε_{II} inverts sign and increases whereas ε_L stagnates. Despite this temperature offset for the strain evolution, it shows a larger absolute slope upon further martensite formation and the curves of M , ε_{II} and ε_L match again around 8 T. However, they deviate again below fields of 7 T leading to the residual strain of a field-induced martensite that has also been observed from the pulsed-field measurements. Also for this measurement, ρ is showing a constant delay for the martensite formation upon field removal compared to the evolution of M . All the described observations are also present for the field application but shifted along the magnetic field axis because of the thermal hysteresis. Therefore, the "delay" of ε_{II} , ε_L and ρ is rather a "delay" of M , which underlines that this is not a time effect but related to the progression of martensite and austenite formation. Assuming a distribution of T_i throughout the sample, this effect can be related to the areas that are detected by the respective individual sensors. Whereas magnetization is measured for the whole sample, the strain

is only detected at a free surface of the sample and is thus dependent on the local stoichiometry and microstructure.

An explanation for the unique spike of the strain evolution at one end of the transition, which deviates from the expected straight decrease from austenite to martensite according to the evolution of M , cannot be provided with certainty at this point. One option can be the formation of a pre-martensite upon first nucleations inside the austenite phase, which has been observed for Ni-Mn-Ga alloys [229–231]. Instead of contracting, these first structures occupy a larger volume before forming the relaxed martensite structure that is energetically stable and contracts as expected. As a consequence, this intermediate stage of the structural transition also happens for the opposite transformation towards austenite forming an intermediate structure just before the last martensite features vanish completely. However, this pre-martensite state in Ni-Mn-Ga was found to be stable in an interval of 30 K to 60 K preceding the martensite transformation [229], whereas the observed behavior for Ni-Co-Mn-Ti is happening within 5 K. Such a behavior could also not be observed from the in-situ observations of the temperature-induced phase transition by optical microscopy in Section 5.3. In order to study this effect in more detail, high resolution methods are necessary that can surveil the structure and microstructure of the sample in-situ during the phase transition.

5.7 Correlation of microstructure and mechanical properties for a multi-stimuli cooling cycle

One promising perspective for the novel all- d Heusler system of Ni-Co-Mn-Ti is the application in the recently proposed multi-stimuli approach that sets up a cooling cycle with large cyclic temperature changes by making use of a large thermal hysteresis in multicaloric materials [43]. Already the first reports that proved the realization of Ni-Co-Mn-Ti Heusler alloys contain discussions about an enhanced mechanical stability, which is suggested to be attributed to the strong d - d hybridization bonds [167]. In combination with the sharp phase transition that is shown in Section 5.1 and the tunable thermal hysteresis and field sensitivity, the prerequisites for this alloy series as a candidate for the novel cooling technique are promising. In addition, the multi-stimuli cycle allows for the application of confined or even pulsed fields because no magnetically induced back transformation is desired. Therefore, the necessary field for inducing the phase transition is required only for a short time period since there is enough time for the heat exchange after the field removal. This fact enables the utilization of larger field changes, which also favors the usage of the Ti-Heusler-system with the large ΔT_{ad} values exceeding all other known magnetocaloric Heusler alloys for field changes of 10 T. However, the second stimulus used in the proposed cycle, namely the application of uniaxial pressure to transform the material back to its initial state, must also be optimized for the material system. Therefore, the mechanical stability as well as the pressure-induced phase transition will be evaluated in the following for arc-molten alloys as well as for net-shaped rods produced by suction casting.

In order to quantify the enhanced mechanical strength of the Ni-Co-Mn-Ti system, samples cut out

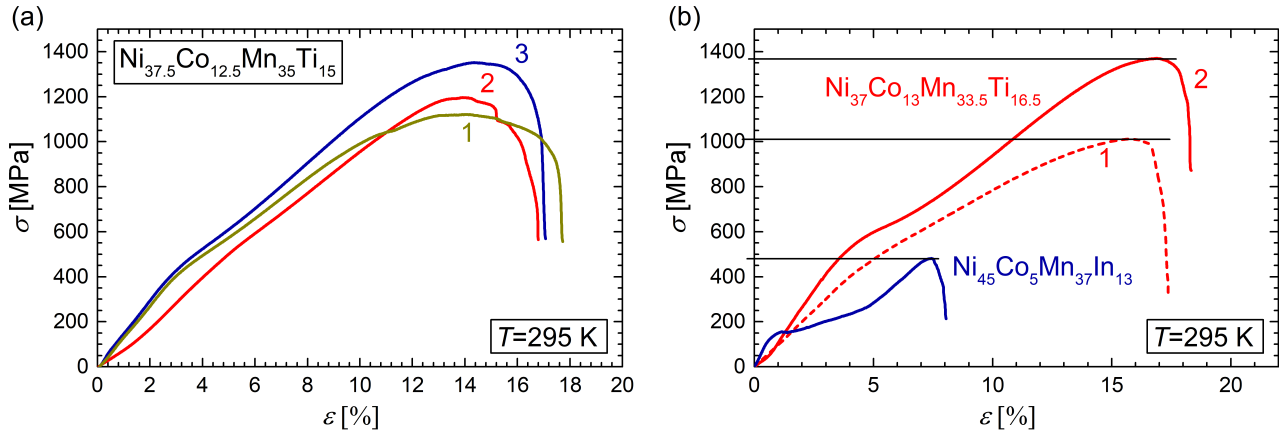


Figure 5.23: Stress-strain curves obtained from compression tests showing the technical stress and strain for three different pieces of the same $\text{Ni}_{37.5}\text{Co}_{12.5}\text{Mn}_{35}\text{Ti}_{15}$ sample in martensite state (a) and for two pieces of a $\text{Ni}_{37}\text{Co}_{13}\text{Mn}_{33.5}\text{Ti}_{16.5}$ sample in the austenite state in comparison with $\text{Ni}_{45}\text{Co}_5\text{Mn}_{37}\text{In}_{13}$. All measurements were conducted at room temperature with a constant strain rate of $4 \times 10^{-4} \text{ s}^{-1}$.

from different areas of an arc-molten sample are tested until failure in a compression test. The resulting stress-strain curves are depicted in Fig. 5.23. The samples in (a) exhibit a phase transformation above room temperature and are therefore assumed to be in the martensitic state at the testing conditions. The microstructure of this sample does not show the abnormal grain growth that has been discussed in Section 5.3, but a regular austenite grain size distribution similar to the one in Fig. 5.4 (b) with grain sizes around $50 \mu\text{m}$ to $200 \mu\text{m}$ for the parent austenite. The three different sample pieces used for statistical distribution show a deviating compression strength upon failure ranging from 1100 MPa to 1350 MPa. This fluctuation is due to variations in the microstructure because the cuboids of $2.5 \times 2.5 \times 5 \text{ mm}^3$ were cut out of one sample slice showing the tendency of finer grain sizes close to the bottom part, where the sample was in direct contact with the cooled plate of the melting setup, thus experienced the highest cooling rates upon solidification (sample piece 3). In addition local defects such as pores can cause preferred failure of the sample at lower stresses as a result of eased crack formation and propagation.

In Fig. 5.23 (b), an austenitic sample with a transition temperature of $M_s = 250 \text{ K}$ upon cooling is shown in comparison to an austenitic Ni-Co-Mn-In sample. There is a clear change in slope at around 600 MPa and 4 % strain. This softening of the curve is attributed to the phase transition that is induced by the uniaxial pressure. In analogy to the magnetic-field-induced transformation, the transition temperature is shifted to higher temperatures (opposite to the effect of a magnetic field) causing a conventional elastocaloric effect. In the ideal case, this effect would be represented by a horizontal line as it is observed for best elastocaloric materials like NiTi alloys, because the transformation-related strain is induced causing an elongation/contraction of the sample without further change in the applied stress. This estimation leads to an approximation for the pressure sensitivity of the transition $\frac{dT_t}{d\sigma}$ of 75 K GPa^{-1} . After the transformation, the characteristic stress-strain behavior of the martensite continues. Also for this sample, the obtained

compression strengths range from 1000 MPa to 1400 MPa. In comparison with the Ni-Co-Mn-In alloy, which experiences a phase transformation from austenite to martensite and fails at around 500 MPa, the mechanical strength of the all-*d* Heusler alloy is significantly enhanced by a factor of 2-3. On the one hand, this is attributed to the reduced grain size compared to main group Ni(-Co)-Mn-X Heusler alloys, which enhances the yield strength according to Hall-Petch [216, 217]. On the other hand, the hybridized *d-d* bonding between Ti and Mn atoms is reported to contribute to the mechanical strength from first-principles calculations [167], which is however difficult to quantify.

Regarding the application of a material in a consecutive cycle of applying magnetic field and pressure, the material needs to be ideally produced already in a shape that enables the application of both stimuli. Cutting cuboids out of an arc-molten drop is a laborious approach and the best geometry for a uniaxial pressure loading is a cylindrical shape to avoid stress concentration at edges. Therefore, the method of suction casting has been applied, where the melt of the alloy is cast into a cylindrical mold by a vacuum inlet at the bottom. An additional beneficial point of this production technique is a tailored fine microstructure of the as-cast state that is produced by the directional solidification towards the center of the sample. This microstructure is usually also leading to much finer grains, which is expected to enhance the mechanical stability of an alloy.

The microstructure of two as-cast samples from suction casting into a mold with diameter of 3 mm is depicted in Fig. 5.24 (a) and (d). A columnar growth of grains with a length of 300 μm is observed starting at the circumference that has been in direct contact with the water-cooled mold. In the center of the samples, a fine microstructure with globular grains of 50 μm to 150 μm occurs. This tendency of more globular grains is again different from Ni-Mn-In suction casting microstructure (similar to arc melting method discussed in Section 5.3), which has been used for the proof-of-concept measurement of the multi-stimuli approach [43].

In order to adjust also the heat treatment to the new production procedure, different annealing steps were carried out at temperatures of 1223 K (Fig. 5.24 (e)), 1273 K (Fig. 5.24 (b) and (f)) and 1323 K (Fig. 5.24 (c)). The sample annealed at 1323 K, which has been found to be ideal for arc-molten samples, exhibits an abnormal grain growth to two very large grains for the suction-cast rod that range over nearly the whole diameter (3 mm) of the cross-section. Only at the edges, some smaller grains represent the former columnar grains of the as-cast structure, which are in the order of 300 μm to 500 μm after annealing. Some individual grains of about 100 μm are still located at grain boundaries of the larger grains. Consequently, the benefit of creating a very fine microstructure by suction-casting is eliminated again after the heat-treatment step.

A reduction of the heat treatment temperature while keeping the time (96 h) constant in order to reduce the grain growth is not successful. Larger fractions of small grains equal in size as for the as-cast structure are present, but still the abnormal grain growth of few grains reaching several millimeter cannot be avoided. Due to the increased defect density resulting from the suction-casting process, the thermal activation for abnormal grain growth is reduced and the highest dislocation density acts as nucleation sites for recrystallization processes. Consequently, the higher grain boundary density also favors diffusion processes

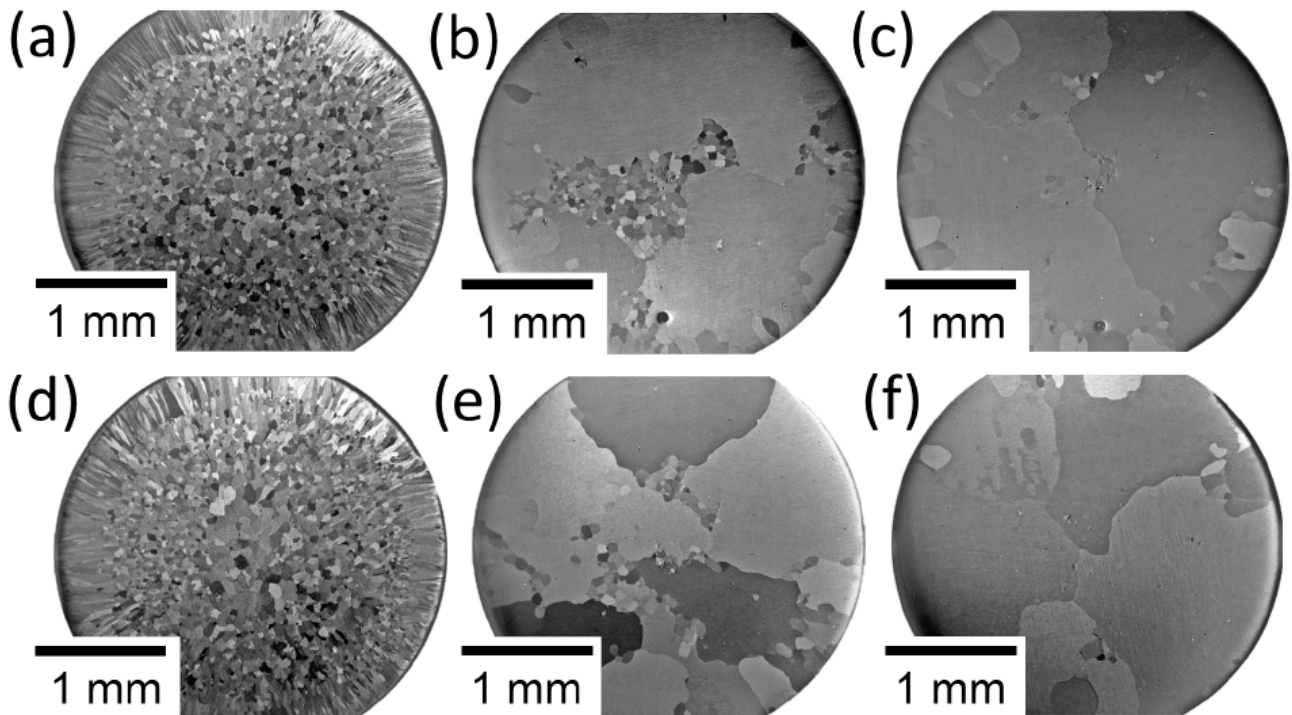


Figure 5.24: Microstructure of the as-cast state for two different suction-cast rods of $\text{Ni}_{37}\text{Co}_{13}\text{Mn}_{34}\text{Ti}_{16}$ (a) and (d). The first rod was annealed at 1273 K (b) and 1323 K (c) for 96 h. The second rod was annealed at 1223 K (e) and 1273 K (f) for 96 h. All images were obtained by optical polarization microscopy. Samples and microscopy images have been produced by Benedikt Beckmann within the framework of his Master Thesis [213].

and the finer microstructure results in more efficient homogenization of the stoichiometric variations already at lower temperatures. As a result, the best annealing for the suction-cast samples is found to be at 1273 K for 96 h, indicated by the temperature-dependent magnetization measurements in Fig. 5.25 (a). However, a further reduction of the annealing temperature in order to reduce the abnormal grain growth is not meaningful because it would deteriorate the transition width. Consequently, an optimal trade-off between preventing large grain growth and homogenizing the sample stoichiometry must be achieved.

In order to assess the properties of these samples under the application of uniaxial pressure, the corresponding stress-strain measurements are illustrated in Fig. 5.25 (b). The as-cast state characterized by a two-phase microstructure and very fine grains shows unsurprisingly the highest compressive strength of up to 1900 MPa. The variation of this value for the two rods is quite large as the second sample only reaches a maximum stress of 1400 MPa before failure. The reason is the even higher fluctuation of pores and inclusions for the suction-cast process, which underlines the influence of the casting process on the mechanical stability of the samples. The same trend can be observed for the two annealing procedures of these rods at 1273 K (red), where the second rod (dashed line) shows a decreased compression strength compared to the other one. This confirms the dependence of the measured strength values on the two rods.

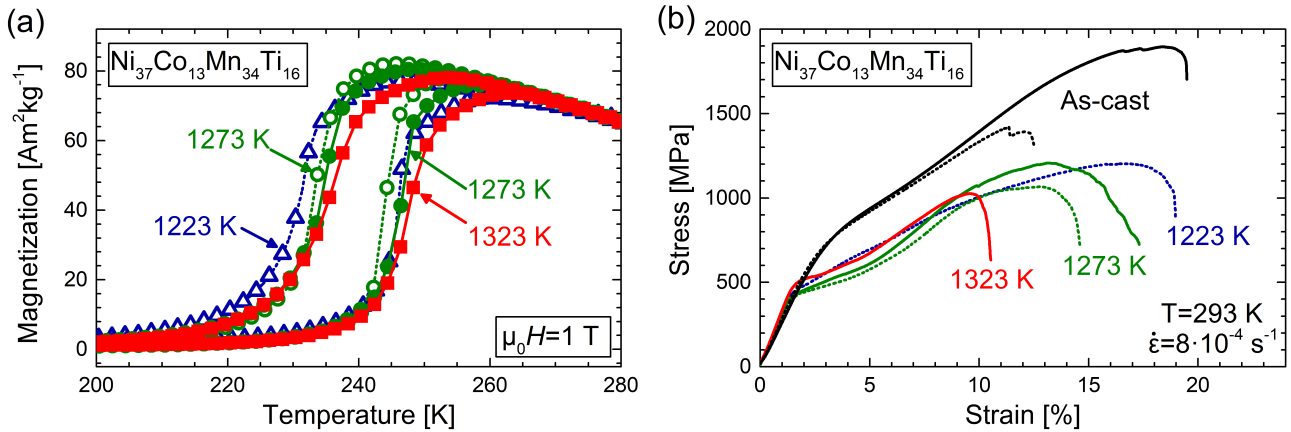


Figure 5.25: Temperature-dependent magnetization measurements in 1 T (a) and corresponding stress-strain measurements (b) for the as-cast state (green) as well as the different annealing temperatures of 1323 K (black), 1273 K (red) and 1223 K (blue) for two parent samples (solid and dashed lines). All measurements were conducted at room temperature with a constant strain rate of $8 \times 10^{-4} \text{ s}^{-1}$. The measurements were carried out by Benedikt Beckmann within the framework of his Master Thesis [213].

Nevertheless, comparing the annealing of the solid lines (rod 1) at 1323 K and 1273 K as well as for the dashed lines (rod 2) at 1373 K and 1223 K clearly shows the trend of a decreasing strength for higher heat treatment temperatures. This result is conform with the lower grain-boundary density due to the increased amount of very large grains that are formed with increasing annealing temperature. As a matter of fact, the suction-cast rod annealed at 1323 K and characterized by the large grain sizes, which are much coarser than for suction-cast and annealed Ni-Co-Mn-In [43], still shows a compression strength of 1000 MPa. This enhanced mechanical stability exceeds the strength measured for suction-cast Ni-Mn-In Heusler alloys, which is in the range of 350 MPa [166]. This cross-correlation of microstructure and compression strength confirms the suggestions in literature about an intrinsically superior mechanical strength for the all- d Heusler system of Ni-Co-Mn-Ti compared to the main group Heusler system of Ni-Co-Mn-In.

A temperature-dependent measurement of the strain under different constant pressures shown in Fig. 5.26 provides information about the behavior of a stress-induced phase transition for a suction-cast rod with a nominal Co content of 14 at. % ($\text{Ni}_{36}\text{Co}_{14}\text{Mn}_{35}\text{Ti}_{15}$). In Fig. 5.26 (a), the strain evolution depicts the phase transition upon cooling and heating. The compression test setup gives a positive strain for compression of the sample by convention. Therefore, the positive strain is equal to a contraction of the sample in the direction of the uniaxial pressure. The heating measurement for 400 MPa does not show the martensite-to-austenite phase transition because the sample failed at the expected transition temperature. Even though the compression strength is expected to be much higher, the volume increase upon first austenite formations leads to sample failure under the applied stress. Both characteristic temperatures T_t^c and T_t^h are shifted to higher temperatures by a uniaxial stress application. Since the transition width also broadens, the shift of the individual transition temperatures A_s , A_f , M_s and M_f do not show a

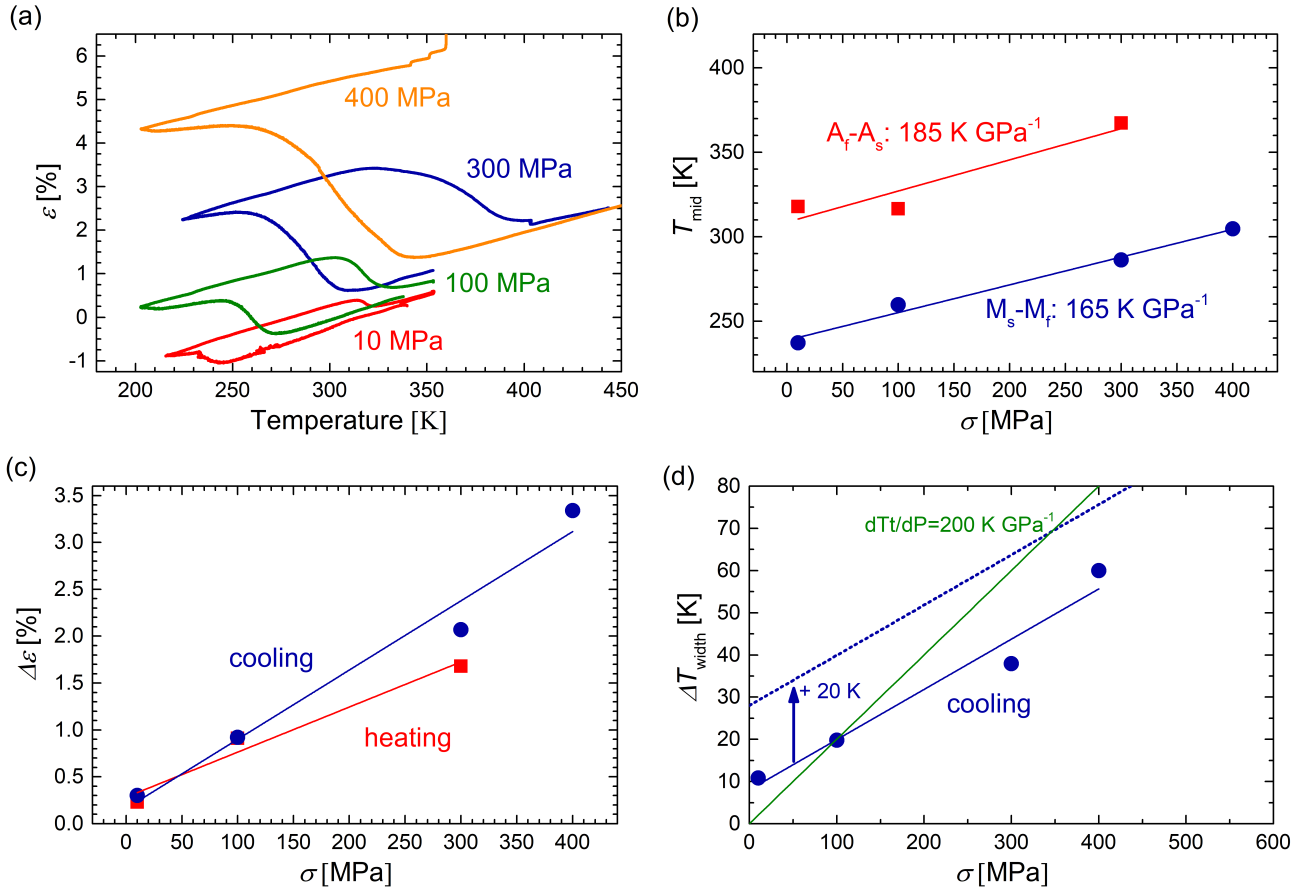


Figure 5.26: Temperature-dependent strain measurements of a $\text{Ni}_{36}\text{Co}_{14}\text{Mn}_{35}\text{Ti}_{15}$ suction cast rod under constant uniaxial loads of 10 MPa to 400 MPa (a). The shift of the transition temperature as a function of external stress is shown in (b), the stress-dependent transition strain in (c) and the stress-dependent transition width in (d).

consistent value for the temperature shift. Therefore, the middle value as the average between start and finish temperature is shown for the applied stresses in Fig. 5.26 (b). In the range of 10 MPa to 400 MPa, the average shift of the transition temperature amounts to 165 K GPa^{-1} to 185 K GPa^{-1} . This is significantly larger than for samples with a Co content of 13 at. %, which has been estimated by the induced transition during stress-strain measurements (75 K GPa^{-1} , Fig. 5.23) and determined in a similar setup for temperature- and stress-dependent strain measurements with stresses up to 80 MPa (45 K GPa^{-1} to 55 K GPa^{-1}) [232]. Consistently, studies on samples with 15 at. % of Co report on even larger values of $\frac{dT_t}{d\sigma}$ up to 220 K GPa^{-1} [211]. This suggests that the sensitivity of the phase transition towards both external stimuli, magnetic field and uniaxial pressure, is enhanced by an increasing Co content in the alloy. This large pressure sensitivities are a result of the large volume change between the austenite and martensite phase and make this alloy system a promising candidate for pure elasto- and barocaloric application. Very large adiabatic temperature changes of up to 30 K are reported for a uniaxial pressure application of 700 MPa [218].

With increasing applied pressure, the initial strain of the austenite state increases as well as the transition strain between the two phases, which is illustrated in Fig. 5.26 (c). At 10 MPa, the straining between austenite and martensite amounts to only 0.3 %, which increases drastically to more than 3 % under 400 MPa. Similar to martensitic variants oriented along the magnetic-field direction for the bidirectional strain investigations in pulsed fields (Section 5.6), the orientation of growing martensite variants is influenced by the applied stresses [233, 234]. The short axis is preferably aligned along the pressure direction, which is more pronounced for higher stresses applied. In addition, the width of the transition broadens with increasing external stresses up to 400 MPa, which is depicted by the data points in Fig. 5.26 (d). This is in agreement with similar measurements in lower stresses on a sample with 13 at. % of Co [232]. The reason is assumed to be a non-uniform stress distribution throughout the sample due to the uniaxial-stress application. As a result, heterogeneous stress fields influence the local transition temperature to varying extents in different areas of the sample. This leads to a broader distribution of transition temperatures, thus to an increased width of the overall phase transition. Both effects of increasing transition strain and transition width have also been found for other shape-memory alloys [233–235]. The direct consequence of the increased transition width are higher pressures required to induce a full phase transition. The intersection of the fit to the growing transition width with the green line representing the shift of T_t with an external uniaxial stress (assumed to be 200 K GPa^{-1}) is around 100 MPa, which is in a feasible range regarding the technical implementations of cyclic stress applications as well as the durability of the alloy. However, the additional consideration of the maximum adiabatic temperature change that has to be overcome in addition to the pure transition width (dashed blue line in Fig. 5.26 (d)) results in required stresses of around 300 MPa. In addition to these assumption, the sample is expected to also heat up because of the compression itself, which is neglected here but would lead to even larger stresses required. This value is close to the uniaxial stress of 400 MPa, at which the sample failed upon temperature-induced austenite formation. For the selection of a suitable material for the multi-stimuli cooling cycle, the changing transition width of the material has to be considered for an assessment of required stresses.

6 The MM'X Material Family

In the following chapter, the properties related to the magnetostructural phase transition of MM'X compounds are discussed in detail. This material system has attracted research attention recently because of sharp phase transitions that can be obtained. Large magnetocaloric effects by means of Δ_{ST} are reported especially for the two systems of MnNiGe and MnCoGe [148, 156]. A unique approach of these systems is the so-called isostructural alloying, which mixes the stoichiometries of two compounds that crystallize in the very same crystal structure. Hence, the production of phase-pure compounds with tailored properties is a major benefit of this method. An isostructural alloying approach will be analyzed for the substitution system of MnNiGe-FeNiSi with respect to the implications, benefits and disadvantages for tuning the martensitic phase transition, the structural and microstructural properties as well as the behavior under external pressure. The goal is to investigate a broad stoichiometry range in order to tailor the phase transition and to eliminate the amount of expensive Ge as much as possible. Furthermore, the magnetocaloric properties in low and high magnetic fields are evaluated in order to assess the viability of this material system for magnetocaloric application. The compounds that are used within this work are summarized together with selected properties of the crystal structure and the phase transition in Table 6.1.

Parts of this chapter are published in

- **A. Taubel**, T. Gottschall, M. Fries, T. Faske, K. P. Skokov, and O. Gutfleisch, *Influence of magnetic field, chemical pressure and hydrostatic pressure on the structural and magnetocaloric properties of the Mn-Ni-Ge system*, Journal of Physics D: Applied Physics **50** (46), 464005 (2017).

Table 6.1: Nominal sample compositions of the produced $\text{Mn}_{1-x}\text{Fe}_x\text{NiGe}_{1-y}\text{Si}_y$ system with the determined structural properties. Lattice constants and volume of the orthorhombic low-temperature phase were determined from XRD data, the transition temperatures upon cooling (T_t^c) and heating (T_t^h) correspond to the maximum of $\frac{dM}{dH}$ in an external magnetic field of 1 T for small pieces or were determined by DTA measurements (*) in zero magnetic field.

x	y	e/a	a_o [Å]	b_o [Å]	c_o [Å]	V_o [Å ³]	T_t^c [K]	T_t^h [K]	ΔT_{hyst} [K]
0	0	7.00	6.052	3.756	7.099	161.40	502.1*	551.1*	49.0
0.11	0	7.03	6.017	3.756	7.092	160.28	321.7	332.2	10.5
0.13	0	7.04	6.009	3.739	7.093	159.35	293.8	302.3	8.5
0.16	0	7.05	5.994	3.734	7.085	158.56	249.8	255.3	5.5
0.18	0	7.06	5.982	3.732	7.083	158.13	229.7	234.2	4.5
0.2	0.1	7.07	5.970	3.721	7.068	157.01	271.9	281.0	9.1
0.3	0.3	7.10	5.900	3.699	7.030	153.44	291.9	302.0	10.1
0.4	0.5	7.13	5.840	3.678	7.000	150.37	325.7	334.2	8.5
0.5	0.5	7.17	5.773	3.679	6.983	148.31	215.9	235.1	19.2
0.6	0.75	7.20	5.701	3.665	6.972	145.69	327.8	346.2	18.4
1	1	7.33	5.012	3.759	7.158	134.84	1136.1*	1164.1*	28.0

6.1 Effects of stoichiometry - the method of isostructural alloying

This work shows the influences of different substitutions on the MnNiGe material system. The favored substitutions for this system are based on the method of isostructural alloying, which was first proposed by Liu *et al.* [148] and applied frequently for this material system [167, 236–242]. It is based on the gradual substitution of one element for another by mixing two compositions of compounds that are stable in the very same crystal structure. The most prominent isostructural compounds for the MnNiGe-based MM'X alloy family are shown in the scheme of Fig. 6.1. Considering the MnNiGe compound as base material, an isostructural substitution can be achieved by replacing Mn by Fe, being equivalent to a mixing of the isostructural compounds of MnNiGe and FeNiGe along the path of creating a substitution series of $\text{Mn}_{1-x}\text{Fe}_x\text{NiGe}$. By this approach, the martensitic transition temperature is decreasing with increasing Fe content because the hexagonal austenite is stabilized and pure FeNiGe does not undergo a phase transformation down to liquid He temperatures. Additionally, the Fe atoms introduce ferromagnetic ordering by breaking the antiferromagnetic coupling of the Mn atoms [148]. For moderate transition temperatures in the room temperature region, an Fe substitution level of below $x = 0.15$ is required to establish a FOMT. Besides this magnetostructural transition, an additional transition from ferromagnetic to antiferromagnetic ordering exists at temperatures below 200 K for low Fe contents [242]. In a similar manner, the MnNiGe can be taken as the base compound to apply a substitutional series of Si on the Ge site towards MnNiSi ($\text{MnNiGe}_{1-y}\text{Si}_y$). In addition, these pathways of single-element substitution series can also be combined to establish a co-substitution of Fe and Si simultaneously. This leads to isostructural alloying systems of $\text{Mn}_{1-x}\text{Fe}_x\text{NiGe}_{1-y}\text{Si}_y$ with $x = y$ (MnNiGe-FeNiSi) and with $x = 1 - y$ (MnNiSi-FeNiGe). In

literature, the notation for these kind of substitutions often use the base compounds for the stoichiometric notation to name a substitution series as $(\text{MnNiGe})_x-(\text{FeNiSi})_{1-x}$.

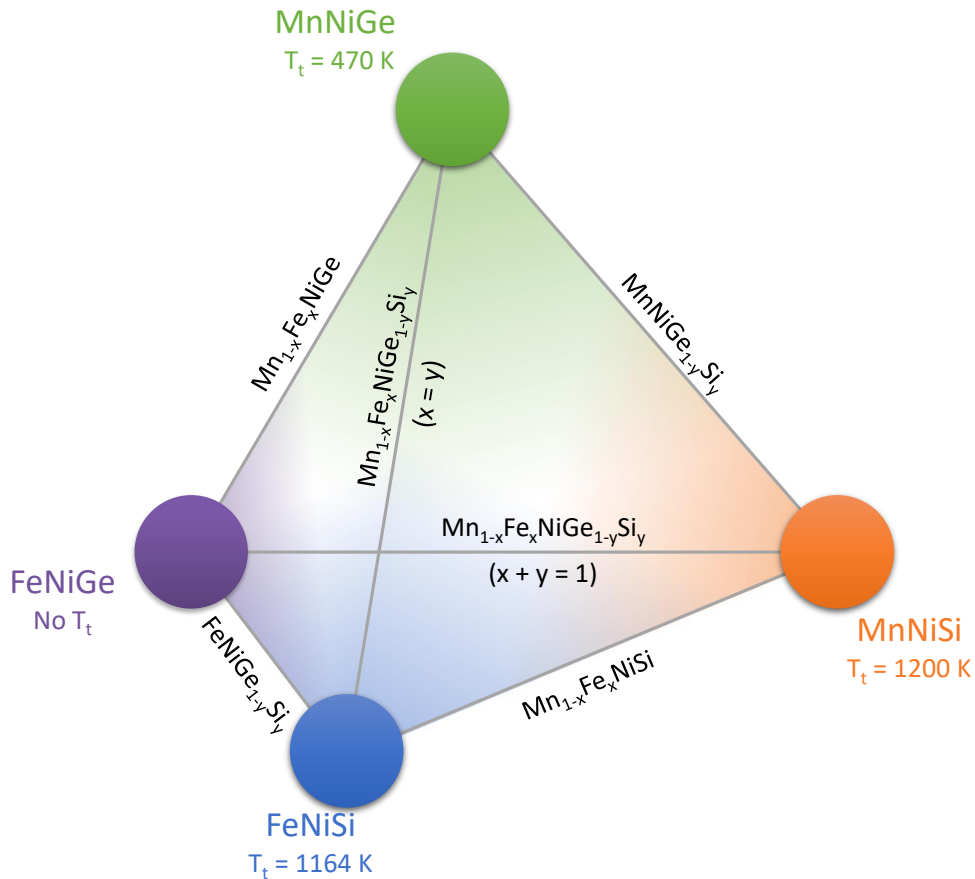


Figure 6.1: Scheme for different pathways of isostructural alloying of the MnNiGe material system. The ternary base compounds are located at the corners with the corresponding temperatures of the structural phase transition from low-temperature orthorhombic to high-temperature hexagonal phase. Single-element and restricted two-element substitutions are located on the edges connecting the corners, whereas the volume in between represents the whole range of the unrestricted $\text{Mn}_{1-x}\text{Fe}_x\text{NiGe}_{1-y}\text{Si}_y$ substitution space. The image is published in [149].

6.1.1 Thermomagnetic properties of the tuned phase transition

In order to evaluate the detailed effects of different pathways for the isostructural alloying, the established phase transitions are first analyzed with respect to the magnetic properties. Figure 6.2 (a) shows the magnetization curves for cooling and heating protocol in a magnetic field of 1 T as a function of temperature for different substitution levels of the $\text{Mn}_{1-x}\text{Fe}_x\text{NiGe}$ system. The phase transition from the high-temperature paramagnetic to the low-temperature ferromagnetic phase is of conventional first-order type and is characterized by a sharp change in magnetization. A thermal hysteresis of around 10 K docu-

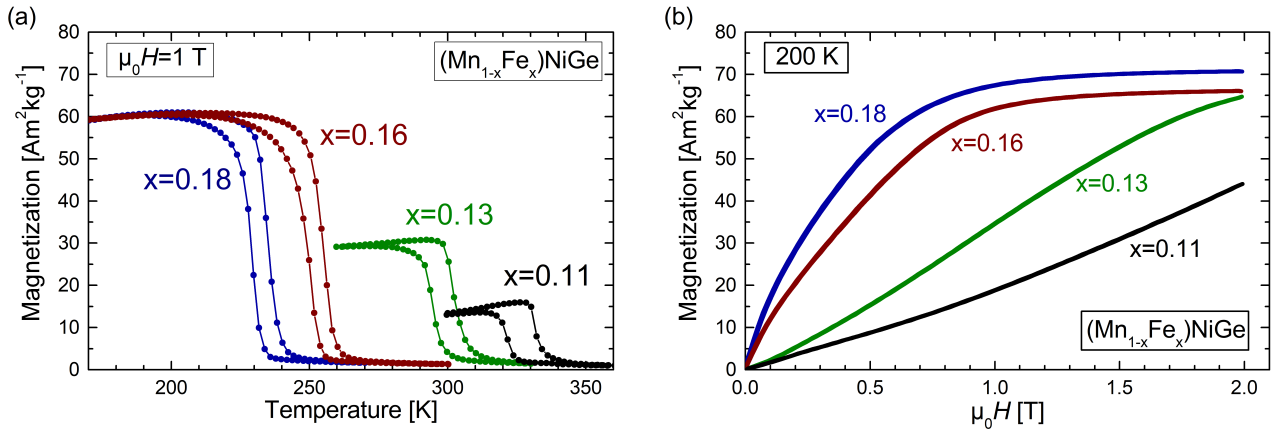


Figure 6.2: $M(T)$ -curves (a) of the $\text{Mn}_{1-x}\text{Fe}_x\text{NiGe}$ system for field cooling and heating in a magnetic field of 1 T with the corresponding $M(H)$ -curves (b) of the low-temperature phase at 200 K for the samples with $x = 0.11$ (black), $x = 0.13$ (green), $x = 0.16$ (brown) and $x = 0.18$ (blue).

ments the first-order nature of the phase transition. The increasing Fe content leads to a shift of T_t towards lower temperatures. Thus, the transition can be tuned from 470 K for MnNiGe to room temperature for Mn_{0.87}Fe_{0.13}NiGe and below. By fitting a linear regression line, the shift of the transition temperature by Fe substitution for Mn is approximately -13.5 K per 1 % of Fe substitution (equivalent to $x = 0.01$). The samples with $x = 0.11$ and $x = 0.13$ show a significantly lower magnetization of the low temperature phase in a magnetic field of 1 T. Thus, the magnetization change ΔM of the transition is reduced compared to the samples with higher Fe content and lower T_t . The reason is the initial antiferromagnetic state of the low-temperature phase for the Fe-free base compound MnNiGe. This can be verified by the field-dependent magnetization curves in the martensitic state for samples with varying Fe content in Fig. 6.2 (b). The saturation field of the material is lowered drastically due to the induced ferromagnetism for $x = 0.18$. The sample with $x = 0.13$ undergoes a transition at room temperature, however, it shows a less intense increase of magnetization with magnetic field and is not saturated for fields below 2 T. This reduced magnetization change of the transition lowers its performance for low-field applications drastically. However, a compound with an Fe content of $x = 0.18$ and a transition temperature at 200 K can show very good magnetocaloric properties, which will be discussed in detail in Section 6.1.2.

Complementary to the Fe substitutions for Mn, a substitution of Si for Ge is highly favored in terms of criticality and costs [36, 40] and leads to a similar substitution mechanism with the isostructural MnNiSi compound as shown for the path of MnNiGe_{1-y}Si_y in Fig. 6.1. However, T_t of pure MnNiSi is around 1200 K resulting in a rise of the structural transition temperature with increasing Si content. A comprehensive study on the magnetic properties of the substitution system MnNiGe_{1-y}Si_y from $y = 0$ to $y = 1$ has been reported by Bazela *et al.* [243]. It has been shown that phase-pure samples of the orthorhombic low-temperature phase can be produced in the whole range of Si substitution. A linear reduction of the orthorhombic lattice parameters is reported, which results in a decreasing cell volume of about 9 % from MnNiGe (162 Å³) to

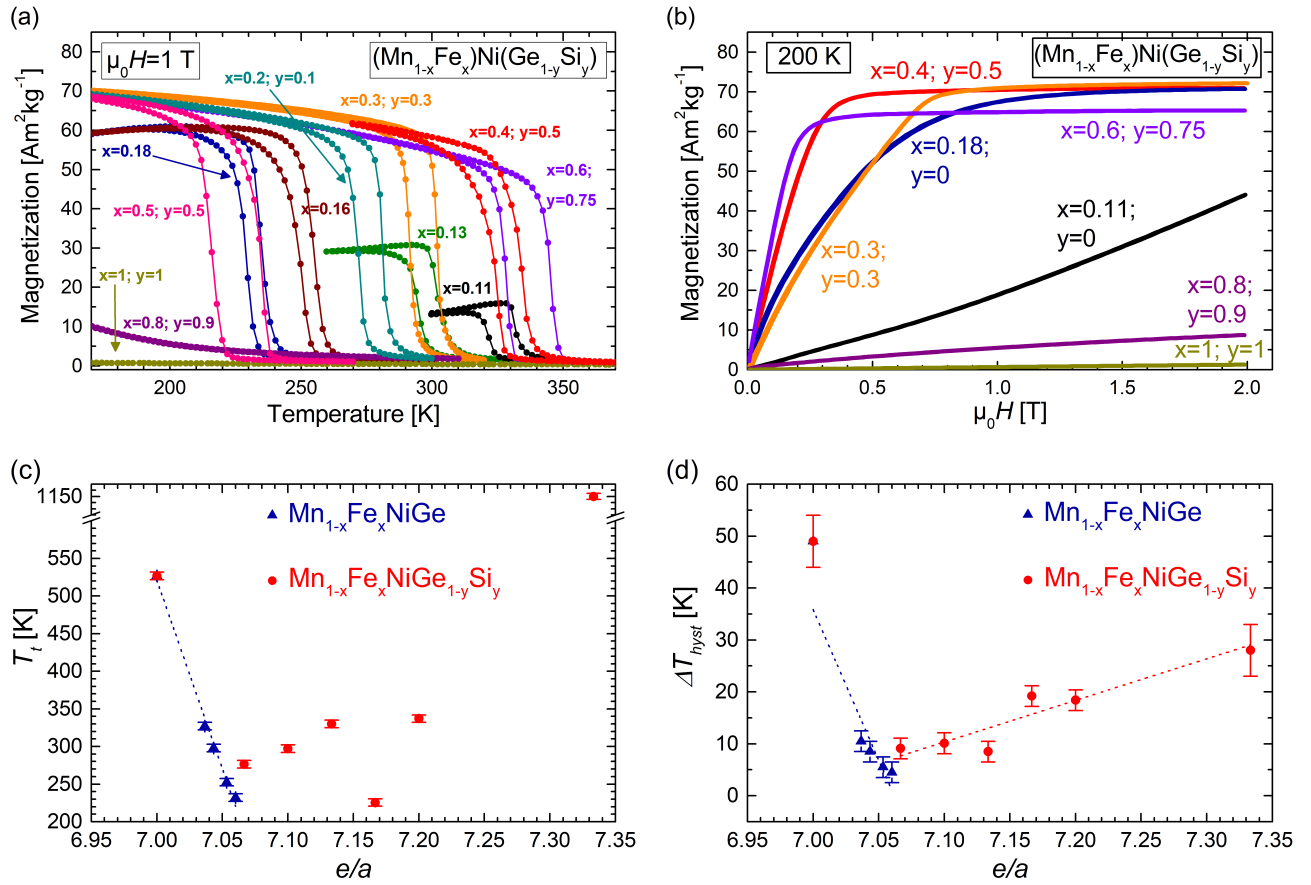


Figure 6.3: $M(T)$ -curves of the $\text{Mn}_{1-x}\text{Fe}_x\text{NiGe}_{1-y}\text{Si}_y$ system for field cooling and heating in a magnetic field of 1 T (a) with the corresponding $M(H)$ -curves for selected samples of varying Fe and Si content in (b). In addition, the evolution of the transition temperature T_t (c) and the thermal hysteresis width ΔT_{hyst} (d) are shown as a function of the e/a ratio for both substitution systems of $\text{Mn}_{1-x}\text{Fe}_x\text{NiGe}$ (blue triangles) and $\text{Mn}_{1-x}\text{Fe}_x\text{NiGe}_{1-y}\text{Si}_y$ (red circles).

MnNiSi (147 \AA^3). Similar to the Fe substitution, the initial antiferromagnetism of the orthorhombic phase of MnNiGe is changing to ferromagnetic behavior for $y \geq 0.3$. Simultaneously, the Néel and Curie temperature are increasing from 346 K for MnNiGe to 615 K for MnNiSi [243].

In order to follow the line of isostructural alloying for MnNiGe and FeNiSi , a substitution of two elements can be carried out simultaneously by fulfilling the condition of $x = y$ for the system of $\text{Mn}_{1-x}\text{Fe}_x\text{NiGe}_{1-y}\text{Si}_y$. Similarly, an isostructural alloying of FeNiGe and MnNiSi leads to the condition of $x + y = 1$ and the phase transition temperature is increased drastically from low to high y -values. This leads to a small region for a phase transition around room temperature for $x = 0.42 - 0.45$ ($y = 0.55 - 0.58$) [236]. In order to tune the structural phase transition in a very broad temperature range and to adjust the magnetic properties accordingly, the Fe and Si content can also be chosen freely for the $\text{Mn}_{1-x}\text{Fe}_x\text{NiGe}_{1-y}\text{Si}_y$ system [167]. This substitution method is then represented by the whole volume of the depicted tetrahedron in Fig. 6.1 and

will be investigated in detail in the following discussion.

In order to maintain a first-order magnetostructural phase transition around room temperature, both substitution systems of Fe for Mn and Si for Ge in the parent MnNiGe can be combined. The rise of the transition temperature with Si substitution for Ge is to be compensated by a simultaneous substitution of Fe for Mn, which in turn stabilizes the austenite phase. By co-substituting Fe and Si towards the FeNiSi material, the amount of Ge in the compound can be reduced drastically. The resulting phase transitions for the produced sample series of $\text{Mn}_{1-x}\text{Fe}_x\text{NiGe}_{1-y}\text{Si}_y$ are shown by the corresponding $M(T)$ -measurements in an external field of 1 T in Fig. 6.3 (a). The transition temperature can be tuned in a broad temperature range around room temperature. The only condition that has to be considered here is that T_t has to be between the Curie temperatures of austenite and martensite in order to establish a ΔM . The main advantage of the simultaneous substitution of Fe and Si becomes obvious when comparing the samples $\text{Mn}_{0.87}\text{Fe}_{0.13}\text{NiGe}$ (green curve) and $\text{Mn}_{0.7}\text{Fe}_{0.3}\text{NiGe}_{0.7}\text{Si}_{0.3}$ (orange curve). The T_t of both samples is exactly the same at 292 K under cooling and 302 K under heating. However, the magnetization change of the Si-containing sample is in 1 T approximately twice as large as for the Si-free sample. The reason is the already mentioned antiferromagnetic contribution that is still present in samples with low Fe content. Introducing Si solves this drawback by two different means. On the one hand, it enhances the ferromagnetic interactions in the orthorhombic martensite phase [243]. On the other hand, it increases T_t , which requires a larger amount of Fe substitution to keep the transition at room temperature and also favors the ferromagnetism of the martensite. The result is an even lower saturation field (see Fig. 6.3 (b)) favoring low-field applications combined with a transition at room temperature for samples with simultaneous Fe and Si doping. As shown in Fig. 6.3 (b), the saturation field is lowest for the $\text{Mn}_{0.4}\text{Fe}_{0.6}\text{NiGe}_{0.25}\text{Si}_{0.75}$ sample reaching the saturation magnetization in external magnetic fields of around 0.3 T.

Furthermore, Fig. 6.3 (a) and (b) shows that there is an optimal level of Fe substitution with respect to the ferromagnetic properties of the orthorhombic martensite. Comparing the two curves of $\text{Mn}_{0.6}\text{Fe}_{0.4}\text{NiGe}_{0.5}\text{Si}_{0.5}$ (red) and $\text{Mn}_{0.4}\text{Fe}_{0.6}\text{NiGe}_{0.25}\text{Si}_{0.75}$ (purple) gives clear evidence that the ΔM of the transition is reduced again for the higher Fe content despite the similar T_t . This trend is confirmed by the even larger Fe substitution levels of $x = 0.8$ and $x = 1$, where the samples show a very low magnetization even though being in the low-temperature orthorhombic phase. Thus, the substitution of Fe cannot be arbitrarily high because the magnetic moment is mainly carried by the Mn atoms [244] and the ferromagnetic coupling between Mn and Fe atoms, respectively [148]. Therefore, no ferromagnetic behavior can be identified for the orthorhombic phase of the pure FeNiSi compound at room temperature and a FOMT cannot be established for those samples with eliminated Ge content.

The evolution of T_t depending on the e/a ratio in Fig. 6.3 (c) only reveals a trend for the sole Fe substitution system ($\text{Mn}_{1-x}\text{Fe}_x\text{NiGe}$). Because the martensitic transition temperature is directly proportional to the Fe content of the compound, a well-fitting linear regression line can be drawn. In contrast, the change of T_t for the simultaneous substitution system $\text{Mn}_{1-x}\text{Fe}_x\text{NiGe}_{1-y}\text{Si}_y$ cannot be reflected by a direct relation to the e/a ratio. Since the substitution of Si for Ge is not changing the total valence electron count of the compound but influences the transition temperature drastically, e/a does not correlate with T_t .

The combination of choosing the ratio between Fe and Si substitution determines the temperature of the martensitic transition because both influence T_t in the opposite direction and with different magnitude. For further systematic evaluation, series of compounds with a fixed Si content (y) and varying Fe content (x) would need to be produced. This is expected to result in linear behavior of T_t within each series of constant y , all starting at the origin of pure MnNiGe. This is a significant difference to the family of Heusler alloys, where T_t can be predicted very well within one Ni(-Co)-Mn-X system by considering its average valence electron count [142, 185, 214]. For Ni-Co-Mn-Ti, it has been shown in Chapter 5 that this is universal for varying both Ni-Co and Mn-Ti ratio simultaneously.

The thermal hysteresis width plays an essential role for the cyclic behavior of a magnetocaloric compound. The $M(T)$ -curves in Fig. 6.3 (a) show that the compounds with medium Fe and Si substitution level ($x = 0.5$; $y = 0.5$ and $x = 0.6$; $y = 0.75$) show a significantly larger thermal hysteresis. The values of ΔT_{hyst} are shown as a function of the e/a ratio for all samples in Fig. 6.3 (d). In agreement with the obtained results from Liu *et al.* [148], the thermal hysteresis is drastically reduced from the parent MnNiGe alloy by the introduction of Fe. Against the usual trend of inverse magnetocaloric materials, where ΔT_{hyst} increases for reduced absolute transition temperatures (see Chapter 4), the $Mn_{1-x}Fe_xNiGe$ system shows a clear trend of reducing the thermal hysteresis with decreasing T_t caused by the Fe substitution. However, this trend is stopped at a minimum thermal hysteresis for the sample with $x = 0.18$. For further Fe and Si substitutions, ΔT_{hyst} is increasing again. A notable step occurs at the composition of $Mn_{0.5}Fe_{0.5}NiGe_{0.5}Si_{0.5}$, where the thermal hysteresis amounts to about 20 K. The FeNiSi compound even exhibits a ΔT_{hyst} of approximately 30 K for the purely structural martensitic transition.

6.1.2 Magnetocaloric properties

For small pieces of approximately 1 mg, very sharp phase transitions can be examined by magnetization measurements. An exemplary measurement is shown in Fig. 6.4 (a). The extraordinary sharp phase transition in combination with the low shift of T_t in an external magnetic field results in very large values for the isothermal entropy change Δ_{sT} . Values for Δ_{sT} of $-37.8 \text{ J kg}^{-1} \text{ K}^{-1}$ (cooling) and $-34.1 \text{ J kg}^{-1} \text{ K}^{-1}$ (heating) can be obtained from isofield $M(T)$ -measurements for a magnetic-field change ΔH of 2 T.

This value even exceeds the high entropy changes that have already been reported in literature for this material system [148, 159, 241]. However, the size and shape of the sample always has to be considered because it can have a drastic influence on the obtained values. Measurements of the transition behavior in terms of $M(T)$ - and Δ_{sT} - curves are strongly depending on the sample selection. Certainly, the behavior of very small fragments of a magnetocaloric material can vary a lot for different material families [57]. Small fragments of inverse magnetocaloric Ni-Mn-In Heusler samples show a broadened phase transition, but combine to a sharp overall transition by stress coupling in bulk samples. On the other hand, small La-Fe-Si and Fe_2P fragments with a conventional MCE show a sharp stepwise behavior and a broader transition for an ensemble of particles in bulk form. For the present conventional $Mn_{1-x}Fe_xNiGe$ system, sharpest transitions are observed for small fragments and their behavior is depending on the sample

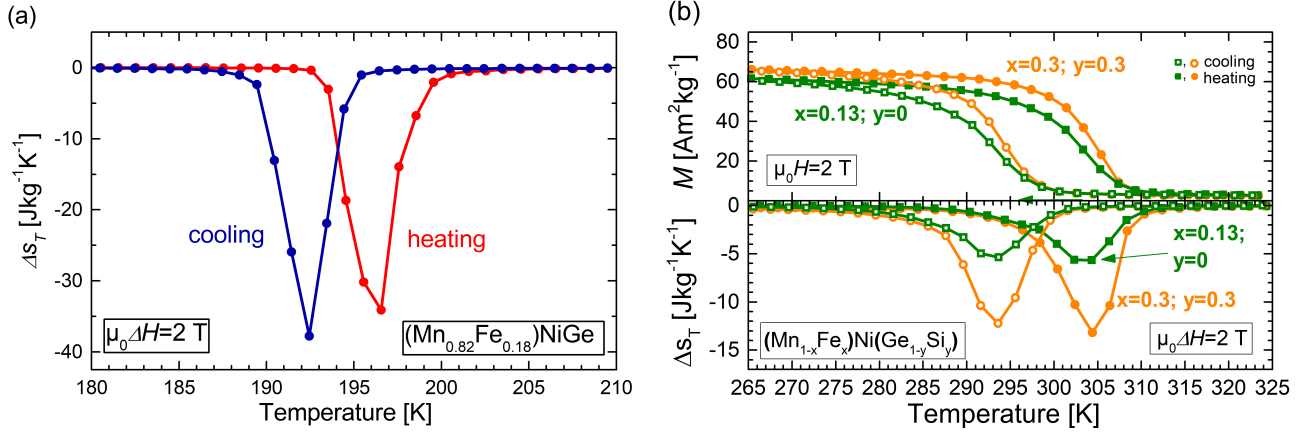


Figure 6.4: Isothermal entropy change for $\text{Mn}_{0.82}\text{Fe}_{0.18}\text{NiGe}$ from $M(T)$ -measurements upon heating (red) and cooling (blue) for a magnetic-field change of 2 T (a) and comparison of Δs_T and ΔT_{ad} of the first field application for the Si-free $\text{Mn}_{0.87}\text{Fe}_{0.13}\text{NiGe}$ and Si substituted $\text{Mn}_{0.7}\text{Fe}_{0.3}\text{NiGe}_{0.7}\text{Si}_{0.3}$ sample in a field change of 1.93 T and 2 T, respectively (b).

selection. Already slight variations in stoichiometry change the transition temperature drastically and the more particles contribute, the broader the overall transition gets. This effect will be discussed detailed in Section 6.3.

In order to give comparable values, a particle ensemble is chosen for the analysis of the magnetocaloric properties. For the determination of Δs_T , loose powder has been measured for the sample series in order to achieve a statistical average of many particles that are not constraint. Figure 6.4 (b) shows the temperature-dependent magnetization curves in 2 T as well as Δs_T for loose powder of $\text{Mn}_{0.87}\text{Fe}_{0.13}\text{NiGe}$ and $\text{Mn}_{0.7}\text{Fe}_{0.3}\text{NiGe}_{0.7}\text{Si}_{0.3}$. The already discussed enhanced ferromagnetism with lower saturation fields for the Si-substituted sample nearly doubles Δs_T from $-5.6 \text{ J kg}^{-1} \text{ K}^{-1}$ ($x = 0.13$) to $-13.2 \text{ J kg}^{-1} \text{ K}^{-1}$ ($x = 0.3$; $y = 0.3$) upon heating in a moderate external field change of 2 T. Despite the almost equal magnetization change in the maximum field of 2 T, the magnetization of the low temperature state is reduced drastically for lower field values. Although the entropy change of the powder does not reach the huge value for the single piece in Fig. 6.4 (a), this significant increase in Δs_T underlines the benefits from the simultaneous substitution of Fe and Si.

This effect of a strengthened FM of the orthorhombic phase with Fe and Si content is also reflected in the directly measured adiabatic temperature change shown in Fig. 6.5 (a) and (b) for a continuous measurement. The measured curves have been determined for loose powder that is held together by a conductive silver paste. In order to ensure a good thermal contact between sample and thermocouple, the powder has been mixed with the silver paste and the tip of the thermocouple has been placed in between. This arrangement has been pressed together by using low manual forces with a vice. This method aims at a good thermal contact between the particles without constraining them too much.

The Si-free samples show rather low maximum effects. The MCE reflected by ΔT_{ad} grows with increasing

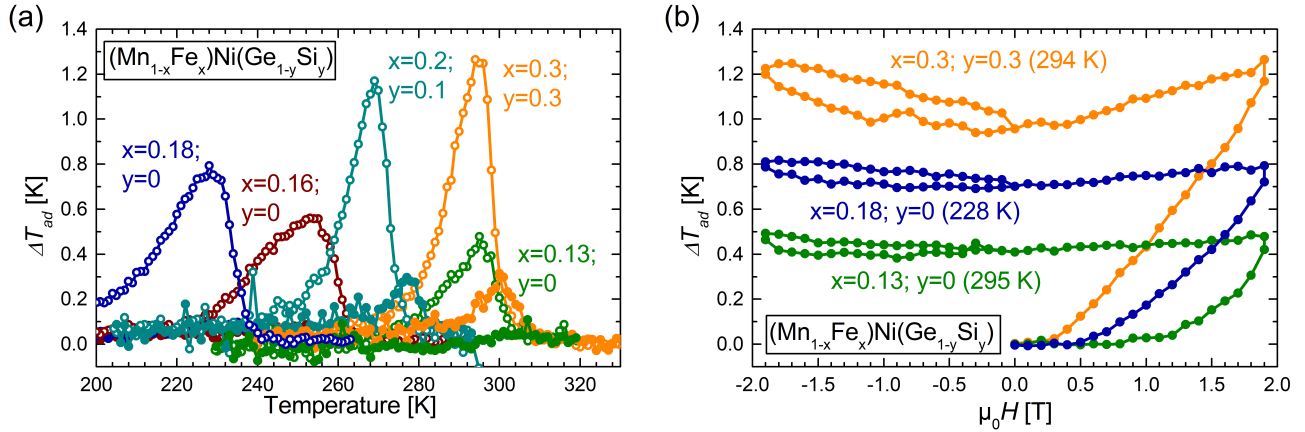


Figure 6.5: Measurements of the adiabatic temperature change for selected samples of the $\text{Mn}_{1-x}\text{Fe}_x\text{NiGe}_{1-y}\text{Si}_y$ series for a magnetic-field change of 1.93 T. The ΔT_{ad} values as a function of the starting temperature for the field application are shown for heating (closed symbols) and cooling (open symbols) in continuous protocol in (a). The magnetic-field-dependent evolution of ΔT_{ad} for two subsequent cycles is shown in (b) for $x = 0.13$, $x = 0.18$ and $x = 0.3$; $y = 0.3$ at the respective starting temperature where they exhibit the maximum effect.

Fe substitution from a maximum value of 0.5 K for $x = 0.13$ to 0.8 K for $x = 0.18$, which is the highest ΔT_{ad} of the Si-free series (see Fig. 6.5(a)). This trend is due to the already discussed AFM contribution still present in the samples with low Fe content, which reduces the magnetization change significantly in low magnetic fields below 2 T. The ΔT_{ad} measurements also support the co-substitution of Fe and Si into the MnNiGe system because they show an enhanced directly measured MCE compared to the Si-free samples. Especially the already discussed comparison between $x = 0.13$ (green) and $x = 0.3$; $y = 0.3$ (orange) gives an enhancement of the maximum ΔT_{ad} at the very same starting temperature from 0.5 K to 1.3 K.

The ΔT_{ad} upon heating is significantly lowered, which is attributed to the low sensitivity of the phase transition towards a magnetic-field application. In consequence, the hysteresis cannot be overcome completely and the magnetocaloric effect of the compound is strongly reduced for field application under heating protocol. This is the corresponding effect to inverse magnetocaloric materials, where the cooling protocol gives lower values of ΔT_{ad} because the transition is mirrored and the shift of T_t in a magnetic field is of opposite sign. Thus, the maximum ΔT_{ad} is always reached upon field application for the measurement protocol in which the sign of the temperature sweep during approaching the measurement temperature is opposite to the sign of $\frac{dT_t}{\mu_0 dH}$. Therefore, there is nearly no ΔT_{ad} signal obtained under heating for the Si-free samples. In contrast, the samples with combined substitution of Fe and Si also show a small ΔT_{ad} upon heating, which amounts to 0.3 K. This significant difference for the absolute ΔT_{ad} and the ability to overcome the thermal hysteresis is also expressed by the magnetic-field-dependent evolution of ΔT_{ad} over two subsequent field cycles shown in Fig. 6.5 (b). The applied magnetic field of 1.93 T is not enough to induce a complete phase transition because the temperature is still rising for the highest field values and suddenly stops for the field removal process. The direct comparison between $x = 0.13$ (green) and $x = 0.3$;

$y = 0.3$ (orange) shows that a significant ΔT_{ad} already starts to build up for field strengths below 0.5 T for the Si-substituted sample, whereas a field stronger than 1 T to 1.5 T is necessary to induce a ΔT_{ad} for the solely Fe-substituted sample. Also the cyclic effect is nearly zero for the Si-free sample series, which can be seen from the field removal process as well as for the second field cycle in the region of negative fields. Upon field removal after the first magnetization step, the temperature is not changing at all. This is clear evidence that the sample is locked in the (partly) induced martensitic state and the thermal hysteresis prevents a back transformation, which would lead to an adiabatic temperature change of opposite sign. Also the absolute temperature for the applied field of -1.93 T for the second field cycle is not significantly changing compared to the value in zero field at the end of the first cycle. In contrast, the $x = 0.3$; $y = 0.3$ sample exhibits a partially cyclic ΔT_{ad} of approximately 0.3 K for the first field removal and 0.25 K during the second field application. This is a consequence of minor loop behavior originating from the incomplete phase transition of the first field-application process.

Despite this increase of the magnetocaloric properties, the absolute temperature changes that can be achieved cyclically need to be improved drastically in order to compete with most promising alloy systems and to be considered for magnetocaloric heat exchanger setups.

6.2 Structural results for varying the stoichiometry

To investigate the structural properties that accompany the investigated systematic substitutions, structural investigations by means of XRD analysis at room temperature were carried out. The main question of interest is whether the substitutions influence the phase purity of the system and how they influence the lattice parameters of the expected phases. The resulting patterns recorded at room temperature for only Fe-substitutions ($\text{Mn}_{1-x}\text{Fe}_x\text{NiGe}$) are shown in Fig. 6.6 (a). The pure MnNiGe is present at room temperature in the low-temperature orthorhombic phase since the transition temperature is far above room temperature at 500 K. For the sample with lowest Fe substitution - $\text{Mn}_{0.89}\text{Fe}_{0.11}\text{NiGe}$ - reflections of both orthorhombic and hexagonal phases occur. The main characteristic orthorhombic signals are visible with reduced intensity compared to pure MnNiGe and the remaining signals originating from this structure are not above the noise of the measurement due to the reduced intensity. The intensities of the reflexes belonging to the hexagonal high-temperature phase are mainly stronger in intensity. The characteristic signals do belong here to the (102) and (110) reflexes at 19° and 20° , respectively. Signals from both phases (orthorhombic and hexagonal) are observed here although from magnetization measurements the transition takes place around 325 to 340 K for this sample (see Figure 6.2 (a)). At room temperature, only the orthorhombic low-temperature phase should be present. However, the preparation of powder for XRD measurement induces stresses in the material influencing the transition temperature of the compound. Similar observations have also been reported by Chen *et al.* [245] for the Mn-Fe-Ni-Si system with Ga substitution and Scheerbaum *et al.* [246] for Ni-Mn-Al Heusler alloys. This problem can be much more drastic for Heusler alloys because they usually show higher ductility and more stress is induced during crushing them into powder. The MnNiGe-system is more brittle and the production of powder can be

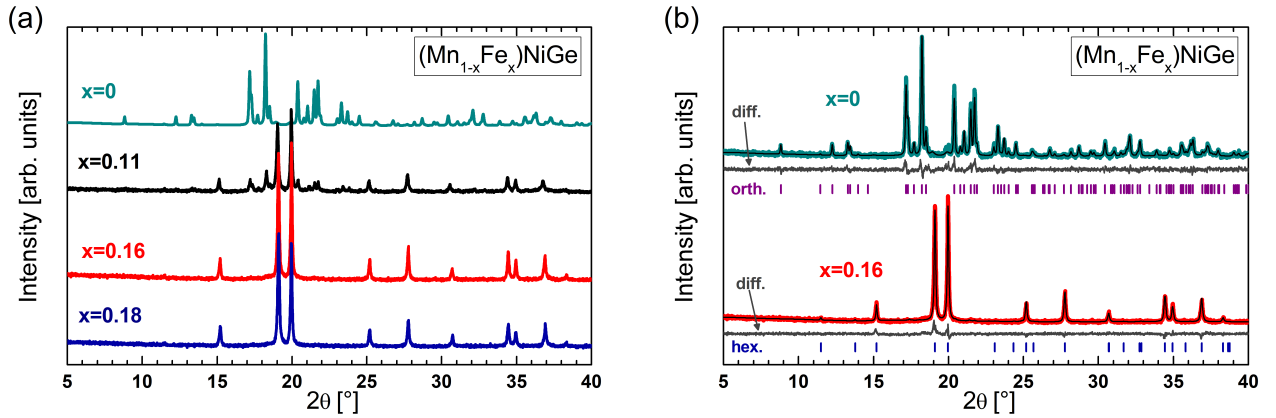


Figure 6.6: XRD patterns recorded at room temperature for varying Fe contents of the Si-free $\text{Mn}_{1-x}\text{Fe}_x\text{NiGe}$ system (a) with two Rietveld refinements for phase-pure sample in the orthorhombic ($x = 0$) and hexagonal ($x = 0.16$) state (b). Calculated patterns are implemented by fine black lines, the respective difference to the measurement is shown in grey. Theoretical reflex positions are illustrated for the orthorhombic (purple) and hexagonal (blue) phase. The respective quality factors for the refinements are $\chi^2 = 1.69$ ($x = 0$) and $\chi^2 = 1.55$ ($x = 0.16$).

carried out much more gently. A possibility to eliminate this effect is by recovering the powder with an additional heat treatment. Nevertheless, the XRD patterns are of good quality and the reflexes do not show much peak broadening. An additional heat-treatment step was avoided in order to not risk changing the thermomagnetic properties by this additional processing step. For further Fe substitution ($x = 0.16$ and $x = 0.18$), the hexagonal high-temperature phase is stabilized even stronger and the samples transform below room temperature. The patterns reveal phase purity within the boundaries of XRD accuracy and only reflections of the hexagonal high-temperature phase are visible.

The indexing of the patterns and the assignment of reflexes to the corresponding crystal structures has been done by the Rietveld refinement method. The exemplary patterns for a phase-pure orthorhombic and hexagonal sample are shown in Fig. 6.6 (b) together with the calculated positions of the reflexes and the corresponding intensity of the patterns. For estimating the quality of the refinement, the difference signal between the measurement and the calculated pattern is included in grey. In addition, the dimensionless quality factor χ^2 can be considered for proving the reliability of the refinement. It is defined as the ratio of the squared deviations between observed (I_{obs}) and calculated (I_{cal}) intensities with the standard deviation $\sigma(I_{obs})$ of the measurement itself (Equation (6.1)) [247]. The lower this factor is, the better is the conformity of the fitted pattern with the measurement. A perfect agreement of measurement and model would give a quality factor of unity. For the two shown refinements, the quality factor is 1.69 (orthorhombic phase) and 1.55 (hexagonal phase).

$$\chi^2 = \frac{(I_{cal} - I_{obs})^2}{\sigma^2(I_{obs})} \quad (6.1)$$

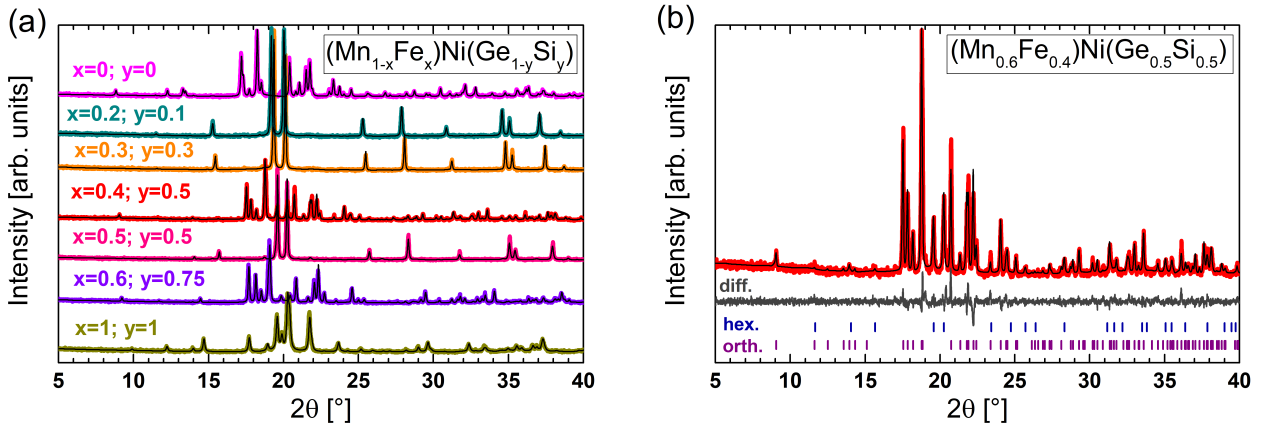


Figure 6.7: XRD patterns recorded at room temperature for varying Fe and Si contents of the $\text{Mn}_{1-x}\text{Fe}_x\text{NiGe}_{1-y}\text{Si}_y$ system (a). Samples with transition above room temperature are in orthorhombic or mixed state. One exemplary Rietveld refinement for $\text{Mn}_{0.6}\text{Fe}_{0.4}\text{NiGe}_{0.5}\text{Si}_{0.5}$ with both orthorhombic and hexagonal phase present is shown in (b). The calculated patterns are overlaid by thin black lines, the respective difference to the measurement is shown in grey. Theoretical reflex positions are illustrated for the orthorhombic (purple) and hexagonal (blue) phase. The respective quality factor for the refinement is $\chi^2 = 1.72$. The Rietveld refinements for samples with Fe contents $x \geq 0.4$ have been performed by Tom Faske (TU Darmstadt).

In Fig. 6.7, XRD patterns recorded at room temperature are shown for the sample series with co-substitution of Fe and Si for Mn and Ge, respectively ($\text{Mn}_{1-x}\text{Fe}_x\text{NiGe}_{1-y}\text{Si}_y$). The reference pattern for the phase-pure orthorhombic crystal structure of MnNiGe ($x = 0; y = 0$) from Fig. 6.6 is also included here. Since the substitution level of Fe and Si has been chosen non-uniformly, the transition temperature for the series depicted here is not representing a continuous trend of shifted transition temperatures. Therefore, some samples do transform below and others above room temperature. All occurring reflexes can be attributed to one of the two expected phases for this alloy system.

Samples transforming significantly above room temperature show a pattern of the low-temperature orthorhombic phase, those below room temperature belong to the hexagonal phase. The pattern of $\text{Mn}_{0.6}\text{Fe}_{0.4}\text{NiGe}_{0.5}\text{Si}_{0.5}$ reveals a mixed state of both phases present at the measurement temperature, even though the transition from magnetization measurements is slightly above room temperature. The indexing of the pattern to the two crystal structures by means of a Rietveld refinement is shown in Fig. 6.7 (b). The positions of the reflections for both phases in Fig. 6.6 (a) and Fig. 6.7 (a) are shifted towards higher diffraction angles with increasing Fe and Si content in comparison to the purely orthorhombic pattern of MnNiGe and the characteristic hexagonal reflexes of $\text{Mn}_{0.89}\text{Fe}_{0.11}\text{NiGe}$ with the lowest Fe-substitution analyzed. This effect is especially pronounced in the different appearance of FeNiSi ($x = 1; y = 1$), which will be discussed later. The XRD evaluations prove that the method of isostructural alloying represents a strong method of tuning the phase transition of a magnetocaloric compound over a broad substitution range. Furthermore, the XRD results show that the paramagnetic phase of FeNiSi from Fig. 6.3 (a) is in the

orthorhombic state. Therefore, the structural phase transition to the hexagonal state cannot be detected by magnetic measurements and is determined by Differential Thermal Analysis (DTA) to be at 1164 K upon heating and at 1136 K upon cooling.

In order to investigate the influence of the substitutions on the lattice parameters of the two involved phases, the results of the Rietveld refinements are evaluated in detail. The calculated intensities match the measurements well over the whole substitution range of Fe and Si, as it is shown in Fig. 6.7 (a). In Fig. 6.8 (a), the unit cell volume and lattice parameters of both phases are depicted for a temperature-dependent XRD measurement for the $\text{Mn}_{0.84}\text{Fe}_{0.16}\text{NiGe}$ sample. At room temperature, only the phase-pure hexagonal pattern is present and only the lattice parameters of this structure appear for the highest measurement temperatures. Down to 230 K, the corresponding lattice parameters $a_h = b_h$ and c_h are slightly decreasing due to the decreasing temperature. As a result also the volume decreases slightly.

The first detectable reflections of the orthorhombic phase appear at 210 K, which is below the transition temperature from magnetization measurements (see figure 6.2 (a)). This is presumably due to stress-induced effects during powder preparation, which stabilizes the high-temperature phase. These stress effects account for a significant influence on the transition properties and phase stabilities. Still at 100 K, where the martensitic phase transition should be completed, a signal of the hexagonal high-temperature phase is detected. For the sake of clarity, the values for the lattice parameters are not shown in Fig. 6.8 (a) for temperatures below 210 K. However, the still obtained hexagonal phase is represented by the data point for the unit cell volume (blue squares). From the co-existing phase patterns at 210 K, the change of crystal structure can be discussed in detail. Since the transformation is of martensitic nature, no diffusion is taking place and the transformation from the lattice of the high-temperature phase to the one of the low-temperature phase can be described by transforming the unit cell axes into each other. Here, c_h transforms to a_o of the orthorhombic cell and is increasing during the phase transition. On the other hand, $a_h = b_h$ is converted to $c_o/\sqrt{3}$ with a decrease of the lattice parameter and to b_o without significant changes [248]. Thus, the change of the unit cell from hexagonal to orthorhombic phase is anisotropic with expansion and contraction happening in different unit cell directions. However, the absolute volume change is positive when taking the high-temperature hexagonal phase as reference.

At all temperatures, where both phases are present, the volume change $\frac{\Delta V}{V}$ that accompanies the phase transition between them can be compared directly. The orthorhombic unit cell has twice the number of formula units per unit cell volume compared to the hexagonal one. Therefore, the unit cell volume of the orthorhombic phase V_{ort} is divided by two for the correct comparison to the hexagonal unit cell volume V_{hex} during the phase transition according to Equation (6.2) [145].

$$\frac{\Delta V}{V} = \frac{\frac{V_{ort}}{2} - V_{hex}}{V_{hex}} \quad (6.2)$$

The resulting volume change between the two coexisting phases is around 2.82 % near the transition temperature and 2.93 % at 100 K. This volume change underlines the discontinuous character of the phase transition and is in good agreement with literature values [148]. Compared to other magnetocaloric

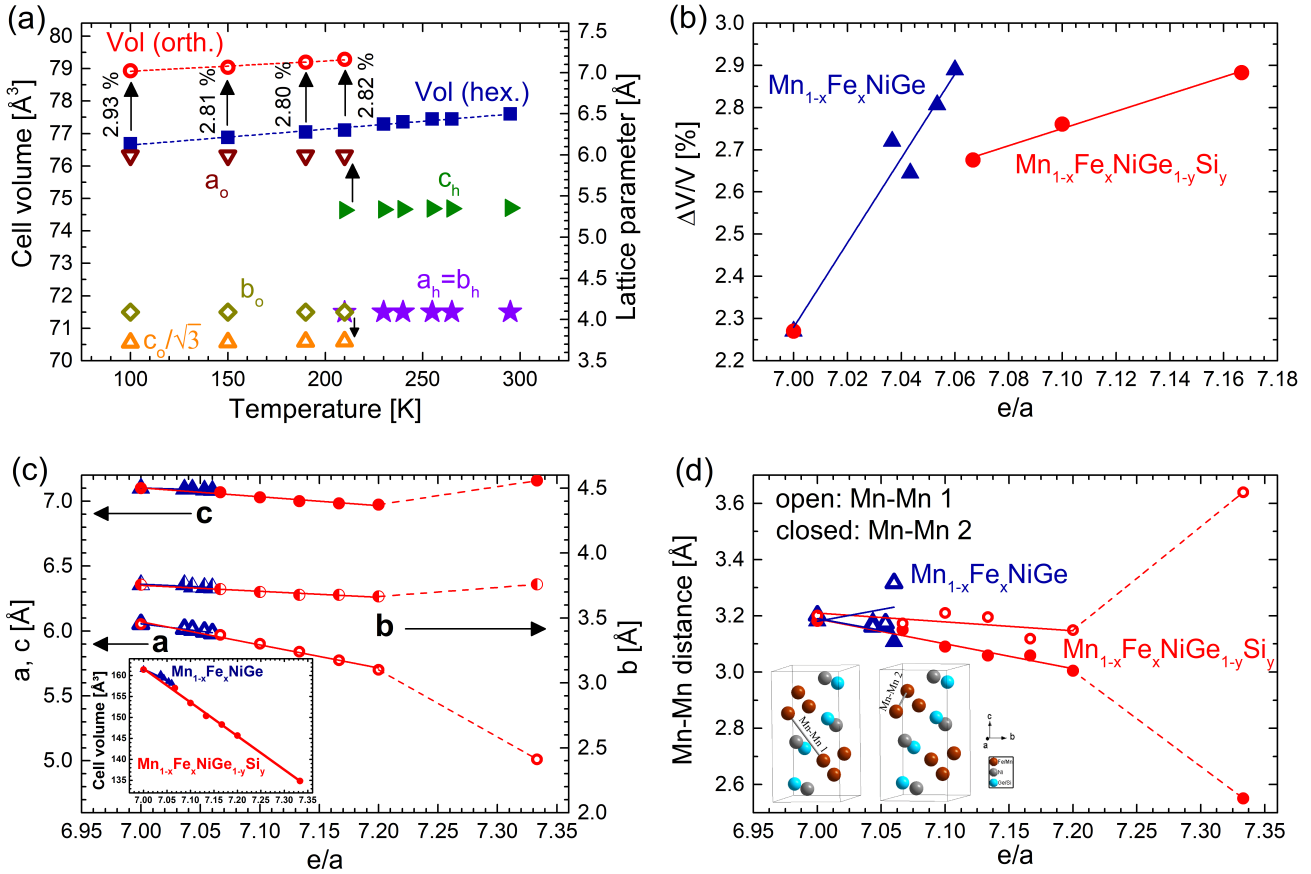


Figure 6.8: Volumes of the hexagonal (red) and orthorhombic phase (blue) determined from temperature-dependent XRD measurements of Mn_{0.84}Fe_{0.16}NiGe powder as well as the evolution of the lattice parameters during the phase transition (a). For the sake of clarity, parameters of the hexagonal phase are not included for temperatures lower than 210 K although a signal is present in the determined pattern. The volume change between hexagonal and orthorhombic phase for varying substitution levels of Fe and Si represented by the e/a ratio is shown for all produced Mn_{1-x}Fe_xNiGe_{1-y}Si_y compounds in (b). The corresponding lattice parameters as well as the evolution of the cell volume of the orthorhombic phase are plotted in (c). The evolution of the two shortest Mn-Mn distances within the orthorhombic unit cell are shown for the two substitutional systems in (d). The temperature-dependent measurement and the respective refinements of (a) as well as the determination of Mn-Mn distances in (d) have been performed by Tom Faske (TU Darmstadt).

materials that involve a magnetostructural phase transition of first-order type, this value is very large. A volume change of around 0.75 % to 1.5 % is obtained for the first-order phase transition of the La-Fe-Si system [111–113] and Ni-Mn-In Heusler alloys [143, 144], which already leads to problems concerning the mechanical stability [121]. A volume change of nearly 3 % - especially an anisotropic one in non-textured polycrystalline materials - creates enormous stresses between the individual grains and poses a problem for the cyclic stability of the compound. This issue will be addressed in more detail in Section 6.3.

The volume change $\frac{\Delta V}{V}$ between the orthorhombic and the hexagonal phase exhibits an increase for larger amounts of substitutions (Fig. 6.8 (b)). The increasing substitution level corresponds to a rising e/a ratio. Since the substitution of Si for Ge does not change the total amount of valence electrons, the e/a ratio is directly proportional to the amount of Fe substitution. The corresponding stoichiometries can be found in Table 6.1. Even though both Fe and Si doping decrease the unit cells of the two phases, the difference in volume between them is increasing. Two different slopes are evolving: a significantly larger slope for the $\text{Mn}_{1-x}\text{Fe}_x\text{NiGe}$ system, followed by a drop of the volume change by the first introduction of Si atoms into the structure. A second, much smaller slope, is then present for the $\text{Mn}_{1-x}\text{Fe}_x\text{NiGe}_{1-y}\text{Si}_y$ system.

As indicated by the shift of the peak positions in the XRD patterns in Fig. 6.6 and Fig. 6.7, the lattice parameters are changing with increasing substitution levels. This is shown for the orthorhombic low-temperature phase as a function of the Fe content in Fig. 6.8 (c). The linear regressions are separated for the two sample series. For the blue symbols, only Fe is substituted for Mn ($\text{Mn}_{1-x}\text{Fe}_x\text{NiGe}$) and the additional Si substitution for Ge ($\text{Mn}_{1-x}\text{Fe}_x\text{NiGe}_{1-y}\text{Si}_y$) is shown in red. For the cell volume shown in the inset, a linear decrease is observed for the complete region from $x = y = 0$ (MnNiGe) to $x = y = 1$ (FeNiSi). For the two systems with and without Si substitution, two slightly different slopes are evolving for the lattice parameters. The simultaneous substitution of two elements leads to a stronger decrease of the unit cell volume. These results are not surprising because the atomic radii of introduced Fe and Si are smaller than the ones of replaced Mn and Ge, respectively. Nevertheless, the slopes are similar even though the single substitution of Fe for Mn should not have a comparable impact because the atomic radius of Fe is only slightly smaller than the one of Mn. This observation indicates an induced magnetic interaction when placing Fe on Mn lattice sites. As a result, not only the magnetic order is affected, also the unit cell can be decreased. However, a similar reduction in the lattice constants is observed for the hexagonal phase, which is present in the paramagnetic state, where no magnetic interactions can cause this contraction.

Besides the linear decrease of the cell volume, also the single lattice parameters decrease in a linear manner for moderate Fe and Si contents (up to $e/a=7.20$). The evolution of the lattice parameters in Fig. 6.8 (c) for the pure FeNiSi is showing an odd behavior. All parameters a_o , b_o and c_o do not coincide with the linear extrapolation of the evolution of the lattice parameters for smaller amounts of Fe and Si substitution. While b_o and c_o experience an increase again to even higher values than for the MnNiGe starting compound, the a_o parameter shows a drastic drop to 5.01 Å. The origin of this phenomenon is a rearrangement of the atomic positions in the orthorhombic unit cell leading to a slight modification of the $Pnma$ structure as discussed by Landrum *et al.* [249]. An unexpected drop in the cell volume has been observed by the authors going from MnNiSi to FeNiSi in the alloy series of MNiSi compounds with

M being a 3d-metal. The authors report on a change in the Mn-Mn (Fe-Fe) bondings that are present in two intracellular distances, as shown in the inset of Fig. 6.8 (d). While the two distances are similar in the compounds with low Fe content, the shortest distance decreases along the *a*-axis and increases along the *c*-axis, leading to the observed trend of the corresponding lattice parameters. Therefore, this rearrangement of the unit cell causes a drastic change of the lattice parameters. However, the volume is still decreasing linearly from MnNiGe to FeNiSi for the produced sample series. This large change regarding the evolution of the lattice parameters by the structure modification can also be seen in the XRD patterns (Fig. 6.7 (a)). The reflexes of the orthorhombic *Pnma* structure shift drastically compared to the other orthorhombic patterns.

The variation in the orthorhombic cell is also demonstrated by the Mn-Mn (Fe-Fe) distances in Fig. 6.8 (d) as a function of the *e/a* ratio. The closed symbols show the evolution of the distance between the two Mn atoms in direction of the *a*-axis and the open symbols correspond to the distance along the *c*-direction, as it is visualized by the unit cells in the inset. The Mn-Mn distances are decreasing with rising amount of Fe as well as Fe and Si substitutions, disregarding the values for the FeNiSi compound. In the case of the substitution path of Si for Ge, this is in accordance with the observed magnetic results that indicate a change from AFM to FM for this individual substitution [243]. Since the interaction of the Mn atoms is responsible for the magnetism in the discussed MM'X compounds, a variation in their distance changes the magnetic behavior. For the Fe substitution on the Mn site, the breaking of the AFM coupling of the Mn atoms by the substituted Fe atoms is the main reason for the introduced ferromagnetism. By the simultaneous substitution of both Mn and Ge atoms, the ferromagnetism of the orthorhombic phase is favored by a combination of the two mechanisms.

These investigations give essential trends for the further development of this material system towards applications. The large volume change during the magnetostructural phase transition depicted by the XRD results leads to drawbacks concerning the usage of the material in bulk form because large evolving stresses result in a destruction of the samples. After several transition cycles, the remaining powder particles are too small in size to be used in a magnetocaloric cooling system in contact with a heat exchanging fluid. On the other hand, the large volume change leads to a high sensitivity of the phase transition to external pressure. With this additional field, the phase transition can be tuned very distinctly towards lower temperatures as discussed in Section 6.6.

6.3 Analyzing microstructure and mechanical stability

The microstructure of a compound is an important aspect that highly influences the mechanical properties of a material as well as the characteristics of the martensitic transition. The microstructures that result from the stoichiometric series of $\text{Mn}_{1-x}\text{Fe}_x\text{NiGe}_{1-y}\text{Si}_y$ are shown by optical microscopy images in Fig. 6.9 for a Si-free compound in (a) as well as for the gradual increase of co-substitution of Fe and Si for Mn and Ge, respectively in (b)-(f), towards the ternary FeNiSi shown in (g) and (h). From the two particles of $\text{Mn}_{0.84}\text{Fe}_{0.16}\text{NiGe}$ in (a), the dependence of the mechanical stability on the grain structure can be derived.

The particle on the right shows a certain contrast by using polarized light representing the different grain orientations on the surface. This particle has experienced severe mechanical destruction due to the large volume change of the phase transition. The different grain orientations lead to an anisotropic expansion exerting pressure on the surrounding. The high brittleness of the system results in crack formation and finally in a total separation of the particle in smaller fragments. On the other hand, a particle that consists of a single grain orientation can expand uniformly and is not experiencing such large pressures from surrounding grains. As a result, the particle is prevented from severe crack formation and disintegration. A consequence of this observation can be to use larger single crystals or textured samples, where the grain orientation is unified throughout the sample. This can be achieved by magnetic-field processing for example in order to align the particles and confine them in this orientation by using a resin matrix. Also a directional solidification approach can be worth investigating in future studies in order to produce textured samples.

An increase of the Si substitution for Ge in moderate amounts up to 20 % (b) and 30 % (c) does not lead to significant changes. Still cracked multi-grain particles are visible as well as faultless single-grain particles. Both images (b) and (c) show that the small grains of multi-grain particles are in the range of 50 μm to 200 μm , whereas the single-grain particles can have dimensions of up to 500 μm . The $\text{Mn}_{0.7}\text{Fe}_{0.3}\text{NiGe}_{0.7}\text{Si}_{0.3}$ compound (c) is in a mixed state at room temperature and shows small martensitic features. They differ from the ones in Heusler compounds, since they show linearly arranged structures over a larger area without clearly observable variant structures.

A further increase of the Si content leads to a change in the characteristic microstructure. Already the $\text{Fe}_{0.6}\text{Si}_{0.75}$ compound (d) illustrates a deviating behavior with less cracks present throughout the shown grain. The few cracks visible are in contrast to the often branching ones in (a) more uniformly going through the material, which is evidence for less nucleation points for the crack formation and indicates an enhanced mechanical stability. The two compounds with the highest Si content, namely $\text{Mn}_{0.2}\text{Fe}_{0.8}\text{NiGe}_{0.1}\text{Si}_{0.9}$ and FeNiSi show very large particles, which are not subject to massive cracking for the lowest magnification images in Fig. 6.9 (e) + (g). This qualitatively observed increase in mechanical stability is attended by larger grain sizes. In (e), elongated grains with dimensions of up to 2 mm along the long axis are observed, which is similar to the characteristic columnar growth of arc-molten Heusler alloys. On the other hand, also large globular grains are present in the millimeter-regime. The higher magnification of the bottom right corner of the particle in (f) depicts a region of refined grain sizes with globular grains in the range of 100 μm like they are characteristic for the edge areas of molten samples, where the direct contact to the cooled plate of the melting setup leads to high local cooling rates and finer grains than in the rest of the sample. Since the martensitic transition temperature of ternary FeNiSi is highly above room temperature, this compound is expected to be in the low-temperature martensitic state. However, martensitic structures are not visible on the first glance throughout the sample. A higher magnification shown in (h) highlights one area of the sample where martensitic features are observed. They can be seen only in certain grains and feature a distinct needle structure with typical twin boundaries and different sizes. The needles are forming an interconnected mesh and are mainly oriented in two different directions.

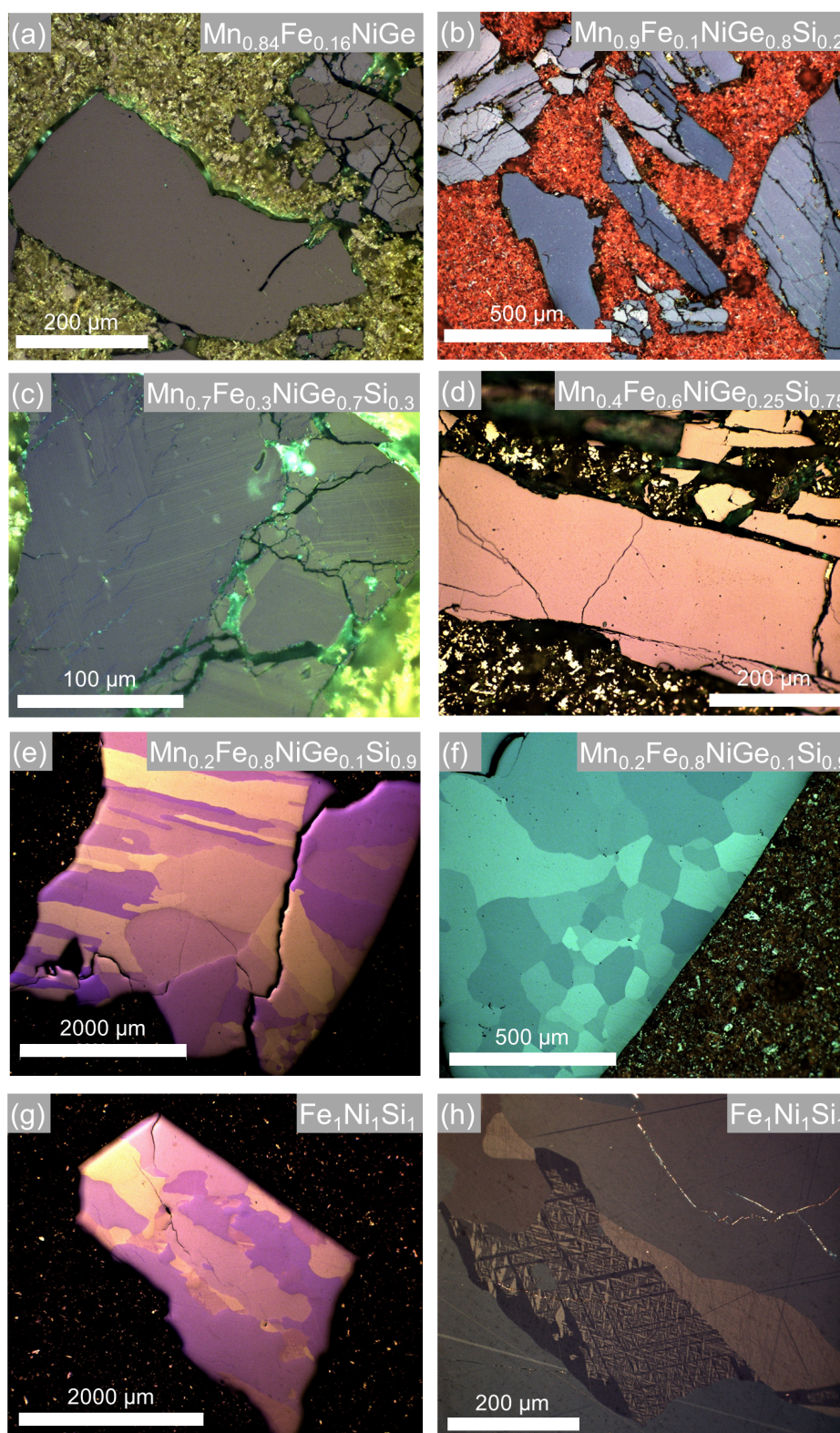


Figure 6.9: Microstructural images of the $\text{Mn}_{1-x}\text{Fe}_x\text{NiGe}_{1-y}\text{Si}_y$ series by optical light microscopy using polarized light for $\text{Mn}_{0.84}\text{Fe}_{0.16}\text{NiGe}$ (a), $\text{Mn}_{0.9}\text{Fe}_{0.1}\text{NiGe}_{0.8}\text{Si}_{0.2}$ (b), $\text{Mn}_{0.7}\text{Fe}_{0.3}\text{NiGe}_{0.7}\text{Si}_{0.3}$ (c), $\text{Mn}_{0.4}\text{Fe}_{0.6}\text{NiGe}_{0.25}\text{Si}_{0.75}$, $\text{Mn}_{0.2}\text{Fe}_{0.8}\text{NiGe}_{0.1}\text{Si}_{0.9}$ (e)+(f), and FeNiSi (g)+(h).

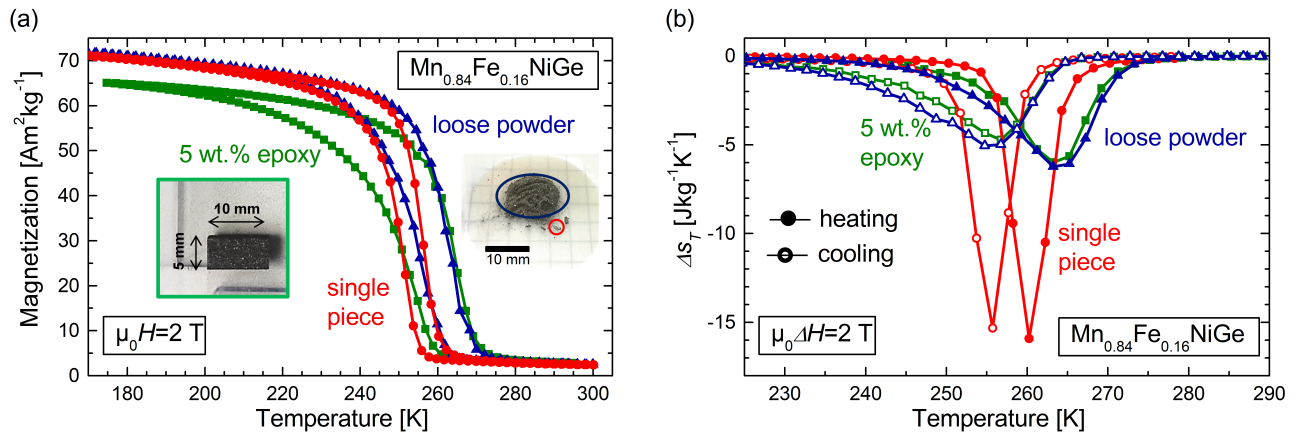


Figure 6.10: Magnetization measurements of $\text{Mn}_{0.84}\text{Fe}_{0.16}\text{NiGe}$ for a single piece (red), loose powder (blue) and epoxy-bonded powder (green) in an external magnetic field of 2 T (a) as well as the corresponding isothermal entropy changes (b) determined from $M(T)$ measurements for a field change of 2 T upon heating (solid symbols) and cooling (open symbols).

Since the transition temperature as well as the magnetic moment of the low-temperature phase are not usable for a FOMT around room temperature, the system is restricted for compounds with a substitution level of Si for Ge and Fe for Mn around 50 % each in order to be tailored towards promising magnetocaloric properties (see Section 6.1.1). For this compositions, the mechanical integrity is highly degraded by the large volume change of the phase transition causing a bulk material to disintegrate into smaller fragments or even fine powder. Small fragments that are found to be stable experiencing very sharp phase transitions with giant isothermal entropy changes are, however, not suitable to be utilized for large-scale applications exploiting a temperature change in a heat exchanger. Therefore, the processing of the material needs to be optimized for that purpose. One possibility can be the utilization of loose powder with particular particle size. Another option can be the bonding of powder with a glue in order to consolidate the material to mechanically stable structures. One advantage of this technique is the possibility to design an advantageous geometry for efficiently working heat exchangers. A comparison of these techniques by means of the temperature-dependent magnetization and the corresponding entropy change of the FOMT for $\text{Mn}_{0.84}\text{Fe}_{0.16}\text{NiGe}$ is depicted in Fig. 6.10 (a) and (b). The inset on the right side of (a) depicts the outcome of thermally cycling a bulk piece of material through the phase transition for ten times. The largest remaining fragments represent stable small pieces that are around 0.5 mm to 1 mm in size, weigh around 0.5 mg to 1 mg and have been used for characterization as single piece (red curves). The remaining fine powder was measured as loose powder (blue curves) and the image framed in green shows a bonded sample of thermally cycled powder with 5 wt. % of a two-component epoxy.

The $M(T)$ behavior demonstrates clearly that the single piece exhibits the sharpest phase transition. Since the loose powder represents a decoupled accumulation of many small particles with statistically distributed transition temperatures, the transition of the ensemble is broader compared to individual

particles. The broadening of the low-temperature end of the transition is explained by the stress coupling effect of multi-grain fragments that are not fallen apart yet [57]. Two particles/grains will transform in a broader manner because the volume expansion of the region with highest local T_t exerts stresses due to the volume change of the structural transition on the surrounding material, which shifts its initial transition to lower temperatures. The influences of stress will be discussed further in Section 6.6. This effect is even enhanced for the epoxy-bonded sample. The coupling of the material over the rigid matrix and the constraining of particles that are hindered to expand shift a large fraction of the single particle's T_t down, which results in the observed broadening of the transition towards lower temperatures. Assuming no negative stresses by the low amount of epoxy this effect is not relevant for the shrinkage of particles during austenite formation and the heating branches for the loose and bonded powder are in good accordance. In addition, the processing of the samples by bonding and pressing was carried out in austenite state, which is hence assumed to be the stress-free state. Because of the reduced amount of magnetic material in the sample, the total magnetization of the low-temperature phase is reduced for the bonded sample.

The respective entropy changes for the three sample morphologies in Fig. 6.10 (b) correlate with the magnetization behavior of the phase transition. Highest Δs_T is measured for the single piece reaching $-16 \text{ J kg}^{-1} \text{ K}^{-1}$ upon heating. The loose powder and the epoxy-bonded sample show strongly decreased values of $-6 \text{ J kg}^{-1} \text{ K}^{-1}$ upon heating and $-5 \text{ J kg}^{-1} \text{ K}^{-1}$ under cooling. This difference for the two branches of the hysteresis is due to the described stronger pronounced broadening of the martensite formation. Also the slight difference in Δs_T between loose and bonded powder is most pronounced for the low-temperature side of the peak, where also the significant differences in absolute magnetization and transition width are observed in the $M(T)$ -curve.

The main result is that the mechanical stability and the microstructure can be tuned to some extent by the stoichiometry of the isostructural alloying series. However, the very large prospects of this system from magnetization and Δs_T measurements of small fragments, which are often reported in literature without a comment on the sample shape and size, cannot be maintained for sample morphologies that are stable upon transition cycling and could be used as a magnetocaloric material in a working AMR. The reduction of Δs_T down to around $-5 \text{ J kg}^{-1} \text{ K}^{-1}$ for magnetic-field changes of 2 T makes the use of this material as a magnetocaloric material in low-field applications a challenge. For the production of a loose powder bed, the particles would need to be shaped spherically. These small spheres are then required to be classified by shape and transition temperature. The sorting by T_t might be carried out magnetically upon systematically controlled temperature variations, since the particles are at a certain temperature either para- or ferromagnetic. In this way, stacked fragments with sharp transition temperature ranges could be set up for an AMR system.

6.4 Effect of magnetic fields on the phase transition

It is essential for using the magnetocaloric effect to drive the phase transition in a cyclic manner by an alternating external magnetic field. As an example, the $M(T)$ behavior of $\text{Mn}_{0.7}\text{Fe}_{0.3}\text{NiGe}_{0.7}\text{Si}_{0.3}$ is

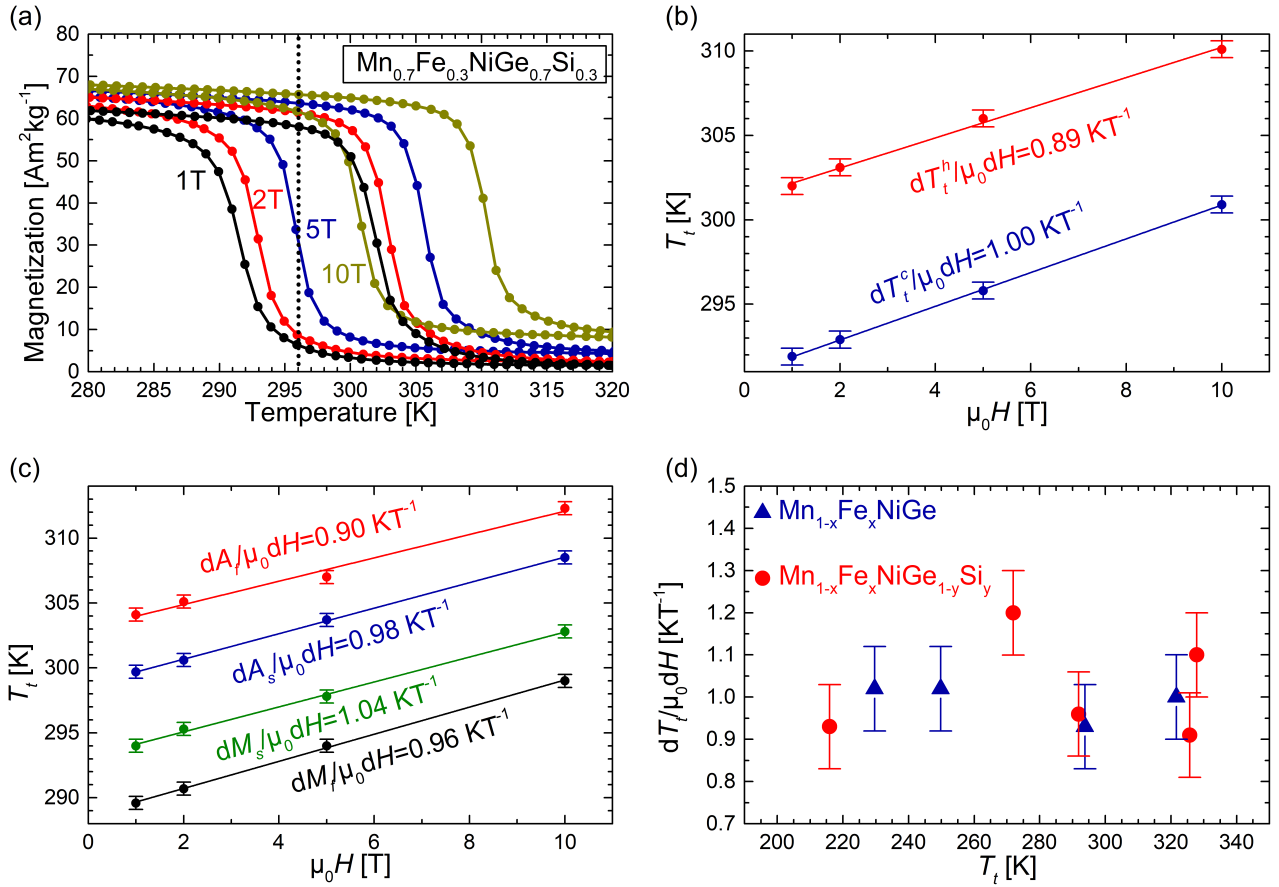


Figure 6.11: Magnetization measurements of $\text{Mn}_{0.7}\text{Fe}_{0.3}\text{NiGe}_{0.7}\text{Si}_{0.3}$ in magnetic fields of 1 T, 2 T, 5 T, and 10 T (a). The corresponding determination of $\frac{dT_t}{\mu_0 dH}$ is shown for the derivative-method (b) and the tangent-method (c), where linear fits are used to describe the shift of the respective transition temperatures in the different magnetic fields. An overview on all averaged values of $\frac{dT_t}{\mu_0 dH}$ for the different stoichiometries is plotted over the respective transition temperature in (d).

shown in external magnetic fields of up to 10 T in Fig. 6.11 (a). This sample is chosen for a representative discussion here since it shows a transition around room temperature, which is the main region of interest for magnetocaloric applications. The sensitivity of the phase-transition temperature towards an applied magnetic field is quite low. The dotted line at 296 K indicates a starting point for a field-induced transition. By considering this point in 1 T (black curve) and full austenite state under isothermal conditions (going along the vertical line without taking a ΔT_{ad} into account), a magnetic-field change to 5 T (blue curve) is not large enough to completely induce the martensite state. Only for even larger fields of 10 T (yellow curve), a complete phase transition from austenite to martensite can be induced.

In order to determine the shift of T_t in magnetic fields of different strength, two methods explained in Section 3.4 are applied. First, the results of the derivative-method are shown in Fig. 6.11 (b). The resulting

transition temperature for the cooling and heating branch are shown in blue and red, respectively, for the represented external field values of (a). Linear fits to the data points match very well. Therefore, it can be assumed that $\frac{dT_t}{\mu_0 dH}$ of this alloy is constant for magnetic fields below 10 T in a first approximation. The value is determined to be 0.89 K T^{-1} for the heating branch and 1.00 K T^{-1} for the cooling branch. In order to validate the method of determining $\frac{dT_t}{\mu_0 dH}$ from the derivatives, the tangent-method is applied here additionally. The determined values of A_s , A_f , M_s , and M_f are shown in Fig. 6.11 (c). It is evident by the good quality of the linear fit that the assumption of a constant $\frac{dT_t}{\mu_0 dH}$ up to 10 T is also valid here. The values are in good agreement with the derivative-method around 0.9 K T^{-1} to 1.0 K T^{-1} . Also for this method, the values for the heating branch (A_s and A_f) are slightly lower than for the cooling branch (M_s and M_f). However, both methods of determination do have sources of error that must be taken into account here. The derivative method relies mainly on a symmetric transition curve. The main property determining the accuracy is the step size between two data points of a $M(T)$ experiment. For the magnetization measurement in Fig. 6.11 (a), data points have been acquired in 1 K steps. The main challenge for the chosen material example is the low absolute value for $\frac{dT_t}{\mu_0 dH}$. Since a field change of 1 T only shifts the curve by 1 K, a larger step size between the data points would not resolve this shift properly. The reason is that the maximum of the first derivative can only be determined on a measured temperature value because the span in between can only be interpolated. The main source of error for the tangent-method is that the application of tangent lines to the measurement is rarely done unambiguously. On the one hand, the slopes of the ferromagnetic austenite region are often different, depending on the absolute field value. On the other hand, all the transition curves are not perfect and the determination of the characteristic transition temperatures is varying depending on the convention for applying the tangent lines, especially for asymmetric transition curves. The example of $\text{Mn}_{0.7}\text{Fe}_{0.3}\text{NiGe}_{0.7}\text{Si}_{0.3}$ shows that the derivative-method works well for a step size of 1 K between the data points. I need to emphasize here that the importance of this value is decreasing for larger slopes of $\frac{dT_t}{\mu_0 dH}$. The results are in good agreement to the tangent-method. However, since many measurement setups using permanent magnets or electromagnets provide fields of below 2 T, especially for samples that are not saturated in low fields, this method can lead to larger uncertainties than shown for this example in Fig. 6.11. An additional example will be shown later in Section 6.6.

The low magnetic-field sensitivity results in an extremely large difficulty of inducing the phase transition in low fields as it is discussed for Fig. 6.11 (a). The temperature difference between austenite/martensite start and finish temperature can be considered as an estimate for the transition width ΔT_{width} . For the $\text{Mn}_{0.7}\text{Fe}_{0.3}\text{NiGe}_{0.7}\text{Si}_{0.3}$ sample, this amounts to 5 K. However, this width does not necessarily represent a completed transition, since it is a graphical approximation and the magnetization at the determined temperature would still lead to minor loops of hysteresis. By taking the starting point of a magnetic-field cycle at 296 K and using the magnetization of the 1 T-curve as an indication for the phase fraction ($M(\text{martensite})=60 \text{ A m}^2 \text{ kg}^{-1}$, $M(\text{austenite})=2 \text{ A m}^2 \text{ kg}^{-1}$), an austenite fraction of 95 % is present at this temperature. The resulting width of the transition in order to reach an austenite fraction of 5 % for the cooling branch is 10 K. Using this approach also for the magnetization curves of other branches and

magnetic fields represented in Fig. 6.11 (a) results in values for ΔT_{width} between 8 K and 10 K. This means that a magnetic-field change ΔH_{ext} of around 7 T to 10 T would be required for inducing a completed phase transition for this definition and by assuming isothermal conditions. Since adiabatic conditions require even higher field changes, building up a significant ΔT_{ad} is not expected in low magnetic-field changes.

Compared to Heusler alloys as inverse magnetocaloric materials, the opportunities of tuning $\frac{dT_t}{\mu_0 dH}$ are decreased for the MM'X material systems with a conventional MCE. In order to investigate whether the applied substitution of Fe for Mn and Si for Ge has an influence on $\frac{dT_t}{\mu_0 dH}$, the averaged values over cooling and heating branch are summarized for all compounds of the produced $Mn_{1-x}Fe_xNiGe_{1-y}Si_y$ series that possess a coupled magnetostructural phase transition in Fig. 6.11 (d). The determined values are plotted depending on the respective transition temperature of the compound for the pure Fe-substitution (blue triangles) and the co-substitution of Fe and Si (red circles). It can be seen that there is no clear trend for an increasing level of substitution - neither for Fe nor for Fe+Si. More clearly, the absolute transition temperature of the compound does not play a role for the effect of an external magnetic field in the regarded temperature range from 200 K to 350 K. This is interesting because the initial magnetic transition of the orthorhombic low-temperature phase for pure MnNiGe is at 346 K [146]. Even though this is initially a Néel temperature that turns into a Curie temperature by elemental substitutions, the absolute value should increase towards the T_C of MnNiSi at 622 K [244]. Since the regarded transitions are far enough away from this T_C or T_N , a significant value of $\frac{dT_t}{\mu_0 dH}$ should be observable for the considerably large magnetization changes, which are varying around $60 \text{ A m}^2 \text{ kg}^{-1}$ to $80 \text{ A m}^2 \text{ kg}^{-1}$. It is possible that the transition is so far away from T_C of the low-temperature orthorhombic phase that the magnetization below room temperature is not changing significantly by varying the composition and thereby tailoring T_t .

Due to the low field-dependence of the transition temperatures, the applicability of the investigated MM'X material system for magnetocaloric cooling cycles is mainly limited by the reduced ability of a moderate magnetic field to induce the phase transition. The magnetization curve of the phase transition can only be shifted by around 2 K in fields of 2 T. This shift is not only too low to efficiently induce the FOMT, it is additionally far too low in order to overcome the thermal hysteresis in a range of 7 K to 10 K and to enable a cyclic application of the material for magnetocaloric cooling purposes. This value of $\frac{dT_t}{\mu_0 dH}$ is also much lower compared to the promising magnetocaloric Heusler system of Ni-Co-Mn-In, where a field-dependence for T_t of -8 K T^{-1} is responsible for directly measured temperature changes of 8 K for the first cycle and 3 K for further cycles [125].

The result is a relatively low adiabatic temperature change for the alloys of this material system investigated here as shown in Fig. 6.5. The sharp phase transitions and the large entropy changes cannot be transferred into reasonable temperature changes because the low magnetic fields are not sufficient to induce the phase transition completely. Even though the thermal hysteresis is quite low, it cannot be overcome by magnetic fields smaller than 2 T and the reversibility of the phase transition in cyclic fields only amounts to 0.3 K for the $Mn_{0.7}Fe_{0.3}NiGe_{0.7}Si_{0.3}$ sample.

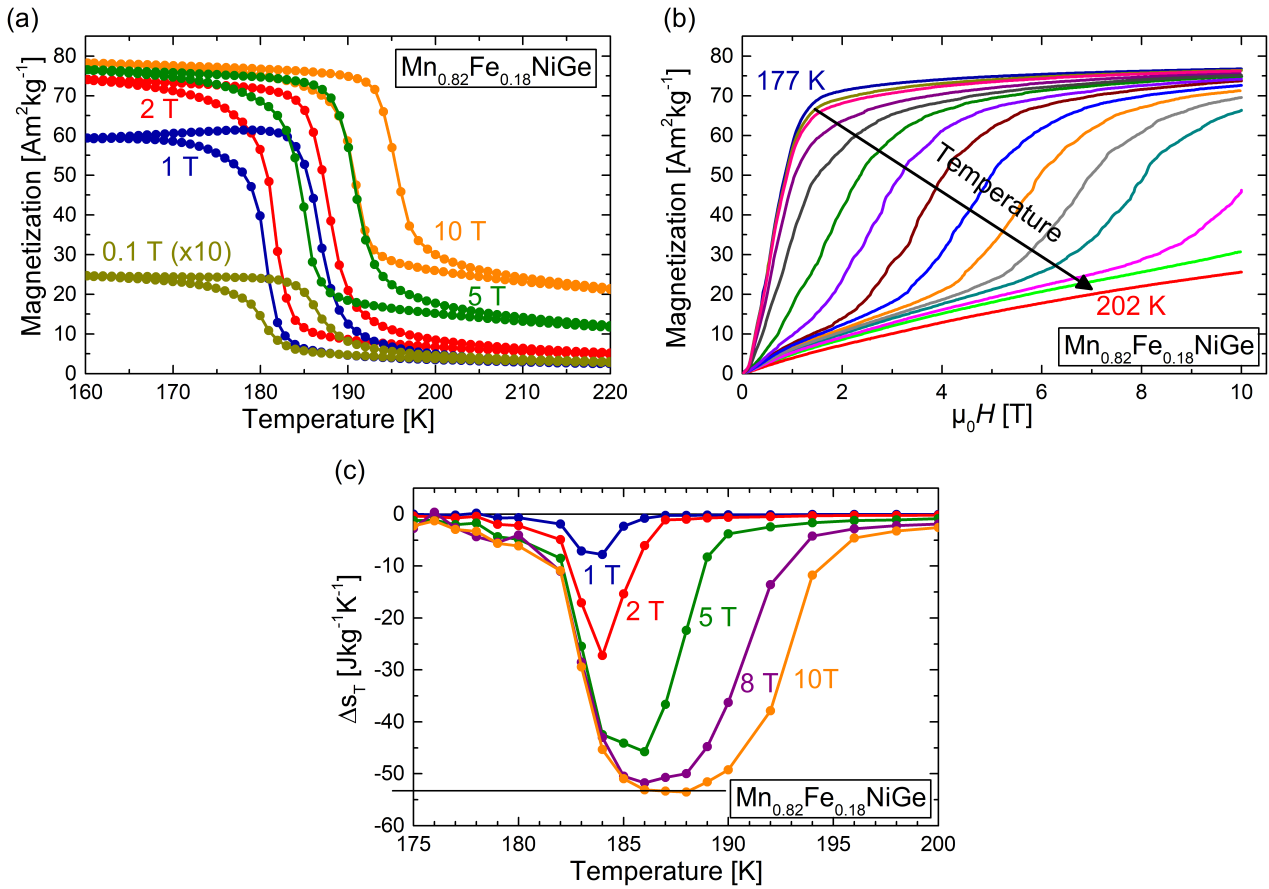


Figure 6.12: Temperature-dependent magnetization curves for a small fragment of $\text{Mn}_{0.82}\text{Fe}_{0.18}\text{NiGe}$ (a). The values of M for the measurement in 0.1 T are multiplied by a factor of 10 for better visualization. Additionally, magnetic-field-dependent isothermal magnetization curves are shown (b) as well as the resulting Δs_T for magnetic-field changes up to 10 T (c) determined from the $M(H)$ -curves upon cooling.

6.5 Magnetocaloric effects in high magnetic fields

As a result of the low magnetic-field sensitivity of the phase transition discussed in the previous section, magnetic fields larger than 2 T are required to investigate the maximum possible magnetocaloric properties Δs_T and ΔT_{ad} . The determination of Δs_T for a Si-free compound ($\text{Mn}_{0.82}\text{Fe}_{0.18}\text{NiGe}$) in high magnetic fields is shown in Fig. 6.12. The $M(T)$ -curves in (a) show a sharp phase transition and the already discussed low shift of T_t in external magnetic fields. The magnetization of the paramagnetic austenite increases much more significantly in high fields of 5 T and 10 T compared to the measurement of the sample in Fig. 6.11 (a). This is due to the decreased temperature of the phase transition for $\text{Mn}_{0.82}\text{Fe}_{0.18}\text{NiGe}$ compared to a transition around room temperature. Therefore, the magnetization change of the transition is reduced in higher fields since the austenite has already a magnetization of 25 A m² kg⁻¹ in an external field of 10 T before

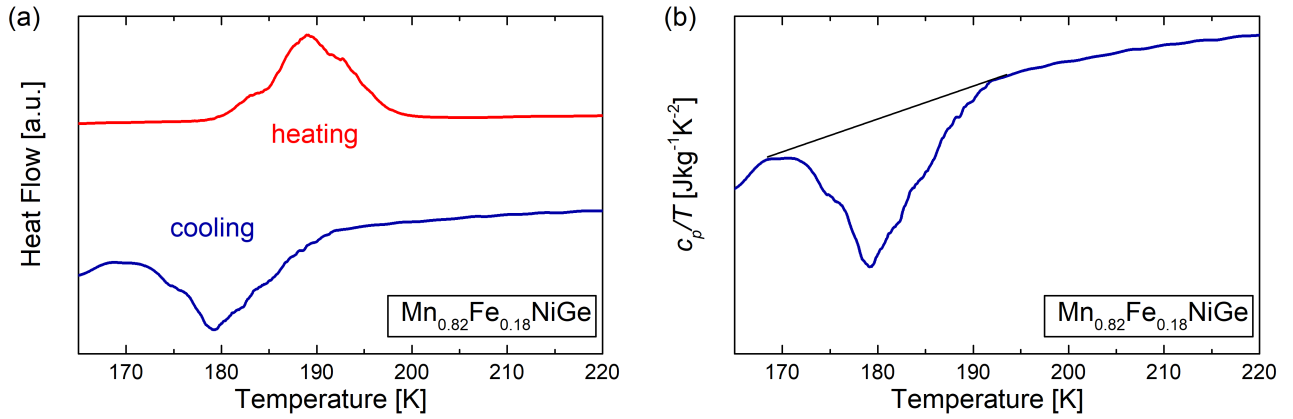


Figure 6.13: DSC measurement of $\text{Mn}_{0.82}\text{Fe}_{0.18}\text{NiGe}$ upon heating and cooling with a temperature-ramping rate of 5 K min^{-1} (a) and the resulting temperature-dependent c_p/T evolution (b).

the phase transition takes place. A consideration of the transition width for the measurement in 1 T gives a value of 11 K between 5 % and 95 % of the martensite magnetization. In combination with an average field shift of 1.06 K T^{-1} , it is expected that Δ_{s_T} saturates in roughly 10.4 T. The isothermal magnetization curves in Fig. 6.12 (b) show the evolution from the ferromagnetic martensite at low temperatures (177 K) to the paramagnetic austenite state at high temperatures (202 K) with the field-induced transition between the two states for intermediate temperatures. Even though the measurements have been carried out on a small fragment of around 1 mg, the sample piece transforms in a non-uniform manner with minor steps during the magnetization process. This indicates that the fragment consists of several smaller pieces that decouple by falling apart due to the large volume change of the transition. This has been confirmed by an inspection of the sample after the measurement showing a cracking and a disintegration of the fragment into several smaller pieces. In order to avoid an influence of this effect on the determination of Δ_{s_T} , the sample has been cycled thermally several times before starting the first $M(H)$ -measurement. Nevertheless, the sample exhibits a sharp transition with a large volume change leading to large entropy changes of maximum $53 \text{ J kg}^{-1} \text{ K}^{-1}$ for a magnetic-field change of 10 T. This value is in good agreement with the saturated effect estimated from the $M(T)$ -measurements in the previous section.

For an investigation of the entropy change of the full transition, DSC measurements have been carried out. The respective heat flow for $\text{Mn}_{0.82}\text{Fe}_{0.18}\text{NiGe}$ is shown upon heating and cooling in Fig. 6.13 (a). The transition temperatures taken at the peak value of the heat flow signal at 188.9 K (heating) and 179.2 K (cooling) are in good agreement with the ones determined from magnetization measurements in 0.1 K in Fig. 6.12 (a). The total entropy change of the transition Δ_{s_t} is determined from the integration of the c_p/T -signal in the transition region by using a baseline correction according to Equations (3.8) and (3.9) for the cooling protocol. The resulting Δ_{s_t} amounts to $-59.2 \text{ J kg}^{-1} \text{ K}^{-1}$, which is slightly larger than the value of Δ_{s_T} determined from magnetization measurements in a magnetic-field change of 10 T. A reason for this discrepancy can be that the value in 10 T is not fully saturated.

Table 6.2: Total entropy changes Δs_t of the magnetostructural phase transitions for the $\text{Mn}_{1-x}\text{Fe}_x\text{NiGe}_{1-y}\text{Si}_y$ series. The respective transition temperatures upon cooling T_t^c were determined at the peak value of the heat flow signal.

x	y	T_t^c [K]	Δs_t [$\text{J kg}^{-1} \text{K}^{-1}$]
0.13	0	291.8	-57.5
0.18	0	179.2	-59.2
0.2	0.1	269.3	-58.5
0.3	0.3	290.9	-59.4
0.4	0.5	320.9	-54.0

This method has been also applied to other samples of the $\text{Mn}_{1-x}\text{Fe}_x\text{NiGe}_{1-y}\text{Si}_y$ series, the resulting values for Δs_t are shown in Table 6.2 together with the respective stoichiometries and transition temperatures. In agreement with the observations from $\frac{dT_t}{\mu_0 dH}$ for the different alloys (Section 6.4), the total entropy change of the full phase transition does not vary with composition or transition temperature and is constant for the different samples slightly below $60 \text{ J kg}^{-1} \text{K}^{-1}$. This value is fitting well to the estimation from the Clausius-Clapeyron equation, which yields $60 \text{ J kg}^{-1} \text{K}^{-1}$ for a ΔM of 60 A m kg^{-2} (see Fig. 6.3) and an average $\frac{dT_t}{\mu_0 dH}$ of 1 K T^{-1} (from Fig. 6.11).

From the large entropy changes of the full phase transition, it can be presumed that a saturation of the effect will also lead to large temperature changes for higher applied magnetic fields under adiabatic conditions like it is the case for the Ni-Co-Mn-Sn and Ni-Co-Mn-Ti Heusler systems experiencing a low $\frac{dT_t}{\mu_0 dH}$ but large ΔT_{ad} in high fields (discussed in Chapter 4 and Chapter 5). In order to investigate this assumption, a sample of $\text{Mn}_{0.84}\text{Fe}_{0.16}\text{NiGe}$ has been exposed to pulsed magnetic fields up to 40 T in the High Magnetic Field Laboratory of the Helmholtz-Zentrum Dresden-Rossendorf (HZDR).

Due to the mechanical instability of the studied MM'X compounds undergoing several transition cycles, the direct measurement of bulk pieces as well as loosely connected particles with a pressed-in thermocouple (like for the measurements of Fig. 6.5) is not possible in combination with the thin and fragile thermocouples used for the detection of ΔT_{ad} signals in pulsed magnetic fields. Therefore, the particles need to be bonded by a silver epoxy, which is strong enough to ensure the long-term mechanical integrity of the sample and enable a proper heat transfer between the particles and to the thermocouple. However, attaching a thermocouple between two pieces of bonded powder using 5 wt. % of two-component silver epoxy glue ("sandwich-mode") does not lead to reasonable signals of ΔT_{ad} . On the one hand, a problem with the heat transfer from the sample to the thermocouple can be a problem because it cannot be ensured that the very small end of the thermocouple does have contact to the sample particles embedded in the epoxy matrix directly. On the other hand, it is possible that the martensitic transition of the sample is too slow in order to follow the very large magnetic-field change rates of the pulsed field setup.

For a further investigation, the properties of the epoxy-bonded sample with a small single piece for slow magnetic fields of a PPMS measurement setup are compared. To determine the magnetization, the

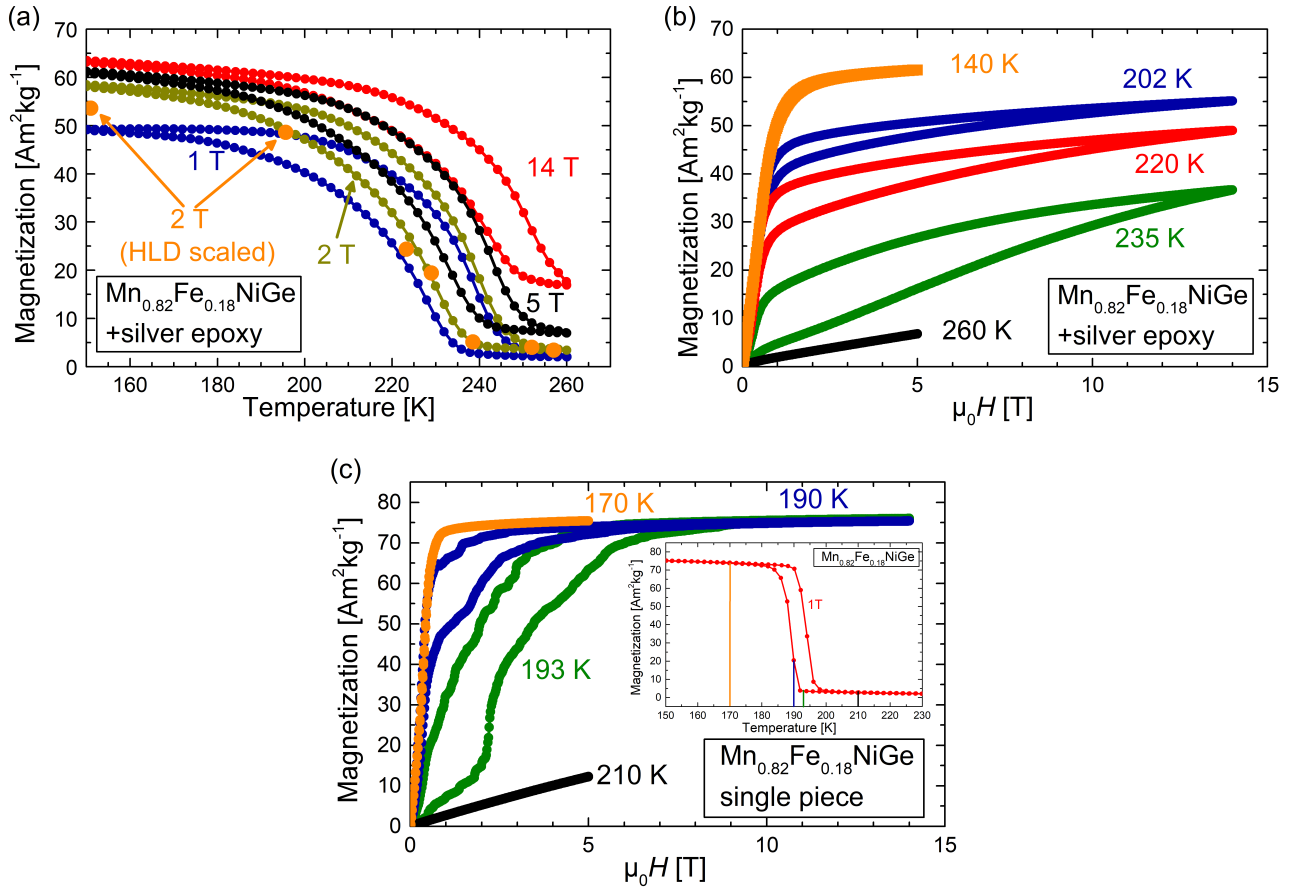


Figure 6.14: Temperature-dependent magnetization of $\text{Mn}_{0.84}\text{Fe}_{0.16}\text{NiGe}$ as bonded powder with silver epoxy in external magnetic fields of 1 T to 14 T together with the scaled values of pulsed $M(H)$ measurements in 2 T as orange data points (a). The corresponding isothermal $M(H)$ measurements of the silver-epoxy-bonded sample at selected temperatures above (black), below (orange) and during the phase transition (red, green and blue) for slow field application rates of 5 mT s^{-1} are shown in (b) and for a small single piece in (c). The inset of (c) shows the respective $M(T)$ measurement in an external magnetic field of 1 T.

mass of powder and epoxy has been considered giving the specific magnetization of the whole sample body. The temperature-dependent magnetization behavior in fields of 1 T to 14 T in Fig. 6.14 (a) already shows that the sharp transition that is characteristic for small fragments is broadened drastically by the bonding process with an epoxy matrix. This is in agreement with the observations in Section 6.3. The broadening by using the silver epoxy is even stronger than for the non-conductive binder. The low $\frac{dT_i}{\mu_0 dH}$ is also obvious here and suggests that a field application of 14 T is not enough to complete a field-induced phase transition when starting at the M_s temperature of 235 K for the 1 T curve. This is confirmed by $M(H)$ measurements in Fig. 6.14 (b), showing that an isothermal application of slow fields (5 mT s^{-1}) up to 14 T does not lead to a completed transformation to the martensite state. The boundary magnetization for the pure martensite and austenite state is represented by the measurements at 140 K and 260 K,

respectively. Converting the magnetization into the martensite/austenite fraction M/A by extrapolating the paramagnetic and ferromagnetic magnetization of both phases to 14 T and using Equation (6.3) gives a maximum field-induced martensite of 38.5 % at T_s of 235 K. Consequently, even under isothermal conditions that neglect the influence of an adiabatic temperature change of the sample, less than half of the sample can be transformed into martensite by an external magnetic-field change of 14 T. An estimation by the width of the transition and its field sensitivity gives an estimation for the necessary magnetic field of 55 T.

$$M/A = \frac{M(14 \text{ T})}{M_{\text{martensite}}(14 \text{ T}) - M_{\text{austenite}}(14 \text{ T})} \quad (6.3)$$

In contrast, the magnetization measurements for a small piece of $\text{Mn}_{0.82}\text{Fe}_{0.18}\text{NiGe}$ in Fig. 6.14 (c) show that the sharp phase transition can be indeed completely induced by a magnetic-field change of 14 T at a starting temperature close to M_s of 193 K (blue curve). The stepwise behavior of the transition indicates that the measured sample piece consists of several smaller fragments with a slightly deviating T_t being decoupled.

Since a magnetization measurement in pulsed fields is not relying on a direct contact of a measurement sensor like it is the case for the signal monitoring of ΔT_{ad} , the magnetic-field-dependent magnetization is determined by measurements at the HZDR for a sample piece of the silver epoxy bonded powder as well as for loose powder. Since the signal is not measured as an absolute magnetization due to the lack of reference calibration, measurements of 2 T at different temperatures are compared with the corresponding $M(T)$ -curve for the PPMS measurement. Both signals are divided for several temperatures and averaged over all taken points in order to gain a multiplication factor. Consequently all measurements of M in pulsed fields are scaled according to this value. The good agreement is reflected in the comparison of the orange points representing the scaled magnetization of pulsed fields with the corresponding $M(T)$ -curve in constant field (dark yellow) in Fig. 6.14 (a). The induced transitions for pulses of 20 T at different starting temperatures in Fig. 6.15 (a) show a similar result like the measurements in slow field changes. Between T_s of the pure austenite (252 K) and martensite starting state (151 K), a field-induced first-order transition is taking place between low-magnetization and high-magnetization state, which is characterized by a shift of the back transition upon field removal due to the thermal hysteresis of the sample. Also for the pulsed fields, the amount of induced martensite in magnetic fields of 20 T is far away from a completed phase transition. The respective measurements of $M(H)$ for loose powder in Fig. 6.15 (b) do not enhance the amount of magnetic-field-induced martensite that can be achieved by pulses of 20 T, even though a slightly sharper phase transition is expected due to the absence of a stress-coupling effect that is discussed in Section 6.3. Only by a field pulse of 58 T, the magnetization of the full martensite state can be reached.

A final comparison between an isothermal field application in the PPMS system and an adiabatic field application by a fast pulse for the same starting temperature of 223 K in Fig. 6.15 indicates that the magnetic behavior is similar. However, the adiabatic field application deviates slightly from 2 T on exhibiting a slower increase of magnetization with rising magnetic field. This is evidence for an adiabatic heating of the sample taking place due to the conventional MCE. This sample heating counteracts the shift of T_t towards higher

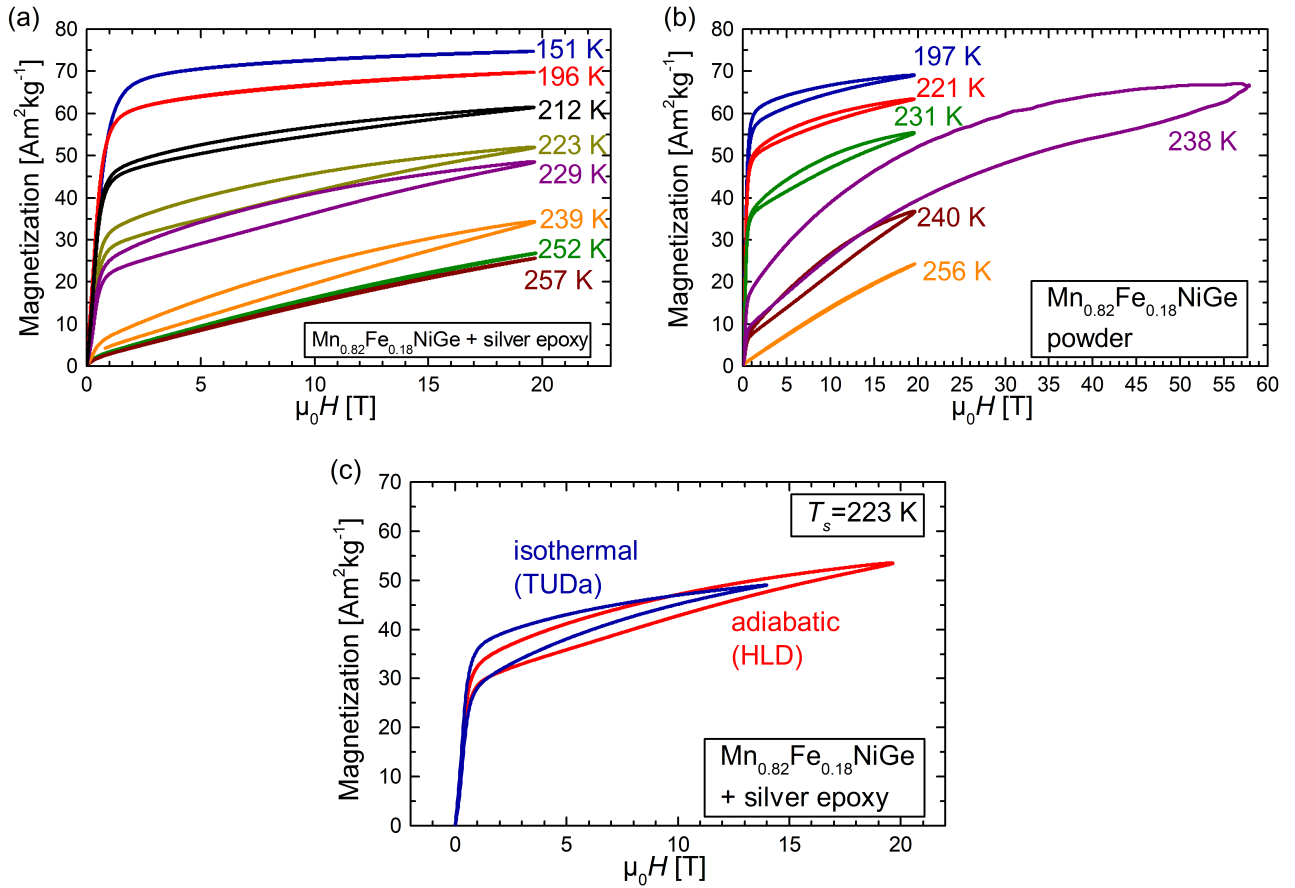


Figure 6.15: Magnetic-field-dependent magnetization curves of $\text{Mn}_{0.84}\text{Fe}_{0.16}\text{NiGe}$ in form of powder bonded with silver epoxy (a) and as loose powder (b) at different starting temperatures for field pulses of 20 T with a maximum field-application rate of 3190 T s^{-1} . One field pulse of 58 T with highest field rates above 8000 T s^{-1} is added in (b). The comparison of an isothermal slow $M(H)$ -measurement (PPMS system at TUDa) with an adiabatic fast $M(H)$ -curve (pulsed magnet at HLD) at the same starting temperature of 223 K is shown in (c).

temperatures and retards the phase transition to high magnetization martensite. This effect is very small and the extent is not suggesting a very large temperature change that causes this difference. A comparable study reports on a significant difference between an isothermal and adiabatic $M(H)$ -measurement caused by a ΔT_{ad} of around 13 K for the conventional phase transition in a $\text{La}(\text{Fe-Co-Si})_{13}$ compound [250]. The difference of the two curves for the MnFeNiGe sample amounts to only $1.5 \text{ A m}^2 \text{ kg}^{-1}$ for the highest field of 14 T by comparing both curves. For a rough estimation of the temperature change causing this difference, the two curves measured at T_s of 223 K and 229 K are compared. Scaling the difference of $4.4 \text{ A m}^2 \text{ kg}^{-1}$ here linearly with the 6 K difference of starting temperature yields an estimated temperature difference of 2 K between the isothermal and the adiabatic curve in Fig. 6.15 (c). It must be considered here that the absolute magnetization of the pulsed experiment has been scaled by considering the isothermal

measurements of the PPMS. Since Fig. 6.14 (a) shows some small deviation, this can represent a significant source of error for the absolute value of the estimated ΔT_{ad} by this approach. This method also assumes that a possible ΔT_{ad} of the two measurements at 223 K and 229 K considered as reference is equal and therefore shifts both curves the same way since they are also recorded adiabatically. Nevertheless, the difference between isothermal and adiabatic measurement clearly suggests a low absolute value of ΔT_{ad} , which in turn serves as justification for a minor influence of this uncertainty to the used approach.

These experiments show that the transition can be induced by fast magnetic fields and an adiabatic temperature change results from the field-induced MCE. However, this effect is expected to be very small as a result of the broadened transition for an epoxy bonded sample in combination with the very small shift of T_t in external magnetic fields. Consequently the problems of the direct measurement of ΔT_{ad} are attributed to the difficulty for a proper contact of the thermocouple to the bonded powder ensemble and not due to a major suppression of the phase transition by the large field application rates.

6.6 Effect of hydrostatic pressure

The sensitivity of the transition by the influence of external pressure gives a perspective for barocaloric or pressure-tuned magnetocaloric applications [76, 251]. The volume difference between the phases acts as the driving force for a shift of the transition temperature under pressure. For applied hydrostatic pressures, the phase with the lower volume is stabilized [57, 67, 252, 253]. For the MnNiGe system, the hexagonal high-temperature phase has the lower unit cell volume and is stabilized under pressure leading to an expected shift of the (magneto-)structural transition temperature towards lower temperatures [254–256].

The pressure-dependence of the phase transition is shown by a magnetization measurement over temperature in a magnetic field of 2 T in Fig. 6.16 (a) for the Si free sample $\text{Mn}_{0.84}\text{Fe}_{0.16}\text{NiGe}$. For lowest applied pressure of 0.1 GPa, a shift of the phase transition to slightly lower temperatures is observable as expected. The properties of the transition namely magnetization change, width and hysteresis are not affected by this hydrostatic pressure. However for higher pressures, the shift of the transition temperature is accompanied by a drastic change of the transition, firstly seen for the measurement under a pressure of 0.38 GPa. Increasing the pressure up to 0.72 GPa results in a shift of the transition temperature down to 142 K and 145 K for cooling and heating, respectively (determined by derivative-method). This corresponds to a shift of the transition temperature of -160 K GPa^{-1} . However, the transition is highly broadened with a ΔT_{width} of over 100 K. Furthermore, the magnetization of the low-temperature phase is decreased from around $67 \text{ A m}^2 \text{ kg}^{-1}$ to $45 \text{ A m}^2 \text{ kg}^{-1}$. This behavior has been reported analogously for the similar composition of $\text{Mn}_{0.85}\text{Fe}_{0.15}\text{NiGe}$ [257]. It is explained in this reference by a decoupling of the magnetic and structural transition following the evidence of the step-like transition for intermediate pressures (around 0.35 GPa). However, it is likely that the effect is attributed to the change of magnetic ordering from ferromagnetic to a canted ferromagnetic or antiferromagnetic state respectively, as it is described for low Fe contents and temperatures below 200 K [242]. For this reason, the martensite phase shows a reduced magnetization in a magnetic field of 2 T and the highest applied pressure of 0.72 GPa. For intermediate

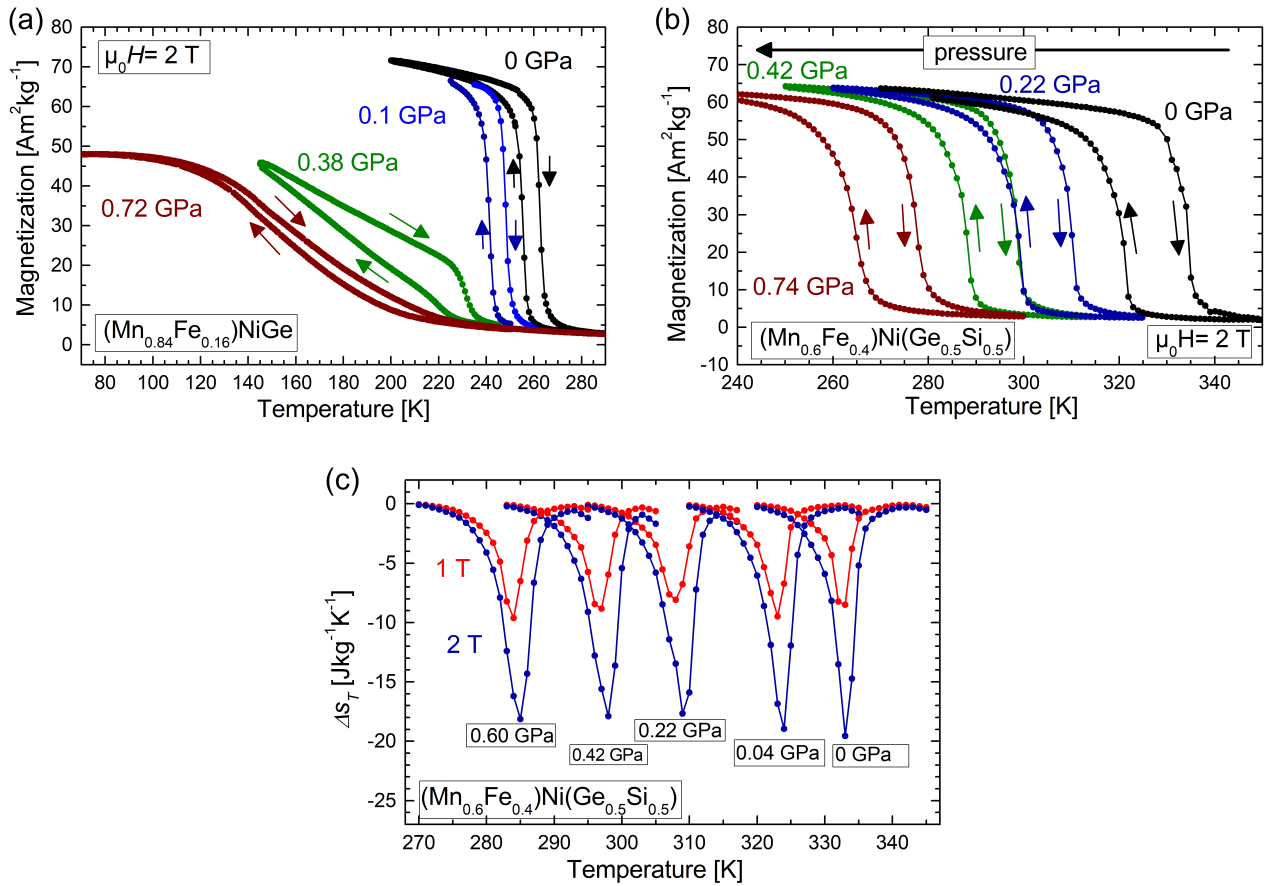


Figure 6.16: Influence of hydrostatic pressure on the temperature-dependent magnetization behavior in an external field of 2 T for a Si free sample $\text{Mn}_{0.84}\text{Fe}_{0.16}\text{NiGe}$ (a) and a sample with Si substitution $\text{Mn}_{0.6}\text{Fe}_{0.4}\text{Ni}(\text{Ge}_{0.5}\text{Si}_{0.5})$ (b). The isothermal entropy change Δs_T upon heating for the latter sample is shown for various pressures in (c).

pressures, the structural and magnetic transition do not overlap completely and the observed two step-like behavior evolves for the magnetization measurement.

The same pressure-tuned experiment for a composition with a partial Si substitution on the Ge site leads to an entirely different behavior as seen in Fig. 6.16 (b). The sharp magnetostructural phase transition is shifted to lower temperatures as well, but the characteristics of the transition, namely transition width, sharpness, hysteresis and magnetization change, are maintained up to the highest applied pressure of 0.74 GPa. Moreover, the determination of Δs_T reveals a nearly constant value in the range of about $-17.7 \text{ J kg}^{-1} \text{ K}^{-1}$ to $-19.5 \text{ J kg}^{-1} \text{ K}^{-1}$ over the examined pressure range, as shown in Fig. 6.16 (c). Despite the increasing magnetic contribution that is expected to influence Δs_T for decreasing temperature, even though much smaller compared to Heusler alloys because it is much further away from T_C of the ferromagnetic martensite, the constant Δs_T is consistent with the findings from the constant entropy change of the full transition by DSC measurements (Tab. 6.2). However, the field-induced transition here is only regarded for a

field change of 2 T and the entropy change of the full transition is not accessible by this measurement. Therefore, a comparison to Heusler alloys, where the maximum Δ_{ST} is influenced by the increasing magnetic contribution for decreasing transition temperature is not meaningful here [67]. The preservation of the phase transition under pressure is in accordance with the investigations of Samanta *et al.* [258] for a Si substituted sample. However, they have even reported a drastic increase in Δ_{ST} for applied pressures of 0.11 GPa and 0.24 GPa.

The shift of the transition temperature by the applied hydrostatic pressure is fitted to the M_s temperature with a linear slope of -72 K GPa^{-1} , which is larger than the literature value for pure MnNiGe of -54 K GPa^{-1} [254, 255]. Despite the linear shift of the phase transition in the range of applied pressures, the overall behavior including larger pressures is supposed to differ. The obtained shift is significantly smaller compared to the Si free sample. However, this large shift is determined by the extreme broadening of the transition for high pressures and is determined in a range of much lower absolute temperatures.

The external hydrostatic pressure can be compared to the "chemical pressure" that is created by the atomic substitutions in the unit cell [252]. The shift of T_t with hydrostatic pressure is determined to be -72 K GPa^{-1} and the negative shift of T_t by the introduction of Fe atoms on the Mn sites in the lattice is approximated to -135 K per 10 % of Fe substitution. By comparing the effective shift of the two stimuli, the effect of 10 % Fe substitution is equivalent to an external pressure of 1.88 GPa.

However, also other factors are likely to influence the change in transition temperature besides the lattice contraction, such as magnetic coupling and changes in the electronic band structure. This follows also clearly from the introduction of Si atoms on the Ge site. Even though this substitution contracts the lattice like hydrostatic pressure does, the transition temperature is increased. Due to the same number of valence electrons and the fact that both Si and Ge atoms do not carry a magnetic moment in these compounds [167, 244, 259], a variation in the electronic band structure is assumed to play a major role for this substitution path.

For the diminished shift of T_t in magnetic fields for the MM'X materials, it is a more efficient way to use the sensitivity towards pressure for inducing the phase transition. In order to completely induce the transition and overcome the thermal hysteresis of 10 K, an external pressure of 0.14 GPa needs to be applied cyclically. To achieve this shift by chemical variation, it would correspond to a Fe substitution on the Mn site of 0.74 %. A magnetic field of more than 10 T is necessary to induce a shift of comparable magnitude [260]. Also a combined usage of magnetic field and external pressure, as proposed in [76] for an inverse magnetocaloric Heusler material, can be efficient to exploit more efficiently the magnetocaloric effect that could be potentially provided by the material system. A cyclic application of pressure on large samples for usable caloric effects needs to be tested first in terms of the mechanical stability of the compound. As discussed in Section 6.3, the MM'X alloys tend to disintegrate after several transition cycles due to the large crystallographic volume change. A frequent application of mechanical pressure is then expected to cause even more problems for long-term operations on these compounds, which is a major drawback regarding the development of MM'X alloys towards feasible caloric applications. A more realistic application scenario is the use of powder for barocaloric applications using hydrostatic pressure, as it has

been investigated in detail already for the related MnCoGe system [251, 261]. Even though hydrostatic pressures are not as problematic for the mechanical stability as uniaxial loads, the technical implementation is more complicated.

6.7 Reducing criticality by Ge-elimination

In Section 6.1, it is demonstrated that the method of isostructural alloying is a powerful tool to tune the relevant properties for magnetocaloric applications precisely for the $\text{Mn}_{1-x}\text{Fe}_x\text{NiGe}_{1-y}\text{Si}_y$ system. However, the elimination of the expensive Ge cannot be achieved because the transition temperature would be too high when using a compound with $y = 1$. In addition, the amount of Mn and Fe needs to be balanced to maintain a ferromagnetic ordering of the orthorhombic martensite phase. In order to establish a phase transition without using Ge, other elements can be considered for tuning the transition temperature. To achieve the goal of producing a compound without Ge, the element Al is used as a substitute for the Ge and Si lattice site. Since very small amounts of Al reduce T_t drastically [152, 160], it is a suitable candidate to adjust a martensitic transition at room temperature without requiring too much of Fe substitution for Mn. Based on the results in Section 6.1, the Fe substitution level of $x = 0.5$ is chosen for the strongest effect of induced ferromagnetic ordering by introducing Fe atoms. Consequently, a systematic series of varying Al content is studied by producing $\text{Mn}_{0.5}\text{Fe}_{0.5}\text{NiSi}_{1-z}\text{Al}_z$ compounds. The temperature-dependent magnetization curves of the resulting transitions are shown in Fig. 6.17 (a). A slight variation in the Al content of only $\Delta z = 0.01$ (from 0.055 to 0.065) is already enough to shift the transition temperature by 70 K. Following the observations from Section 6.1, the large Si content results also in these compounds in a large thermal hysteresis of around 25 K.

For a closer investigation, the properties of this substitution approach will be discussed with respect to the compound with $z = 0.06$ ($\text{Mn}_{0.5}\text{Fe}_{0.5}\text{NiSi}_{0.94}\text{Al}_{0.06}$). One important observation for these compounds is, in analogy to the microstructures of the $\text{Mn}_{1-x}\text{Fe}_x\text{NiGe}_{1-y}\text{Si}_y$ series (Section 6.3), that the brittleness of the material is reduced with the elimination of Ge. The samples show a better mechanical integrity compared to the samples of the Si-free sample series. Nevertheless, the large volume change still leads to a destruction of larger bulk pieces after several transition cycles. The slightly increased mechanical stability results in the occurrence of a training effect for the first temperature cycles, as shown in Fig. 6.17 (b). During the first cooling of the sample, the austenite is constraint because the increase of the volume during the phase transformation causes a pressure effect that lowers T_t of the surrounding grains. The increased mechanical stability does not lead to a direct destruction of the bulk structure. As a consequence, the overall transition is suppressed from the "free" transition temperature upon cooling at 240 K down to around 190 K, where still a large amount of austenite is present. At this temperature the stresses within the material are too large and the expanding grains lead to cracks in the material. These formed voids now allow the austenite to transform into martensite upon volume expansion. For the second cooling cycle (black curve), the already formed cracks do not hinder the material from transforming like it is the case for the first cooling because the material can expand its volume more freely into the present voids. There is still a slight difference in

T_t compared to the third cooling because some cracks are still forming during this step. After the third cycle, all further measurement curves coincide and thus represent the equilibrium transition temperature upon cooling. This feature of deviating T_t is not observed at all for the heating curves. These coincide because the material is contracting upon heating through the phase transition, which does not lead to a constraint of the grains. This effect is in analogy to the so-called "virgin effect" that is most prominent for Fe₂P-type magnetocaloric materials [109, 110]. For this material family the sintered samples do experience cracking during the virgin effect but keep their mechanical integrity after many cycles. In contrast, the (Mn, Fe)Ni(Si, Al) sample is breaking apart completely after several cycles and the obtained measurements are corresponding to an ensemble of different pieces from the parent bulk sample. As a consequence, the sharp phase transition cannot be used for well-performing magnetocaloric heat exchangers because an additional processing step, e. g. polymer bonding, which diminishes the magnetocaloric properties due to a broadening of the transition (see Section 6.3), is necessary.

In order to investigate the influence of the Al addition for a Ge-free sample on the magnetic-field sensitivity of the phase transition, the magnetization curves in magnetic fields up to 7 T are shown in Fig. 6.17 (c). The slope of the fitted line for the respective transition temperatures of the austenite and martensite formation (by tangent method) gives the value for $\frac{dT_t}{\mu_0 dH}$ in the range from 1 T to 7 T. The temperatures in 0.05 T and 0.1 T are not used for this fit in order to enhance the accuracy because the different shape of the magnetization curve might lead to uncertainties by using the tangent-method. The average value for $\frac{dT_t}{\mu_0 dH}$ is 1.2 K T⁻¹, which is slightly larger than the average of the samples from the Mn_{1-x}Fe_xNiGe_{1-y}Si_y series in Section 6.4 but still within the range of determined values and errors and for example equal to the shift of Mn_{0.8}Fe_{0.2}NiGe_{0.9}Si_{0.1}. Consequently, the increasing Si content to almost one combined with the addition of Al does not enhance the sensitivity of T_t towards an external magnetic field.

The determination of Δ_{ST} shown in Fig. 6.17 (d) leads to a value of -23 J kg⁻¹ K⁻¹ for $\mu_0 \Delta H = 2$ T. This large value is here a result of the sharp phase transition in combination with the low field sensitivity ($\frac{dT_t}{\mu_0 dH}$). It is not saturated for this magnetic-field change and a much larger entropy change is expected in higher magnetic-field changes. Due to the large thermal hysteresis, the peaks for heating and cooling curve do not overlap at all and no significant cyclic caloric effect can be expected for this sample.

Despite the sharp phase transition, a large magnetocaloric effect cannot be expected due to the still low sensitivity of T_t towards an external magnetic field. A large effect may occur in larger magnetic fields, similar to the situation in the Ti-Heusler alloys in Chapter 5. The Ge-free compound would also represent nearly ideal conditions for the multi-stimuli cycle with a sharp phase transition, a large thermal hysteresis and a good sensitivity of T_t towards (hydrostatic) pressure. The reduced $\frac{dT_t}{\mu_0 dH}$ may be overcome with a large pulsed field that could be used in this cooling approach. The largest drawback here is the very low mechanical stability of the material system. Because of the destruction of larger bulk geometries that would be required in a heat exchanger system, a practical cyclic application of pressure would not be possible. Also the mechanical instability due to the large volume change would require alternative processing solutions for a stable material without reducing the excellent properties of the sharp phase transition.

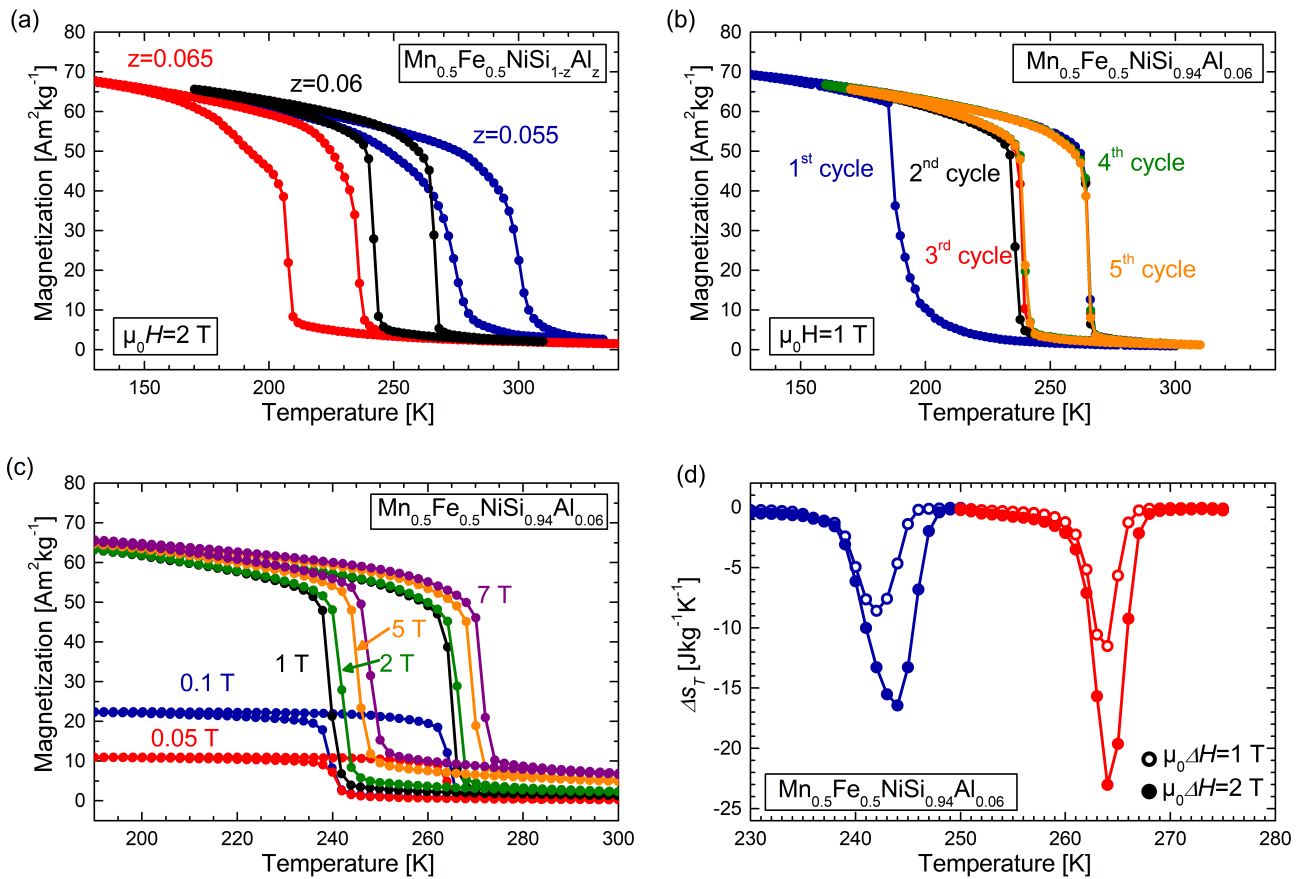


Figure 6.17: Temperature-dependent magnetization measurements for the Ge-free alloy series of $Mn_{0.5}Fe_{0.5}NiSi_{1-z}Al_z$ in an external field of 2 T (a). $M(T)$ -curves of $Mn_{0.5}Fe_{0.5}NiSi_{0.94}Al_{0.06}$ are shown for different subsequent temperature cycles in 1 T (b) and for different external field strengths from 0.05 T to 7 T (c) together with the determined Δs_T in a magnetic-field change of 2 T (d).

7 Principal Design Rules for Magneto- and Multicaloric Compounds

The most promising materials that are intensively developed and tested for magnetocaloric cooling applications are La-Fe-Si and Fe₂P-type alloys because of their sharp and tunable phase transition, a narrow hysteresis and the usage of abundant elements [36]. Also Heusler alloys are often considered with good prospects for magnetocaloric cooling. However, the comparably large thermal hysteresis and the usage of critical elements In and Co for the best performing Ni-Co-Mn-In alloys represent a major drawback here. The introduction of a new concept for using multicaloric materials in a cooling cycle that applies two different stimuli, magnetic field and uniaxial pressure, instead makes use of the thermal hysteresis for a full exploitation of the cyclic MCE [43]. This innovative approach opens up the necessity to evaluate the known systems as well as new materials on a slightly modified basis. Also new methods arise that enable the theoretical prediction of new compounds and broaden the understanding of existing phenomena with respect to an efficient material design. This chapter is about providing an overview on the suitability of the discussed materials within this thesis for magnetocaloric and multicaloric cooling cycles and giving prospects or principal design rules for future caloric materials development.

7.1 Designing magnetocaloric compounds by experiment and theory

As already pointed out in the previous chapters, the key point for good caloric properties is a sharp phase transition resulting in large isothermal entropy changes as well as large adiabatic temperature changes. Ideally, the transition temperature can be tuned by stoichiometric variation of the respective compounds. An equally important aspect is the sensitivity of the transition temperature with respect to an external field in order to induce the phase transition that is accompanied with the desired caloric effect. For the case of a magnetocaloric cycle, a magnetic field acts as the driving force leading to $\frac{dT_t}{\mu_0 dH}$ as the crucial property. In Chapter 4, the behavior of $\frac{dT_t}{\mu_0 dH}$ is compared for the different systems of Ni(-Co)-Mn-In, Ni(-Co)-Mn-Sn and Ni(-Co)-Mn-Al. This analysis provides the finding that the sensitivity of T_t towards an external magnetic field scales with the absolute temperature of the transition. This effect is due to a larger magnetization change evolving for lower temperatures, which supports the stabilization of the ferromagnetic phase in an external magnetic field. Also the introduction of 5 at. % of Co on the Ni-sites leads to a similar behavior, but with a shift towards higher temperatures as a result of the increased Curie temperature. The latter

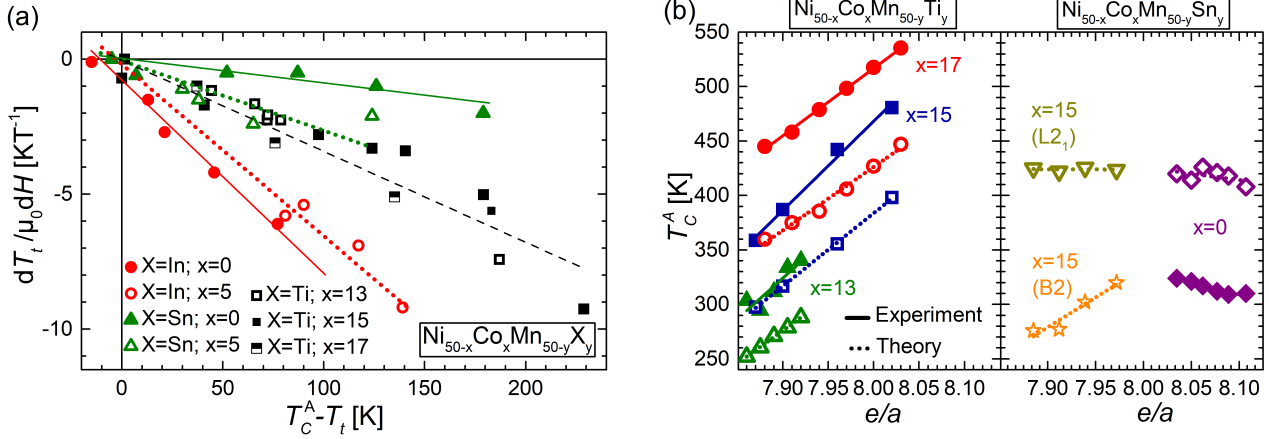


Figure 7.1: Comparison of the shift of the transition temperature in external magnetic fields $\frac{dT_t}{\mu_0 dH}$ as a function of the difference between Curie temperature and transition temperature ($T_C^A - T_t$) for different Ni(-Co)-Mn-X Heusler-alloy systems (X = In (red), Sn (green), and Ti (black)) with linear fits to the data points of each system (a). The influence of the e/a ratio by variations in the Mn-X content on T_C^A for $\text{Ni}_{50-x}\text{Co}_x\text{Mn}_{50-y}\text{Ti}_y$ and $\text{Ni}_{50-x}\text{Co}_x\text{Mn}_{50-y}\text{Sn}_y$ from experiment (closed symbols and solid lines) and DFT calculations (open symbols and dashed lines) is shown in (b). DFT calculations have been performed by Nuno Fortunato (TU Darmstadt).

finding is also true for the new group of all- d Heusler alloys of Ni(-Co)-Mn-Ti at higher Co content of around 13 at. % to 17 at. %. Here, a universal behavior is found for all Co contents produced in this work with a linear dependence of $\frac{dT_t}{\mu_0 dH}$ on the difference between the transition temperature and the Curie temperature of the austenite ($T_C^A - T_t$). In order to check the validity of transferring this result to other Heusler systems, the data from Fig. 4.4 (e) is converted to the absolute difference of $T_C^A - T_t$ and compared to the Ni-Co-Mn-Ti system in Fig. 7.1 (a).

By comparing the Ti-system (black symbols) with the respective In(-Co)- (red) and Sn(-Co)-systems (green), it can be concluded that the trend is comparable but the slope indicating the change of $\frac{dT_t}{\mu_0 dH}$ with $T_C^A - T_t$ varies strongly. As a result, the magnetic-field dependence of the transition temperature can be tuned more sensitively for certain Ni(-Co)-Mn-X systems. The Ni(-Co)-Mn-In system shows the strongest sensitivity (slope of 0.063 T^{-1}), which means that $\frac{dT_t}{\mu_0 dH}$ is influenced stronger by a change of the transition temperature itself or by the change of T_C^A than it is the case for Ni-Co-Mn-Ti and Ni(-Co)-Mn-Sn (slope of 0.009 T^{-1} to 0.026 T^{-1}). In addition, the uniform behavior of different Co-contents for Ni-Co-Mn-Ti seems to be unique because the slope of the linear approximation varies significantly for Ni-Mn-Sn and Ni-Co-Mn-Sn. On the other hand, the In-system shows a comparable slope without and with 5 at. % of Co but with a slight shift in temperature scale despite the normalization to $T_C^A - T_t$.

This analysis points out that the cyclic response for the magnetic-field-induced magnetocaloric effect can be influenced drastically by tuning the transition temperature as well as the Curie temperature of the alloy. To draw a conclusion as a design strategy for a magnetocaloric Heusler alloy working around room temperature, T_C^A must be increased significantly in order to be shifted as far away as possible from the

martensitic phase transition temperature. This can be realized the most efficient for the Ni(-Co)-Mn-In Heusler alloy system. Since the variation of T_C^A is usually carried out by partially substituting Ni with the critical element Co, it is desirable to use as little Co as possible. This consideration favors Ni-Mn-In for designing a promising magnetocaloric alloy. In addition, T_t should not be too close to T_C^A in order to avoid a contribution of the conventional MCE of the ferromagnetic austenite during and after the austenite formation upon magnetic-field application. A further point to consider in this context is the reduced magnitude of the maximum possible MCE for large values of $\frac{dT_t}{\mu_0 dH}$ according to the Clausius-Clapeyron relation (Equation (5.1)). As a consequence the all-d Heusler system of Ni-Co-Mn-Ti can be regarded as a good candidate for medium shifts of the transition temperature in external magnetic fields and a reasonable tunability of T_t and $\frac{dT_t}{\mu_0 dH}$ by stoichiometric variations. Since the new multicaloric cooling cycle can allow for the application of higher magnetic-field strengths than it is possible for a purely magnetocaloric cycle, this effect of a medium $\frac{dT_t}{\mu_0 dH}$ can be regarded as an ideal trade-off.

In order to tune the austenite Curie temperature by stoichiometric variations, it is found in Chapter 5 that the e/a ratio being proportional to the Mn-X ratio has a different effect for the all-d Heusler alloy systems (X = Ti) than for the well-known Ni(-Co)-Mn-X alloys with X = In, Sn, Al, Sb. In order to investigate these differences in more detail, the powerful tool of theoretical calculations based on Density Functional Theory (DFT) has been used in collaboration with Nuno Fortunato (TU Darmstadt). The comparison between the calculations (open symbols and dashed lines) and the experimentally found data points (closed symbols and solid lines) is depicted in Fig. 5.3 (b). The theoretical results can reproduce the slope of the e/a -dependent T_C^A for the individual sample series of the all-d Ni-Co-Mn-Ti alloys with a certain Co content (left panel of Fig. 7.1 (b)), but with an absolute offset of 90 K. In order to compare this with a representative Heusler system with a main group element, the data for a Ni-Mn-Sn sample series is added (right panel of Fig. 7.1 (b)). The observed trend fits to the theoretical model for the sample series without Co ($x = 0$, purple symbols). The trend of T_C^A with respect to e/a for the all-d Ni-Co-Mn-Ti alloy system is much stronger compared to the flat behavior (however, of opposite sign) in the well-studied Ni(-Co)-Mn-X systems with X = Al, In, Sn, Sb [139, 214]. The reason can be attributed to the fact that the increasing amount of Mn on Ti lattice sites (equivalent to increasing e/a) results in an enhancement of ferromagnetic interactions J_{ij} between Co and Mn atoms. Consequently, the ferromagnetic ordering of the austenite phase is stabilized leading to an increase in T_C^A . On the other hand, in the Ni-Mn-Sn system, the additional Mn introduced on the D-sites couples antiferromagnetically with the regular B-site Mn, counteracting with the ferromagnetic interactions between Ni-Mn pairs, which gives rise to a flat decrease of T_C^A with respect to the Mn content. However, Co-doping with a concentration as high as 15 at. % leads to a diverse effect. It is found that the flat behavior of T_C^A over e/a is obtained assuming a L2₁ order for the Sn-based austenite phases, whereas assuming a B2 disorder leads to the same steep variation with decreasing T_C^A for decreasing e/a as it is observed for the Ti-based cases. Therefore, it can be suggested that the significant change of T_C^A for Ni-Co-Mn-Ti is driven by the B2 disorder. In contrast Ni(-Co)-Mn-Sn samples are experimentally observed in the preferred L2₁ state leading to the discrepancy in the behavior of T_C^A [139, 214]. Moreover, the different configurations of the Mn-Co interaction for the B2 and L2₁ order

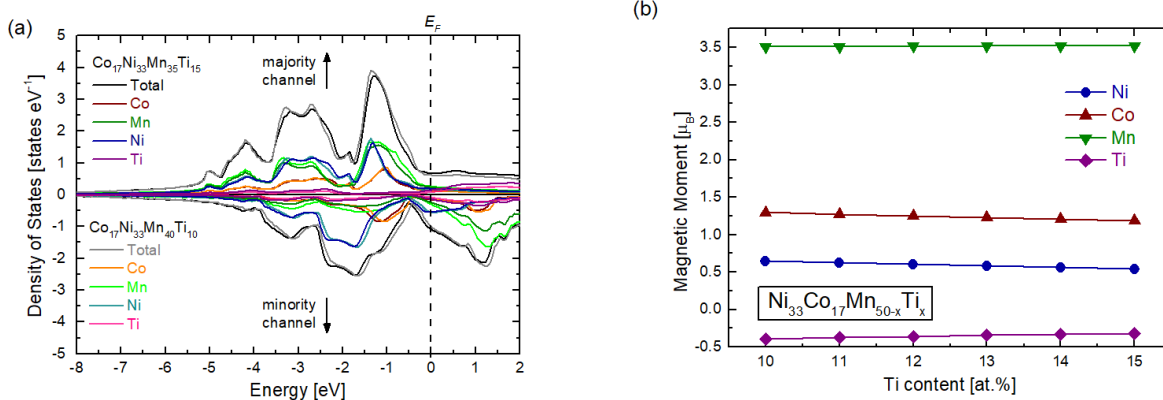


Figure 7.2: Calculated density of states (DOS) around E_F for $\text{Ni}_{33}\text{Co}_{17}\text{Mn}_{40}\text{Ti}_{10}$ in B2 disordered austenite state together with the magnetic moments carried by the individual atoms depending on the Ti content.

types are responsible for such significant differences in T_C^A with respect to e/a . The preferred occurrence of B2 austenite for Ni-Co-Mn-Ti samples is also in agreement with the reports so far on this material system [167, 205, 206]. However, in contrast to the other well-known Ni(-Co)-Mn-X Heusler alloys, no distinct phase diagram including a order-disorder transition between $L2_1$ and B2 phase has been proposed in literature.

Furthermore, the electronic structure of the Ni-Co-Mn-Ti system shows that the moments of Co, Mn and Ti atoms are all lowered with increasing Ti content. Increasing the Ti content from 10 to 15 at. % for a constant Co content of 17 at. %, leads to a reduction of 8.7%, 16.8% and 0.4% for Co, Ni and Mn moments, respectively. This results in a decrease of the magnitude of the exchange interactions, particularly in the ferromagnetic Ni-Mn interaction, which in turn enhances the sharp compositional dependence of T_C^A with Ti content, in addition to the reduction of Mn-Co interactions. The origin of this behavior in the moments is tied to the unique feature of the all- d -metal Heusler exhibiting a remarkable d - d orbital hybridization [167]. Such strong hybridization creates sharp peaks with a noticeable pseudo-gap feature of the density of states (DOS) just below the Fermi energy in the minority spin channel, which is depicted in Fig. 7.2 (a) for $\text{Ni}_{33}\text{Co}_{17}\text{Mn}_{40}\text{Ti}_{10}$. By changing the e/a ratio, the number of states in the minority spin channel increases faster than the flat and smaller DOS of the majority spin channel, reducing the moments of all magnetic species. A different picture is seen in the Ni-Co-Mn-Sn system assuming $L2_1$ ordering in Fig 7.3 (b), where the Mn and Co/Ni have an opposite trend in moments with Mn being augmented and Co/Ni being reduced. Consequently, the exchange interactions are reduced slightly, but to much lesser extent than in the Ti-system.

The investigations of Chapter 6 show in comparison to the observed trends for Heusler alloys that the sensitivity of T_t for the conventional first-order phase transition with respect to an external magnetic field is not sensitive to stoichiometric changes at all. As a result, the tuning of $\frac{dT_t}{\mu_0 dH}$ in order to enhance the magnetocaloric performance is not easily accessible as a degree of freedom. In order to assess the

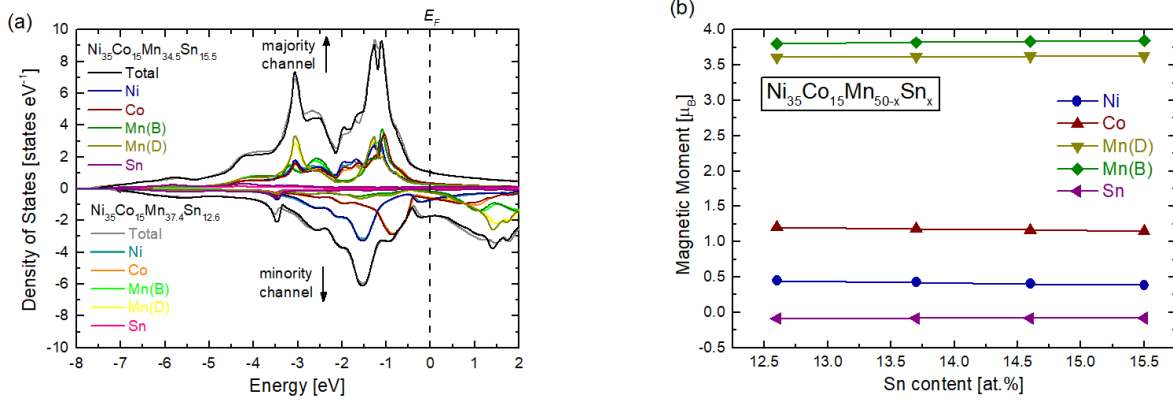


Figure 7.3: Calculated density of states (DOS) around E_F for $\text{Ni}_{35}\text{Co}_{15}\text{Mn}_{37.4}\text{Sn}_{12.6}$ in L_{21} ordered austenite state together with the magnetic moments carried by the individual atoms depending on the Ti content.

possibilities of designing a material towards an efficient field sensitivity, theoretical calculations would be a very valuable tool. Even though the driving force for shifting the transition temperature in a magnetic field is in a simple approximation according to the Zeeman term ($-\mu_0MH$) in the free energy proportional to the magnetization of the sample, similar magnetization changes between the austenite and martensite state for the $\text{MM}'\text{X}$ alloy system and the different Heusler alloys lead to very diverse values for $\frac{dT_t}{\mu_0 dH}$ in these systems. A reason could be found by also investigating the total shape of the free energy curves for high- and low-temperature state of different systems, since the behavior of the free energy curves in different fields scale with the driving force for the transition. Unfortunately, this is not easily accessible by theoretical modeling since particularly the vibrational phonon contribution to the free energy has many degrees of freedom, especially for off-stoichiometric systems and substitutional series like it is the case for the studied materials in this thesis. In a first approximation the Gibbs free energy depends besides the Zeeman term on the product of entropy S and temperature T (see Equation (2.4)). Material systems with a large contribution of this entropy term therefore show a reduced sensitivity of the total G towards changes of magnetization in external magnetic fields. In Chapter 6, it has been shown that the entropy change of the full transition is very large for $\text{MM}'\text{X}$ compounds compared to Heusler alloys. This can be a reason for the generally low $\frac{dT_t}{\mu_0 dH}$ that is a characteristic of this material system (see Section 6.4). Consequently, the asymmetry of the magnetostructural phase transition from hexagonal to orthorhombic (compared to cubic-tetragonal/modulated for Heusler compounds) that results in large entropy changes also hinders an efficient $\frac{dT_t}{\mu_0 dH}$ to induce the transition by an external magnetic field. Hence, a moderate entropy change that enables large magnetocaloric effects but still allows for tailoring the shift of T_t in external magnetic fields is ideal, which is the case for the Ni-Co-Mn-Ti alloys. Consequently, the Ni-Co-Mn-Ti Heusler alloys represent an ideal candidate for a strong magnetocaloric effect for medium magnetic-field changes. Considering low magnetic-field changes below 2 T, Ni(Co)-Mn-In is superior to all other Heusler alloys because of the outstanding $\frac{dT_t}{\mu_0 dH}$ in combination with the sharp phase transition.

7.2 Assessing the potential of Heusler alloys for a multi-stimuli cycle

The search for new materials is guided primarily by finding a material system, for which the promising transition properties can be tuned by stoichiometric substitutions. Therefore, DFT calculations can predict the variation in the stability of certain phases and model the corresponding magnetic moments of both phases as well as the Curie temperatures. However, especially the design of potentially well-performing materials for the novel multi-stimuli cycle requires new considerations in order to assess suitable materials. For example the thoroughly characterized all-*d* Heusler system of Ni-Co-Mn-Ti shows a low ΔT_{ad} in low magnetic-field changes but outperforms the so-far best Heusler alloy of Ni-Co-Mn-In in magnetic-field changes of larger than 10 T. In addition, the high mechanical stability and the huge volume change of the phase transition makes it a very suitable candidate for pressure-induced caloric effects. This example shows that the catalog of material choices needs to be revised for a different view on the application of multicaloric effects and the same is true for the modeling of new materials.

As a continuation of the thoughts in Chapter 5, the optimal material for a reversible multi-stimuli cycle will be discussed here by using the conditions described in Chapter 2 (Equations (2.11) - (2.15)) for two examples. The very sharp phase transition that is investigated for the ideal heat-treatment conditions of $\text{Ni}_{37}\text{Co}_{13}\text{Mn}_{34}\text{Ti}_{16}$ will be evaluated first. It is characterized by a transition width of 8 K, a thermal hysteresis of 10 K, a field sensitivity of -1.7 K T^{-1} and a pressure sensitivity (as determined for a suction-cast rod of similar stoichiometry) of 120 K GPa^{-1} . In order to account for the upper limit of requirements, the maximum ΔT_{ad} of -20 K , which has been determined for the completed phase transition of another compound ($\text{Ni}_{37}\text{Co}_{13}\text{Mn}_{34.5}\text{Ti}_{15.5}$) by high field measurements. The resulting magnetic field that would be required to induce a complete phase transition would be

$$\mu_0 H_{sat} = \frac{8 \text{ K} + 20 \text{ K}}{1.7 \text{ K T}^{-1}} = 16.5 \text{ T}. \quad (7.1)$$

Since the evolution of $\frac{dT_t}{\mu_0 dH}$ is not constant over the applied magnetic field but increasing, it is expected that the determined value is an overestimation by roughly 25 % (see Section 5.5). The respective uniaxial pressure that is needed for a fully induced phase transition under the assumption that the maximum pressure-induced ΔT_{ad} is the same as for a magnetic-field-induced ΔT_{ad} is determined as

$$\sigma_{sat} = \frac{8 \text{ K} + 20 \text{ K}}{120 \text{ K GPa}^{-1}} = 230 \text{ MPa}. \quad (7.2)$$

A constant transition width is assumed here for simplicity, which was shown in Section 5.7 to deviate with increasing pressure. Therefore, the assessment of the required pressure represents the lower limit. In order to operate this material in a fully reversible cycle, a magnetic field of around 15 T and a pressure of 230 MPa are required. The magnetic-field value is already quite large for practical applications in a cyclic manner even though pulsed fields or superconductors might be considered. The required pressure is already reduced since an isothermal application of the pressure is in the range of possibilities and considered

here. As a result, the obtained ΔT_{ad} would be dissipated during the pressure application step by the direct thermal contact with the large thermal load of the pistons. Otherwise it would be significantly larger. Furthermore the condition for the thermal hysteresis (10 K) is not fulfilled since it is indeed larger than T_t (8 K) but not larger than $T_t + \Delta T_{ad}$ (28 K). This means that the induced austenite would partially transform back to martensite upon field removal due to the temperature reduction by ΔT_{ad} , which is not desired for the multicaloric operation.

The optimization of the phase transition for a multi-stimuli cycle can be done by adjusting the Co and Ti content of the alloy. Therefore, the same assessment is carried out for the compound $\text{Ni}_{35}\text{Co}_{15}\text{Mn}_{37}\text{Ti}_{13}$ with a transition around room temperature, a broader hysteresis of 18 K, but also a larger T_{width} of 32 K as well as an increased $\frac{dT_t}{\mu_0 dH}$ of -2.8 K T^{-1} in low magnetic fields. The other parameters are assumed to stay the same. As a result the required stimuli amount to $\mu_0 H_{sat} = 18.5 \text{ T}$ and $\sigma_{sat} = 430 \text{ MPa}$. In addition, the thermal hysteresis is smaller than T_{width} and much smaller than $T_t + \Delta T_{ad}$, which will not lead to the desired circumvention of the back transformation. Despite the increased hysteresis and the enhanced magnetic-field sensitivity, further ways of designing an ideal material for the multicaloric cooling cycle need to be considered. One example can be the introduction of Fe instead of Co, which is known to drastically increase the thermal hysteresis for Ni-Mn-In alloys [262]. In addition, the use of Fe instead of Co would highly contribute to reduce the criticality and consequently the costs of the material. The introduction of secondary phases by precipitation or a distinct tailoring of the microstructure can also be efficient tools to optimize the promising Ni-Mn-Ti based Heusler alloys towards a reversible and efficient caloric cooling cycle. One main advantage of tuning the microstructure is the fact that it can influence both the thermal hysteresis and the mechanical properties.

Additional options can be the consideration of the Ni-Mn-Sn system because of the sharp phase transition and the large thermal hysteresis. The main drawback for this system is the low magnetic-field sensitivity of around 1 K T^{-1} . As a result, magnetic fields of 25 T would be required to induce a full phase transformation under adiabatic conditions. The large temperature changes that can be achieved with this system make it promising for the exploiting-hysteresis approach, but at the same time require large stimuli fields and a large thermal hysteresis. Consequently, the thermal hysteresis has to be designed further in order to be larger than the adiabatic temperature change to prevent a back transformation of the material after the field removal. The behavior under uniaxial pressure taken from literature shows a stress sensitivity of the transition temperature of around 200 K GPa^{-1} [233, 263], which results in required stresses of 125 MPa - without considering an expected broadening of the transition. Increasing the hysteresis width together with enhancing $\frac{dT_t}{\mu_0 dH}$ while maintaining the narrow transition width is the challenging task to develop Ni-Mn-Sn samples towards multicaloric applications.

8 Conclusions and Outlook

The research on caloric materials is a dominant topic for the development of energy efficient and environmentally friendly alternatives for future refrigeration applications. This thesis focuses on a profound analysis of different material families that are frequently considered as promising candidates due to large caloric effects reported. By the comparison of different inverse Heusler alloys and the family of MM'X compounds as one conventional multicaloric material system, the content of this thesis sets up general design rules for magnetocaloric and multicaloric cooling applications. By regarding the similarities and differences, the choice for a suitable material system is discussed comprehensively for the two presented caloric cooling approaches of a pure magnetocaloric system and a multi-stimuli setup using magnetic field and pressure alternately to induce the phase transition. The assessment of different substitution approaches and their influence on the caloric performance of the discussed compounds provides an outlook for future challenges and prospects.

The family of Heusler alloys experiences a broad range of functional properties and especially Ni-Mn-based compounds are attractive for shape-memory and magneto- as well as mechanocaloric applications. First, a systematic optimization of the annealing procedure has been carried out in order to achieve the best possible sample quality for sharp phase transitions and large magnetocaloric effects. It is found out that the optimal annealing temperature correlates with the melting point. For Ni(-Co)-Mn-Sn and Ni-Co-Mn-Ti the best heat treatment temperature is around 200 K below the respective melting/solidification temperature. Therefore, the enabling of high diffusion rates for individual atoms is a crucial factor to achieve best possible chemical homogeneity and sharp phase transitions. Since the transition temperatures for atomic disordering between L2₁ and B2 crystal structure are different for the investigated systems, Ni-Co-Mn-Al and Ni-Co-Mn-Ti tend to form a B2 disordered phase at the optimal annealing temperature, whereas Ni-Co-Mn-In and Ni-Co-Mn-Sn tend to form L2₁ during the heat treatment. In order to establish a desired atomic order for each system, a subsequent post-treatment has to be done after assuring an optimal chemical homogeneity.

A systematic study for a subsequent heat treatment of a Ni-Mn-In sample at different temperatures underlines that the sharpness of the FOMT can be enhanced further by this procedure at a post-treatment step at 773 K for 24 h, which is significantly below the L2₁/B2 transition temperature. This annealing step additionally shifts the transition temperature to slightly higher temperatures (+20 K compared to T_t of the initial homogenization treatment). Consequently, the MCE can be enhanced by 45 % for Δs_T and by 10 % in terms of the directly measured ΔT_{ad} .

The comparison of the three classical Heusler systems of Ni(-Co)-Mn-In, Ni(-Co)-Mn-Sn, and Ni(-Co)-Mn-Al, which all have main group elements on the D-sites of the Heusler lattice, provides principle trends for the design of a well-performing magnetocaloric Heusler alloy. Not only the transition temperature can be tuned by the stoichiometry, also the magnetic-field sensitivity $\frac{dT_t}{\mu_0 dH}$ as well as the thermal hysteresis are linearly (as a first, simple approximation) changing for the region of interest around room temperature as a function of the e/a ratio. Both thermal hysteresis and $\frac{dT_t}{\mu_0 dH}$ increase for decreasing T_t , which means that a trade-off between a large field-induced MCE and a good cyclic performance needs to be made. However, adding a certain amount of Co as substitution for Ni can increase $\frac{dT_t}{\mu_0 dH}$ with different impact on the thermal hysteresis. This approach is ideal for tailoring the MCE of Ni(-Co)-Mn-Sn because the addition of Co even reduces the thermal hysteresis. Nevertheless, the values for $\frac{dT_t}{\mu_0 dH}$ around room temperature cannot compete with those of Ni-Co-Mn-In making this system still the best performing Heusler alloys at low magnetic-field changes of 1 T to 2 T. Even though Δ_{sT} of Ni(-Co)-Mn-Sn is similar for this low-field region as a result of the lower field sensitivity, no reasonable cyclic ΔT_{ad} can be measured. The ΔT_{ad} of the second field cycle for best Ni-Co-Mn-Sn amounts to only 1 K, which is only one third of the best Ni-Co-Mn-In sample so far with a cyclic ΔT_{ad} of 3 K in magnetic-field changes of 2 T.

The drawback of moderate magnetic-field sensitivities can turn into an advantage when using larger field changes. For magnetic-field changes of 10 T to 20 T, the shift of the transition temperature can be enough to induce a complete magnetostructural phase transition and saturate the MCE under adiabatic conditions. In this case, the effect expressed by ΔT_{ad} is much larger than for samples with a large $\frac{dT_t}{\mu_0 dH}$ and lower saturation fields. In addition, the use of large fields can be made feasible by using pulsed or confined permanent magnetic fields. This can be realized by a novel approach of a multi-stimuli cooling cycle, which uses a magnetic field in combination with a uniaxial stress to transform a multicaloric material back and forth. The addition of a second stimulus to transform the material back to its initial state offers more opportunities for designing the magnetic-field source because the field only needs to be active for a short amount of time or over a small volume. This also provides more time for the heat exchange. Much more importantly, this cycle requires a material with a sufficiently large thermal hysteresis in order to lock the materials in its transformed state once the magnetic field is removed again.

The novel all- d Heusler material system of Ni-Co-Mn-Ti is very promising for this innovative approach since its transition temperature, magnetic-field sensitivity, stress sensitivity and thermal hysteresis can be tailored by varying the composition. Opposite to the classical Heusler systems, it consists only of transition metals. A comprehensive integration of the characteristic magnetocaloric properties in comparison with the other well-known Ni(-Co)-Mn-X Heusler alloys reveals that most of the trends are also applicable here. Regardless of the Co-content, the transition temperature can be described universally by the e/a ratio of the compound and $\frac{dT_t}{\mu_0 dH}$ can be tailored distinctly by varying the Co content. Particularly, the field sensitivity depends universally on the difference between T_t and T_C^A . However, the slope of this dependence varies for the different Heusler systems investigated. Consequently, chemical variations influence the tunability of $\frac{dT_t}{\mu_0 dH}$ differently. For the Ni-Co-Mn-Ti system, this slope is found to be ideal in order to tailor $\frac{dT_t}{\mu_0 dH}$ not to be too high (reduces the maximum possible MCE) or too low (hinders an efficient magnetic-field-induced

transition). A difference between the novel all-*d* Heusler system of Ni-Co-Mn-Ti and the classical Heusler compounds is the behavior of a strongly decreasing T_C^A with increasing amount of Ti. A correlation with DFT calculations shows that this is rather an effect of the preferred B2 disorder present in this alloy system.

By the optimized annealing procedure, Ni-Co-Mn-Ti samples can be produced that show a very sharp phase transition with isothermal entropy changes of up to $38 \text{ J kg}^{-1} \text{ K}^{-1}$. Temperature-dependent optical microscopy studies underline that non-ideally heat treated samples have a broad distribution of martensite nucleations upon cooling the sample. This is a consequence of stoichiometric differences and hence of a broad distribution of locally different transition temperatures throughout the sample. Sharpest transitions occur within a temperature range of 4 K for a sample with abnormal grain growth during annealing. The sharp transition is therefore a combined effect of an optimized homogeneity and a reduced number of grain boundaries that can act as barriers for the martensite growth.

Despite the sharp transition and large isothermal entropy changes, the directly measured temperature change for magnetic-field changes of 1.93 T only amounts to -4 K for the first field application and -1 K under cyclic conditions. The reason is the moderate $\frac{dT_t}{\mu_0 dH}$ that hinders a cyclic field-induced transition under adiabatic conditions for low field changes. However, the saturated effect in pulsed fields amounts to -20 K in magnetic-field changes of 20 T, which is much larger than highest saturated ΔT_{ad} measured so far for Ni(-Co)-Mn-In. In combination with a good mechanical stability and tunable thermal hysteresis, Ni-Co-Mn-Ti represents an ideal candidate for the novel multi-stimuli cooling cycle. For using fast pulsed fields, the field-rate-dependence must be considered for rates above 710 T s^{-1} , at which the first-order transition is delayed.

In order to evaluate the stress-induced phase transition, the temperature- and stress-dependent strain has been examined. For Co contents of 14 at. %, stress sensitivities for T_t of around 170 K GPa^{-1} have been found under applying a uniaxial load. The transition width as well as the transition strain are both increasing linearly with applied stresses up to 400 MPa. As a consequence, larger stresses are needed to induce a complete phase transition than by considering the transition behavior for a zero-stress case. In a first approximation, a Ni-Co-Mn-Ti sample with 14-15 at. % of Co would require magnetic fields of 10 T and uniaxial stresses of 300 MPa applied alternately under adiabatic conditions in order to exploit the full potential of the FOMT. For this multi-stimuli cycle, an ideal thermal hysteresis of 30 K to 40 K is necessary - depending on the stoichiometry, the transition width and the maximum ΔT_{ad} achieved.

The next step for the development of Ni-Co-Mn-Ti alloys is the performance assessment in a testing device that enables the subsequent measurement of ΔT_{ad} for alternately applied magnetic field and uniaxial pressure. A similar setup has been realized already by using a 2 T electromagnet and a uniaxial press setup for the proof-of-principle of the multi-stimuli cooling approach with a suction-cast Ni-Mn-In sample [43]. The implementation of Ni-Co-Mn-Ti would require larger fields in order to fully exploit the cooling potential of the phase transition. A possible way can be the use of a uniaxial press setup with a temperature chamber like the one used for the temperature- and stress-dependent strain measurements (described in Section 3.7). A pulsed magnet providing a magnetic field of up to 10 T can be established around the sample position between the two pistons of the press. According to the assessment of ΔT_{ad} in pulsed fields in Section 5.5,

this field is sufficient to use 75 % of the maximum possible ΔT_{ad} for the analyzed sample with a Co content of 13 at. %. An increase towards 14 or 15 at. % of Co increases $\frac{dT_L}{\mu_0 dH}$ and should facilitate the full MCE for magnetic-field changes of 10 T. Simultaneously, the increasing thermal hysteresis ensures that the sample stays in the transformed state after the short field pulse. Since direct contact to the pistons must be possible for the load application, a complete insulation of the sample is hardly achieved. The necessary adiabatic conditions are ensured by the fast field pulse used. In addition, using ceramic or metal plates with low thermal conductivity at the pistons of the press is a possibility to reduce thermal contact. Experiments are necessary to check whether this setup would withstand the applied loads since ceramics are prone to crack propagation by local stress fields. In fact, a good thermal contact during the stress application is beneficial in order to avoid a temperature change of the elastocaloric effect. Since adiabatic conditions would mean a heating of the sample counteracting the stress-induced martensitic transformation, much larger stresses are necessary. In an isothermal setup, the stress-application step cannot be used to determine the elastocaloric effect of the sample. It is instead only used to transform the sample back to its initial martensite state.

For an even further sophisticated testing setup, close-to-application conditions must be established. That means primarily that the heat exchange by a fluid needs to be introduced and the whole setup must be scaled down in total size. An efficient way of producing high fields in narrow volumes can be the use of high-temperature superconducting magnets. For example, layered cuprate compounds like Yttrium-Barium-Copperoxide (YBCO) can be operated below the superconducting transition temperature by using cryocoolers that do not rely on a permanent feed of liquid nitrogen. A pressure application may be done using step motors and pistons that are able to exert uniaxial stresses in a precisely controlled way. Due to the non-adiabatic stress-application step, the heat produced by the induced FOMT is expelled over the piston setup. Consequently, the heat exchange fluid does not need to be pumped back and forth like in other AMR setups in order to alternately heat and cool the sample. The fluid can be cooled by the magnetocaloric material after the magnetic-field step and absorb heat from the cooling load at the cold end. Afterwards it has to cool either the pistons that absorb the heat after the field-application process or the fluid is used in a cycle for the next cooling step of the setup. That would mean that the pistons are connected to another thermal bath in order to avoid their overheating. Alternatively, the heat exchange fluid is used to cool the pistons, which sets up the heat exchange cycle of a conventional magnetocaloric AMR. By using this proposed setup, new thermodynamic considerations have to be addressed because the cooling cycle consists of one adiabatic, one isofield and one isothermal step and is not Brayton-like any more.

On a long-term perspective, the suitability of this material system (or any other possible candidate system for the multi-stimuli cycle) has to be proven by fatigue measurements. In a first step, the high cycle fatigue can give an estimate of the amount of cycles that the material can withstand for frequent stress application that are limited to the elastic regime of the stress-strain curve. This should be carried out for a sample in austenite and martensite state since both phases are expected to show different mechanical properties as a result of their characteristic microstructure. In a further step, the fatigue resistance of the material has to be tested for a large amount of cycles upon inducing the martensitic phase transition by each cycle. However,

first tests showed that the sample failed after a few temperature-induced transition cycles at a maximum constant stress of 400 MPa. It must be evaluated how this changes for a dynamical stress application. For this test, the optimal sample has to have a small transition width as well as a narrow thermal hysteresis so that lowest possible stresses can be applied in a cyclic manner to simulate subsequent martensite and austenite formation cycles.

The MM'X family with the MnNiGe base compound can exhibit very large isothermal entropy changes of up to $38 \text{ J kg}^{-1} \text{ K}^{-1}$ for small pieces of material. By the powerful method of isostructural alloying, it has been shown within Chapter 6 that the phase transition can be tailored distinctly by stoichiometric variations using substitutional elements that also form stable compounds of the same crystal structure. This can be used to increase the ferromagnetic character of the low-temperature phase and additionally to decrease the amount of expensive Ge used in the compounds. However, one of the most important properties for the application of a magnetocaloric material, which is the sensitivity of T_t towards externally applied magnetic fields, cannot be influenced effectively and stays constant at a low level of around 1 K T^{-1} .

The magnetostructural phase transition is accompanied by a huge volume change of 2.7%. In contrast to the Ni-Co-Mn-Ti alloys with similar values, the MM'X alloys are not strong enough to withstand the large stresses occurring during the phase transformation. Bulk samples degrade into small fragments after a few transition cycles and cannot be used for cyclic applications. An alternative option is using polymer-bonded powder samples, which are more stable. However, the constraint volume expansion results in large stresses in the sample. The stress-coupling of the individual particles results in a significantly broadened transition width, which reduces the maximum possible MCE drastically. In combination with the low $\frac{dT_t}{\mu_0 dH}$ of these compounds, only very small cyclic temperature changes can be achieved for field changes of 1.93 T. A classification of the particles by separating a powder by the individual transition temperatures of the particles can be a promising method to enhance the performance of this material system. Therefore, a temperature-dependent setup is needed, where at each temperature, particles are attracted by a permanent magnet. Cooling down by a certain temperature step would then lead to a selection of all particles that become ferromagnetic and thus have their individual T_t within this temperature width. Consequently, all particles that are in paramagnetic state remain in the powder and are used for the subsequent temperature steps. This method can lead to powder beds with a very sharp distribution of T_t . It would be necessary to investigate in a subsequent study, how the cyclic transition influences the stability and shape of these small particles in order to assess the potential for using stacks of powder beds in a heat exchanger setup.

Due to the large volume change of this material system, a very good response for the application of external hydrostatic pressure is observed. The sensitivity of 72 K GPa^{-1} upon maintaining the transition width and ΔS_T of the FOMT makes samples of MnNiGe with simultaneous Fe and Si substitution for Mn and Ge, respectively, very attractive for barocaloric applications.

Especially the Ge-free samples with small amounts of Al substitution ($\text{Mn}_{0.5}\text{Fe}_{0.5}\text{NiSi}_{0.94}\text{Al}_{0.06}$) show ideal properties for a multi-stimuli cycle. By eliminating the Ge content, the compound consists of abundant elements and possesses a very sharp phase transition ($T_{width} = 8 \text{ K}$) with a large thermal hysteresis ($T_{hyst} = 25 \text{ K}$). The mechanical stability is enhanced by this substitution, but is still not good enough to

enable a stable operation over tens and hundreds of cycles (which is still below the desired millions and billions of cycles necessary for long-term applications). Additionally, the disadvantageous low $\frac{dT_t}{\mu_0 dH}$ for this compound is still present.

For future research the key point is to reduce the volume change of the MM'X compounds. This might lead to reduced sensitivities towards external pressure, but the benefits are expected to outweigh this sacrifice. On the one hand, the total entropy change of the complete transition is expected to be reduced, which should influence $\frac{dT_t}{\mu_0 dH}$ when maintaining the ΔM of the transition (according to Clausius-Clapeyron relation). In addition, the mechanical stability will be enhanced. These adjustments would make the isostructurally alloyed compounds of the MM'X family extremely promising for magnetocaloric applications as well as for using them in a multi-stimuli cooling cycle - if the mechanical stability can be tailored towards a long-term stable compound that also withstands cyclic applications of uniaxial pressure of several hundred MPa.

Bibliography

- [1] Title image (inset): T. Gottschall, K. P. Skokov, M. Fries, A. Taubel, I. Radulov, F. Scheibel, D. Benke, S. Riegg, and O. Gutfleisch. Magnetic Refrigeration: Making a Cool Choice: The Materials Library of Magnetic Refrigeration (Adv. Energy Mater. 34/2019). *Advanced Energy Materials*, 9:1970130, 2019. doi:[10.1002/aenm.201970130](https://doi.org/10.1002/aenm.201970130). Copyright Wiley-VCH Verlag GmbH & Co. KGaA. Reproduced with permission.
- [2] Population Reference Bureau (PRB). 2019 world population data sheet. Data Sheet, 2019.
- [3] United Nations Department of Economic and Social Affairs. World population prospects: Ten key findings, 2019.
- [4] W. S. Jevons. *The Coal Question*. London: Macmillan and Co., 2nd edition, 1866.
- [5] J. Watt. New Invented Method of Lessening the Consumption of Steam and Fuel in Fire Engines. British Patent No. 913, 1769.
- [6] J. Watt. Extension of Patent No. 913. British Patent No.913, 1775.
- [7] L. G. Brookes. Energy policy, the energy price fallacy and the role of nuclear energy in the UK. *Energy Policy*, 6(6):94–106, 1978. doi:[10.1016/0301-4215\(78\)90031-9](https://doi.org/10.1016/0301-4215(78)90031-9).
- [8] J. D. Khazzoom. Economic implications of mandated efficiency in standard household appliances. *The Energy Journal*, 1(4):21–40, 1980. doi:[10.5547/ISSN0195-6574-EJ-Vol1-No4-2](https://doi.org/10.5547/ISSN0195-6574-EJ-Vol1-No4-2).
- [9] H. G. Berkhout, J. C. Muskens, and J. W. Velthuisen. Defining the rebound effect. *Energy Policy*, 28: 425–432, 2000. doi:[10.1016/S0301-4215\(00\)00022-7](https://doi.org/10.1016/S0301-4215(00)00022-7).
- [10] P. Nejat, F. Jomehzadeh, M. M. Taheri, M. Gohari, and M. Z. Abd. Majid. A global review of energy consumption, CO₂ emissions and policy in the residential sector (with an overview of the top ten CO₂ emitting countries). *Renewable and Sustainable Energy Reviews*, 43:843–862, 2015. doi:[10.1016/j.rser.2014.11.066](https://doi.org/10.1016/j.rser.2014.11.066).
- [11] International Institute of Refrigeration (IIR). The Role of Refrigeration in the Global Economy. 29th Informatory Note on Refrigeration Technologies.

-
- [12] International Institute of Refrigeration (IIR). The impact of the refrigeration sector on climate change. 35th Informatory Note on Refrigeration Technologies.
- [13] M. Isaac and D. P. van Vuuren. Modeling global residential sector energy demand for heating and air conditioning in the context of climate change. *Energy Policy*, 37(2):507–521, 2009. doi:[10.1016/j.enpol.2008.09.051](https://doi.org/10.1016/j.enpol.2008.09.051).
- [14] International Energy Agency (IEA). The future of cooling - opportunities for energy-efficient air conditioning. Report, 2018.
- [15] United Nations Environment Programme (UNEP). Global warming potential (GWP) of refrigerants: why are particular values used? Fact Sheet, 2020.
- [16] United Nations Environment Programme (UNEP). The Montreal Protocol on Substances that Deplete the Ozone Layer. Report, 1987.
- [17] European Union (EU). Regulation (EU) no 517/2014 of the European Parliament and of the Council of 16 april 2014 on fluorinated greenhouse gases and repealing Regulation (EC) No 842/2006, 2014.
- [18] United Nations Environment Programme (UNEP). Amendment to the Montreal Protocol on Substances that Deplete the Ozone Layer. Report, 2016.
- [19] International Energy Agency (IEA). Global air conditioner stock, 1990-2050, IEA, Paris. URL <https://www.iea.org/data-and-statistics/charts/global-air-conditioner-stock-1990-2050>. Last access: 15.08.2020.
- [20] P. Weiss and A. Piccard. Le phénomène magnétocalorique. *Journal de Physique Théorique et Appliquée*, 7(1):103–109, 1917. doi:[10.1051/jphys/019170070010300](https://doi.org/10.1051/jphys/019170070010300).
- [21] W. F. Giauque and D. P. MacDougall. Attainment of temperatures below 1° absolute by demagnetization of $\text{Gd}_2(\text{SO}_4)_3 \cdot 8\text{H}_2\text{O}$. *Physical Review*, 43:768, 1933. doi:[10.1103/PhysRev.43.768](https://doi.org/10.1103/PhysRev.43.768).
- [22] The Nobel Prize. Nobel Prize in Chemistry 1949. Website. URL <https://www.nobelprize.org>.
- [23] C. Zimm, A. Jastrab, A. Sternberg, V. Pecharsky, K. Gschneidner, M. Osborne, and I. Anderson. *Description and Performance of a Near-Room Temperature Magnetic Refrigerator*, pages 1759–1766. Springer US, Boston, MA, 1998. ISBN 978-1-4757-9047-4. doi:[10.1007/978-1-4757-9047-4_222](https://doi.org/10.1007/978-1-4757-9047-4_222).
- [24] P. Bansal, E. Vineyard, and O. Abdelaziz. Status of not-in-kind refrigeration technologies for household space conditioning, water heating and food refrigeration. *International Journal of Sustainable Built Environment*, 1:85–101, 2012. doi:[10.1016/j.ijsbe.2012.07.003](https://doi.org/10.1016/j.ijsbe.2012.07.003).
- [25] J. S. Brown and P. A. Domanski. Review of alternative cooling technologies. *Applied Thermal Engineering*, 64:252–262, 2014. doi:[10.1016/j.applthermaleng.2013.12.014](https://doi.org/10.1016/j.applthermaleng.2013.12.014).
-

-
- [26] S. Qian, D. Nasuta, A. Rhoads, Y. Wang, Y. Geng, Y. Hwang, R. Radermacher, and I. Takeuchi. Not-in-kind cooling technologies: A quantitative comparison of refrigerants and system performance. *International Journal of Refrigeration*, 62:177–192, 2016. doi:[10.1016/j.ijrefrig.2015.10.019](https://doi.org/10.1016/j.ijrefrig.2015.10.019).
- [27] United Nations (UN). Paris Agreement, 2015.
- [28] United Nations Environment Programme (UNEP) Technical Options Committee. 2018 Report of the Refrigeration, Air Conditioning and Heat Pumps. Report, 2018.
- [29] M. O. McLinden, J. S. Brown, R. Brignoli, A. F. Kazakov, and P. A. Domanski. Limited options for low-global-warming-potential refrigerants. *Nature Communications*, 8:14476, 2017. doi:[10.1038/ncomms14476](https://doi.org/10.1038/ncomms14476).
- [30] C. Vasile and C. Muller. Innovative design of a magnetocaloric system. *International Journal of Refrigeration*, 29:1318–1326, 2006. doi:[10.1016/j.ijrefrig.2006.07.016](https://doi.org/10.1016/j.ijrefrig.2006.07.016).
- [31] A. Tura and A. Rowe. Permanent magnet magnetic refrigerator design and experimental characterization. *International Journal of Refrigeration*, 34(3):628–639, 2011. doi:[10.1016/j.ijrefrig.2010.12.009](https://doi.org/10.1016/j.ijrefrig.2010.12.009).
- [32] K. Engelbrecht, C. R. H. Bahl, and K. K. Nielsen. Experimental results for a magnetic refrigerator using three different types of magnetocaloric material regenerators. *International Journal of Refrigeration*, 34(4):1132–1140, 2011. doi:[10.1016/j.ijrefrig.2010.11.014](https://doi.org/10.1016/j.ijrefrig.2010.11.014).
- [33] M. Balli, O. Sari, C. Mahmed, Ch. Besson, Ph. Bonhote, D. Duc, and J. Forchelet. A pre-industrial magnetic cooling system for room temperature application. *Applied Energy*, 98:556–561, 2012. doi:[10.1016/j.apenergy.2012.04.034](https://doi.org/10.1016/j.apenergy.2012.04.034).
- [34] GE Reports. Not your average fridge magnet: These high-tech magnets will keep your butter (and beer) cold. Web Article, 2014. URL <https://www.ge.com/reports/post/75911607449/not-your-average-fridge-magnet/>. Last access: 27.08.2020.
- [35] Cooling Post. Debut for magnetic refrigeration wine cooler. Web Article, 2015. URL <https://www.coolingpost.com/world-news/debut-for-magnetic-refrigeration-wine-cooler/>. Last access: 27.08.2020.
- [36] R. Gauß, G. Himm, and O. Gutfleisch. The resource basis of magnetic refrigeration. *Journal of Industrial Ecology*, 2016. ISSN 1530-9290. doi:[10.1111/jiec.12488](https://doi.org/10.1111/jiec.12488).
- [37] O. Gutfleisch, T. Gottschall, M. Fries, D. Benke, I. Radulov, K. P. Skokov, H. Wende, M. Gruner, M. Acet, P. Entel, and M. Farle. Mastering hysteresis in magnetocaloric materials. *Philosophical Transactions of the Royal Society A: Mathematical, Physical and Engineering Sciences*, 374(2074): 20150308, 2016. doi:[10.1098/rsta.2015.0308](https://doi.org/10.1098/rsta.2015.0308).
-

-
- [38] F. Scheibel, T. Gottschall, A. Taubel, M. Fries, K. P. Skokov, A. Terwey, W. Keune, K. Ollefs, H. Wende, M. Farle, M. Acet, O. Gutfleisch, and M. E. Gruner. Hysteresis Design of Magnetocaloric Materials - From Basic Mechanisms to Applications. *Energy Technology*, 6(8):1397–1428, 2018. doi:[10.1002/ente.201800264](https://doi.org/10.1002/ente.201800264).
- [39] R. Bjørk, C. R. H. Bahl, A. Smith, and N. Pryds. Review and comparison of magnet designs formagnetic refrigeration. *International Journal of Refrigeration*, 33(3):437–448, 2010. doi:[10.1016/j.ijrefrig.2009.12.012](https://doi.org/10.1016/j.ijrefrig.2009.12.012).
- [40] European Commission. Communication from the Commission to the European Parliament, the Council, the European Economic and Social Committee and the Committee of the Regions on the 2017 list of Critical Raw Materials for the EU, 2017.
- [41] A. Kitanovski, U. Plaznik, U. Tomc, and A. Poredoš. Present and future caloric refrigeration and heat-pump technologies. *International Journal of Refrigeration*, 57:288–298, 2015. doi:[10.1016/j.ijrefrig.2015.06.008](https://doi.org/10.1016/j.ijrefrig.2015.06.008).
- [42] A. Greco, C. Aprea, A. Maiorino, and C. Masselli. A review of the state of the art of solid-state caloric cooling processes at room-temperature before 2019. *International Journal of Refrigeration*, 106:66–88, 2019. doi:[10.1016/j.ijrefrig.2019.06.034](https://doi.org/10.1016/j.ijrefrig.2019.06.034).
- [43] T. Gottschall, A. Gràcia-Condal, M. Fries, A. Taubel, L. Pfeuffer, L. Mañosa, A. Planes, K. P. Skokov, and O. Gutfleisch. A multicaloric cooling cycle that exploits thermal hysteresis. *Nature Materials*, 17(10):929–934, 2018. doi:[10.1038/s41563-018-0166-6](https://doi.org/10.1038/s41563-018-0166-6).
- [44] L. Landau. On the theory of phase transitions. *Zh. Eksp. Fiz*, 7:19–32, 1937.
- [45] P. Ehrenfest. Phasenumwandlungen im üblichen und erweiterten Sinn, classifiziert nach den entsprechenden Singularitäten des thermodynamischen Potentials. *Verhandlungen der Koninklijke Akademie van Wetenschappen (Amsterdam)*, 36:153–157, 1933.
- [46] W. H. Keesom. On the jump in the expansion coefficient of liquid helium in passing the lambda point. *Verhandlungen der Koninklijke Akademie van Wetenschappen (Amsterdam)*, 36:147–152, 1933.
- [47] G. Jaeger. The Ehrenfest Classification of Phase Transitions: Introduction and Evolution. *Archive for History of Exact Sciences*, 53(1):51–81, 1998. doi:[10.1007/s004070050021](https://doi.org/10.1007/s004070050021).
- [48] Deutsches Institut für Normung (DIN). Din SPEC 91373:2018-06, Magnetocalorics: Terminology, 2018.
- [49] E. C. Bain and N. Y. Dunkiri. The nature of martensite. *Transactions of the American Institute of Mining and Metallurgical Engineers*, 70:25, 1924.

-
- [50] A. Diestel, R. Niemann, B. Schleicher, S. Schwabe, L. Schultz, and S. Fähler. Field-temperature phase diagrams of freestanding and substrate-constrained epitaxial Ni-Mn-Ga-Co films for magnetocaloric applications. *Journal of Applied Physics*, 118:023908, 2015. doi:[10.1063/1.4922358](https://doi.org/10.1063/1.4922358).
- [51] R. Tickle, R. D. James, T. Shield, M. Wuttig, and V. V. Kokorin. Ferromagnetic Shape Memory in the NiMnGa System. *IEEE Transactions on Magnetics*, 35(5):4301–4310, 1999. doi:[10.1109/20.799080](https://doi.org/10.1109/20.799080).
- [52] S. Kaufmann, R. Niemann, T. Thersleff, U. K. Rößler, O. Heczko, J. Buschbeck, B. Holzapfel, L. Schultz, and S. Fähler. Modulated martensite: why it forms and why it deforms easily. *New Journal of Physics*, 13:053029, 2011. doi:[10.1088/1367-2630/13/5/053029](https://doi.org/10.1088/1367-2630/13/5/053029).
- [53] R. Niemann, U. K. Rößler, M. E. Gruner, O. Heczko, L. Schultz, and S. Fähler. The Role of Adaptive Martensite in Magnetic Shape Memory Alloys. *Advanced Engineering Materials*, 14(8):562–581, 2012. doi:[10.1002/adem.201200058](https://doi.org/10.1002/adem.201200058).
- [54] S. Ener, T. Mehaddene, B. Pedersen, M. Leitner, J. Neuhaus, and W. Petry. Vibrational properties of Ni–Mn–Ga shape memory alloy in the martensite phases. *New Journal of Physics*, 15:123016, 2013. doi:[10.1088/1367-2630/15/12/123016](https://doi.org/10.1088/1367-2630/15/12/123016).
- [55] M. E. Gruner, R. Niemann, P. Entel, R. Pentcheva, U. K. Rößler, K. Nielsch, and S. Fähler. Modulations in martensitic Heusler alloys originate from nanotwin ordering. *Scientific Reports*, 8:8489, 2018. doi:[10.1038/s41598-018-26652-6](https://doi.org/10.1038/s41598-018-26652-6).
- [56] A. G. Khachatryan, S. M. Shapiro, and S. Semenovskaya. Adaptive phase formation in martensitic transformation. *Physical Review B*, 43(13):10832, 1991. doi:[10.1103/PhysRevB.43.10832](https://doi.org/10.1103/PhysRevB.43.10832).
- [57] T. Gottschall, D. Benke, M. Fries, A. Taubel, I. A. Radulov, K. Skokov, and O. Gutfleisch. A matter of size and stress: Understanding the first-order transition in materials for solid-state refrigeration. *Advanced Functional Materials*, 27:1606735, 2017. doi:[10.1002/adfm.201606735](https://doi.org/10.1002/adfm.201606735).
- [58] V. Franco, J.S. Blázquez, B. Ingale, and A. Conde. The Magnetocaloric Effect and Magnetic Refrigeration Near Room Temperature: Materials and Models. *Annu. Rev. Mater. Res.*, 42:305–342, 2012. doi:[10.1146/annurev-matsci-062910-100356](https://doi.org/10.1146/annurev-matsci-062910-100356).
- [59] R. A. Swalin. *Thermodynamics of Solids*. New York: Wiley, 1962.
- [60] A. M. Tishin and Y. I. Spichkin. *The Magnetocaloric Effect and its Applications*. Institute of Physics Publishing, 2013.
- [61] N. A. de Oliveira and P. J. von Ranke. Theoretical aspects of the magnetocaloric effect. *Physics Reports*, 489:89–159, 2010. doi:[10.1016/j.physrep.2009.12.006](https://doi.org/10.1016/j.physrep.2009.12.006).
- [62] V. K. Pecharsky, K. A. Gschneidner Jr., A. O. Pecharsky, and A. M. Tishin. Thermodynamics of the magnetocaloric effect. *Phys. Rev. B*, 64:144406, 2001. doi:[10.1103/PhysRevB.64.144406](https://doi.org/10.1103/PhysRevB.64.144406).
-

-
- [63] A. Kitanovski, J. Tušek, U. Tomc, U. Plaznik, M. Ozbolt, and A. Poredoš. *Magnetocaloric Energy Conversion: From Theory to Applications*. Green Energy and Technology. Springer International Publishing, 2014. ISBN 9783319087405.
- [64] K. A. Gschneidner Jr., V. K. Pecharsky, and A. O. Tsokol. Recent developments in magnetocaloric materials. *Reports on Progress in Physics*, 68:1479–1539, 2005. doi:[10.1088/0034-4885/68/6/R04](https://doi.org/10.1088/0034-4885/68/6/R04).
- [65] M. Wolloch, M. E. Gruner, W. Keune, P. Mohn, J. Redinger, F. Hofer, D. Suess, R. Podloucky, J. Landers, S. Salamon, F. Scheibel, D. Spoddig, R. Witte, B. Roldan Cuenya, O. Gutfleisch, M. Y. Hu, J. Zhao, T. Toellner, E. E. Alp, M. Siewert, P. Entel, R. Pentcheva, and H. Wende. Impact of lattice dynamics on the phase stability of metamagnetic FeRh: Bulk and thin films. *Physical Review B*, 94:174435, 2016. doi:[10.1103/PhysRevB.94.174435](https://doi.org/10.1103/PhysRevB.94.174435).
- [66] T. Kihara, X. Xu, W. Ito, R. Kainuma, and M. Tokunaga. Direct measurements of inverse magnetocaloric effects in metamagnetic shape-memory alloy NiCoMnIn. *Physical Review B*, 90:214409, 2014. doi:[10.1103/PhysRevB.90.214409](https://doi.org/10.1103/PhysRevB.90.214409).
- [67] T. Gottschall, K. P. Skokov, D. Benke, M. E. Gruner, and O. Gutfleisch. Contradictory role of the magnetic contribution in inverse magnetocaloric Heusler materials. *Phys. Rev. B*, 93:184431, 2016. doi:[10.1103/PhysRevB.93.184431](https://doi.org/10.1103/PhysRevB.93.184431).
- [68] G. V. Brown. Magnetic heat pumping near room temperature. *Journal of Applied Physics*, 47:3673–3680, 1976. doi:[10.1063/1.323176](https://doi.org/10.1063/1.323176).
- [69] W. A. Steyert. Stirling-cycle rotating magnetic refrigerators and heat engines for use near room temperature. *Journal of Applied Physics*, 49:1216, 1978. doi:[10.1063/1.325009](https://doi.org/10.1063/1.325009).
- [70] J. A. Barclay and W. A. Steyert. Active Magnetic Regenerator. US Patent No. 4,332,135, 1982.
- [71] T. Gottschall, K. P. Skokov, M. Fries, A. Taubel, I. Radulov, F. Scheibel, D. Benke, S. Riegg, and O. Gutfleisch. Making a Cool Choice: The Materials Library of Magnetic Refrigeration. *Advanced Energy Materials*, 9:1901322, 2019. doi:[10.1002/aenm.201901322](https://doi.org/10.1002/aenm.201901322).
- [72] J. Romero Gómez, R. Ferreiro Garcia, A. De Miguel Catoira, and M. Romero Gómez. Magnetocaloric effect: A review of the thermodynamic cycles in magnetic refrigeration. *Renewable and Sustainable Energy Reviews*, 17:74–82, 2013. doi:[10.1016/j.rser.2012.09.027](https://doi.org/10.1016/j.rser.2012.09.027).
- [73] B. Yu, M. Liu, P. W. Egolf, and A. Kitanovski. A review of magnetic refrigerator and heat pump prototypes built before the year 2010. *International Journal of Refrigeration*, 33:1029–1060, 2010. doi:[10.1016/j.ijrefrig.2010.04.002](https://doi.org/10.1016/j.ijrefrig.2010.04.002).
- [74] X. Moya, S. Kar-Narayan, and N. D. Mathur. Caloric materials near ferroic phase transitions. *Nature Materials*, 13:439–450, 2014. doi:[10.1038/nmat3951](https://doi.org/10.1038/nmat3951).

-
- [75] D.R. Brown, T.B. Stout, J.A. Dirks, and N. Fernandez. The prospects of alternatives to vapor compression technology for space cooling and food refrigeration applications. *Energy Engineering*, 109(6):7–20, 2012. doi:[10.1080/01998595.2012.10554226](https://doi.org/10.1080/01998595.2012.10554226).
- [76] J. Liu, T. Gottschall, K. P. Skokov, J. D. Moore, and O. Gutfleisch. Giant magnetocaloric effect driven by structural transitions. *Nature Materials*, 11:620–626, 2012. doi:[10.1038/NMAT3334](https://doi.org/10.1038/NMAT3334).
- [77] A. Planes, T. Castán, and A. Saxena. Thermodynamics of multicaloric effects in multiferroic materials: application to metamagnetic shape-memory alloys and ferrotoroidics. *Phil. Trans. R. Soc. A*, 374:20150304, 2016. doi:[10.1098/rsta.2015.0304](https://doi.org/10.1098/rsta.2015.0304).
- [78] Y. Liu, L. C. Phillips, R. Mattana, M. Bibes, A. Barthélémy, and Brahim Dkhil. Large reversible caloric effect in FeRh thin films via a dual-stimulus multicaloric cycle. *Nature Communications*, 7:11614, 2016. doi:[10.1038/ncomms11614](https://doi.org/10.1038/ncomms11614).
- [79] A. Czernuszewicz, J. Kalet, and D. Lewandowski. Multicaloric effect: Toward a breakthrough in cooling technology. *Energy Conversion and Management*, 178:335–342, 2018. doi:[10.1016/j.enconman.2018.10.025](https://doi.org/10.1016/j.enconman.2018.10.025).
- [80] E. Stern-Taulats, T. Castán, L. Mañosa, A. Planes, N. D. Mathur, and X. Moya. Multicaloric materials and effects. *MRS Bulletin*, 43:295–299, 2018. doi:[10.1557/mrs.2018.72](https://doi.org/10.1557/mrs.2018.72).
- [81] E. Lovell, H. N. Bez, D. C. Boldrin, K. K. Nielsen, A. Smith, C. R. H. Bahl, and L. F. Cohen. The La(Fe,Mn,Si)₁₃H_z magnetic phase transition under pressure. *Physica Status Solidi RRL*, 11:1700143, 2017. doi:[10.1002/pssr.201700143](https://doi.org/10.1002/pssr.201700143).
- [82] D. R. Lide, editor. "Definitions of Scientific Terms" in *CRC Handbook of Chemistry and Physics*. CRC Press/Taylor and Francis, Boca Raton, FL, 89th edition, 2009.
- [83] A. Kitanovski and P. W. Egolf. Innovative ideas for future research on magnetocaloric technologies. *Int. J. Refrig.*, 33(3):449–464, 2010. doi:[10.1016/j.ijrefrig.2009.11.005](https://doi.org/10.1016/j.ijrefrig.2009.11.005).
- [84] A. Kitanovski. Energy applications of magnetocaloric materials. *Advanced Energy Materials*, 10:1903741, 2020. doi:[10.1002/aenm.20190374](https://doi.org/10.1002/aenm.20190374).
- [85] J. D. Moore, D. Klemm, D. Lindackers, S. Grasemann, R. Träger, J. Eckert, L. Löber, S. Scudino, M. Katter, A. Barcza, K. P. Skokov, and O. Gutfleisch. Selective laser melting of La(Fe,Co,Si)₁₃ geometries for magnetic refrigeration. *Journal of Applied Physics*, 114:043907, 2013. doi:[10.1063/1.4816465](https://doi.org/10.1063/1.4816465).
- [86] A. Mostafaei, K. A. Kimes, E. L. Stevens, J. Toman, Y. L. Krimer, K. Ullakko, and M. Chmielus. Microstructural evolution and magnetic properties of binder jet additive manufactured Ni-Mn-Ga magnetic shape memory alloy foam. *Acta Materialia*, 131:482–490, 2017. doi:[10.1016/j.actamat.2017.04.010](https://doi.org/10.1016/j.actamat.2017.04.010).
-

-
- [87] V. Laitinen, M. Merabtene, E. Stevens, M. Chmielus, J. Van Humbeeck, and K. Ullakko. *Additive Manufacturing from the Point of View of Materials Research*, chapter Additive Manufacturing of Magnetocaloric Materials, pages 61–64. Springer International Publishing, 2020. ISBN 978-3-030-46103-4. doi:[10.1007/978-3-030-46103-4_3](https://doi.org/10.1007/978-3-030-46103-4_3).
- [88] T. Lei, K. Engelbrecht, K. K. Nielsen, and C. T. Veje. Study of geometries of active magnetic regenerators for room temperature magnetocaloric refrigeration. *Applied Thermal Engineering*, 111: 1232–1243, 2017. doi:[10.1016/j.applthermaleng.2015.11.113](https://doi.org/10.1016/j.applthermaleng.2015.11.113).
- [89] I. A. Radulov, K. P. Skokov, D. Yu. Karpenkov, T. Gottschall, and O. Gutfleisch. On the preparation of $\text{La}(\text{Fe},\text{Mn},\text{Si})_{13}\text{H}_x$ polymer-composites with optimized magnetocaloric properties. *Journal of Magnetism and Magnetic Materials*, 396:228–236, 2015. doi:[10.1016/j.jmmm.2015.08.044](https://doi.org/10.1016/j.jmmm.2015.08.044).
- [90] I. A. Radulov, D. Yu. Karpenkov, K. P. Skokov, A. Yu. Karpenkov, T. Braun, V. Brabänder, T. Gottschall, M. Pabst, B. Stoll, and O. Gutfleisch. Production and properties of metal-bonded $\text{La}(\text{Fe},\text{Mn},\text{Si})_{13}\text{H}_x$ composite material. *Acta Materialia*, 127:389–399, 2017. doi:[10.1016/j.actamat.2017.01.054](https://doi.org/10.1016/j.actamat.2017.01.054).
- [91] J. A. Lozano, M. S. Capovilla, P. V. Trevizoli, K. Engelbrecht, C. R.H. Bahl, and J. R. Barbosa. Development of a novel rotary magnetic refrigerator. *International Journal of Refrigeration*, 68: 187–197, 2016. doi:[10.1016/j.ijrefrig.2016.04.005](https://doi.org/10.1016/j.ijrefrig.2016.04.005).
- [92] S. Wieland and F. Petzoldt. Powder-extrusion and sintering of magnetocaloric $\text{LaCe}(\text{FeMnSi})_{13}$ alloy. *Journal of Alloys and Compounds*, 719:182–188, 2017. doi:[10.1016/j.jallcom.2017.05.168](https://doi.org/10.1016/j.jallcom.2017.05.168).
- [93] T. E. Graedel, R. Barr, C. Chandler, T. Chase, J. Choi, L. Christoffersen, E. Friedlander, C. Henly, C. Jun, N. T. Nassar, D. Schechner, S. Warren, M.-Y. Yang, and Charles Zhu. Methodology of Metal Criticality Determination. *Environmental Science and Technology*, 46:1063–1070, 2012. doi:[10.1021/es203534z](https://doi.org/10.1021/es203534z).
- [94] N. A. Mancheri, B. Sprecher, G. Bailey, J. Ge, and A. Tukker. Effect of chinese policies on rare earth supply chain resilience. *Resources, Conservation and Recycling*, 142:101–112, 2019. doi:[10.1016/j.resconrec.2018.11.017](https://doi.org/10.1016/j.resconrec.2018.11.017).
- [95] V. K. Pecharsky and K. A. Gschneidner Jr. Giant Magnetocaloric Effect in $\text{Gd}_5(\text{Si}_2\text{Ge}_2)$. *Physical Review Letters*, 78(23):4494–4497, 1997. doi:[10.1103/PhysRevLett.78.4494](https://doi.org/10.1103/PhysRevLett.78.4494).
- [96] S. A. Nikitin, G. Myalikhulyev, A. M. Tishin, M. P. Annaorazov, K. A. Asatryan, and A. L. Tyurinkau. The magnetocaloric effect in $\text{Fe}_{49}\text{Rh}_{51}$ compound. *Physics Letters A*, 148:363–366, 1990. doi:[10.1016/0375-9601\(90\)90819-A](https://doi.org/10.1016/0375-9601(90)90819-A).
- [97] M. P. Annaorazov, K. A. Asatryan, G. Myalikhulyev, S. A. Nikitin, A. M. Tishin, and A. L. Tyurinkau. Alloys of the Fe-Rh system as a new class of working material for magnetic refrigerators. *Cryogenics*, 32:867–872, 1992. doi:[10.1016/0011-2275\(92\)90352-B](https://doi.org/10.1016/0011-2275(92)90352-B).
-

-
- [98] E. M. Hofer and P. Cucka. Magnetic properties of Rh-rich FeRh alloy. *Journal of Physics and Chemistry of Solids*, 27:1552–1555, 1966. doi:[10.1016/0022-3697\(66\)90151-X](https://doi.org/10.1016/0022-3697(66)90151-X).
- [99] M. Takahashi and R. Oshima. Annealing Effect on Phase Transition of Equiatomic FeRh Alloy. *Materials Transactions*, 36(6):735–742, 1995. doi:[10.2320/matertrans1989.36.735](https://doi.org/10.2320/matertrans1989.36.735).
- [100] L. H. Lewis, C. H. Marrows, and S. Langridge. Coupled magnetic, structural, and electronic phase transitions in FeRh. *J. Phys. D: Appl. Phys.*, 49:323002, 2016. doi:[10.1088/0022-3727/49/32/323002](https://doi.org/10.1088/0022-3727/49/32/323002).
- [101] A. Chirkova, F. Bittner, K. Nenkov, N. V. Baranov, L. Schultz, K. Nielsch, and T. G. Woodcock. The effect of the microstructure on the antiferromagnetic to ferromagnetic transition in FeRh alloys. *Acta Materialia*, 131:31–38, 2017. doi:[10.1016/j.actamat.2017.04.005](https://doi.org/10.1016/j.actamat.2017.04.005).
- [102] A. Chirkova, K. P. Skokov, L. Schultz, N. V. Baranov, O. Gutfleisch, and T. G. Woodcock. Giant adiabatic temperature change in FeRh alloys evidenced by direct measurements under cyclic conditions. *Acta Materialia*, 106:15–21, 2016. doi:[10.1016/j.actamat.2015.11.054](https://doi.org/10.1016/j.actamat.2015.11.054).
- [103] V. K. Pecharsky and K. A. Gschneidner Jr. Magnetocaloric effect and magnetic refrigeration. *Journal of Magnetism and Magnetic Materials*, 200:44–56, 1999.
- [104] X. X. Zhang, G. H. Wen, F. W. Wang, W. H. Wang, and C. H. Yu. Magnetic entropy change in Fe-based compound $\text{LaFe}_{10.6}\text{Si}_{2.4}$. *Applied Physics Letters*, 77:3072–3074, 2000. doi:[10.1063/1.1323993](https://doi.org/10.1063/1.1323993).
- [105] F.-X. Hu, B.-G. Shen, J.-R. Sun, Z.-H. Cheng, G.-H. Rao, and X.-X. Zhang. Influence of negative lattice expansion and metamagnetic transition on magnetic entropy change in the compound $\text{LaFe}_{11.4}\text{Si}_{1.6}$. *Applied Physics Letters*, 78:3675–3677, 2001. doi:[10.1063/1.1375836](https://doi.org/10.1063/1.1375836).
- [106] A. Fujita, S. Fujieda, Y. Hasegawa, and K. Fukamichi. Itinerant-electron metamagnetic transition and large magnetovolume effects in $\text{La}(\text{Fe}_x\text{Si}_{1-x})_{13}$ compounds and their hydrides. *Physical Review B*, 67:104416, 2003. doi:[10.1103/PhysRevB.67.104416](https://doi.org/10.1103/PhysRevB.67.104416).
- [107] O. Gutfleisch, A. Yan, and K.-H. Müller. Large magnetocaloric effect in melt-spun $\text{LaFe}_{13-x}\text{Si}_x$. *Journal of Applied Physics*, 97(10):10M305, 2005. doi:[10.1063/1.1847871](https://doi.org/10.1063/1.1847871).
- [108] O. Tegus, E. Brück, K. H. J. Buschow, and F. R. de Boer. Transition-metal-based magnetic refrigerants for room-temperature applications. *Nature*, 415:150–152, 2002. doi:[10.1038/415150a](https://doi.org/10.1038/415150a).
- [109] N. H. Dung, Z. Q. Ou, L. Caron, L. Zhang, D. T. Cam Thanh, G. A. de Wijs, R. A. de Groot, K. H. J. Buschow, and E. Brück. Mixed magnetism for refrigeration and energy conversion. *Advanced Energy Materials*, 1(6):1215–1219, 2011. doi:[10.1002/aenm.201100252](https://doi.org/10.1002/aenm.201100252).
- [110] M. Fries, L. Pfeuffer, E. Bruder, T. Gottschall, S. Ener, L. V. B. Diop, T. Gröb, K. P. Skokov, and O. Gutfleisch. Microstructural and magnetic properties of Mn-Fe-P-Si (Fe_2P -type) magnetocaloric compounds. *Acta Materialia*, 132:222–229, 2017. doi:[10.1016/j.actamat.2017.04.040](https://doi.org/10.1016/j.actamat.2017.04.040).

-
- [111] A. Fujita, S. Fujieda, K. Fukamichi, H. Mitamura, and T. Goto. Itinerant-electron metamagnetic transition and large magnetovolume effects in $\text{La}(\text{Fe}_x\text{Si}_{1-x})_{13}$ compounds. *Physical Review B*, 65: 014410, 2001. doi:[10.1103/PhysRevB.65.014410](https://doi.org/10.1103/PhysRevB.65.014410).
- [112] A. Fujita and K. Fukamichi. X-ray diffraction study in high magnetic fields of magnetovolume effect in itinerant-electron metamagnetic $\text{La}(\text{Fe}_{0.88}\text{Si}_{0.12})_{13}$ compound. *Journal of Applied Physics*, 95:6687, 2004. doi:[10.1063/1.1667455](https://doi.org/10.1063/1.1667455).
- [113] A. Waske, E. Lovell, A. Funk, K. Sellschopp, A. Rack, L. Giebeler, P. F. Gostin, S. Fähler, and L. F. Cohen. The impact of surface morphology on the magnetovolume transition in magnetocaloric $\text{LaFe}_{11.8}\text{Si}_{1.2}$. *APL Materials*, 4:106101, 2016. doi:[10.1063/1.4963840](https://doi.org/10.1063/1.4963840).
- [114] J. Lyubina, O. Gutfleisch, M. Kuzmin, and M. Richter. $\text{La}(\text{Fe},\text{Si})_{13}$ -based magnetic refrigerants obtained by novel processing routes. *Journal of Magnetic Materials*, 321:3571–3577, 2009. doi:[10.1016/j.jmmm.2008.03.063](https://doi.org/10.1016/j.jmmm.2008.03.063).
- [115] J. Liu, J. D. Moore, K. P. Skokov, M. Krautz, K. Löwe, A. Barcza, M. Katter, and O. Gutfleisch. Exploring $\text{La}(\text{Fe},\text{Si})_{13}$ -based magnetic refrigerants towards application. *Scripta Materialia*, 67(6):584–589, 2012. doi:[10.1016/j.scriptamat.2012.05.039](https://doi.org/10.1016/j.scriptamat.2012.05.039).
- [116] S. Fujieda, A. Fujita, K. Fukamichi, Y. Yamazaki, and Y. Iijima. Giant isotropic magnetostriction of itinerant-electron metamagnetic $\text{La}(\text{Fe}_{0.88}\text{Si}_{0.12})_{13}\text{H}_y$ compounds. *Applied Physics Letters*, 79: 653–655, 2001. doi:[10.1063/1.1388157](https://doi.org/10.1063/1.1388157).
- [117] K. Mandal, D. Pal, O. Gutfleisch, P. Kersch, and K.-H. Müller. Magnetocaloric effect in reactively-milled $\text{LaFe}_{11.57}\text{Si}_{1.43}\text{H}_y$ intermetallic compounds. *Journal of Applied Physics*, 102:053906, 2007. doi:[10.1063/1.2775877](https://doi.org/10.1063/1.2775877).
- [118] S. Fujieda, Y. Hasegawa, A. Fujita, and K. Fukamichi. Direct measurement of magnetocaloric effects in itinerant-electron metamagnets $\text{La}(\text{Fe}_x\text{Si}_{1-x})_{13}$ compounds and their hydrides. *Journal of Magnetism and Magnetic Materials*, 272-276:2365–2366, 2004. doi:[10.1016/j.jmmm.2003.12.968](https://doi.org/10.1016/j.jmmm.2003.12.968).
- [119] The Institute of Rare Earths and Metals eV. Webpage. URL <https://en.institut-seltene-erden.de/our-service-2/Metal-prices/rare-earth-prices/>. Last accessed 08.10.2020.
- [120] J. Lyubina, R. Schäfer, N. Martin, L. Schultz, and O. Gutfleisch. Novel design of $\text{La}(\text{Fe},\text{Si})_{13}$ alloys towards high magnetic refrigeration performance. *Advanced Materials*, 22:3735–3739, 2010. doi:[10.1002/adma.201000177](https://doi.org/10.1002/adma.201000177).
- [121] E. Brück. *Handbook of Magnetic Materials*, volume 17, chapter Magnetocaloric refrigeration at ambient temperature. Elsevier Science, 2007. ISBN 9780080553863.

-
- [122] A. Bartok, M. Kustov, L. F. Cohen, A. Pasko, K. Zehani, L. Bessais, F. Mazaleyrat, and M. LoBue. Study of the first paramagnetic to ferromagnetic transition in as prepared samples of Mn–Fe–P–Si magnetocaloric compounds prepared by different synthesis routes. *Journal of Magnetism and Magnetic Materials*, 400:333–338, 2016. doi:[10.1016/j.jmmm.2015.08.045](https://doi.org/10.1016/j.jmmm.2015.08.045).
- [123] L. Zhang, O. Moze, K. Prokes, O. Tegus, and E. Brück. Neutron diffraction study of history dependence in $\text{MnFeP}_{0.6}\text{Si}_{0.4}$. *Journal of Magnetism and Magnetic Materials*, 290-291:679–681, 2005. doi:[10.1016/j.jmmm.2004.11.335](https://doi.org/10.1016/j.jmmm.2004.11.335).
- [124] X. F. Miao, L. Caron, Z. Gercsi, A. Daoud-Aladine, N. H. van Dijk, and E. Brück. Thermal-history dependent magnetoelastic transition in $(\text{Mn,Fe})_2(\text{P,Si})$. *Applied Physics Letters*, 107:042403, 2015. doi:[10.1063/1.4927285](https://doi.org/10.1063/1.4927285).
- [125] T. Gottschall, K. P. Skokov, B. Frincu, and O. Gutfleisch. Large reversible magnetocaloric effect in Ni-Mn-In-Co. *Applied Physics Letters*, 106:021901, 2015. doi:[10.1063/1.4905371](https://doi.org/10.1063/1.4905371).
- [126] F. Heusler, W. Starck, and E. Haupt. Über magnetische Manganlegierungen. *Verhandlungen der deutschen physikalischen Gesellschaft*, 5:219–228, 1903.
- [127] J. C. Slayter. Cohesion in monovalent metals. *Physical Review*, 35(5):509–529, 1930. doi:[10.1103/PhysRev.35.509](https://doi.org/10.1103/PhysRev.35.509).
- [128] A. Sommerfeld and H. Bethe. *Handbuch der Physik*. Springer, 1933.
- [129] O. Heusler. Kristallstruktur und Ferromagnetismus der Mangan-Aluminium-Kupferlegierungen. *Annalen der Physik*, 5(19):155–201, 1934.
- [130] P. J. Webster. Heusler alloys. *Contemporary Physics*, 10(6):559, 577 1969. doi:[10.1080/00107516908204800](https://doi.org/10.1080/00107516908204800).
- [131] G. E. Bacon and J. S. Plant. Chemical ordering in Heusler alloys with the general formula A_2BC or ABC . *Journal of Physics F: Metal Physics*, 1(4):524, 1971. doi:[10.1088/0305-4608/1/4/325](https://doi.org/10.1088/0305-4608/1/4/325).
- [132] T. Graf, C. Felser, and S. S. P. Parkin. Simple rules for the understanding of Heusler compounds. *Progress in Solid State Chemistry*, 39:1–50, 2011. doi:[10.1016/j.progsolidstchem.2011.02.001](https://doi.org/10.1016/j.progsolidstchem.2011.02.001).
- [133] T. Graf, S. S. Parkin, and C. Felser. Heusler Compounds - A Material Class With Exceptional Properties. *IEEE Transactions on Magnetics*, 47(2):367–373, 2011. doi:[10.1109/TMAG.2010.2096229](https://doi.org/10.1109/TMAG.2010.2096229).
- [134] J. Yang, H. Li, T. Wu, W. Zhang, L. Chen, and J. Yang. Evaluation of half-Heusler compounds as thermoelectric materials based on the calculated electrical transport properties. *Advanced Functional Materials*, 18:2880–2888, 2008. doi:[10.1002/adfm.200701369](https://doi.org/10.1002/adfm.200701369).
- [135] K. Nikolaev, P. Kolbo, X. Pokhil, T. and Peng, Y. Chen, T. Ambrose, and O. Mryasov. “all-Heusler alloy” current-perpendicular-to-plane giant magnetoresistance. *Applied Physics Letters*, 94(22):222501, 2009. doi:[10.1063/1.3126962](https://doi.org/10.1063/1.3126962).
-

-
- [136] C. Felser, L. Wollmann, S. Chadov, G. H. Fecher, and S. S. P. Parkin. Basics and prospective of magnetic Heusler compounds. *APL Materials*, 3:041518, 2015. doi:[10.1063/1.4917387](https://doi.org/10.1063/1.4917387).
- [137] L. Wollmann, A. K. Nayak, S. S. P. Parkin, and C. Felser. Heusler 4.0: Tunable Materials. *Annual Review of Materials Research*, 47:247–270, 2017. doi:[10.1146/annurev-matsci-070616-123928](https://doi.org/10.1146/annurev-matsci-070616-123928).
- [138] K. Ullakko, J. K. Huang, C. Kantner, R. C. O’Handley, and V. V. Kokorin. Large magnetic-field-induced strains in Ni₂MnGa single crystals. *Applied Physics Letters*, 69:1966–1968, 1996. doi:[10.1063/1.117637](https://doi.org/10.1063/1.117637).
- [139] Y. Sutou, Y. Imano, N. Koeda, T. Omori, R. Kainuma, K. Ishida, and K. Oikawa. Magnetic and martensitic transformations of NiMnX(X = In,Sn,Sb) ferromagnetic shape memory alloys. *Appl. Phys. Lett.*, 85:4358–4360, 2004. doi:[10.1063/1.1808879](https://doi.org/10.1063/1.1808879).
- [140] Igor Dubenko, Mahmud Khan, Arjun Kumar Pathak, Bhoj Raj Gautam, Shane Stadler, and Naushad Ali. Magnetocaloric effects in Ni-Mn-X based Heusler alloys with X=Ga, Sb, In. *J. Magn. Magn. Mater.*, 321:754–757, 2009. doi:[10.1016/j.jmmm.2008.11.043](https://doi.org/10.1016/j.jmmm.2008.11.043).
- [141] R. Kainuma, K. Oikawa, W. Ito, Y. Sutou, T. Kanomata, and K. Ishida. Metamagnetic shape memory effect in NiMn-based Heusler-type alloys. *Journal of Materials Chemistry*, 18:1837–1842, 2008. doi:[10.1039/b713947k](https://doi.org/10.1039/b713947k).
- [142] A. Taubel, T. Gottschall, M. Fries, S. Riegg, C. Soon, K. P. Skokov, and O. Gutfleisch. A comparative study on the magnetocaloric properties of Ni-Mn-X(-Co) Heusler alloys. *Phys. Status Solidi B*, 255:1700331, 2018. doi:[10.1002/pssb.201700331](https://doi.org/10.1002/pssb.201700331).
- [143] B. Li, W. J. Ren, Q. Zhang, X. K. Lv, X. G. Liu, H. Meng, J. Li, D. Li, and Z. D. Zhang. Magnetostructural coupling and magnetocaloric effect in Ni–Mn–In. *Applied Physics Letters*, 95:172506, 2009. doi:[10.1063/1.3257381](https://doi.org/10.1063/1.3257381).
- [144] T. Gottschall. *On the magnetocaloric properties of Heusler compounds: Reversible, time- and size-dependent effects of the martensitic phase transition*. PhD thesis, Technical University of Darmstadt, 2016.
- [145] V. Johnson. Diffusionless orthorhombic to hexagonal transitions in ternary silicides and germanides. *Inorganic Chemistry*, 14(5):1117–1120, 1975. doi:[10.1021/ic50147a032](https://doi.org/10.1021/ic50147a032).
- [146] W. Bazela, A. Szytula, J. Todorovic, Z. Tomkowicz, and A. Zieba. Crystal and magnetic structure of NiMnGe. *Physica status solidi (a)*, 38:721–729, 1976. doi:[10.1002/pssa.2210380235](https://doi.org/10.1002/pssa.2210380235).
- [147] S Niziol, A Weselucha, W. Bazela, and A. Szytula. Magnetic properties of the Co_xNi_{1-x}MnGe system. *Solid State Communications*, 39:1081–1085, 1981. doi:[10.1016/0038-1098\(81\)90213-1](https://doi.org/10.1016/0038-1098(81)90213-1).

-
- [148] E. Liu, W. Wang, L. Feng, W. Zhu, G. Li, J. Chen, H. Zhang, G. Wu, C. Jiang, H. Xu, and F. de Boer. Stable magnetostructural coupling with tunable magneto-responsive effects in hexagonal ferromagnets. *Nature Communications*, 3:873, 2012. doi:[10.1038/ncomms1868](https://doi.org/10.1038/ncomms1868).
- [149] A. Taubel, T. Gottschall, M. Fries, T. Faske, K. P. Skokov, and Oliver Gutfleisch. Influence of magnetic field, chemical pressure and hydrostatic pressure on the structural and magnetocaloric properties of the Mn-Ni-Ge system. *J. Phys. D:Appl. Phys.*, 50:464005, 2017. doi:[10.1088/1361-6463/aa8e89](https://doi.org/10.1088/1361-6463/aa8e89).
- [150] C. L. Zhang, D. H. Wang, Q. Q. Cao, Z. D. Han, H. C. Xuan, and Y. W. Du. Magnetostructural phase transition and magnetocaloric effect in off-stoichiometric $\text{Mn}_{1.9-x}\text{Ni}_x\text{Ge}$ alloys. *Applied Physics Letters*, 93(12):122505, 2008. doi:[10.1063/1.2990649](https://doi.org/10.1063/1.2990649).
- [151] N. T. Trung, L. Zhang, L. Caron, K. H. J. Buschow, and E. Brück. Giant magnetocaloric effects by tailoring the phase transitions. *Applied Physics Letters*, 96:172504, 2010. doi:[10.1063/1.3399773](https://doi.org/10.1063/1.3399773).
- [152] A. Quetz, T. Samanta, I. Dubenko, M. J. Kangas, J. Y. Chan, S. Stadler, and N. Ali. Phase diagram and magnetocaloric effects in aluminum doped MnNiGe alloys. *Journal of Applied Physics*, 114:153909, 2013. doi:[10.1063/1.4826260](https://doi.org/10.1063/1.4826260).
- [153] Z. Wang, Z. Nie, J. Zeng, R. Su, Y. Zhang, D. E. Brown, Y. Ren, and Y. Wang. First-order magnetostructural transformation in Fe doped Mn-Co-Ge alloys. *Journal of Alloys and Compounds*, 577:486–490, 2013. doi:[10.1016/j.jallcom.2013.05.205](https://doi.org/10.1016/j.jallcom.2013.05.205).
- [154] R. R. Wu, L. F. Bao, F. X. Hu, X. Q. Zheng, Y. Liu, J. R. Sun, and B. G. Shen. Effect of substitution of In for Co on magnetostructural coupling and magnetocaloric effect in $\text{MnCo}_{1-x}\text{In}_x\text{Ge}$ compounds. *Journal of Applied Physics*, 115:17A911, 2014. doi:[10.1063/1.4863255](https://doi.org/10.1063/1.4863255).
- [155] E. K. Liu, W. Zhu, L. Feng, J. L. Chen, W. H. Wang, G. H. Wu, H. Y. Liu, F. B. Meng, H. Z. Luo, and Y. X. Li. Vacancy-tuned paramagnetic/ferromagnetic martensitic transformation in Mn-poor $\text{Mn}_{1-x}\text{CoGe}$ alloys. *EPL (Europhysics Letters)*, 91(1):17003, 2010. doi:[10.1209/0295-5075/91/17003](https://doi.org/10.1209/0295-5075/91/17003).
- [156] J. Liu, K. Skokov, and O. Gutfleisch. Magnetostructural transition and adiabatic temperature change in Mn-Co-Ge magnetic refrigerants. *Scripta Materialia*, 66(9):642–645, 2012. doi:[10.1016/j.scriptamat.2012.01.048](https://doi.org/10.1016/j.scriptamat.2012.01.048).
- [157] Y. Li, H. Zhang, K. Tao, Y. Wang, M. Wu, and Y. Long. Giant magnetocaloric effect induced by reemergence of magnetostructural coupling in Si-doped $\text{Mn}_{0.95}\text{CoGe}$ compounds. *Materials and Design*, 114:410–415, Jan 2017. doi:[10.1016/j.matdes.2016.11.002](https://doi.org/10.1016/j.matdes.2016.11.002).
- [158] C. L. Zhang, H. F. Shi, Z. D. Han, B. Qian, C. Zhu, J. Chen, T. Z. Wang, and D. H. Wang. The TiNiSi-to-Ni₂In-type magnetostructural transitions in alloys with largely reduced Ge-concentrations. *Solid State Communications*, 190:1–4, 2014. doi:[10.1016/j.ssc.2014.03.016](https://doi.org/10.1016/j.ssc.2014.03.016).
- [159] T. Samanta, I. Dubenko, A. Quetz, S. Stadler, and N. Ali. Giant magnetocaloric effects near room temperature in $\text{Mn}_{1-x}\text{Cu}_x\text{CoGe}$. *Applied Physics Letters*, 101(24):242405, 2012. doi:[10.1063/1.4770379](https://doi.org/10.1063/1.4770379).
-

-
- [160] C. L. Zhang, H. F. Shi, Y. G. Nie, E. J. Ye, Z. D. Han, and D. H. Wang. Thermal-cycling-dependent magnetostructural transitions in a Ge-free system $\text{Mn}_{0.5}\text{Fe}_{0.5}\text{Ni}(\text{Si},\text{Al})$. *Applied Physics Letters*, 105: 242403, 2014. doi:[10.1063/1.4904464](https://doi.org/10.1063/1.4904464).
- [161] F. Albertini, J. Kamarád, Z. Arnold, L. Pareti, E. Villa, and L. Righi. Pressure effects on the magnetocaloric properties of Ni-rich and Mn-rich Ni_2MnGa alloys. *Journal of Magnetism and Magnetic Materials*, 316:364–367, 2007. doi:[10.1016/j.jmmm.2007.03.020](https://doi.org/10.1016/j.jmmm.2007.03.020).
- [162] E. Stern-Taulats, P. Lloveras, M. Barrio, E. Defay, M. Egilmez, A. Planes, J.-L. Tamarit, L. Mañosa, N. D. Mathur, and X. Moya. Inverse barocaloric effects in ferroelectric BaTiO_3 ceramics. *APL Materials*, 4: 091102, 2016. doi:[10.1063/1.4961598](https://doi.org/10.1063/1.4961598).
- [163] A. Chauhan, S. Patel, and R. Vaish. Multicaloric effect in $\text{Pb}(\text{Mn}_{1/3}\text{Nb}_{2/3})\text{O}_3$ - 32PbTiO_3 single crystals. *Acta Materialia*, 89:384–395, 2015. doi:[10.1016/j.actamat.2015.01.070](https://doi.org/10.1016/j.actamat.2015.01.070).
- [164] Y.-Y. Gong, D.-H. Wang, Q.-Q. Cao, E.-K. Liu, J. Liu, and Y.-W. Du. Electric field control of the magnetocaloric effect. *Advanced Materials*, 27:801–805, 2014. doi:[10.1002/adma.201404725](https://doi.org/10.1002/adma.201404725).
- [165] A. Shen, W. Sun, D. Zhao, and J. Liu. Influence of Cr on microstructure and elastocaloric effect in Ni–Mn–In–Co–Cr polycrystalline alloys. *Physics Letters A*, 382(39):2876–2879, 2018. doi:[10.1016/j.physleta.2018.06.022](https://doi.org/10.1016/j.physleta.2018.06.022).
- [166] X.-M. Huang, L.-D. Wang, H.-X. Liu, H.-L. Yan, N. Jia, B. Yang, Z.-B. Li, Y.-D. Zhang, C. Esling, X. Zhao, and L. Zuo. Correlation between microstructure and martensitic transformation, mechanical properties and elastocaloric effect in Ni–Mn-based alloys. *Intermetallics*, 113:106579, 2019. doi:[10.1016/j.intermet.2019.106579](https://doi.org/10.1016/j.intermet.2019.106579).
- [167] Z. Y. Wei, E. K. Liu, J. H. Chen, Y. Li, G. D. Liu, H.Z. Luo, X. K. Xi, H. W. Zhang, W. H. Wang, and G. H. Wu. Realization of multifunctional shape-memory ferromagnets in all-d-metal Heusler phases. *Applied Physics Letters*, 107:022406, 2015. doi:[10.1063/1.4927058](https://doi.org/10.1063/1.4927058).
- [168] H. M. Rietveld. A profile refinement method for nuclear and magnetic structures. *Journal of Applied Crystallography*, 2(2):65–71, Jun 1969. doi:[10.1107/S0021889869006558](https://doi.org/10.1107/S0021889869006558).
- [169] Juan Rodriguez-Carvajal. Recent advances in magnetic structure determination by neutron powder diffraction. *Physica B: Condensed Matter*, 192(1–2):55–69, 1993. doi:[10.1016/0921-4526\(93\)90108-I](https://doi.org/10.1016/0921-4526(93)90108-I).
- [170] K. Momma and F. Izumi. VESTA3 for three-dimensional visualization of crystal, volumetric and morphology data. *Journal of Applied Crystallography*, 44(6):1272–1276, 2011. doi:[10.1107/S0021889811038970](https://doi.org/10.1107/S0021889811038970).
- [171] L. Caron, Z. Q. Ou, T. T. Nguyen, D. T. Cam Thanh, O. Tegus, and E. Brück. On the determination of the magnetic entropy change in materials with first-order transitions. *Journal of Magnetism and Magnetic Materials*, 321:3559–3566, 2009. doi:[10.1016/j.jmmm.2009.06.086](https://doi.org/10.1016/j.jmmm.2009.06.086).

-
- [172] H. Neves-Bez, H. Yibole, A. Pathak, Y. Mudryk, and V. K. Pecharsky. Best practices in evaluation of the magnetocaloric effect from bulk magnetization measurements. *Journal of Magnetism and Magnetic Materials*, 458:301–309, 2018. doi:[10.1016/j.jmmm.2018.03.020](https://doi.org/10.1016/j.jmmm.2018.03.020).
- [173] C. Wheatstone. An account of several new instruments and processes for determining the constants of a voltaic circuit. *Philosophical Transactions of the Royal Society of London*, 4:469–471, 1843. doi:[10.1098/rspl.1837.0240](https://doi.org/10.1098/rspl.1837.0240).
- [174] *Physical Property Measurement System - Heat Capacity Option User's Manual*. Part Number 1085-150, H-1, Quantum Design GmbH.
- [175] I. Titov, M. Acet, M. Farle, D. González-Alonso, L. Mañosa, A. Planes, and T. Krenke. Hysteresis effects in the inverse magnetocaloric effect in martensitic Ni-Mn-In and Ni-Mn-Sn. *Journal of Applied Physics*, 112:073914, 2012. doi:[10.1063/1.4757425](https://doi.org/10.1063/1.4757425).
- [176] C. Soon. Magnetostrukturelle Umwandlungen in Co-Substituierten Ni-Mn-Sn-Heusler-Legierungen für thermomagnetische Anwendungen. Bachelor Thesis, Technical University of Darmstadt, 2017.
- [177] A. Taubel. Study of magnetocaloric and microstructural properties of Heusler-type alloys. Master Thesis, Technical University of Darmstadt, 2015.
- [178] Y. Sutou, I. Ohnuma, R. Kainuma, and K. Ishida. Ordering and martensitic transformations of Ni₂AlMn Heusler alloys. *Metallurgical and Materials Transactions A*, 29A:2225–2227, 1998. doi:[10.1007/s11661-998-0047-8](https://doi.org/10.1007/s11661-998-0047-8).
- [179] R. Kainuma, F. Gejima, Y. Sutou, I. Ohnuma, and K. Ishida. Ordering, martensitic and ferromagnetic transformations in Ni-Al-Mn Heusler shape memory alloys. *Materials Transactions*, 41(8):943–949, 2000. doi:[10.2320/matertrans1989.41.943](https://doi.org/10.2320/matertrans1989.41.943).
- [180] W. Ito, M. Nagasako, R. Y. Umetsu, R. Kainuma, T. Kanomata, and K. Ishida. Atomic ordering and magnetic properties in the Ni₄₅Co₅Mn_{36.7}In_{13.3} metamagnetic shape memory alloy. *Applied Physics Letters*, 93:232503, 2008. doi:[10.1063/1.3043456](https://doi.org/10.1063/1.3043456).
- [181] T. Miyamoto, W. Ito, Y. Umetsu, T. Kanomata, K. Ishida, and R. Kainuma. Influence of annealing conditions on magnetic properties of Ni₅₀Mn_{50-x}In_x Heusler-type alloys. *Material Transactions*, 52(9):1836–1839, 2011. doi:[10.2320/matertrans.M2011125](https://doi.org/10.2320/matertrans.M2011125).
- [182] G. Gottstein. *Physical Foundations of Materials Science*. Springer-Verlag Berlin Heidelberg, 1st edition, 2004. ISBN 978-3-540-40139-1. Chapter 5: *Diffusion*.
- [183] D. L. Schlagel, R. W. McCallum, and T. A. Lograsso. Influence of solidification microstructure on the magnetic properties of Ni–Mn–Sn Heusler alloys. *Journal of Alloys and Compounds*, 463(1):38–46, 2008. doi:[10.1016/j.jallcom.2007.09.049](https://doi.org/10.1016/j.jallcom.2007.09.049).

-
- [184] E. Wachtel, F. Henninger, and B. Predel. Constitution and magnetic properties of Ni-Mn-Sn alloys - solid and liquid state. *Journal of Magnetism and Magnetic Materials*, 38(3):305 – 315, 1983. doi:[10.1016/0304-8853\(83\)90372-4](https://doi.org/10.1016/0304-8853(83)90372-4).
- [185] T. Krenke, M. Acet, and E. F. Wassermann. Ferromagnetism in the austenitic and martensitic states of Ni-Mn-In alloys. *Physical Review B*, 73:174413, 2006. doi:[10.1103/PhysRevB.73.174413](https://doi.org/10.1103/PhysRevB.73.174413).
- [186] T. Krenke, E. Duman, M. Acet, X. Moya, L. Mañosa, and A. Planes. Effect of Co and Fe on the inverse magnetocaloric properties of Ni-Mn-Sn. *J. Appl. Phys.*, 102:033903, 2007. doi:[10.1063/1.2761853](https://doi.org/10.1063/1.2761853).
- [187] D.Y. Cong, S. Roth, and L. Schultz. Magnetic properties and structural transformations in Ni-Co-Mn-Sn multifunctional alloys. *Acta Mater.*, 60:5335 – 5351, 2012. ISSN 1359-6454. doi:[10.1016/j.actamat.2012.06.034](https://doi.org/10.1016/j.actamat.2012.06.034). URL <http://www.sciencedirect.com/science/article/pii/S1359645412004065>.
- [188] P. W. Egolf, A. Kitanovski, M. Diebold, C. Gonin, and D. Vuarnoz. Magnetic power conversion with machines containing full or porous wheel heat exchangers. *J. Mag. Mag. Mater*, 321:758 – 762, 2009. doi:<http://dx.doi.org/10.1016/j.jmmm.2008.11.044>.
- [189] Y. Song, K. Preet Bhatti, V. Srivastava, C. Leighton, and R. D. James. Thermodynamics of energy conversion via first order phase transformation in low hysteresis magnetic materials. *Energy Environ. Sci.*, 6:1315–1327, 2013. doi:[10.1039/C3EE24021E](https://doi.org/10.1039/C3EE24021E).
- [190] E. Christiaanse, T. and Brück. Proof-of-Concept Static Thermomagnetic Generator Experimental Device. *Metall. Mater. Trans. E*, 1:36–40, 2014. doi:[10.1007/s40553-014-0006-9](https://doi.org/10.1007/s40553-014-0006-9).
- [191] Maximilian Fries, Zsolt GerCSI, Semih Ener, Konstantin P. Skokov, and Oliver Gutfleisch. Magnetic, magnetocaloric and structural properties of manganese based monoborides doped with iron and cobalt – A candidate for thermomagnetic generators. *Acta Mater.*, 113:213 – 220, 2016. doi:<http://dx.doi.org/10.1016/j.actamat.2016.05.005>.
- [192] S. Aksoy, O. Posth, M. Acet, R. Meckenstock, J. Lindner, M. Farle, and E. F. Wassermann. Ferromagnetic resonance in Ni-Mn based ferromagnetic Heusler alloys. *Journal of Physics: Conference Series*, 200:092001, 2010. doi:[10.1088/1742-6596/200/9/092001](https://doi.org/10.1088/1742-6596/200/9/092001).
- [193] F. Orlandi, S. Fabbrici, F. Albertini, P. Manuel, D. D. Khalyavin, and L. Righi. Long-range antiferromagnetic interactions in Ni-Co-Mn-Ga metamagnetic Heusler alloys: A two-step ordering studied by neutron diffraction. *Phys. Rev. B*, 94:140409, Oct 2016. doi:[10.1103/PhysRevB.94.140409](https://doi.org/10.1103/PhysRevB.94.140409).
- [194] H. C. Xuan, F. H. Chen, P. D. Han, D. H. Wang, and Y. W. Du. Effect of Co addition on the martensitic transformation and magnetocaloric effect of Ni-Mn-Al ferromagnetic shape memory alloys. *Intermetallics*, 47:31 – 35, 2014. doi:<http://dx.doi.org/10.1016/j.intermet.2013.12.007>.
-

-
- [195] J. S. Blázquez, V. Franco, A. Conde, T. Gottschall, K. P. Skokov, and O. Gutfleisch. A unified approach to describe the thermal and magnetic hysteresis in Heusler alloys. *Appl. Phys. Lett.*, 109:122410, 2016. doi:[10.1063/1.4963319](https://doi.org/10.1063/1.4963319).
- [196] V. V. Khovaylo, K. P. Skokov, O. Gutfleisch, H. Miki, R. Kainuma, and T. Kanomata. Reversibility and irreversibility of magnetocaloric effect in a metamagnetic shape memory alloy under cyclic action of a magnetic field. *Appl. Phys. Lett.*, 97:052503, 2010. doi:<http://dx.doi.org/10.1063/1.3476348>.
- [197] V. V. Khovaylo, K. Skokov, O. Gutfleisch, H. Miki, S. Takagi, T. Kanomata, V. V. Koledov, V. G. Shavrov, G. Wang, E. Palacios, J. Bartolomé, and R. Burriel. Peculiarities of the magnetocaloric properties in Ni-Mn-Sn ferromagnetic shape memory alloys. *Phys. Rev. B*, 81:214406, 2010. doi:[10.1103/PhysRevB.81.214406](https://doi.org/10.1103/PhysRevB.81.214406).
- [198] M. K. Chattopadhyay, M. A. Manekar, V. K. Sharma, P. Arora, P. Tiwari, M. K. Tiwari, and S. B. Roy. Contrasting magnetic behavior of Ni₅₀Mn₃₅In₁₅ and Ni₅₀Mn_{34.5}In_{15.5} alloys. *J. Appl. Phys.*, 108:073909, 2010. doi:[10.1063/1.3478774](https://doi.org/10.1063/1.3478774).
- [199] E. Palacios, J. Bartolomé, G. Wang, R. Burriel, K. Skokov, S. Taskaev, and V. Khovaylo. Analysis of the Magnetocaloric Effect in Heusler Alloys: Study of Ni₅₀CoMn₃₆Sn₁₃ by Calorimetric Techniques. *Entropy*, 17:1236–1252, 2015. doi:[10.3390/e17031236](https://doi.org/10.3390/e17031236).
- [200] P. J. Shamberger and F. S. Ohuchi. Hysteresis of the martensitic phase transition in magnetocaloric-effect Ni-Mn-Sn alloys. *Phys. Rev. B*, 79:144407, 2009. doi:[10.1103/PhysRevB.79.144407](https://doi.org/10.1103/PhysRevB.79.144407).
- [201] V. Basso, C. P. Sasso, K. P. Skokov, O. Gutfleisch, and V. V. Khovaylo. Hysteresis and magnetocaloric effect at the magnetostructural phase transition of Ni-Mn-Ga and Ni-Mn-Co-Sn Heusler alloys. *Phys. Rev. B*, 85:014430, 2012. doi:[10.1103/PhysRevB.85.014430](https://doi.org/10.1103/PhysRevB.85.014430).
- [202] K. P. Skokov, K. H. Müller, J. D. Moore, J. Liu, A. Y. Karpenkov, M. Krautz, and O. Gutfleisch. Influence of thermal hysteresis and field cycling on the magnetocaloric effect in LaFe_{11.6}Si_{1.4}. *Journal of Alloys and Compounds*, 552:310–317, 2013. doi:[10.1016/j.jallcom.2012.10.008](https://doi.org/10.1016/j.jallcom.2012.10.008).
- [203] T. Gottschall, M. D. Kuz'min, K. P. Skokov, Y. Skourski, M. Fries, O. Gutfleisch, M. Ghorbani Zavareh, D. L. Schlagel, Y. Mudryk, V. Pecharsky, and J. Wosnitza. Magnetocaloric effect of gadolinium in high magnetic fields. *Physical Review B*, 99:134429, 2019. doi:[10.1103/physrevb.99.134429](https://doi.org/10.1103/physrevb.99.134429).
- [204] T. Gottschall, K. P. Skokov, F. Scheibel, M. Acet, M. Ghorbani Zavareh, Y. Skourski, J. Wosnitza, M. Farle, and O. Gutfleisch. Dynamical Effects of the Martensitic Transition in Magnetocaloric Heusler Alloys from Direct ΔT_{ad} Measurements under Different Magnetic-Field-Sweep Rates. *Phys. Rev. Applied*, 5:024013, 2016. doi:[10.1103/PhysRevApplied.5.024013](https://doi.org/10.1103/PhysRevApplied.5.024013).
- [205] Z. Y. Wei, E. K. Liu, Y. Li, X. L. Han, Z. W. Du, H. Z. Luo, G. D. Liu, X. K. Xi, H. W. Zhang, W. H. Wang, and G. H. Wu. Magnetostructural martensitic transformations with large volume changes

-
- and magneto-strains in all-d-metal Heusler alloys. *Applied Physics Letters*, 109(7):071904, 2016. doi:[10.1063/1.4961382](https://doi.org/10.1063/1.4961382).
- [206] H. Neves-Bez, A. K. Pathak, A. Biswas, N. Zarkevich, V. Balema, Y. Mudryk, D. D. Johnson, and V. K. Pecharsky. Giant enhancement of the magnetocaloric response in Ni-Co-Mn-Ti by rapid solidification. *Acta Materialia*, 173:225–230, 2019. doi:[10.1016/j.actamat.2019.05.004](https://doi.org/10.1016/j.actamat.2019.05.004).
- [207] F. Guillou, H. Yibole, N. H. van Dijk, L. Zhang, V. Hardy, and E. Brück. About the mechanical stability of MnFe(P,Si,B) giant-magnetocaloric materials. *Journal of Alloys and Compounds*, 617:569 – 574, 2014. doi:[10.1016/j.jallcom.2014.08.061](https://doi.org/10.1016/j.jallcom.2014.08.061).
- [208] K. Liu, S. Ma, C. Ma, X. Han, K. Yu, S. Yang, Z. Zhang, Y. Song, X. Luo, C. Chen, S. U. Rehman, and Z. Zhong. Martensitic transformation and giant magneto-functional properties in all-d-metal Ni-Co-Mn-Ti alloy ribbons. *Journal of Alloys and Compounds*, 790:78–92, 2019. doi:[10.1016/j.jallcom.2019.03.173](https://doi.org/10.1016/j.jallcom.2019.03.173).
- [209] K. Liu, X. Han, K. Yu, C. Ma, Z. Zhang, Y. Song, S. Ma, H. Zeng, C. Chen, X. Luo, S. U. Rehman, and Z. Zhong. Magnetic-field-induced metamagnetic reverse martensitic transformation and magnetocaloric effect in all-d-metal Ni_{36.0}Co_{14.0}Mn_{35.7}Ti_{14.3} alloy ribbons. *Intermetallics*, 110:106472, 2019. doi:[10.1016/j.intermet.2019.106472](https://doi.org/10.1016/j.intermet.2019.106472).
- [210] A. Aznar, A. Gràcia-Condal, A. Planes, P. Lloveras, M. Barrio, J.-L. Tamarit, W. Xiong, D. Cong, C. Popescu, and L. Mañosa. Giant barocaloric effect in all-d-metal heusler shape memory alloys. *Physical Review Materials*, 3:044406, 2019. doi:[10.1103/physrevmaterials.3.044406](https://doi.org/10.1103/physrevmaterials.3.044406).
- [211] Z. Y. Wei, W. Sun, Q. Shen, Y. Shen, Y. F. Zhang, E. K. Liu, and J. Liu. Elastocaloric effect of all-d-metal heusler NiMnTi(Co) magnetic shape memory alloys by digital image correlation and infrared thermography. *Applied Physics Letters*, 114(10):101903, 2019. doi:[10.1063/1.5077076](https://doi.org/10.1063/1.5077076).
- [212] H.-L. Yan, L.-D. Wang, H.-X. Liu, X.-M. Huang, N. Jia, Z.-B. Li, B. Yang, Y.-D. Zhang, C. Esling, X. Zhao, and L. Zuo. Giant elastocaloric effect and exceptional mechanical properties in an all-d-metal Ni-Mn-Ti alloy: Experimental and ab-initio studies. *Materials & Design*, 184:108180, 2019. doi:[10.1016/j.matdes.2019.108180](https://doi.org/10.1016/j.matdes.2019.108180).
- [213] B. Beckmann. Magnetocaloric, microstructural and mechanical properties of Ni-Co-Mn-Ti Heusler alloys. Master thesis, Technical University of Darmstadt, 2019.
- [214] T. Krenke, M. Acet, E. Wassermann, X. Moya, L. Mañosa, and A. Planes. Martensitic transitions and the nature of ferromagnetism in the austenitic and martensitic states of Ni-Mn-Sn alloys. *Physical Review B*, 72:014412, 2005. doi:[10.1103/PhysRevB.72.014412](https://doi.org/10.1103/PhysRevB.72.014412).
- [215] J. Liu, S. Aksoy, N. Scheerbaum, M. Acet, and O. Gutfleisch. Large magnetostrain in polycrystalline Ni–Mn–In–Co. *Applied Physics Letters*, 95:232515, 2009. doi:[10.1063/1.3273853](https://doi.org/10.1063/1.3273853).
-

-
- [216] E. O. Hall. The deformation and ageing of mild steel: III discussion of results. *Proc. Phys. Soc. B*, 64: 747–753, 1951. doi:[10.1088/0370-1301/64/9/303](https://doi.org/10.1088/0370-1301/64/9/303).
- [217] N. J. Petch. The cleavage strength of polycrystals. *Journal of the Iron and Steel Institute*, 174:25–28, 1953.
- [218] D. Cong, W. Xiong, A. Planes, Y. Ren, L. Mañosa, P. Cao, Z. Nie, X. Sun, Z. Yang, X. Hong, and Y. Wang. Colossal elastocaloric effect in ferroelastic Ni-Mn-Ti alloys. *Physical Review Letters*, 122: 255703, 2019. doi:[10.1103/physrevlett.122.255703](https://doi.org/10.1103/physrevlett.122.255703).
- [219] R. Niemann, A. Backen, S. Kauffmann-Weiss, C. Behler, U.K. Rößler, H. Seiner, O. Heczko, K. Nielsch, L. Schultz, and S. Fähler. Nucleation and growth of hierarchical martensite in epitaxial shape memory films. *Acta Materialia*, 132:327–334, 2017. doi:[10.1016/j.actamat.2017.04.032](https://doi.org/10.1016/j.actamat.2017.04.032).
- [220] S. Cui, Y. Cui, J. Wan, Y. Rong, and J. Zhang. Grain size dependence of the martensite morphology – a phase-field study. *Computational Materials Science*, 121:131–142, 2016. doi:[10.1016/j.commatsci.2016.05.007](https://doi.org/10.1016/j.commatsci.2016.05.007).
- [221] C. Celada-Casero, J. Sietsma, and M. J. Santofimia. The role of the austenite grain size in the martensitic transformation in low carbon steels. *Materials & Design*, 167:107625, 2019. doi:[10.1016/j.matdes.2019.107625](https://doi.org/10.1016/j.matdes.2019.107625).
- [222] M. Thomas, O. Heczko, J. Buschbeck, U. K. Rößler, J. McCord, N. Scheerbaum, L. Schultz, and S. Fähler. Magnetically induced reorientation of martensite variants in constrained epitaxial Ni-Mn-Ga films grown on MgO(001). *New Journal of Physics*, 10:023040, 2008. doi:[10.1088/1367-2630/10/2/023040](https://doi.org/10.1088/1367-2630/10/2/023040).
- [223] C. P. Sasso, V. A. L'voy, V. A. Chernenko, J. M. Barandiaran, and M. Pasquale. Reorientation of Ni-Mn-Ga martensite in rotating magnetic field. *Physics Procedia*, 10:149–153, 2010. doi:[10.1016/j.phpro.2010.11.091](https://doi.org/10.1016/j.phpro.2010.11.091).
- [224] P. Debye. Zur Theorie der spezifischen Waerme. *Annalen der Physik*, 39(4):789–839, 1912. doi:[10.1002/andp.19123441404](https://doi.org/10.1002/andp.19123441404).
- [225] Charles Kittel. *Einführung in die Festkörperphysik*. Oldenbourg Verlag, 15th edition, 2013.
- [226] A.-T. Petit and P.-L. Dulong. Recherches sur quelques points importants de la Théorie de la Chaleur. *Annales de Chimie et de Physique*, 10:395–413, 1819.
- [227] V. A. Chernenko, J. M. Barandiarán, J. Rodríguez Fernández, D. P. Rojas, J. Gutiérrez, P. Lázpita, and I. Orue. Magnetic and magnetocaloric properties of martensitic Ni₂Mn_{1.4}Sn_{0.6} Heusler alloy. *Journal of Magnetism and Magnetic Materials*, 324:3519–3523, 2012. doi:[10.1016/j.jmmm.2012.02.080](https://doi.org/10.1016/j.jmmm.2012.02.080).

-
- [228] T. Gottschall, K. P. Skokov, R. Burriel, and O. Gutfleisch. On the S(T) diagram of magnetocaloric materials with first-order transition: Kinetic and cyclic effects of Heusler alloys. *Acta Materialia*, 107:1–8, 2016. doi:[10.1016/j.actamat.2016.01.052](https://doi.org/10.1016/j.actamat.2016.01.052).
- [229] V. V. Kokorin, V. A. Chernenko, E. Cesari, J. Pons, and C. Segui. Pre-martensitic state in Ni-Mn-Ga alloys. *Journal of Physics: Condensed Matter*, 8:6457–6463, 1996. doi:[10.1088/0953-8984/8/35/014](https://doi.org/10.1088/0953-8984/8/35/014).
- [230] A. Planes, E. Obradó, A. González-Comas, and L. Mañosa. Premartensitic Transition Driven by Magnetoelastic Interaction in bcc Ferromagnetic Ni₂MnGa. *Phys. Rev. Lett.*, 79:3926–3929, 1997. doi:[10.1103/PhysRevLett.79.3926](https://doi.org/10.1103/PhysRevLett.79.3926).
- [231] E. Cesari, V. A. Chernenko, V. V. Kokorin, J. Pons, and C. Segui. Internal friction associated with the structural phase transformations in Ni-Mn-Ga alloys. *Acta Materialia*, 45:999–1004, 1997. doi:[10.1016/S1359-6454\(96\)00244-3](https://doi.org/10.1016/S1359-6454(96)00244-3).
- [232] T. Gottschall, E. Bykov, A. Gràcia-Condal, B. Beckmann, A. Taubel, L. Pfeuffer, O. Gutfleisch, L. Mañosa, A. Planes, Y. Skourski, and J. Wosnitza. Advanced characterization of multicaloric materials in pulsed magnetic fields. *Journal of Applied Physics*, 127:185107, 2020. doi:[10.1063/5.0006079](https://doi.org/10.1063/5.0006079).
- [233] Z. Yang, D. Y. Cong, L. Huang, Z. H. Nie, X. M. Sun, Q. H. Zhang, and Y. D. Wang. Large elastocaloric effect in a Ni-Co-Mn-Sn magnetic shape memory alloy. *Materials and Design*, 92:932–936, 2016. doi:[10.1016/j.matdes.2015.12.118](https://doi.org/10.1016/j.matdes.2015.12.118).
- [234] R. Millán-Solsona, E. Stern-Taulats, E. Vives, A. Planes, J. Sharma, A. K. Nayak, K. G. Suresh, and L. Mañosa. Large entropy change associated with the elastocaloric effect in polycrystalline Ni-Mn-Sb-Co magnetic shape memory alloys. *Applied Physics Letters*, 105:241901, 2014. doi:[10.1063/1.4904419](https://doi.org/10.1063/1.4904419).
- [235] G. S. Bigelow, S. A. Padula II, A. Garg, D. Gaydosh, and R. D. Noebe. Characterization of Ternary NiTiPd High-Temperature Shape-Memory Alloys under Load-Biased Thermal Cycling. *Metallurgical and Materials Transactions A*, 41A:3065–3079, 2010. doi:[10.1007/s11661-010-0365-5](https://doi.org/10.1007/s11661-010-0365-5).
- [236] C. L. Zhang, D. H. Wang, Z. D. Han, B. Qian, and H. F. Shi. The tunable magnetostructural transition in MnNiSi-FeNiGe system. *Applied Physics Letters*, 103:132411, 2013. doi:[10.1063/1.4823510](https://doi.org/10.1063/1.4823510).
- [237] G. J. Li, E. K. Liu, H. G. Zhang, Y. J. Zhang, J. L. Chen, W. H. Wang, H. W. Zhang, G. H. Wu, and S. Y. Yu. Phase diagram, ferromagnetic martensitic transformation and magneto-responsive properties of Fe-doped MnCoGe alloys. *Journal of Magnetism and Magnetic Materials*, 332:146 – 150, 2013. doi:<http://dx.doi.org/10.1016/j.jmmm.2012.12.001>.
- [238] J. Zeng, Z. Wang, Z. Nie, and Y. Wang. Crystal structural transformation accompanied by magnetic transition in MnCo_{1-x}Fe_xGe alloys. *Intermetallics*, 52:101 – 104, 2014. doi:<http://dx.doi.org/10.1016/j.intermet.2014.03.014>.
-

-
- [239] C. L. Zhang, H. F. Shi, E. J. Ye, Y. G. Nie, Z. D. Han, B. Qian, and D. H. Wang. Magnetostructural transition and magnetocaloric effect in MnNiSi-Fe₂Ge system. *Applied Physics Letters*, 107:212403, 2015. doi:[10.1063/1.4936610](https://doi.org/10.1063/1.4936610).
- [240] J. Liu, Y. Gong, G. Xu, G. Peng, I. A. Shah, N. ul Hassan, and F. Xu. Realization of magnetostructural coupling by modifying structural transitions in MnNiSi-CoNiGe system with a wide Curie-temperature window. *Scientific Reports*, 6:23386, 2016. doi:[10.1038/srep23386](https://doi.org/10.1038/srep23386).
- [241] Y. Li, Z. Y. Wei, H. G. Zhang, E. K. Liu, H. Z. Luo, G. D. Liu, X. K. Xi, S. G. Wang, W. H. Wang, M. Yue, G. H. Wu, and X. X. Zhang. Windows open for highly tunable magnetostructural phase transitions. *Applied Physics Letters*, 4:071101, 2016. doi:[10.1063/1.4955214](https://doi.org/10.1063/1.4955214).
- [242] K. Xu, Z. Li, E. Liu, H. Zhou, Y. Zhang, and C. Jing. Magnetocaloric effect and negative thermal expansion in hexagonal Fe doped MnNiGe compounds with a magnetoelastic AFM-FM-like transition. *Scientific Reports*, 7:41675, 2017. doi:[10.1038/srep41675](https://doi.org/10.1038/srep41675).
- [243] W. Bazela, A. Szytula, J. Todorovic, and A. Zieba. Crystal and magnetic structure of the NiMnGe_{1-n}Si_n system. *Physica status solidi (a)*, 64:367–378, 1981. doi:[10.1002/pssa.2210640140](https://doi.org/10.1002/pssa.2210640140).
- [244] O. Beckman and L. Lundgren. *Handbook of Magnetic Materials*, volume 6. Elsevier, 1991.
- [245] J. Chen, H. G. Zhang, E. K. Liu, M. Yue, Q. M. Lu, W. H. Wang, G. H. Wu, and J. X. Zhang. Wide temperature window of magnetostructural transition achieved in Mn_{0.4}Fe_{0.6}NiSi_{1-x}Ga_x by a two-step isostructural alloying process. *AIP Advances*, 6(5):056220, 2016. doi:[10.1063/1.4944704](https://doi.org/10.1063/1.4944704).
- [246] N. Scheerbaum, R. Kraus, J. Liu, W. Skrotzki, L. Schultz, and O. Gutfleisch. Reproducibility of martensitic transformation and phase constitution in Ni-Co-Al. *Intermetallics*, 20(1):55–62, 2012. doi:[10.1016/j.intermet.2011.08.015](https://doi.org/10.1016/j.intermet.2011.08.015).
- [247] R. A. Young, editor. *The Rietveld Method*, chapter Introduction to the Rietveld method, pages 1–38. Cambridge University Press, 1993. ISBN 9780198559122.
- [248] V. Johnson and C. G. Frederick. Magnetic and crystallographic properties of ternary manganese silicides with ordered Co₂P structure. *Physica Status Solidi (a)*, 20:331–335, 1973. doi:[10.1002/pssa.2210200133](https://doi.org/10.1002/pssa.2210200133).
- [249] G. A. Landrum, R. Hoffmann, J. Evers, and H. Boysen. The TiNiSi family of compounds: Structure and bonding. *Inorganic Chemistry*, 37(22):5754–5763, 1998. doi:[10.1021/ic980223e](https://doi.org/10.1021/ic980223e).
- [250] M. Ghorbani Zavareh, Y. Skourski, K. P. Skokov, D. Yu. Karpenkov, L. Zvyagina, A. Waske, D. Haskel, M. Zhernenkov, J. Wosnitza, and O. Gutfleisch. Direct measurement of the magnetocaloric effect in La(Fe,Si,Co)₁₃ compounds in pulsed magnetic fields. *Physical Review Applied*, 8(1):014037, 2017. doi:[10.1103/physrevapplied.8.014037](https://doi.org/10.1103/physrevapplied.8.014037).

-
- [251] R.-R. Wu, L.-F. Bao, F.-X. Hu, H. Wu, Q.-Z. Huang, J. Wang, X.-L. Dong, G.-N. Li, J.-R. Sun, F.-R. Shen, T.-Y. Zhao, X.-Q. Zheng, L.-C. Wang, Y. Liu, W.-L. Zuo, Y.-Y. Zhao, M. Zhang, X.-C. Wang, C.-Q. Jin, G.-H. Rao, X.-F. Han, and B.-G. Shen. Giant barocaloric effect in hexagonal Ni₂In-type Mn-Co-Ge-In compounds around room temperature. *Scientific Reports*, 5:18027, 2015. doi:[10.1038/srep18027](https://doi.org/10.1038/srep18027).
- [252] J. Lyubina, K. Nenkov, L. Schultz, and O. Gutfleisch. Multiple metamagnetic transitions in the magnetic refrigerant La(Fe,Si)₁₃H_x. *Phys. Rev. Lett.*, 101:177203, 2008. doi:[10.1103/PhysRevLett.101.177203](https://doi.org/10.1103/PhysRevLett.101.177203).
- [253] L. Mañosa, X. Moya, A. Planes, O. Gutfleisch, J. Lyubina, M. Barrio, J.-L. Tamarit, S. Aksoy, T. Krenke, and M. Acet. Effects of hydrostatic pressure on the magnetism and martensitic transition of Ni–Mn–In magnetic superelastic alloys. *Applied Physics Letters*, 92(1):012515, 2008. doi:[10.1063/1.2830999](https://doi.org/10.1063/1.2830999).
- [254] S. Anzai and K. Ozawa. Coupled nature of magnetic and structural transition in MnNiGe under pressure. *Physical Review B*, 18(5):2173–2178, 1978. doi:[10.1103/PhysRevB.18.2173](https://doi.org/10.1103/PhysRevB.18.2173).
- [255] S. Niziol, A. Zieba, R. Zach, M. Baj, and L. Dmowski. Structural and magnetic phase transition in Co_xNi_{1-x}MnGe system under pressure. *Journal of Magnetism and Magnetic Materials*, 38:205–213, 1983. doi:[10.1016/0304-8853\(83\)90046-X](https://doi.org/10.1016/0304-8853(83)90046-X).
- [256] L. Caron, N. T. Trung, and E. Brück. Pressure-tuned magnetocaloric effect in Mn_{0.93}Cr_{0.07}CoGe. *Physical Review B*, 84:020414(R), 2011. doi:[10.1103/PhysRevB.84.020414](https://doi.org/10.1103/PhysRevB.84.020414).
- [257] P. Dutta, S. Pramanick, D. Das, and S. Chatterjee. Hydrostatic pressure tuned magneto-structural transition and occurrence of pressure induced exchange bias effect in Mn_{0.85}Fe_{0.15}NiGe alloy. *Journal of Physics D*, 49(38):385001, 2016. doi:[10.1088/0022-3727/49/38/385001](https://doi.org/10.1088/0022-3727/49/38/385001).
- [258] T. Samanta, D. L. Lepkowski, A. U. Saleheen, A. Shankar, J. Prestigiacomo, I. Dubenko, A. Quetz, I. W. H. Oswald, G. T. McCandless, J. Y. Chan, P. W. Adams, D. P. Young, N. Ali, and S. Stadler. Hydrostatic pressure-induced modifications of structural transitions lead to large enhancements of magnetocaloric effects in MnNiSi-based systems. *Physical Review B*, 91:020401(R), 2015. doi:[10.1103/PhysRevB.91.020401](https://doi.org/10.1103/PhysRevB.91.020401).
- [259] F. Guillou, F. Wilhelm, O. Tegus, and A. Rogalev. Microscopic mechanism of the giant magnetocaloric effect in MnCoGe alloys probed by x-ray circular dichroism. *Applied Physics Letters*, 108:122405, 2016. doi:[10.1063/1.4944643](https://doi.org/10.1063/1.4944643).
- [260] S. Yuce, N. M. Bruno, B. Emre, and I. Karaman. Accessibility investigation of large magnetic entropy change in CoMn_{1-x}Fe_xGe. *Journal of Applied Physics*, 119(13):133901, 2016. doi:[10.1063/1.4945118](https://doi.org/10.1063/1.4945118).
- [261] A. Aznar, P. Lloveras, J.-Y. Kim, E. Stern-Taulats, M. Barrio, J. L. Tamarit, C. F. Sánchez-Valdés, J. L. Sánchez Llamazares, N. D. Mathur, and X. Moya. Giant and reversible inverse barocaloric effects

near room temperature in ferromagnetic MnCoGeB_{0.03}. *Advanced Materials*, 31(37):1903577, 2019. doi:[10.1002/adma.201903577](https://doi.org/10.1002/adma.201903577).

- [262] H. Sepehri-Amin, A. Taubel, T. Ohkubo, K. P. Skokov, O. Gutfleisch, and K. Hono. Microstructural origin of hysteresis in Ni-Mn-In based magnetocaloric compounds. *Acta Materialia*, 147:342 – 349, 2018. doi:[10.1016/j.actamat.2018.01.044](https://doi.org/10.1016/j.actamat.2018.01.044).
- [263] P. O. Castillo-Villa, L. Mañosa, A. Planes, D. E. Soto-Parra, J. L. Sánchez-Llamazares, H. Flores-Zúñiga, and Carlos Frontera. Elastocaloric and magnetocaloric effects in Ni-Mn-Sn(Cu) shape-memory alloy. *Journal of Applied Physics*, 113:053506, 2013. doi:[10.1063/1.4790140](https://doi.org/10.1063/1.4790140).

Curriculum Vitae

Personal information

Name	Andreas Taubel
Date of birth	29 July, 1989
Place of birth	Gelnhausen, Germany
Citizenship	German

Education

2016 - 2020	Ph.D. student in Material Science Degree sought: Doctor of Engineering (Dr.-Ing.) Supervisor: Prof. O. Gutfleisch Technische Universität Darmstadt, Germany
2015	Research assistant Material Science Department, Group of Functional Materials Synthesis and characterization of magnetocaloric compounds Technische Universität Darmstadt, Germany
2013 - 2015	Master Studies of Material Science Degree: Master of Science (M.Sc.) Thesis: Study of magnetocaloric and microstructural properties of Heusler-type alloys Supervisor: Prof. O. Gutfleisch Technische Universität Darmstadt, Germany
2010 - 2013	Bachelor Studies of Material Science Degree: Bachelor of Science (B.Sc.) Thesis: Measurement of Electrical Fields on Metal-Matrix-Composites using Scanning Kelvin Probe Microscopy Supervisor: Prof. R. Stark Technische Universität Darmstadt, Germany

2009 - 2010	Alternative civilian service Kindertagesstätte "Am Sportfeld", Freigericht, Germany
2009	Abitur Kopernikusschule Freigericht, Germany
Conference contributions and Workshops	<p>MMM 2020, Palm Beach, USA (Virtual Conference), Oral presentation</p> <p>Kalorik-Workshop 2019, Freiburg, Germany</p> <p>DPG-Frühjahrstagung 2019, Regensburg, Germany, Oral presentation</p> <p>Thermag 2018, Darmstadt, Germany, Poster presentation</p> <p>DPG-Frühjahrstagung 2018, Berlin, Germany, Oral presentation</p> <p>Danish Days on Caloric Materials and Devices, Risø, Denmark, Poster presentation</p> <p>IEEE Magnetics Society Summer School 2017, Santander, Spain, Poster presentation</p> <p>INTERMAG 2017, Dublin, Ireland, Poster presentation</p> <p>DPG-Frühjahrstagung 2017, Dresden, Germany, Oral presentation</p> <p>International workshop on Hysteresis in magnetocaloric, electrocaloric and elastocaloric refrigeration 2017, Dresden, Germany, Poster presentation</p> <p>Thermag 2016, Torino, Italy, Poster presentation</p> <p>DPG-Frühjahrstagung 2016, Regensburg, Germany, Oral presentation</p>

List of Publications

- [1] T. Gottschall, D. Benke, M. Fries, **A. Taubel**, I. A. Radulov, K. P. Skokov, and O. Gutfleisch, *A Matter of Size and Stress: Understanding the First-Order Transition in Materials for Solid-State Refrigeration*, *Advanced Functional Materials* **27** (32), 1606735 (2017).
- [2] **A. Taubel**, T. Gottschall, M. Fries, T. Faske, K. P. Skokov, and O. Gutfleisch, *Influence of magnetic field, chemical pressure and hydrostatic pressure on the structural and magnetocaloric properties of the Mn-Ni-Ge system*, *Journal of Physics D: Applied Physics* **50** (46), 464005 (2017).
- [3] H. Sepehri-Amin, **A. Taubel**, T. Ohkubo, K. P. Skokov, O. Gutfleisch, and K. Hono, *Microstructural origin of hysteresis in Ni-Mn-In based magnetocaloric compounds*, *Acta Materialia* **147**, 342-349 (2018).
- [4] **A. Taubel**, T. Gottschall, M. Fries, S. Riegg, C. Soon, K. P. Skokov, and O. Gutfleisch, *A Comparative Study on the Magnetocaloric Properties of Ni-Mn-X(-Co) Heusler Alloys*, *physica status solidi (b)* **255** (2), 1700331 (2018).
- [5] F. Scheibel, T. Gottschall, **A. Taubel**, M. Fries, K. P. Skokov, A. Terwey, W. Keune, K. Ollefs, H. Wende, M. Farle, M. Acet, O. Gutfleisch, and M. E. Gruner, *Hysteresis Design of Magnetocaloric Materials-From Basic Mechanisms to Applications*, *Energy Technology* **6** (8), 1397-1428 (2018).
- [6] T. Gottschall, A. Gràcia-Condal, M. Fries, **A. Taubel**, L. Pfeuffer, L. Mañosa, A. Planes, K. P. Skokov, and O. Gutfleisch, *A multicaloric cooling cycle that exploits thermal hysteresis*, *Nature Materials* **17** (10), 929 (2018).
- [7] I. Poenaru, A. Lixandru, S. Riegg, B. Fayyazi, **A. Taubel**, K. Güth, R. Gauß, and O. Gutfleisch, *Ce and La as substitutes for Nd in Nd₂Fe₁₄B-based melt-spun alloys and hot-deformed magnets: a comparison of structural and magnetic properties*, *Journal of Magnetism and Magnetic Materials* **478**, 198-205 (2019).
- [8] T. Gottschall, K. P. Skokov, M. Fries, **A. Taubel**, I. Radulov, F. Scheibel, D. Benke, S. Riegg, and O. Gutfleisch, *Making a Cool Choice: The Materials Library of Magnetic Refrigeration*, *Advanced Energy Materials* **9**, 1901322 (2019).
- [9] T. Gottschall, E. Bykov, A. Gràcia-Condal, B. Beckmann, **A. Taubel**, L. Pfeuffer, O. Gutfleisch, L. Mañosa, A. Planes, Y. Skourski, J. Wosnitza, *Advanced characterization of multicaloric materials in pulsed magnetic fields*, *Journal of Applied Physics* **127**, 185107 (2020).

-
- [10] L. Pfeuffer, T. Gottschall, T. Faske, **A. Taubel**, F. Scheibel, A. Y. Karpenkov, S. Ener, K. P. Skokov and O. Gutfleisch, *Influence of the martensitic transformation kinetics on the magnetocaloric effect in Ni-Mn-In*, Physical Review Materials 4, 111401(2020).
- [11] **A. Taubel**, B. Beckmann, L. Pfeuffer, N. Fortunato, F. Scheibel, S. Ener, T. Gottschall, K. P. Skokov, H. Zhang, and O. Gutfleisch, *Tailoring magnetocaloric effect in all-d-metal Ni-Co-Mn-Ti Heusler alloys: a combined experimental and theoretical study*, Acta Materialia 201, 425-434 (2020).

Others

- [A] **A. Taubel**, T. Gottschall, K. P. Skokov, and O. Gutfleisch, *Study on the viability of MnNiGe-system for magnetocaloric applications*, 2017 IEEE International Magnetics Conference (INTERMAG) Proceedings, Dublin, pp. 1-2, (2017).
- [B] O. Gutfleisch, D. Benke, M. Fries, **A. Taubel**, C. Bahl, A. Barcza, K. Bartholomé, I. Colombo, I. Dumkow, B. Hurley, S. Fähler, B. Schleicher, C. Molin, T. Lorkin, A. Pastore, V. Pecharsky, S. Russek, DIN SPEC 91373: *Magnetocalorics – Terminology* (2018).

Acknowledgments

I thank **Prof. Oliver Gutfleisch** for supervising this PhD work and giving me the opportunity to comprehensively study caloric effects in his research group for Functional Materials. I highly appreciate the possibility to work on the exciting topic of future cooling solutions and develop the content of the thesis throughout the years. It was an exciting time in which I gained valuable scientific experience in the lab and by meeting the worldwide experts during conferences and project meetings. I am also grateful for his trust in the freedom he provided for my research and for the responsibilities regarding teaching activities.

In addition, I would like to thank **Prof. Heiko Wende** for agreeing to referee my thesis.

A colossal thanks goes to the *Functional Materials* group. I enjoyed working with you in a very productive atmosphere and having fun at the group activities. I especially thank everyone who was involved in the proofreading process. In detail I want to underline the support by:

- **Dr. Konstantin Skokov**, who introduced me into many sophisticated characterization techniques, helped a lot with his experience regarding interpretation of measurement results and conducted the c_p and simultaneous measurements at the PPMS.
- my former colleague **Dr. Tino Gottschall**, who taught me my first knowledge on magnetocaloric materials by supervising my Master Thesis and was still always open for consultation during my PhD. In addition, I thank him together with the High-Magnetic-Field Lab of the Helmholtz-Zentrum Dresden-Rossendorf for the measurement support with the pulsed field setup.
- **Dimitri Benke** and **Dr. Maximilian Fries** for the many discussions within the magnetocaloric team
- my former research assistant and Master student **Benedikt Beckmann**, who supported me with his excellent lab work and contributed significantly with his superb Thesis about the Ti-Heusler. It was also a great help to always discuss the peculiarities of the Ti-Heusler system. It is very hard to find a more productive student researcher.
- the whole team of the ERC "CoolInnov" for the fruitful discussions about developing Heusler alloys towards multi-stimuli cooling. Especially, I want to mention **Lukas Pfeuffer** for the support with his expertise in mechanical testing and microstructural analysis as well as **Nuno Fortunato and Jun. Prof. Hongbin Zhang** for the support with theoretical calculations in order to explain experimentally found trends for the all-*d* Heusler.
- the best officemate (and kicker-partner) imaginable, **Dr. Semih Ener**. It was a perfect mixture of personal attitude and research experience which I could always count on when I encountered scientific problems or when I needed to solve technical issues with Latex and Origin of varying difficulty.

In addition, I thank **Tom Faske and David Koch** from the *Structure Research* group for temperature dependent XRD measurements and the help with the respective data analysis and interpretation.

I also acknowledge financial support of my PhD work by DFG over the Priority Program "SPP 1599" Ferrocic Cooling and by the EU over the ERC Advanced Grant "Cool Innov".

Finally I thank my **family and friends** for all the support. I deeply thank my wife **Chantal** for always being on my side and encouraging me also in stressful times.